EFFECTS OF CAVITATION ON THE WAKE CHARACTERISTICS BEHIND BLUNT TRAILING EDGE HYDROFOILS

Jian Chen

Supervisor: Francesc Xavier ESCALER i PUIGORIOL

Submitted in fulfilment of the requirements for the degree of
Doctor of Philosophy

Fluid Mechanics department
Universitat Politècnica de Catalunya
2024

"*Rather than love, than money, than fame, give me truth*"

Henry David Thoreau (1817-1862)

Acknowledgements

First and foremost, I would like to express my sincere gratitude to my advisor, Prof. Xavier Escaler, for his unwavering support throughout my PhD program. His patience, motivation, enthusiasm, and vast knowledge have been invaluable assets to my academic journey.

In addition to my advisors, I extend my sincere appreciation to all members of my thesis committee: Prof. Victor Hugo Hidalgo, Prof. Roberto Castilla Lopez, Prof. Alfredo Guardo Zabaleta, Prof. Desheng Zhang, and Prof. Ruijie Zhao. Their encouragement, insightful comments, and thoughtful questions have been invaluable in shaping this work. I am grateful for their constructive suggestions, which have a great contribution to improving the quality of my research.

I would like to express my gratitude to the China Scholarship Council (CSC) and Universitat Politècnica de Catalunya (UPC) for their generous financial support, which has been instrumental in facilitating my research. Additionally, I am indebted to my colleagues at the Barcelona Fluids & Energy Lab for their collaboration and support throughout this work. Special thanks to Dr. David Bermejo, Dr. Rafel Roig, Mr. Xavier Sánchez, Dr. Oscar de la Torre, Dr. Linlin Geng, Mr. Ismael Fernández, and Mr. Longyue Sun for their invaluable assistance and contributions to my research.

My deepest gratitude goes to my family for their unflagging love and support throughout my life; this dissertation is simply impossible without them. I am indebted to my parents for their unconditional support and love. I have no suitable words that can fully describe their everlasting love for me.

My special gratitude is due to my friends in Barcelona, for their support.

Abstract

The recent developments in hydraulic machinery will increase the possibility of damage resulting from cavitation and/or vortex-induced vibrations. Yet, many researchers have shed light on the vortex street flow and the associated vortex-induced vibration in cavitating-free regimes, but less attention has been paid to the presence of cavitation. In the present study, the effects of cavitation on the vortex street flow behind a blunt trailing edge hydrofoil and its interaction with the vortex-induced vibration have been investigated. This will help to understand the mechanisms involved and to predict the dynamic of vortex-induced vibration with the presence of cavitation, allowing further control of this complex phenomenon in hydraulic machinery and systems.

Thus, numerical solvers have been developed that are capable of accounting for the cavitating vortex street flow behind bluff bodies which have been validated and verified using some benchmark cases. Then, the effects of the fluid compressibility in the vortex street flow behind the wedge have been determined. Moreover, a series of numerical studies on cavitating vortex street flow behind a blunt trailing edge hydrofoil NACA 0009 have been conducted by predicting the boundary layer transition. As a result, the effects of cavitation on flow dynamics and its interaction with vortex-induced vibration have been examined.

The impacts of fluid compressibility on the dynamics of the cavitating wake flow have been found to depend on the frequency range. At low frequencies, the effects of fluid compressibility are minimal and can be disregarded. On the other hand, fluid compressibility has been observed to amplify spectral energy at high frequencies. Interestingly, it has been found that almost identical numerical results with and without fluid compressibility are obtained in terms of predicted mean pressure profiles, dominant vortex shedding frequencies, and instantaneous and mean void fraction fields, which suggests that the compressibility effects on cavitating vortex shedding can be neglected.

For the cavitating vortex street flow behind a blunt trailing edge hydrofoil NACA 0009, high-fidelity numerical simulations have been established in the current thesis. Based on the results, it has been observed that cavitation has a significant impact on the wake flow dynamics, notably increasing the shedding frequency of the primary vortices. Additionally, cavitation growth leads to increased hydrodynamic loads on the hydrofoil surface. Furthermore, cavitation development enhances the advected velocity of the vortices while decreasing the streamwise inter-vortex spacing. Both factors are believed to contribute to the increase of the vortex shedding frequency while the reduction of streamwise inter-vortex spacing tends to dominate this increase.

The numerical results related to cavitating vortex street flow behind a blunt trailing edge hydrofoil NACA 0009 subjected to forced oscillation have shown that the induced dynamic response due to the oscillation is influenced by the presence of cavitation. In the lock-in regime, cavitation appears to widen the upper bound of this regime and cause a decrease in the added moment of inertia and an increase in the added damping. Moreover, the timing of the vortex shedding changes with the presence of cavitation. On the other hand, the oscillation of the hydrofoil affects the dynamics of cavitation in terms of cavitation inception and cavity length. Generally, the cavitation inception number gradually increases with the forced oscillation frequency. Meanwhile, approaching the bounds of the lock-in regime will cause local decreases in cavitation inception numbers. Besides, the length of the cavitating wake is influenced by the variation of the oscillation frequency, and the maximum cavitating wake length occurs under stationary conditions.

List of Abbreviations

CFD	Computational Fluid Dynamics
DNS	Direct-Numerical Simulation
DDES	Delayed Detached Eddy Simulation
EOS	Equation of State
FFT	Fast Fourier Transform
FVM	Finite Volume Method
ITM	Interface Tracking Model
LES	Large Eddy Simulation
MWI	Momentum-Weighted Interpolation
MUL	MULtiscale
PRESTO!	PREssure STaggering Option
RANS	Reynolds Averaged Navier Stokes
RMS	Root Mean Square
RPE	Rayleigh-Plesset Equation
SDOF	Single-Degree-Of-Freedom
SST	Shear Stress Transport
TEM	Transport Equation Model
VIV	Vortex-Induced Vibrations
VOF	Volume of Fraction
ZGB	Zwart-Gerber-Belamri

Nomenclature

a_v	Streamwise inter-vortex spacing	(m)
b_v	Cross-stream inter-vortex spacing	(m)
c	Sound speed	(m/s)
C	Chord length of hydrofoil	(m)
C_D	Drag coefficient	(-)
C_f	Skin friction coefficient	(-)
C_L	Lift coefficient	(-)
C_M	Moment coefficient	(-)
C_p	Pressure coefficient	(-)
$C_{p\,min}$	Minimum pressure coefficient	(-)
D	Circular cylinder diameter	(m)
EVR	Eddy viscosity ratio	(-)
f	Shedding frequency	(Hz)
f_{air} or f_{vac}	Natural frequency	(Hz)
f_{ex}	Excitation frequency	(Hz)
f_{vs}	Vortex shedding frequency	(Hz)
f_{sta_non}	Vortex shedding frequency at non-cavitating and stationary conditions	(Hz)
F_c	Condensation coefficient	(-)
F_v	Evaporation coefficient	(-)
J_f	Added moment of inertia	(kg·m^2)
J_s	Moment of inertia of structure	(kg·m^2)
K_f	Added Stiffness	(kg·m^2 s^2)
K_s	Stiffness of the structure	(kg·m^2 s^2)
L	Sponge layer length	(m)
M_{ex}	External excitation moment	(N m)
M_{vs}	Vortex induced moment	(N m)
M_f	Fluid moment	(N m)
nFTLE	negative time Finite Time Lyapunov Exponent	(-)
p_∞	Reference pressure	(Pa)
p_v	Saturated vapor pressure	(Pa)
p_{ref}	Reference pressure	(Pa)
R_0	Initial bubble radius	(mm)
R	Bubble radius	(mm)
$\dot{R}$	Time derivation of bubble radius	(m/s)
$Re = \frac{U_{ref}D}{\upsilon}$	Reynolds number	(-)
$St = \frac{f_{vs}D}{U_{ref}}$	Strouhal number	(-)
Δt	Time step size	(s)
T_{ex}	Period of the forced oscillation	(s)
TI	Turbulent intensity	(-)
U_{ref}	Free stream velocity	(m/s)
U_∞	Inflow velocity	(m/s)

τ_C	Bubble collapse time	(s)
ρ	Mixture density	(kg/m^3)
ρ_l	Liquid density	(kg/m^3)
η	Reflection coefficient	(-)
$\boldsymbol{\sigma}$	Sponge damping function	(-)
$\sigma = \frac{p_{ref} - p_v}{0.5\rho_l {U_{ref}}^2}$	Cavitation number	(-)
σ_i	Cavitation inception number	(-)
$\Delta\sigma$	Difference between σ and σ_i	(-)
ν	Fluid dynamic viscosity	(m^2/s)
α	Angle of attack	(°)
α_v	Vapor volume fraction	(-)
ζ_s	Damping of the structure	(kg·m^2 s)
ζ_f	Added damping	(kg·m^2 s)
τ_w	Wall shear stress	(Pa)
ω_{ex}	Angular velocity of forced oscillation	(s^{-1})
φ	Phase angle at lock-in regime	(°)
φ_{vs}	Phase angle due to vortex shedding	(°)
φ_f	Phase angle of fluid moment	(°)

Contents

List of Figures

List of Tables

Part I

Chapter 1: Introduction

1.1 MOTIVATION

In recent years, the multi-point design for modern hydraulic machinery has increasingly approached the material limits, causing a more flexible structure. As blade/runner or guide vanes are placed in the fluid, they exhibit complex flow structures that extend to their wakes. Above a critical value of Reynolds number, the classical flow pattern consisting of periodic vortices array termed von Kármán vortices tends to appear at the trailing edge (C. H. Williamson, 1996). The alternating shed vortices lead to the fluctuation of force acting on the surface, which is known as vortex-induced vibrations. Now, it has become one of the primary failure mechanisms. When the ambient pressure is low enough, the vaporous cavity will be initiated and persist inside the center of the alternating shed vortices (Brennen, 2014). As these cavities inside the vortices are advected to the high-pressure region and then collapse, they will induce a higher impact load, resulting in severe material erosion on the adjacent surface. In addition, the dynamic behavior of vortex street flow will be strongly altered by the occurrence and development of cavitation (J. O. Young & Holl, 1966; Belahadji et al., 1995; Ausoni et al., 2007; J. Wu et al., 2021). For example, it has been reported that the occurrence of cavitation tends to enhance the amplitude of the vortex-induced vibrations (Ausoni, 2009). Therefore, a deep understanding of the effect of cavitation inside the vortex street flow is necessary, if we are to limit the damage caused by the cavitation and/or vortex-induced vibrations.

The investigation of cavitating vortex street flow can be conducted through both experimental and numerical methods. Although experimental measurements have expanded our comprehension of the phenomenon, detecting and measuring the flow field in the presence of cavitation presents inherent difficulties and challenges. On the other hand, numerical simulation serves as an alternative methodology that can provide additional insights from the resolved flow field at a relatively lower cost. Still, it is a challenge to conduct the high-fidelity numerical simulation for the cavitating vortex street behind the blunt trailing edge hydrofoil. Such complex flow includes multiple principles in terms of cavitation, vortex street, and boundary layer transition.

Many researchers have focused on the turbulent models and cavitation models for the attached cavitating flow over the different geometries (Arndt, 1981; Kawanami et al., 1997; Callenaere et al., 2001; Laberteaux & Ceccio, 2001; Leroux et al., 2004; Ganesh et al., 2016; J. Wu et al., 2019; A. Bhatt et al., 2023), where the cavitation is relatively insensitive to the free stream nuclei concentration (Ram et al., 2020). Two major mechanisms have been well numerically identified accounting for the transition from sheet cavitation to cloud cavitation: (i) liquid re-entrant jet (Arndt, 1981; Callenaere et al., 2001; Kawanami et al., 1997; Laberteaux & Ceccio, 2001; Leroux et al., 2004) and (ii) condensation shock (J. Wu et al., 2019; Ganesh et al., 2016; A. Bhatt et al., 2023). However, in the context of the developed cavitation inside the shear layers and wake flow, the bubble-vortex interaction makes the growth and collapse of the cavitation different (Katz, 1984; O'Hern, 1990; Iyer & Ceccio, 2002; J. Choi & Ceccio, 2007; Agarwal et al., 2023). Besides, such flow also suffers from the water quality scale effects and Reynold number scale effects (J. Choi et al., 2009). Therefore, the numerical model for the cavitation developing in the shed vortices has not been well addressed (Cheng et al., 2021; Brandao & Mahesh, 2022), making the accurate prediction difficult.

Another issue in the cavitating vortex street over the blunt trailing edge hydrofoil NACA 0009 is the boundary layer transition. To numerically model the boundary layer transition, the Direct-Numerical Simulation (DNS) is highly expensive since the required number of grid points N for the boundary layer transition using DNS increases significantly with the estimation of $N \propto Re^{2.64}$ (H. Choi & Moin, 2012). In recent years, there has been a growing interest in using LES to simulate the boundary layer transition although it is still quite expensive and time-consuming for engineering applications (Georgiadis et al., 2010). In practice, the unsteady Reynolds averaged Navier-Stokes coupled with the empirical correlation, $Re_{\theta t}$, and intermittency, γ, can be used to capture the flow feature of the boundary layer transition (Langtry & Menter, 2009). Nonetheless, the accuracy of transition models depends on inlet boundary turbulence conditions (Spalart & Rumsey, 2007) and correlation functions derived from experimental calibration (Babajee & Arts, 2012).

To date, obtaining a high-fidelity simulation for the cavitating vortex street behind the blunt trailing edge hydrofoil is still a challenging task. Therefore, it is necessary to develop and optimize the numerical modellings addressing the multiple

principles in terms of cavitation, vortex street, and boundary layer transition. The overall objective of this dissertation is to develop a high-fidelity numerical tool to simulate the cavitating vortex street flow and to elucidate the effects of cavitation.

1.2 AIMS AND OBJECTIVES

The escalation in both the sizes and operational range of modern hydraulic machinery will increase the likelihood of vortex street flow occurrence. Furthermore, structures are becoming thinner and more flexible as the designers look for power concentration and reduce the dimensions by bringing materials to their limits. Both trends are promoting the appearance of deleterious phenomena such as strong vortex-induced vibrations and cavitation. The combination of both damaging mechanisms is a complex fluid-structure interaction problem that still needs to be fully understood and solved. In particular, it is necessary to ascertain how the interaction of cavitation and vortex street affects the flow and the structure dynamic behaviors. In this way, it will be possible to develop new technologies capable of preventing induced vibrations, erosion of materials, and fatigue damage.

Many researchers have attempted to study the vortex street flow and associated vortex-induced vibration in cavitating-free regimes, but less attention has been paid to the role of cavitation in such flows at high Reynolds numbers. Previous studies have observed that the occurrence and development of cavitation can modify the vortex-shedding frequency and the amplitude of loads acting on the hydrofoils. However, the underlying physics behind it is not well explained and understood. Therefore, the main objective of the present work is to investigate the effect of cavitation on the wake flow behind a blunt trailing edge hydrofoil and its interaction with the vortex-induced vibration.

To fully understand the effects of cavitation on such a complex flow phenomenon, the following steps have been taken in this thesis:

1. Build a high-fidelity numerical tool to simulate the cavitating vortex street flows under cavitation conditions, which includes the development, implementation, optimization, and validation of an incompressible and a compressible cavitation solver.

2. Clarify the effect of fluid compressibility on the cavitating vortex street flows using the validated and verified incompressible and compressible cavitation solvers.

3. Analyze the effect of cavitation on the dynamics of the vortex street behind a blunt trailing edge hydrofoil in terms of the spatio-temporal distribution of vortex structures and the induced unsteady loads.

4. Investigate the effect of cavitation on the vortex-induced vibration and its interaction mechanism.

1.3 THESIS OUTLINE

The thesis is organized into four parts:

The first part includes Chapters 1-3. Chapter 1 is the introduction of this thesis. Chapter 2 is devoted to some related fundamentals. Chapter 3 focuses on the literature review of the thesis topic.

In the second part, Chapter 4 describes the general framework of the numerical method, and then Chapters 5 and 6 are devoted to performing the validation and verification for the implemented incompressible and compressible cavitation solvers.

Part three is devoted to the main results of the current investigation. It includes Chapters 7-9. First, Chapter 7 focuses on the role of fluid compressibility in the cavitating vortex street flow. Then, Chapter 8 presents the high-fidelity numerical model accounting for the flow characteristic of the cavitating vortex street behind the blunt hydrofoil NACA 0009 in terms of boundary layer transition, vortex street, and cavitation. Moreover, the influence of cavitation development level on the dynamic of the vortex street flow behind the blunt hydrofoil NACA 0009 is well discussed. Finally, Chapter 9 is devoted to the investigation of the cavitating vortex street behind the hydrofoil NACA 0009 subjected to forced oscillation.

Part four includes Chapter 10 and Chapter 11. Chapter 10 summarizes the conclusions of the current investigation and the suggestions for further work are provided in Chapter 11.

Chapter 2: Fundamentals

This section includes a general description of the boundary layer, the wake produced by the immersed bodies, vortex-induced vibration, and cavitation. Specifically, it introduces some fundamentals related to the boundary layer, boundary layer transition, boundary layer separation, characteristics of vortex shedding, vortex street wake, and vibrations induced by shedding vortices behind solid bodies. Moreover, a brief introduction associated with cavitation is included.

2.1 BOUNDARY-LAYER

The solution at $Re=\infty$ often produces a satisfactory approximation for flows with extremely high Reynolds numbers in numerous practical applications. To satisfy the no-slip condition, L. Prandtl (1904) first proposed the concept of the boundary layer, which facilitates a velocity transition from the limiting solution at $Re=\infty$ to the value of zero at the wall when viscosity is considered. In particular, at high Reynolds numbers, the flow can be divided into two regions. In the bulk of the flow region, viscosity can be neglected, corresponding to the inviscid limiting solution, termed the inviscid outer layer. In a very thin boundary layer near the wall, viscosity must be considered where termed the inner boundary layer.

2.1.1 Boundary-layer thickness

Conventionally, the boundary-layer thickness δ is defined as the perpendicular distance from the surface where the flow reaches 99% of the external velocity, U_e. However, a more interpretable measure of the thickness of the boundary layer is the displacement thickness, δ_1, defined as follows:

$$U_e\delta_1 = \int_0^\infty (U_e - u)\, dy \quad (2.1)$$

The wall shear stress arises between the walls and the adjacent fluids due to fluid viscosity, which can be estimated by the following equation:

$$\tau_w = \mu \left(\frac{\partial u}{\partial y}\right)_{y=0} \quad (2.2)$$

In addition, based on the reference velocity, U_{ref}, the skin friction coefficient can be defined as follows:

$$C_f = \frac{\tau_w}{1/2\rho {U_{ref}}^2} \quad (2.3)$$

2.1.2 Boundary layer transition

On a hydraulically smooth surface, a natural turbulent transition can occur beyond a certain distance from the leading edge. The transition to a turbulent boundary layer is not sudden but occurs via the subsequent formation of three-dimensional structures. As one moves downstream from the leading edge, the transition consists of the following regimes as sketched in Fig. 2.1.

Regime a: Steady laminar flow

Regime b: Two-dimensional Tollmien-Schlichting waves

Regime c: Development of three-dimensional waves

Regime d: Formation of turbulent spots

Regime e: Fully turbulent flow

It is noted that span-wise non-uniformity in the boundary layer transition occurs even if the free-stream velocity is uniform.

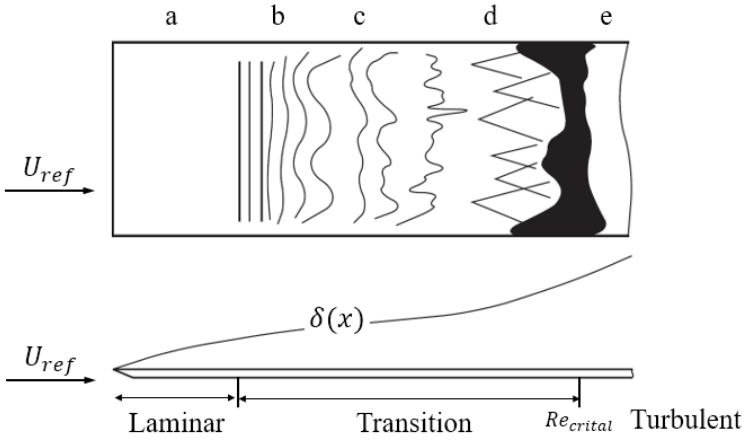

Fig. 2.1 Sketch of the laminar-turbulent transition over the flat plate.

2.1.3 Boundary layer separation

Separation condition

Fig. 2.2 displays the streamline within the boundary layer near the separation point. Due to the occurrence of the backflow, there is a significant increase in the thickness of the boundary layer, leading to the transport of boundary-layer mass into

the outer flow. At the separation point, streamlines depart from the wall at a specific angle. The separation position is determined by the condition at which the velocity gradient perpendicular to the wall vanishes, namely, the wall shear stress τ_w becomes zero:

$$\tau_w = \mu \left(\frac{\partial u}{\partial y}\right)_{y=0} = 0 \quad (2.4)$$

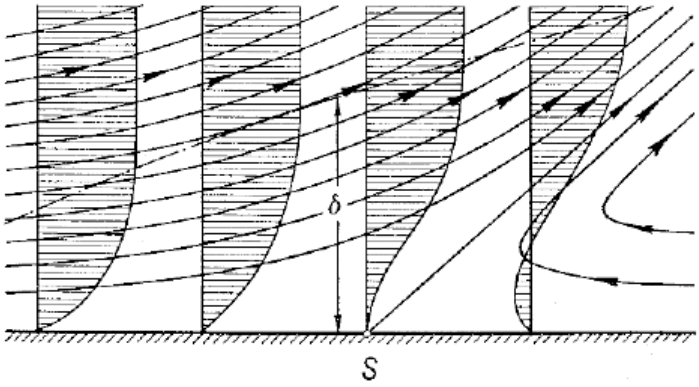

Fig. 2.2 Plot of streamlines within the boundary layer near the separation point, where *S* represents the separation point.

Types of separation

There are two distinct types of flow separation depending on the surface curvature (Brennen, 2014): abrupt separation and smooth separation, as illustrated in Fig. 2.3. Abrupt separation refers to the case where the flow streamlines depart from the solid body at a fixed vertex or corner, as depicted in Fig. 2.3 (a). According to potential flow analysis, the fluid acceleration tends to be infinite when it approaches the discontinuous point, e.g. vertex or corner, and this implies an infinite, favorable pressure gradient as well. As a result, the flow adjacent to the wall near the discontinuous point will be subjected to an infinite adverse pressure gradient, leading to flow separation. In Fig. 2.3 (b), smooth separation represents the case where the flow streamline leaves the solid body with finite curvature. Approaching the smooth separation point, the velocity and pressure gradients tend toward zero rather than infinity.

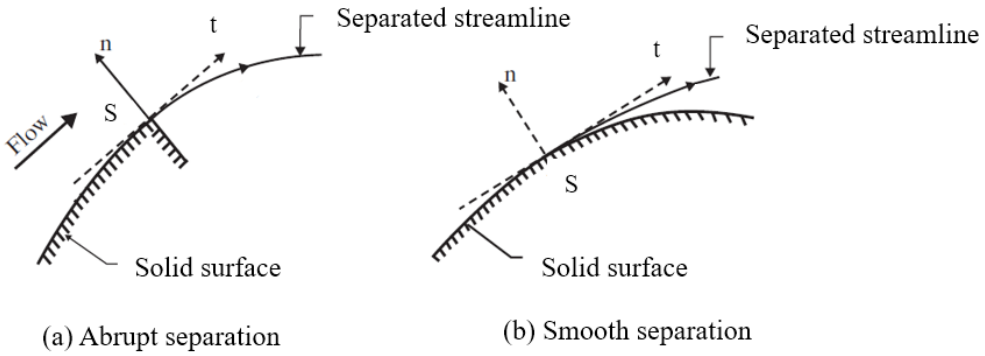

Fig. 2.3 Two types of flow separation from a solid body.

2.2 VORTEX SHEDDING

In fluid dynamics, vortex street flow refers to an alternating shedding vortical flow phenomenon that occurs in a wake behind the solid body if the Reynolds number exceeds a certain threshold value. Gerrard (1961) provides a physical description of the mechanism of the vortex formation region. The mutual interaction between the two separating shear layers is the key to understanding the formation of a vortex street. As shown in Fig. 2.4, the lower vortex continues to grow, fed by circulation from its connected shear layer, until it becomes strong enough to draw the opposing shear layer across the wake. The approach of the oppositely signed vorticity in sufficient concentration cuts off the further circulation supply to the growing vortex, which is then shed and moves downstream. Hence, body wakes are complex due to the interactions among three shear layers: namely, a boundary layer, a separating free shear layer, and a wake (C. H. Williamson, 1996).

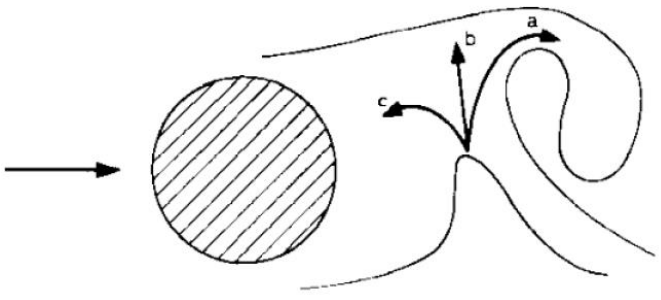

Fig. 2.4 Illustration of the vortex-formation model behind the circular cylinder.

2.2.1 Vortex shedding frequency

The vortex shedding frequency is commonly expressed in a non-dimensional form called Strouhal number, denoted as St:

$$St = \frac{fL_{char}}{U_{ref}} \quad (2.5)$$

where f is the vortex shedding frequency, L_{char} is the body characteristic length and U_{ref} represents the free stream velocity.

Flow regimes can be identified based on the relationship between the Strouhal number and the Reynolds number. In the flow around the circular cylinder, Fig. 2.5 (Sumer, 2006) shows the Strouhal number as a function of the Reynolds number at different flow regimes (C. H. Williamson, 1996).

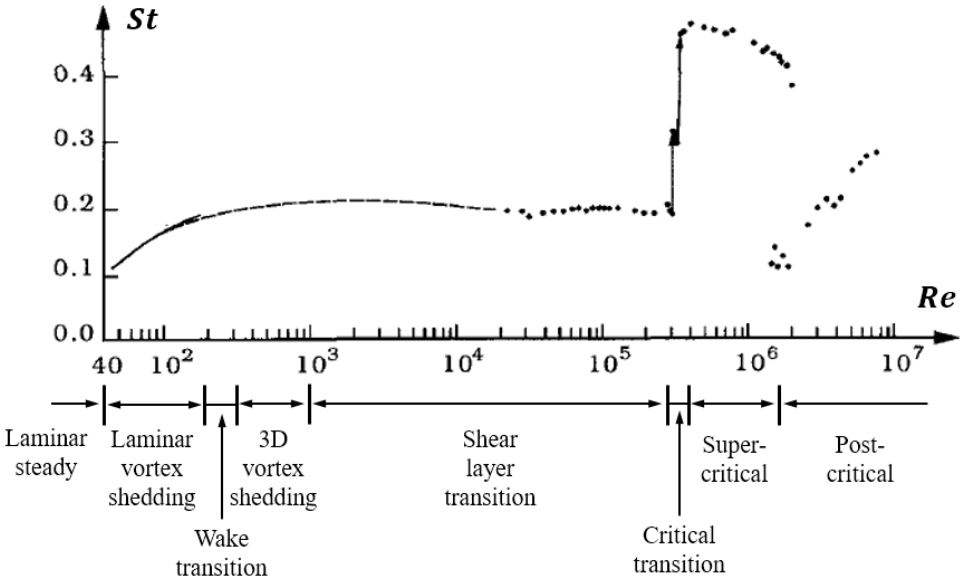

Fig. 2.5 The dependence between the Strouhal number and Reynolds number at the different flow regimes.

It can be seen that the laminar vortex shedding first appears at Re = 40 and the corresponding St approximates 0.1. Then, it gradually increases as Re increases and approaches a value of about 0.2 at Re = 300, which denotes the lower bound of the subcritical flow regime. From this Re number onwards throughout the subcritical range, St remains constant at a value of 0.2. This suggests that vortex shedding in the subcritical range occurs in a consistently regular manner. Next, as Re further increases, the Strouhal frequency undergoes a sudden jump, from 0.2 to a value of about 0.45, at $Re = 3 - 3.5 \times 10^5$, namely the critical Re number range. This high value of St can be maintained over a rather large part of the supercritical Re range. After that, it experiences a slight decrease with further increases in Reynolds number.

2.2.2 The geometry effect on the relationship between St and Re

The relationship between St and Re can be affected by the geometry of the bluff body. Blevins (1977) has conducted a series of experimental studies to characterize this influence regarding the geometries such as spheres, cylinders, and plates. Indeed, the Strouhal number is very sensitive to the nature of the separation within the boundary layers, which is governed by the geometry of the bluff body. According to Blevins (1977), Fig. 2.6 summarizes the relationship between St and Re for different geometries.

For geometries with abrupt separation points, such as plates with sharp trailing edges, triangle cylinders (wedge), and D-shapes cylinders, the Reynolds number has less influence on the Strouhal number since the nature of separation is relatively insensitive to the Reynolds number (Ramamurthy & Bhaskaran, 1977; Ramamurthy & Balachandar, 1990). Conversely, for geometries with smooth separation points, such as circular cylinders and spheres, the Reynolds number has a noticeable influence on the Strouhal number due to the excursion of the separation point depending on the Reynolds number (Sarpkaya, 2004).

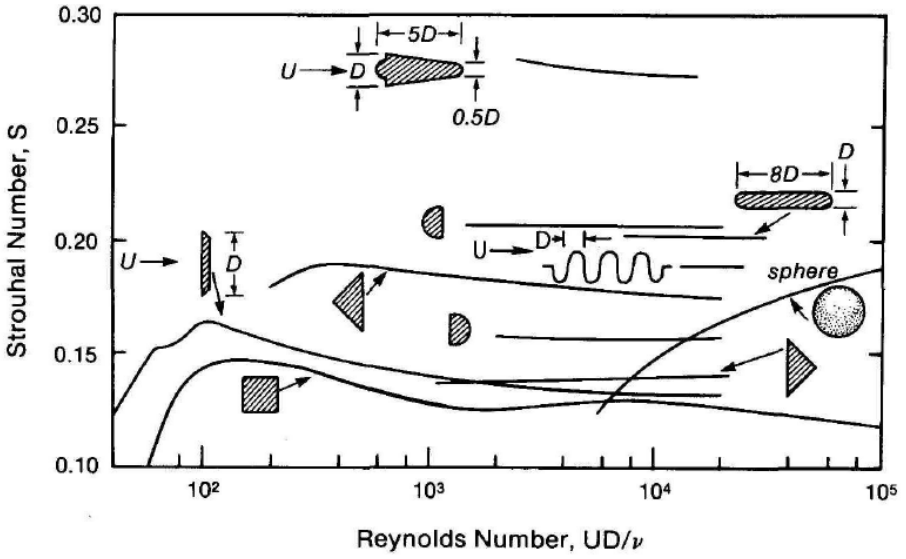

Fig. 2.6 The relation between St and Re for different geometries.

2.3 VORTEX-INDUCED VIBRATIONS

Vortex-induced vibration (VIV) is a fluid-structure interaction phenomenon, which is difficult to define but easy to describe. It accounts for the mechanical response of structures to oscillating forces due to the alternating shedding vortices. It is known

to be inherently nonlinear, self-governed, or self-regulated (Sarpkaya, 2004). VIV has been extensively studied over the years since it is commonly encountered in various engineering applications. More comprehensive related works have been reviewed and summarised by Sarpkaya (2004) and Williamson and Govardhan (2004).

2.3.1 Single-degree-of-freedom (SDOF) vibration model

Naudascher and Rockwell (1980) have categorized oscillators into two types: body and flow oscillators. Body oscillators describe a rigid structure that is either elastically supported or inherently elastic, while fluid oscillators consist of a fluid mass that can oscillate, being governed by fluid compressibility or by gravity. For the present study, only body oscillators will be considered due to the specific interest in the interactions between vibrating solid structures and the cavitating wake. As illustrated in Fig. 2.7, a body oscillator can be represented by a simple SDOF vibration model (as expressed in equation (2.6)), consisting of a mass body oscillating over one degree of freedom, supported by a linear spring and a linear damper.

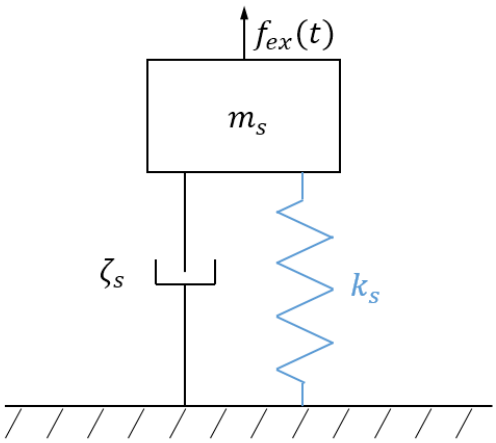

Fig. 2.7 Sketch of the SDOF vibration model.

$$m_s\ddot{x} + \zeta_s\dot{x} + k_s x = f_{ex}(t) \quad (2.6)$$

where m_s is the structural mass, ζ_s is the structural damping, and k_s is the structural stiffness. When evaluating the dynamic response of a submerged structure in a fluid, the added mass, m_f, damping, ζ_f, and stiffness, k_f, need to be considered, equation (2.6) can be rewritten as:

$$(m_s + m_f)\ddot{x} + (\zeta_s + \zeta_f)\dot{x} + (k_s + k_f)x = f_{ex}(t) \quad (2.7)$$

By solving equation (2.7), the damped resonance frequency is obtained:

$$f_{d,water} = \frac{1}{2\pi}\sqrt{\frac{\left[\left(k_s+k_f\right)-\frac{\left(\zeta_s+\zeta_f\right)^2}{4\left(m_s+m_f\right)}\right]}{m_s+m_f}} \quad (2.8)$$

If the terms $\frac{\left(\zeta_s+\zeta_f\right)^2}{4\left(m_s+m_f\right)}$ and k_f are small, then the equation (2.8) reduces to the undamped natural frequency, f_{water}, as follows:

$$f_{water} = \frac{1}{2\pi}\sqrt{\frac{k_s}{m_s+m_f}} \quad (2.9)$$

such a model helps us understand the physics of VIV. Furthermore, the frequencies used in the VIV problem are summarized as follows:

- f_{air} or f_{vac}: The natural frequency of the structure in vacuum or air. Due to the density of air being quite small, the difference between f_{air} and f_{vac} can be neglected.
- f_{ex}: The excitation frequency, which represents the frequency of an oscillation of a body.
- f_{sta_non}: The vortex shedding frequency of a body at non-cavitating and stationary conditions.
- f_{vs}: The vortex shedding frequency.
- f_{com}: The common frequency at the condition where synchronization or lock-in occurs.

2.3.2 Lock-in phenomenon

The resonance occurs when the vortex shedding frequency aligns with one of the eigenfrequencies of the combined fluid-structure system. Near the resonance condition, the response amplitude may significantly increase, allowing the structural displacement to dominate fluid excitation, namely, the lock-in phenomenon. Alternatively, if the body is forced to oscillate at a reasonable frequency and amplitude, out of the lock-in region, the force acting on the body surface will exhibit both vortex shedding frequency and body oscillation frequency. However, with the lock-in region, only one frequency can be detected where $f_{vs} = f_{ex} = f_{com}$. Note that, it differs from perfect synchronization because of the continuous interaction between the body and

the fluctuations of added mass, separation line, amplitude, correlation length, and the phase angle.

In the lock-in region, shedding vortices play two distinct roles depending on the sign of the average modal work done by the flow on the structure, W_{model}, which can be obtained by projecting the modal force onto the modal velocity, $\dot{x}$:

$$W_{model} = \frac{1}{N}\int_{t_0}^{t_0+2\pi N/\omega_n} f(t)\dot{x}\, dt \quad (2.10)$$

The modal work W_{model} can be positive or negative, depending on the sign of the system damping. Positive damping or modal work indicates that the natural vibration amplitude is smaller than the imposed amplitude. Conversely, negative damping implies that the natural vibration amplitude will be larger than the imposed amplitude.

2.4 CAVITATION

Cavitation in liquid flows is a two-phase flow with phase transition driven only by pressure change. At a given temperature T, it is commonly considered that cavitation occurs whenever the local pressure p in the liquid drops below the saturated vapor pressure, $p_v(T)$. Different types of cavitation are observed depending on the flow conditions. As shown in Fig. 2.8, Knapp (1955) classified cavitation into two families: (i) Attached cavitation, where the cavity interface is partly attached to the solid surface, and (ii) Advected cavitation, where the entire cavity interface moves with the flow:

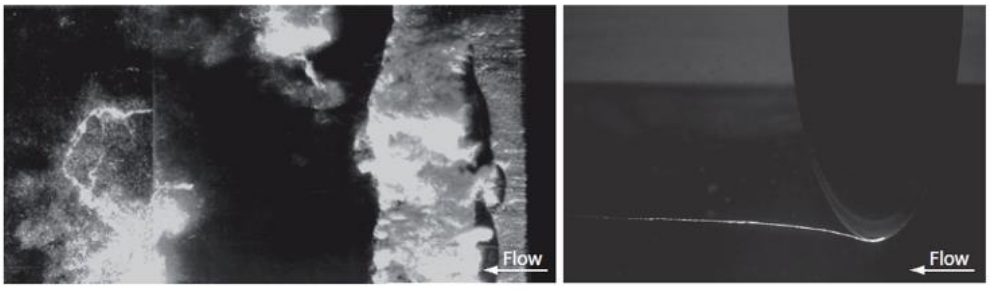

(a) Leading edge cavitation (NACA 0009, α=4.5°, U_{ref}=14 m/s, σ=1.2)

(b) Tip vortex cavitation (NACA 16020, α=10°, U_{ref}=14 m/s, σ=1.7)

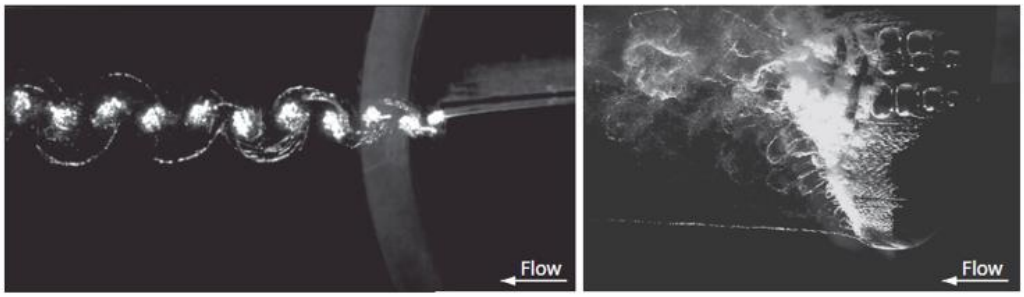

(c) Vortex street cavitation
(NACA 0009, α=0°, U_{ref}=12 m/s, σ=0.8)

(d) Bubble cavitation
(NACA 16020, α=6°, U_{ref}=14 m/s, σ=0.4)

Fig. 2.8 Two families of cavitation: (i) Attached cavitation: (a) leading edge cavitation and (b) tip vortex cavitation; Advected cavitation: (c) vortex street cavitation and (d) bubble cavitation (pictures from (Ausoni, 2009)).

(i) Attached cavitation

Fig. 2.8(a): The attached cavitation in the forms of sheet cavitation and cloud cavitation occurs on the solid surface. Sheet cavitation is defined as a cavity that is thin and quasi-steady while cloud cavitation refers to the transient cavities.

Fig. 2.8(b): The tip vortex cavitation is formed inside the tip vortex core, which is characterized by the quasi-steady tip vortex flow.

(ii) Advected cavitation

Fig. 2.8(c): The vaporous cavities occur inside the core of the shedding vortices.

Fig. 2.8(d): The bubble cavitation refers to the growth and collapse of the individual transient bubbles governed by the flow advection.

Chapter 3: Literature review

While wake flows behind various bluff bodies, e.g. circular and square cylinders, have received extensive study, the phenomenon of vortex shedding past hydrofoils has been relatively overlooked, despite its high relevance in hydraulic machinery and marine engineering applications. With more flexible materials applied in these fields, the vibration induced by the alternating vortex shedding, also known as vortex-induced vibration (VIV), becomes one of the primary causes of machinery failure (Ausoni et al., 2007). For example, Donaldson (1956) reported that vortex shedding is a source of vibration and noise in hydraulic turbines. The vortex shedding occurs at both the trailing edge of the turbine runner blades (Coutu, et al., 2003) and guide vanes (Lockey et al., 2006; Papillon et al., 2006). Due to the long cycles of alternating stresses induced by the vortex shedding, fatigue failures in the guide vanes were reported by Gummer and Hensman (1992). In addition to the potential damages directly attributed to vortex shedding or cavitation, the intricate interactions between vortex shedding and cavitation can significantly affect the flow dynamics and pose substantial threats to the stability and safety of the hydraulic systems (Ausoni et al., 2007). Therefore, these interactions are particularly critical in hydraulic systems, prompting the need for a comprehensive understanding, prediction, and control of the cavitating vortex shedding behind hydrofoils in modern hydraulic systems' design and operation.

As highlighted by Sarpkaya (2004), the characteristics of the vortex shedding behind the bluff body are influenced by the type of separation point, such as abrupt separation and smooth separation. These two distinct separations yield different velocity and pressure gradient profiles near the separation point. As a result, extending the knowledge gained from the observations of the cavitating wake behind a circular cylinder with smooth separation points to the flow behind a wedge with abrupt separation points can be proved to be debatable (Ramamurthy & Balachandar, 1990; Sarpkaya, 2004). Due to the similarity in flow characteristics resulting from abrupt separation, the flow features within the cavitating wake behind the blunt trailing edge hydrofoil resemble those observed in the wake of a wedge. Therefore, these

experimental and numerical investigations of cavitating vortex street flow behind both the wedge and the blunt trailing edge hydrofoil are reviewed.

3.1 CAVITATION EFFECTS ON THE VORTEX STREET FLOW

3.1.1 Cavitation inception

Coupled with the Rankine vortex model, Arndt (1976) and Belahadji et al. (1995) proposed a model for the prediction of the cavitation inception in the wake of bluff bodies with abrupt separation points, which establishes a linear relationship between the cavitation inception index and the square root of the Reynolds number.

$$\sigma_i = -C_{pb} + b_1\sqrt{Re} \quad (3.1)$$

where C_{pb} is the pressure coefficient at the base, b_1 is an empirical coefficient. As shown in Fig. 3.1, the model agrees well with the experimental measurement done by Belahadji et al. (1995).

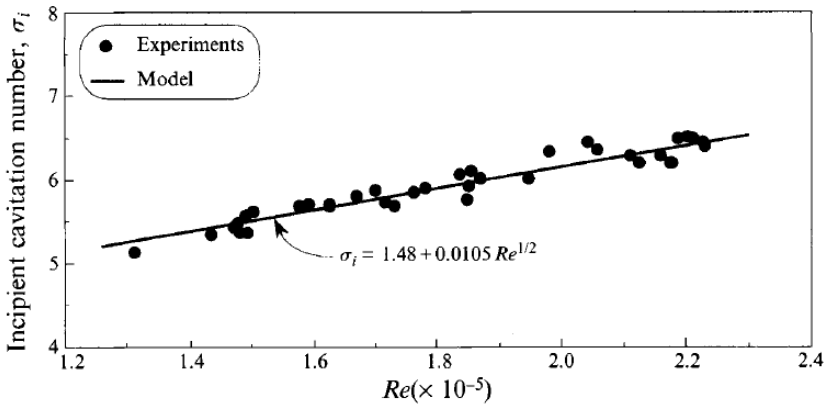

Fig. 3.1 Comparison of the cavitation inception obtained by the experiment and the model in the wake of the wedge (Belahadji et al., 1995).

Within the lock-in regime, σ_i, can be determined by the following equation (Ausoni et al., 2007) for the blunt trailing edge hydrofoil NACA 0009:

$$\sigma_i = a_1 + b_1\sqrt{Re} + c_1\frac{A_{vib}^2}{U_{ref}^2} \quad (3.2)$$

where A_{vib} is the hydrofoil trailing edge vibration velocity, a_1, b_1, c_1 are the empirical coefficients. Fig. 3.2 displays the comparison in cavitation inception obtained by the experimental measurement and the model.

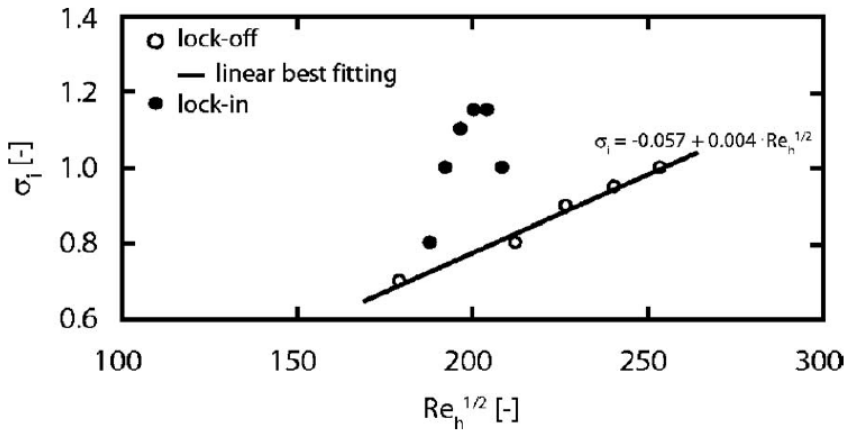

Fig. 3.2 Comparison of the cavitation inception obtained by the experiment and the model in the wake of the blunt trailing edge hydrofoil NACA 0009 (Ausoni et al., 2007).

3.1.2 Effects of cavitation on vortex shedding frequency

The results regarding the effects of cavitation on vortex shedding frequency behind wedges can be found in the investigation done by Young and Holl (1966), followed by Ramamurthy and Balachandar (1990), Belahadji et al. (1995), Kim et al. (2019), and Wu et al. (2021). Young and Holl (1966) experimented with four wedges with apex angles of 15, 30, 60, and 90 degrees and found that Strouhal number also depends on the cavitation number for cavitating wakes, employing high-speed film visualization techniques. They established a relationship between the Strouhal number, *St*, and the cavitation number. Their observations indicated a constant St before cavitation inception. However, as the cavitation number decreases from the inception, St yields a gradual increase up to a maximum and then it is followed by a decay. Subsequent experiments have validated these findings (J. O. Young & Holl, 1966; Ramamurthy & Balachandar, 1990; Belahadji et al., 1995; J. Kim et al., 2019; J. Wu et al., 2021).

Compared with the wedge with different apex angles, Fig. 3.3 presents the experimentally obtained *St* values as a function of the cavitation number, σ, for the cavitating wake flow behind the truncated hydrofoil NACA 0009 by Ausoni et al. (2007) where the subtitle "sta_non" represents the non-cavitating and stationary conditions and the vertical axis represents the ratio of the cavitating *St* to the non-cavitating one. The subtitle "i" refers to the cavitation inception and the horizontal axis is the ratio of the cavitation number to the incipient one. It can be seen that a discernible trend emerges before the peak of the *St* curves: a decrease in σ corresponds to an

increase in *St*. This trend is consistent in both the NACA 0009 hydrofoil with a truncated trailing edge and in wedges with different apex angles. However, the underlying mechanism driving the rise of *St* as a function of σ remains incompletely elucidated.

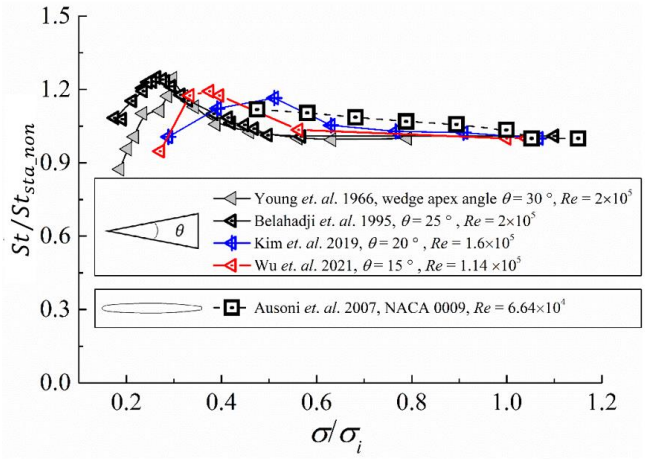

Fig. 3.3 $St/St_{sta\text{-}non}$ versus σ/σ_i for the truncated NACA 0009 hydrofoil and wedges with different apex angles.

3.1.3 Effect of cavitation on the vortex morphology inside the vortex street

On vortex spacing ratio b_v/a_v

Prior evidence suggests that cavitation, rather than serving as a passive visualization agent within turbulent wake flows, alters the morphology of the vortex street wake (Belahadji et al., 1995; Ausoni et al., 2007). Normally, the streamwise and cross-stream inter-vortex spacings, which are denoted as a_v, and b_v respectively, are used to account for the morphology of vortex street wake, as shown in Fig. 3.4. It was first established by Von Kármán (1912) that a 2D inviscid vortex street is stable only with a specific vortex spacing ratio of $b_v/a_v = 0.28$.

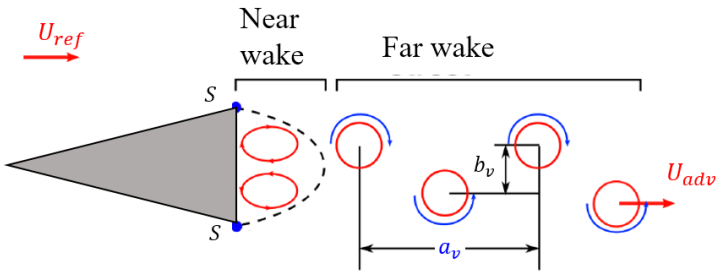

Fig. 3.4 Sketch of the morphology of vortex street wake, where *S* represents the separation points.

However, with the presence of viscosity, previous experimental observations by Schaefer and Eskinazi (1959) showed that the vortex street wake can maintain stability with varying vortex spacing ratios ranging from 0.08 to 0.525. Later, I. Kim (2019) conducted an experimental investigation of the wake flow behind the triangle with different apex angles. He found that in the form of a vortex street, the vortex spacing ratios can range from 0.2 to 0.5, as presented in Fig. 3.5. Those observations suggested that the morphology of vortex street wake may be independent of any stability arrangement.

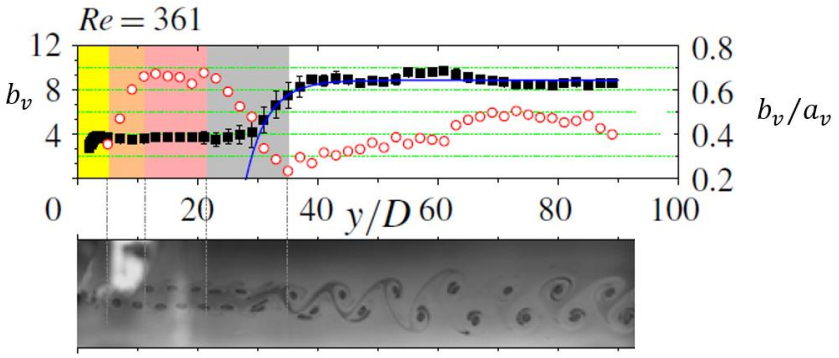

Fig. 3.5 Vortex spacing ratio in the vortex street behind the wedge with an apex angle of 90° and *Re* =361 (I. Kim, 2019).

In the context of the cavitating wake, several studies have reported distinctive values of b_v/a_v: ranging from 0.2 to 0.35 (Fig. 3.6 (a)) by Young and Holl (1966), 0.07 to 0.25 (Fig. 3.6 (b)) by Belahadji et al. (1995), and 0.19 to 0.30 (Fig. 3.6 (c)) by Wu et al. (2021). Therefore, it is feasible that b_v/a_v is the key factor in understanding the variations in vortex street morphology in the presence of cavitation. These primary results revealed that there may be no unambiguous relationship between f and b_v/a_v under the cavitating condition.

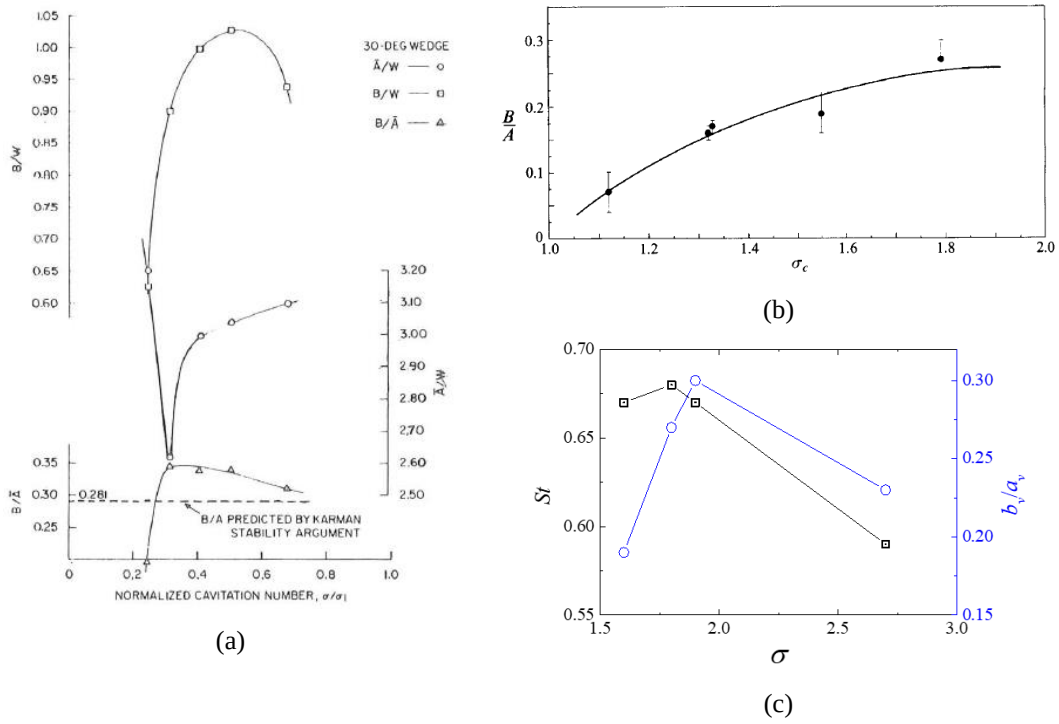

Fig. 3.6 Vortex spacing ratio in the vortex street behind the wedge with different cavitation numbers obtained by (a) Young and Holl (1966), (b) Belahadji et al. (1995), and (c) Wu et al. (2021).

On the correlation between the vortex-shedding frequency and vortex morphology

A simple model for vortex street arrangement was proposed by Schaefer and Eskinazi (1959) and further adopted by Ausoni et al. (2007), as shown in Fig. 3.7(a). It associates the vortex-shedding frequency, f_{vs}, with the vortex advection velocity, U_{adv}, and inter-vortex spacing, a_v, represented by the equation:

$$f_{vs} = U_{adv}/2a_v \quad (3.1)$$

It becomes apparent that instead of a specific vortex spacing ratio, a_v serves as the characteristic length scale to elucidate the impact of cavitation on the flow morphology of the vortex street wake. Furthermore, the increase in f_{vs}, which is attributed to the development of the cavitation, can arise from several factors: (i) an increase of U_{adv}; (ii) a reduction of a_v; or (iii) a combination of both (i) and (ii), as depicted in Fig. 3.7.

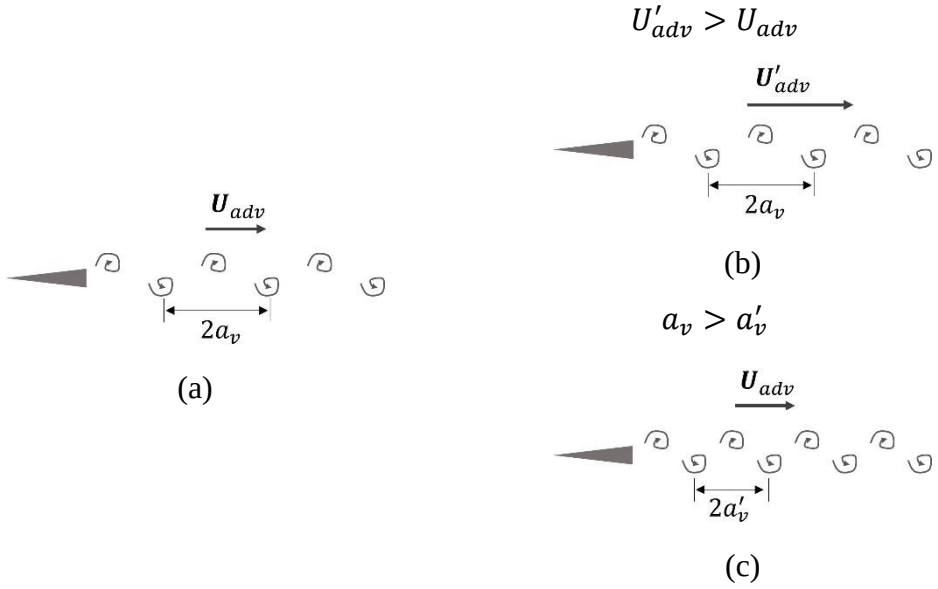

Fig. 3.7 Schematic of the vortex street behind a wedge with the characteristic parameters (a) and conditions increasing the vortex shedding frequency as an increase in U_{adv} (b) or a reduction in a_v (c).

Young and Holl (1966) have proposed a correlation between a_v and f_{vs}. Subsequently, Belahadji et al. (1995) observed an approximate 80% decrease in a_v and a 30% increase in f_{vs}. Their observations are aligned with the argument that the reduction of a_v contributes to the rise of f_{vs} in the presence of cavitation. On the other hand, in the case of the cavitating wake behind the NACA 0009 hydrofoil, Ausoni et. al. (2007) reveals that U_{adv} increases by around 4% with the development of the wake cavitation meanwhile a_v decrease, as shown in Fig. 3.8. Nevertheless, the findings mentioned above are primarily based on qualitative experimental observations. A comprehensive understanding of the influence of cavitation on the vortex shedding frequency needs further quantitative analysis.

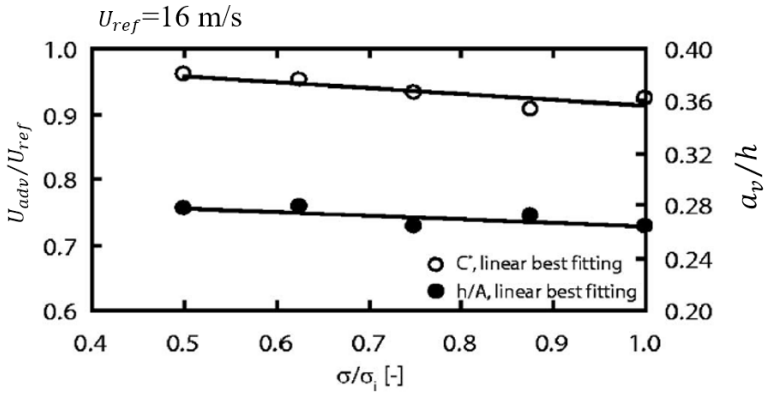

Fig. 3.8 Estimation of U_{adv} and a_v at different cavitation numbers (Ausoni et al., 2007).

3.1.4 Fluid compressibility effect on the characteristic of the cavitating wake

Many authors (Ganesh et al., 2016; J. Wu et al., 2019; A. Bhatt et al., 2023) focus on the presence of condensation shocks, also known as bubbly shocks, in the cavitating flow over hydrofoil surfaces. Ganesh et al. (2016) attributed the presence of a condensation shock as a mechanism for the transition from sheet to cloud cavitation in their experiments. They observed that this bubbly shock travels upstream and destabilizes the sheet cavity, leading to the formation of a cloud cavity. Similarly, as shown in Fig. 3.9, Wu et al. (2019) reported that the transition from sheet to cloud cavitation on a hydrofoil is influenced by the pressure waves, which are induced by the collapse of cavity clouds downstream.

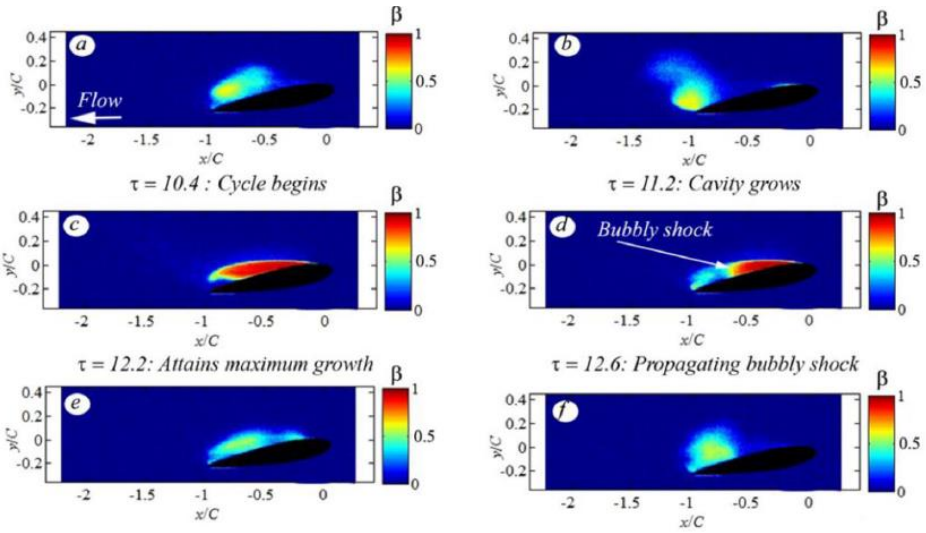

Fig. 3.9 Condensation shock during the transition from sheet cavitation to cloud cavitation using X-ray density meter (J. Wu et al., 2019).

Regarding the cavitating wake flow behind a wedge, Wu et al. (2021) observed a correlation between the Strouhal number and the local speed of sound, noting that the flow becomes supersonic at conditions of maximum Strouhal number. However, they did not consider mass transfer in their estimation of the local speed of sound. Therefore, the effects of fluid compressibility in the cavitating wake still need further discussion.

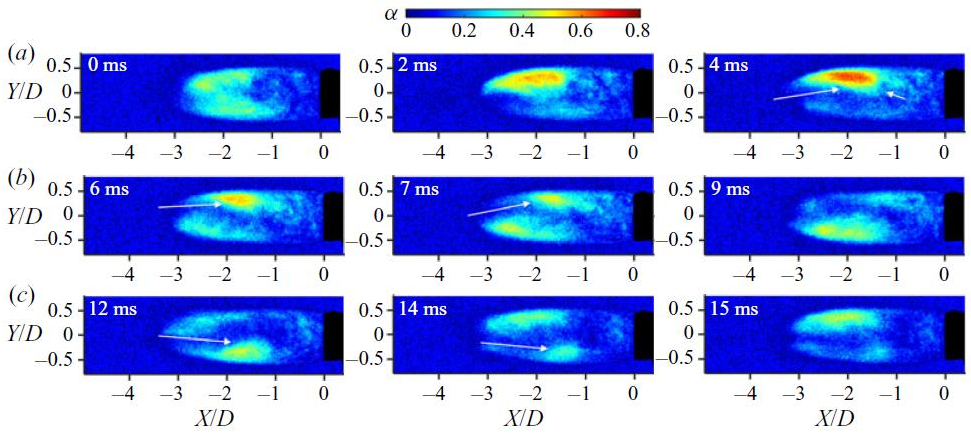

Fig. 3.10 Condensation shock observed in the shedding vortices behind the trailing edge of the wedge using an X-ray densitometer (J. Wu et al., 2021).

3.2 CAVITATION EFFECTS ON VIV

Ausoni et. al. (2007) investigated the coupling between the hydro-elasticity and the vortex street cavitation. They observed a mutual influence between cavitation and structural vibrations: cavitation affected the vibrations, and vice versa. Waterfall spectra of accelerometer signals for various cavitation numbers are presented in Fig. 3.11. As shown in Fig. 3.2, the lock-in condition can increase the cavitation inception thereby enhancing cavitation development. However, vortex shedding frequency tends to increase with cavitation development, making it possible to disable hydro-elastic couplings by allowing sufficient cavitation development.

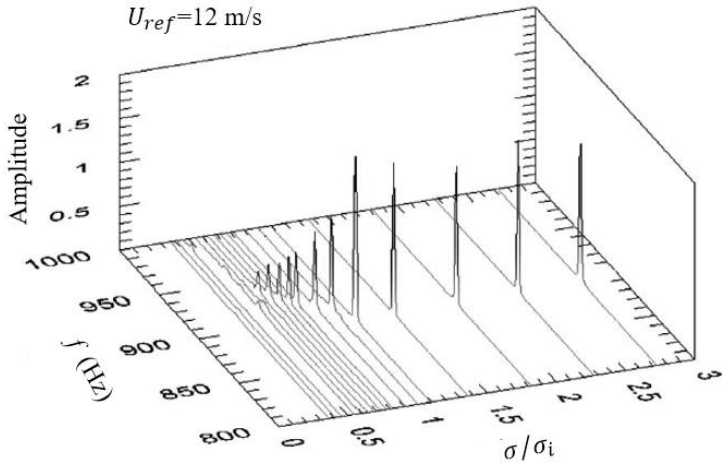

Fig. 3.11 Vortex shedding frequency and VIV amplitude as a function of cavitation number at 12 m/s (lock-in condition).

Cavitation is found to affect the natural frequencies and mode shape for the fluid-structure interaction. The unsteady cavitating flow leads to asymmetry (Benaouicha & Astolfi, 2012) and fluctuation (Akcabay et al., 2014) of added mass. As a result, the

variation in added mass can alter the natural frequencies (Ducoin et al., 2011) and the corresponding mode shapes(W. Wang et al., 2023). Compared with the fully submerged solid body, the reduction in added mass due to cavitation results in an increase in the natural frequency of the structure (X. Liu et al., 2017; Y. L. Young et al., 2022). Moreover, the added mass decreases and the natural frequency increases when the length of the hydrofoil surface cavitation bubble increases (De La Torre et al., 2013, 2014). On the other hand, the "bending-torsion coupling mode" becomes the second bending mode of the hydrofoil due to the presence of cavitation (De La Torre et al., 2013, 2014; Zeng et al., 2022), resulting from the change of sound speed in cavitation bubbles (L. Wang & Tian, 2020).

Apart from natural frequencies and mode shape, cavitation also affects the added damping characteristics of structures. Added damping determines the vibration amplitude: the larger the damping ratio, the smaller the resonance amplitude value, in particular, within the resonance regime. In unsteady cavitating flow, the high amplitude pressure waves generated by the collapse of cavitation bubbles increase the complexity of fluid damping, leading to variations in the sign of the damping coefficient (Benaouicha & Astolfi, 2012). Moreover, experiments conducted by De La Torre et al (2013) and Zeng et al. (2022) show that the added damping of the hydrofoil decreases with the development of cloud cavitation. Still, the variation law of added damping with cavitation number needs to be further clarified and studied.

3.3 NUMERICAL METHOD FOR CAVITATING WAKE

Numerical simulation serves as an alternative methodology that can provide additional insights from the resolved flow field at a relatively lower cost. Still, it is a challenge to conduct a high-fidelity numerical simulation of the cavitating vortex street behind the blunt trailing edge hydrofoil. This is because such complex flow includes multiple principles in terms of boundary layer transition, cavitation, and vortex street. In this section, we will review the published numerical methods and results concerning the boundary layer transition and cavitating vortex street.

3.3.1 Numerical methods for transitional flow

Accurate evaluation of the laminar-turbulent transition in the blunt trailing edge hydrofoil has proven to be important in predicting the flow characteristic of the cavitating or non-cavitating vortex shedding flow (Ausoni, 2009). There are three

methods available for simulating the laminar-turbulent transition, including Direct Numerical Simulations (DNS), large eddy simulation (LES), and Reynolds-averaged Navier-Stokes (RANS).

Direct Numerical Simulation (DNS) can provide the most accurate results for the transitional flow without the extra model. DNS was applicable to simulate either natural or bypass transition processes in different geometries, such as flat plate (Sayadi et al., 2013; Yan et al., 2014), curved surface (Jones et al., 2008) and blade (Sandberg et al., 2015). However, resolving all turbulence length and time scales requires extensive grids and high-order accurate numerical schemes, restricting the application of DNS inflows at high Reynolds numbers. On the other hand, Large-Eddy Simulation (LES) can resolve large-scale eddies, making it applicable for the prediction transitional flow to some extent (W. Wu & Piomelli, 2018). The subgrid-scale (SGS) stress model for LES is the key to predicting the transition. Simulation conducted by Germano et al., (1991) showed that Smagorinsky model was found to fail in capturing transition. However, Yu et al. (2013) proposed a new SGS model that is capable of predicting transition in flat-plate boundary layers and compression ramps (Zhou et al., 2019). However, LES still faces challenges in predicting boundary layer transition with varying inlet turbulence intensities (Michelassi et al., 2002) and requires expensive computational resources for simulating the flow at high Reynolds numbers (Georgiadis et al., 2010).

In industrial applications, Reynolds Averaged Navier Stokes (RANS) methods are widely used for their acceptable accuracy, high efficiency, and low computational cost. The transition prediction models are integrated with RANS models to realize the prediction in transitional flow. Among these transition prediction models, the local-correlation-based transition modeling concept is a popular approach (Langtry & Menter, 2009; Cakmakcioglu et al., 2020; Sandhu & Ghosh, 2021), for handling the laminar to turbulence transition processes in different flows. Notably, Langtry and Menter (2009) introduce the γ-$Re_{\theta t}$ model, incorporating two additional transport equations accounting for intermittency factor, γ, and transition momentum thickness Reynolds number, $Re_{\theta t}$. This model exhibits superior accuracy in the transitional flow (R. Wang & Xiao, 2020; Lopes et al., 2021). Nonetheless, the efficacy of transition models depends on inlet boundary turbulence conditions (Spalart & Rumsey, 2007)

and correlation functions derived from experimental calibration (Babajee & Arts, 2012).

In the following, the published numerical simulations for the vortex shedding flow around the blunt trailing edge hydrofoil NACA 0009 will be summarised. Given the computational cost of DNS is unaffordable, only LES and RANS methods were utilized for such complex flows. Ausoni (2009) conducted studies on the vortex-shedding frequency in hydrofoils and found that the capability to capture transitional flow is the key to accurately predicting the vortex-shedding frequency. Later, Lee et al. (2015) performed a comparative analysis of the vortex shedding frequency obtained using the hybrid particle mesh method in vortex shedding behind the truncated hydrofoil. Moreover, Hu et al. (2020) performed a 2D simulation to analyze the characteristics of the vortex shedding frequency using the RANS method with the Spalart–Allmaras turbulence model under the rough leading edge. These studies do not emphasize the phenomenon of the transition over the blunt trailing edge hydrofoil. Furthermore, Chen et al. (2018) investigated the transition phenomenon occurring on the surface of a truncated hydrofoil using the LES WALE model at a high Reynolds number. Ye et al. (2020) assessed the capability of different turbulence models on boundary layer transition along a hydrofoil, including LES WALE, LES Smagorinsky, as well as DDES γ-$Re_{\theta t}$, DDES, SSTCC γ-$Re_{\theta t}$, SST γ-$Re_{\theta t}$, and SST model. Their results suggest that the transitional flow can be well captured by LES WALE, DDES γ-$Re_{\theta t}$, SSTCC γ-$Re_{\theta t}$, and SST γ-$Re_{\theta t}$. To balance the computational cost and accuracy, the SST γ-$Re_{\theta t}$ or SSTCC γ-$Re_{\theta t}$ is more suitable for simulating the such complex flow. However, the dependence of transition models to inlet boundary conditions is well explained in these published studies.

3.3.2 Numerical methods for simulating the cavitating flow

Currently, various numerical approaches with different levels of complexity are available to simulate the cavitating flow. For a more comprehensive review of the cavitation modeling approaches, see (Niedźwiedzka et al., 2016; Folden & Aschmoneit, 2023). According to Folden and Aschmoneit (2023), the cavitation models can be categorized as follows:

(i) Rayleigh-Plesset Equation (RPE), where the model employs bubble dynamics as expressed via a (simplified) RPE;

(ii) Transport Equation Model (TEM), where the model employs a transport equation to approximate the mass transfer rates and thus the growth and collapse of cavities;

(iii) Equation Of State (EOS), where the model employs an EOS to relate the vapor volume fraction to thermodynamic variables;

(iv) Interface Tracking Model (ITM), where the model employs a scheme that directly tracks the interface between the liquid and the vapor phase;

(v) Multiscale (MUL) Model, where the model employs several schemes for simulating the growth and collapse of cavities at various length scales.

The aforementioned cavitation models can incorporate fluid compressibility. Therefore, the forthcoming short review and comments on these models will encompass fluid compressibility. Here, the term "incompressible cavitation model" refers to a cavitation model that does not consider fluid compressibility, while "compressible cavitation" indicates a cavitation model that includes fluid compressibility.

Incompressure cavitation model

The usage of the full RPE to modeling cavitation was first proposed by Kubota et al. (1992) and now it is only used in simulating the cavitating flow using DNS.

TEM may be the most popular incompressible cavitation model, which incorporates an additional transport equation accounting for the volume fraction of the vapor phase, along with a source term that represents the mass transfer occurring between each phase. The TEM has been proven to be successful in capturing the re-entrant jet dominant transition from the sheet to the cloud cavitation over different geometries (Coutier-Delgosha et al., 2003; Ji et al., 2014; Gnanaskandan & Mahesh, 2016a). The performance of the cavitation model is not only dependent on the form of the source terms inside the cavitation model (Sauer & Schnerr, 2001; Zwart et al., 2004) but also on empirical constants attributed to evaporation and condensation terms. Therefore, tuning the empirical constants has demonstrated a substantial potential to enhance the predictions in the evolution of cloud cavitation (Morgut et al., 2011; Yakubov et al., 2015; Geng & Escaler, 2020). However, it should be pointed out that experiences gained from tuning these empirical constants according to the

unsteady cloud cavitation scenarios might not be directly used in simulations of cavitating wake flows behind a bluff body, such as a blunt trailing edge hydrofoil.

As for EOS, fluid compressibility is always needed to be considered. Hence, it will be reviewed in the following section of the compressible cavitation model. Moreover, ITM can precisely capture the shape of the cavity interface and the flow characteristics near the interface. It works well for the steady cavity, e.g. sheet cavitation over the hydrofoil but faces challenges associated with unsteady cavity, e.g. the cloud cavitation inside the wake region of the bluff bodies (Deshpande et al., 1997).

Moreover, MUL can track all cavities within the flow, using two separate schemes for modeling cavitation depending on the size of the cavity: for larger singular cavities or clouds of bubbles, TEM is commonly used. Meanwhile, the small size of bubbles is tracked in a Lagrangian framework. Recently, different MUL models have been proposed (Hsiao et al., 2017; Ghahramani et al., 2018, 2021). However. MUL models show dependence in regards to the transition threshold from the TEM to the Lagrangian model (Ghahramani, 2018). In addition, the spherical model of small bubbles can significantly overpredict the peak pressures (Tiwari et al., 2015).

Despite extensive studies of transition from the sheet cavitation to the cloud cavitation over solid body using the incompressible cavitation model, few numerical studies have been reported for the cavitating wake flow behind the wedge. Recently, Kim et al. (2019) applied the realizable k-epsilon model coupled with the Schnerr-Sauer model to successfully capture the effect of the cavitation development on the vortex shedding frequency.

Compressible cavitation model

TEM can be coupled with the equation of state for the liquid, vapor, and the mixture phase. Recently, numerical studies using the compressible TEM model successfully demonstrate the existence of condensation shock and its impact on the transition from sheet cavitation to cloud cavitation (Gnanaskandan & Mahesh, 2016a, 2016b; C. Wang et al., 2020; A. Bhatt et al., 2023; Vaca-Revelo & Gnanaskandan, 2023). Note that, such a compressible TEM model still suffers from the inherent disadvantages of the incompressible cavitation model, such as the dependence of the form of the cavitation model and empirical coefficients associated with evaporation and condensation rate.

Methods that fall in the EOS category are barotropic EOS and the full thermodynamic model. Compared with the full thermodynamic model (Seo et al., 2008), the barotropic model does not need to resolve the energy equation thereby significantly reducing the computational cost (Budich et al., 2018). Moreover, the dynamics of shock waves generated by the collapse of vapor structures can be well resolved using the barotropic model. Coupled with the implicit LES model, Egerer et al. (Egerer et al., 2014, 2016) detected erosion events related to the shock waves in open and confined cavitating turbulent shear flows. Using a barotropic model based on the equilibrium speed of sound, Budich et al. (2018) demonstrated the presence of bubbly shocks. Furthermore, they pointed out that both the pressure waves and the high adverse pressure gradients can trigger condensation shocks in the flow past a sharp convergent-divergent wedge. Later, Brunhart et al. (2020) confirmed the existence of the re-entrant jet and condensation shock mechanisms for the vapor shedding in an axisymmetric converging-diverging Venturi nozzle using the barotropic model based on the frozen speed of sound. However, these aforementioned barotropic models are normally integrated into an in-house density-based solver and they are not easy to reproduce and use. Few attempts have been made to implement these barotropic models into the general numerical framework of commercial CFD software (M. Bhatt et al., 2015; Brunhart et al., 2020).

Until now, the compressible MUL model is still under development and only used in simple cases (Madabhushi & Mahesh, 2023).

For low Reynolds numbers, DNS coupled with different cavitation models is applicable in the simulation of the cavitating vortex shedding behind the bluff body. For example, at Re =200, Seo et al. (2008) used DNS coupled with the full thermodynamic model to compute the cavitating flow over a circular cylinder. They found that the development and collapse of the cavity inside the shedding vortices will alter the Karman vortex shedding frequency. Gnanaskandan and Mahesh (2016b) used DNS coupled with a homogeneous mixture model to repeat the simulation and examine the effects of cavitation on the pressure, the boundary layer, and the loads on the cylinder surface as well as the Karman vortex shedding frequency. They found that the presence of vapor in the wake leads to the reduction of vorticity and vortex formation length, resulting in a reduction of the vortex shedding frequency. Furthermore, the effects of non-condensable gas were considered by Brandao et al.

(2020) in the numerical simulation of the cavitating cavitating vortex shedding behind the circular cylinder. They confirmed that cavitation delays the transition to the Karman vortex street and increases the vortex formation length. As Re increases to a higher value, it is possible to use LES to simulate the cavitating turbulent wake. For example, Gnanaskandan and Mahesh (2016b) applied LES to investigate the characteristics of cavitating flow over a circular cylinder at Re= 3900. They found that LES can well capture the flow characteristic and the presence of the cavitation suppresses turbulence and delays the three-dimensional breakdown of Kármán vortices. Still, the numerical investigations related to the cavitating vortex street flow behind the bluff body, e.g. wedge and blunt trailing edge hydrofoil at the practical Reynolds number using the compressible cavitation model are less mentioned.

3.3.3 Numerically assess the effects of cavitation on VIV

Most numerical studies regarding the effect of cavitation on fluid-structure interaction have focused on the attached cavitation, such as sheet cavitation and cloud cavitation. It has been found that cavitation can affect the natural frequencies (De La Torre et al., 2013; Akcabay et al., 2014), the mode shape (De La Torre et al., 2014; Hu et al., 2023), and the added damping (Kashyap & Jaiman, 2023). Moreover, the cavity length and evolution of the attached cavitation around the solid surface tend to be affected by the movement of the body (B. Huang et al., 2013). However, few numerical studies have been reported for cavitating flows behind the VIV bodies. Among recent related numerical works, Roig et al. (2021) found that the added damping is negatively correlated with the cavitation coefficient. Hong and Son (2021) have reported that, under a lock-in regime, cavitation can modify the unsteady load acting on the surface of a circular cylinder. Until now, the interactions between the cavitation and the VIV body are still not well explored.

Part II

Chapter 4: Numerical modelling

This chapter introduces the physical modeling and the numerical method employed in this study. First, the governing equations are presented in section 4.1. Section 4.2 lists the turbulence modelling used in the current study. Then section 4.3 presents the cavitation modelling and section 4.4 details the equation of state accounting for the fluid compressibility. Moreover, the sponge layer boundary conditions are presented in section 4.5. Finally, the numerical method is detailed in section 4.6.

4.1 GOVERNING EQUATIONS

In the following, the governing equations are introduced, which include the mass conservation equation, and the momentum conservation equations.

4.1.1 Mass conservation equation

The equation for the conserved mass without external mass source is given by:

$$\partial\rho/\partial t + \nabla\cdot(\rho\boldsymbol{u}) = 0 \quad (4.1)$$

Here, ρ is the density, $\boldsymbol{u}$ is the velocity, and t is the time. This equation is valid for both incompressible and compressible flows.

4.1.2 Momentum conservation equation

In an inertial reference frame, the conserved momentum equation can be written as follows:

$$\partial(\rho\boldsymbol{u})/\partial t + \nabla\cdot(\rho\boldsymbol{u}\boldsymbol{u}) = -\nabla p + \nabla\cdot\boldsymbol{\tau} \quad (4.2)$$

where p denotes the static pressure, $\boldsymbol{\tau}$ is the stress tensor.

For the inviscid flow, $\boldsymbol{\tau} = \mathbf{0}$.

For the laminar flow, the $\boldsymbol{\tau}$ is defined as

$$\boldsymbol{\tau} = \mu[\nabla\boldsymbol{u} + \nabla\boldsymbol{u}^T - 2/3\,(\nabla\cdot\boldsymbol{u})\boldsymbol{I}] \quad (4.3)$$

here, μ is the fluid molecular viscosity, $\boldsymbol{I}$ is the unit tensor.

4.2 TURBULENCE MODELLING

For turbulence modellings, Shear Stress Transport (SST) coupled with γ-$Re_{\theta t}$, realizable, and k-epsilon Delayed Detached Eddy Simulation are introduced in the current study.

4.2.1 SST model

The turbulence kinetic energy, k, and the specific dissipation rate, ω , can be given by the following transport equations

$$\partial(\rho k)/\partial t + \nabla \cdot (\rho \boldsymbol{u} k) = P_k - \beta^* \rho \omega k \ + \nabla \cdot [(\mu + \sigma_k \mu_t)\nabla k] \quad (4.4)$$

$$\partial(\rho \omega)/\partial t + \nabla \cdot (\rho \boldsymbol{u} \omega) = (\alpha \rho/\mu_t) P_k - \beta \rho \omega^2 + \nabla \cdot [(\mu + \sigma_\omega \mu_t)\nabla \omega] + 2\rho(1 - F_1)\frac{\sigma_{\omega 2}}{\omega}\nabla k \cdot \nabla \omega \quad (4.5)$$

here μ_t is the turbulent eddy viscosity, which is computed from

$$\mu_t = \frac{\rho a_1 k}{\max(a_1 \omega, \Omega F_2)} \quad (4.6)$$

where Ω is vorticity magnitude and described by

$$\Omega = \sqrt{2\boldsymbol{W}:\boldsymbol{W}} \quad (4.7)$$

with

$$\boldsymbol{W} = \frac{1}{2}(\nabla \boldsymbol{u} - \nabla \boldsymbol{u}^T) \quad (4.8)$$

Here, the operator : denotes the double dot of two tensors. The term P_k represents the production of turbulence kinetic energy and it can be evaluated using the Boussinesq hypothesis as follows:

$$P_k = -\rho(\boldsymbol{u}'\boldsymbol{u}'):\nabla \boldsymbol{u} \quad (4.9)$$

where $-\rho(\boldsymbol{u}'\boldsymbol{u}')$ is the Reynolds stress tensor, it can be described as follows:

$$-\rho(\boldsymbol{u}'\boldsymbol{u}') = \mu_t[\nabla \boldsymbol{u} + \nabla \boldsymbol{u}^T - 2/3\,(\nabla \cdot \boldsymbol{u})\boldsymbol{I}] - 2/3\,\rho k \boldsymbol{I} \quad (4.10)$$

The constants are obtained using the blending function F_1

$$F_1 = \tanh(\phi_1^4) \quad (4.11)$$

$$\phi_1 = min\left\{max\left(\frac{\sqrt{k}}{0.09\omega y}, \frac{500\mu}{\rho \omega y^2}\right), \frac{4\rho k}{\sigma_{\omega 2} CD_{k\omega} y^2}\right\} \quad (4.12)$$

$$CD_{k\omega} = max\,(2\rho\sigma_{\omega 2}\frac{1}{\omega}\nabla k \cdot \nabla \omega, 10^{-20}) \quad (4.13)$$

and the blending function F_2 are given by:

$$F_2 = \tanh(\phi_2^4) \quad (4.14)$$

$$\phi_2 = max\left(2\frac{\sqrt{k}}{0.09\omega y}, \frac{500\mu}{\rho\omega y^2}\right) \quad (4.15)$$

here, y is the distance from the field point to the nearest wall.

Therefore, σ_k, σ_ω, and α_ω are computed from:

$$\sigma_k = 1/[F_1\sigma_{k1} + (1 - F_1)\sigma_{k2}] \quad (4.16)$$

$$\sigma_\omega = 1/[F_1\sigma_{\omega1} + (1 - F_1)\sigma_{\omega2}] \quad (4.17)$$

$$\alpha_\omega = F_1\alpha_{\omega1} + (1 - F_1)\alpha_{\omega2} \quad (4.18)$$

where

$$\alpha_{\omega1} = \beta_1/\beta^* - (\sigma_{\omega1}\kappa^2)/\sqrt{\beta^*} \quad (4.19)$$

$$\alpha_{\omega2} = \beta_2/\beta^* - (\sigma_{\omega2}\kappa^2)/\sqrt{\beta^*} \quad (4.20)$$

The constants used in the model are:

σ_{k1}=0.85	$\sigma_{\omega1}$=0.5	β_1=0.075
σ_{k1}=1.0	$\sigma_{\omega2}$=0.856	β_2=0.0828
β^*=0.09	κ=0.41	a_1=0.31

4.2.2 Controlled decay SST model

The controlled decay method interacts with the SST turbulence model by modification of the source terms inside k and ω equations as follows:

$$\partial(\rho k)/\partial t + \nabla\cdot(\rho\boldsymbol{u}k) = P_k - \beta^*\rho\omega k + \nabla\cdot[(\mu + \sigma_k\mu_t)\nabla k] + \beta^*\rho\omega_{amb}k_{amb} \quad (4.21)$$

$$\partial(\rho\omega)/\partial t + \nabla\cdot(\rho\boldsymbol{u}\omega) = (\alpha\rho/\mu_t)P_k - \beta\rho\omega^2 + \nabla\cdot[(\mu + \sigma_\omega\mu_t)\nabla\omega] + 2\rho(1 - F_1)\frac{\sigma_{\omega2}}{\omega}\nabla k\cdot\nabla\omega + \beta\rho{\omega_{amb}}^2 \quad (4.22)$$

here, the subtitle "amb" in source terms $\beta^*\rho\omega_{amb}k_{amb}$ and $\beta\rho{\omega_{amb}}^2$ represents the turbulent variables in the freestream.

4.2.3 γ-$Re_{\theta t}$ model

To describe the laminar-turbulent transition, the γ-$Re_{\theta t}$ model is used. The transport equation for the intermittency, γ, and transition momentum thickness Reynolds number, $\widehat{Re}_{\theta t}$, are written as follows:

$$\partial(\rho\gamma)/\partial t + \nabla\cdot(\rho\boldsymbol{u}\gamma) = P_{\gamma 1} - E_{\gamma 1} + P_{\gamma 2} - E_{\gamma 2} + \nabla\cdot\left[\left(\mu + \mu_t/\sigma_\gamma\right)\nabla\gamma\right] \quad (4.23)$$

$$\partial\left(\rho\widehat{Re}_{\theta t}\right)/\partial t + \nabla\cdot\left(\rho\boldsymbol{u}\widehat{Re}_{\theta t}\right) = P_{\theta t} + \nabla\cdot\left[\sigma_{\theta t}(\mu + \mu_t)\nabla\widehat{Re}_{\theta t}\right] \quad (4.24)$$

These source terms inside γ equation are defined as follows:

$$P_{\gamma 1} = C_{a1}F_{length}\rho S(\gamma F_{onset})^{C_{\gamma 3}} \quad (4.25)$$

$$E_{\gamma 1} = C_{e1}P_{\gamma 1}\gamma \quad (4.26)$$

$$P_{\gamma 2} = C_{a2}\rho\Omega\gamma F_{turb} \quad (4.27)$$

$$E_{\gamma 2} = C_{e2}P_{\gamma 2}\gamma \quad (4.28)$$

where F_{length} is an empirical correlation that controls the length of the transition region, S is the strain rate magnitude and described by:

$$S = \sqrt{2\boldsymbol{S}:\boldsymbol{S}} \quad (4.29)$$

with

$$\boldsymbol{S} = (\nabla\boldsymbol{u} + \nabla\boldsymbol{u}^T)/2 \quad (4.30)$$

The transition onset is controlled by the following functions:

$$Re_\omega = \frac{\rho y^2\omega}{\mu} \quad (4.31)$$

$$R_T = \frac{\rho k}{\mu\omega} \quad (4.32)$$

$$Re_v = (\rho y^2 S)/\mu \quad (4.33)$$

$$F_{sublayer} = e^{-\left(\frac{Re_\omega}{200}\right)^2} \quad (4.34)$$

$$F_{length} = F_{length\,1}\left(1 - F_{sublayer}\right) + 40.0F_{sublayer} \quad (4.35)$$

$$F_{onset1} = \frac{Re_v}{2.193Re_{\theta c}} \quad (4.36)$$

$$F_{onset2} = min[max(F_{onset1}, F_{onset1}^4), 2.0] \quad (4.37)$$

$$F_{onset3} = max\left(1 - \left(\frac{R_T}{25}\right)^3, 0\right) \quad (4.38)$$

$$F_{onset} = \max\left(F_{onset2} - F_{onset3}, 0\right) \quad (4.39)$$

$$F_{turb} = e^{-\left(\frac{R_T}{4}\right)^4} \quad (4.40)$$

The source terms inside $Re_{\Theta t}$ equation are defined as follows:

$$U = \sqrt{\boldsymbol{u} \cdot \boldsymbol{u}} \quad (4.41)$$

$$t = \frac{500\mu}{\rho U^2} \quad (4.42)$$

$$\delta = \frac{375\Omega\mu y\widehat{Re}_{\Theta t}}{\rho U^2} \quad (4.43)$$

$$\lambda_\Theta = \frac{\rho\Theta_t^2}{\mu}\frac{dU}{ds} \quad (4.44)$$

$$\frac{dU}{ds} = \frac{\boldsymbol{uu}}{U^2} : \nabla \boldsymbol{u}^T \quad (4.45)$$

$$Re_{\Theta t} = \frac{\rho U \Theta_t}{\mu} \quad (4.46)$$

$$P_{\Theta t} = C_{\Theta t}\frac{\rho}{t}\left(Re_{\Theta t} - \widehat{Re}_{\Theta t}\right)(1.0 - F_{\Theta t}) \quad (4.47)$$

$$F_{\Theta t} = min\left\{max\left[F_{wake}e^{-\left(\frac{y}{\delta}\right)^4}, 1.0 - \left(\frac{C_{e2}\gamma - 1}{C_{e2} - 1}\right)^2\right], 1.0\right\} \quad (4.48)$$

$$F_{wake} = e^{-\left(\frac{Re_\omega}{10^5}\right)^2} \quad (4.49)$$

where $Re_{\Theta t}$ is the onset of the boundary layer transition, $F_{length\,1}$ is an empirical factor that controls the length of the transition region. $Re_{\Theta c}$ is the activated point to match both F_{length} and $Re_{\Theta t}$. These empirical correlations are provided by Langtry and Menter

$$Re_{\Theta t} = f_1(Tu, F(\lambda_\Theta)) \quad (4.50)$$

$$F(\lambda_\Theta) = f_2(Tu, \lambda_\Theta) \quad (4.51)$$

$$F_{length\,1} = f_3\left(\widehat{Re}_{\Theta t}\right) \quad (4.52)$$

$$Re_{\Theta c} = f_4\left(\widehat{Re}_{\Theta t}\right) \quad (4.53)$$

The constants for the γ and $\widehat{Re}_{\Theta t}$equations are:

C_{a1}=2.0	C_{e1}=1.0	$C_{\gamma 3}$=0.5
C_{a2}=0.06	C_{e1}=50.0	σ_{γ}=1.0
$C_{\Theta t}$=0.03	$\sigma_{\Theta t}$=2.0	

4.2.4 SST coupled with γ-$Re_{\theta t}$ model

The γ-$Re_{\theta t}$ model interplays with the SST model by modification of the terms P_k and $\beta^* \rho \omega k$ inside k equation as follows:

$$\partial(\rho k)/\partial t + \nabla \cdot (\rho \boldsymbol{u} k) = P_k^* - D_k^* + \nabla \cdot [(\mu + \sigma_k \mu_t) \nabla k] \quad (4.54)$$

$$P_k^* = \gamma_{eff} P_k \quad (4.55)$$

$$D_k^* = min\left[max\left(\gamma_{eff}, 0.1\right), 1.0\right] \beta^* \rho \omega k \quad (4.56)$$

where P_k is the original production term for the SST model and γ_{eff} is defined using:

$$\gamma_{sep} = min\left\{C_{s1} max\left[\left(\frac{Re_v}{3.235 Re_{\Theta c}}\right) - 1{,}0\right] F_{reattch}, 2.0\right\} F_{\Theta t} \quad (4.57)$$

$$F_{reattch} = e^{-\left(\frac{R_T}{25}\right)^4} \quad (4.58)$$

$$\gamma_{eff} = max\left(\gamma_{sep}, \gamma\right) \quad (4.59)$$

here, C_{s1} is a constant with a value of 2.

4.2.5 Controlled decay SST coupled with γ-$Re_{\theta t}$ model

The controlled decay SST interacts with γ-$Re_{\theta t}$ model as follows:

$$\partial(\rho k)/\partial t + \nabla \cdot (\rho \boldsymbol{u} k) = \gamma_{eff} P_k - min\left[max\left(\gamma_{eff}, 0.1\right), 1.0\right] \beta^* \rho \omega k + \nabla \cdot [(\mu + \sigma_k \mu_t) \nabla k] + \beta^* \rho \omega_{amb} k_{amb} \quad (4.60)$$

$$\partial(\rho \omega)/\partial t + \nabla \cdot (\rho \boldsymbol{u} \omega) = (\alpha \rho/\mu_t) P_k - \beta \rho \omega^2 + \nabla \cdot [(\mu + \sigma_\omega \mu_t) \nabla \omega] + 2\rho(1 - F_1) \frac{\sigma_{\omega 2}}{\omega} \nabla k \cdot \nabla \omega + \beta \rho {\omega_{amb}}^2 \quad (4.61)$$

4.2.6 Realizable k-epsilon model

The modelled transport equations for k and ε in the realizable k-epsilon are:

$$\partial(\rho k)/\partial t + \nabla \cdot (\rho \boldsymbol{u} k) = P_k - \rho \varepsilon + \nabla \cdot [(\mu + \mu_t/\sigma_k) \nabla k] \quad (4.62)$$

$$\partial(\rho \varepsilon)/\partial t + \nabla \cdot (\rho \boldsymbol{u} \varepsilon) = C_1 \rho S \varepsilon - C_2 \rho \frac{\varepsilon^2}{k + \sqrt{(\varepsilon \mu)/\rho}} + \nabla \cdot [(\mu + \mu_t/\sigma_\varepsilon) \nabla \varepsilon] \quad (4.63)$$

here,

$$C_1 = max\ (0.43, \frac{Sk}{Sk+5\varepsilon}) \quad (4.64)$$

and, the eddy viscosity is computed from

$$\mu_t = \rho C_\mu \frac{k}{\varepsilon^2} \quad (4.65)$$

where C_μ is given by

$$C_\mu = \frac{1}{A_0 + A_s \frac{kU^*}{\varepsilon}} \quad (4.66)$$

U^* and A_s are given by:

$$U^* = \sqrt{\boldsymbol{S}:\boldsymbol{S} + \boldsymbol{W}:\boldsymbol{W}} \quad (4.67)$$

$$A_s = \sqrt{6}\cos\varphi \quad (4.68)$$

$$\varphi = \frac{1}{3}\cos^{-1}\left(\sqrt{6}\widehat{W}\right) \quad (4.69)$$

$$\widehat{W} = \frac{\boldsymbol{S}\cdot\boldsymbol{S}^T:\boldsymbol{S}^T}{\hat{S}^3} \quad (4.70)$$

$$\hat{S} = \sqrt{\boldsymbol{S}:\boldsymbol{S}} \quad (4.71)$$

The model constants are

A_0=4.04 C_2=1.9 σ_k=1.0 σ_ε=1.2

4.2.7 Realizable *k*-epsilon Delayed Detached Eddy Simulation (DDES) Model

In the realizable k-epsilon DDES model, the dissipation term, $Y_k = \rho\varepsilon$, in k equation is modified:

$$\partial(\rho k)/\partial t + \nabla\cdot(\rho \boldsymbol{u} k) = P_k - Y_k^* + \nabla\cdot[(\mu + \mu_t/\sigma_k)\nabla k] \quad (4.72)$$

with

$$Y_k^* = \frac{\rho k^{\frac{3}{2}}}{l_{des}} \quad (4.73)$$

where

$$l_{des} = min\ (l_{rke}, l_{les}) \quad (4.74)$$

$$l_{rke} = \frac{k^{\frac{3}{2}}}{\varepsilon} \quad (4.75)$$

$$l_{les} = C_{des}\Delta_{max} \quad (4.76)$$

here, Δ_{max} is the maximum edge length of the cell. If l_{rke}= l_{les}, l_{des} is replaced by the following functions:

$$l_{des} = l_{rke} - f_y max(0, l_{rke} - C_{des}\Delta_{max}) \quad (4.77)$$

$$f_y = 1 - \tanh\left[\left(20.0r_y\right)^3\right] \quad (4.78)$$

$$r_y = \frac{(\mu+\mu_t)/\rho}{\sqrt{\boldsymbol{u}:\boldsymbol{u}}\kappa y^2} \quad (4.79)$$

4.3 CAVITATION MODELLING

The volume fraction transport equation for vapor volume fraction, α_v, is given by:

$$\partial(\rho_v\alpha_v)/\partial t + \nabla\cdot(\rho_v\alpha_v\boldsymbol{u}) = \dot{m} \quad (4.80)$$

The mixture density, ρ, and the mixture flow dynamic viscosity, μ, are defined respectively, as:

$$\rho = \alpha_v\rho_v + (1-\alpha_v)\rho_l \quad (4.81)$$

$$\mu = \alpha_v\mu_v + (1-\alpha_v)\mu_l \quad (4.82)$$

where ρ_v and ρ_l are water and vapor density, μ_v and μ_l are water and vapor dynamic viscosities, respectively.

The mass transfer between the liquid and vapor due to the cavitation is modelled with a source term, $\dot{m}$ in equation (4.80). Neglect the effect of viscosity, non-condensable gas, surface tension, and second-order derivation, the Rayleigh-Plesset equation can be simplified and written as:

$$\dot{R}^2 = \sqrt{\frac{2(P_{ref}-p_v)}{3\rho_l}} \quad (4.83)$$

where p is the saturated vapor pressure and R is the bubble radius.

Assume that the distribution of the nucleation inside the flow field is uniform and independent of the flow structures, then the relationship between the bubble radius R and vaporous volume fraction α_v is given by:

$$\alpha_v = n\frac{4\pi}{3}R^3 \quad (4.84)$$

where n is the number of nucleation per unit volume. Then, the total interphase mass transfer rate per unit volume ($\dot{m}$) is calculated by:

$$\dot{m} = \rho_v \dot{\alpha} = n\rho_v 3\frac{4\pi}{3}R^2\dot{R} \quad (4.85)$$

Submit n given by equations (4.84) and (4.83) into equation (4.85), $\dot{m}$ can be expressed as:

$$\dot{m} = \frac{3\rho_v \alpha}{R}\sqrt{\frac{2(P_{ref}-p_v)}{3\rho_l}} \quad (4.86)$$

In the vaporization process, nucleation site density must decrease as the vapor volume fraction increases. To model this process, α needs to be replaced with $(1-\alpha)\alpha_{nuc}$ in equation (4.86). Then, the final ZGB cavitation model (Zwart et al., 2004) is presented as follows:

$$\dot{m} = \begin{cases} F_c \frac{3\alpha_v \rho_v}{R_0}\sqrt{\frac{2}{3}\frac{(p-p_v)}{\rho_l}} & p > p_v \\ F_v \frac{3\rho_v(1-\alpha)\alpha_{nuc}}{R_0}\sqrt{\frac{2}{3}\frac{(p_v-p)}{\rho_l}} & p < p_v \end{cases} \quad (4.87)$$

where p_v is the saturated vapor pressure. The initial value of the bubble radius is $R = 1\,\mu$m, the nucleation site of the volume fraction $\alpha_{\text{nuc}} = 5 \times 10^{-4}$. By default, the empirical condensation and vaporization coefficients $F_c = 0.01$ and $F_v = 50.0$, respectively. Further optimization for the F_c and F_v will be discussed in the result validation section.

4.4 EQUATION OF STATE

The density of the compressible liquid phase is computed using the Tait equation (Egerer et al., 2016; C. Wang et al., 2020):

$$\rho(p)_l = \rho_{l,sat}\left(\frac{p+B}{p_v+B}\right)^{1/N} \quad (4.88)$$

and the corresponding sound speed is defined as

$$c(p)_l = \sqrt{\frac{\partial p}{\partial \rho}} = \sqrt{\frac{N}{\rho_{l,sat}}(p_v+B)\left(\frac{p+B}{p_v+B}\right)^{(N-1)/N}} \quad (4.89)$$

where B is the water bulk modulus, 3.1×10^8 Pa, $\rho_{l,sat}$ is the liquid density at p_v, 998.18 kg/m^3, and N is 7.15.

The density of the compressible vapor phase using the polytropic equation of state (Tong et al., 2022),can be written as:

$$\rho(p)_v = (p/C_v)^{1/n} \quad (4.90)$$

and the corresponding sound speed is:

$$c(p)_v = \sqrt{\frac{\partial p}{\partial \rho}} = \sqrt{C_v n (p/C_v)^{(n-1)/n}} \quad (4.91)$$

where the model constant C_v can be estimated from a density of 0.017 kg/m^3 at p_v. The polytropic exponent n for an adiabatic assumption is 1.41.

4.5 SPONGE LAYER CONDITIONS

Up to date, although the use of the pressure-based method has achieved notable success in a wide range of compressible cavitating flows (Li & Vasquez, 2013; Brunhart et al., 2020), several unresolved numerical difficulties remain, particularly concerning the determination of the inlet and outlet boundary conditions in CFD simulations. Typically, such calculations are conducted on a truncated domain of the entire system and the standard inlet/outlet boundary conditions may fail to allow the flow features to leave the computational domain as physically expected. For that reason, artificial treatments of the truncated domains are required at the fluid domain edges. In this study, the sponge layer is adopted for its flexibility and simplicity (Mani, 2012). The set of formulas of the sponge layer based on the pressure and velocity for the pressure-based method is given as follows:

$$\partial\rho/\partial t + \nabla \cdot (\rho \boldsymbol{u}) = \boldsymbol{\sigma}(\boldsymbol{x}) \frac{\partial \rho}{\partial p}\Big|_{p=p_{ref}} \left(p_{ref} - p\right) \quad (4.92)$$

$$\partial(\rho \boldsymbol{u})/\partial t + \nabla \cdot (\rho \boldsymbol{u}\boldsymbol{u} + p\boldsymbol{I} - \boldsymbol{\tau}) = \boldsymbol{\sigma}(\boldsymbol{x})\rho\left(\boldsymbol{u}_{ref} - \boldsymbol{u}\right) \quad (4.93)$$

where the subtitle “ref” refers to a target value of the flow variable and $\boldsymbol{\sigma}(\boldsymbol{x})$ is the function of the damping coefficient, which is defined as:

$$\boldsymbol{\sigma}(\boldsymbol{x}) = \frac{3\alpha_{pol}(\boldsymbol{x}/L)^{\beta_{pol}}}{2\Delta t^{\gamma_{pol}}} \quad (4.94)$$

Here, $\alpha_{pol} = 1.0$, $\beta_{pol} = 3.0$, $\gamma_{pol} = 1.0$ and x is the distance from the leading edge of the sponge layer and L is the length of the sponge layer, as shown in Fig. 4.1.

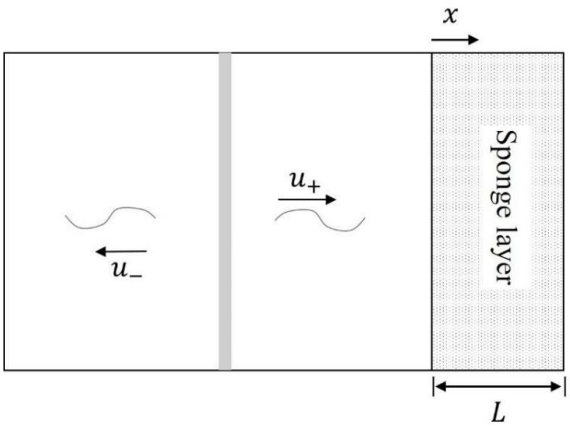

Fig. 4.1 Schematic of the sponge layer implementation.

4.6 NUMERICAL METHOD

In this section, the governing equations are discretized using the Finite Volume Method (FVM) over the collocated unstructured mesh. More specifically, the transient term is estimated using a bound second-order implicit or second-order implicit scheme. The convective flux can be discretized by a second-upwind scheme. The face pressure is estimated by PRESTO! scheme for the multiphase flow while second-order upwind for the single-phase flow.

More attention will be paid to the numerical algorithm for the pressure-based multiphase solver with/without consideration of fluid compressibility using the predefined macro "DEFINE_LINEARIZED_MASS_TRANSFER" inside the ANSYS Fluent platform, see the Appendix.

4.6.1 Incompressible mixture/VOF model

Without consideration of fluid compressibility, the fluid densities are constant. The numerical algorithm for the mass conservation and volume fraction transport equation with linearized source terms is detailed.

(i) Volume continuity equation

To guarantee mass conservation and numerical stability, the pressure-correction equation is based on the total volume continuity instead of the mass conservation equation.

$$\frac{1}{\rho_v}[\partial(\rho_v\alpha_v)/\partial t + \nabla\cdot(\rho_v\alpha_v\boldsymbol{u}) - \dot{m}] + \frac{1}{\rho_l}[\partial(\rho_l\alpha_l)/\partial t + \nabla\cdot(\rho_l\alpha_l\boldsymbol{u}) + \dot{m}] = 0 \quad (4.95)$$

Integrating equation (2.98) over a control volume, the discretized form of the volume continuity is given by:

$$\frac{1}{\rho_v}\left(\frac{\rho_v\alpha_v-\rho_v{\alpha_v}^0}{\Delta t}dV+\sum_f \rho_v\alpha_v\boldsymbol{u}_f\boldsymbol{A}_f\right)+\frac{1}{\rho_v}\left(\frac{\rho_l\alpha_l-\rho_l{\alpha_l}^0}{\Delta t}dV+\sum_f \rho_l\alpha_l\boldsymbol{u}_f\,\boldsymbol{A}_f\right)=$$
$$\left(\frac{1}{\rho_v}-\frac{1}{\rho_l}\right)\left[\dot{m}^*-\left(\frac{\partial\dot{m}}{\partial p}\right)^*(p^*-p_v)\right]+\underbrace{\left(\frac{\partial\dot{m}}{\partial p}\right)^*\left(\frac{1}{\rho_v}-\frac{1}{\rho_l}\right)}_{ds/dp}(p-p_v) \quad (4.96)$$

where dV is the volume of the control cell, $\boldsymbol{A}_f$ is the face area vector within the control volume, $\rho_v\alpha_v\boldsymbol{u}_f$ and $\rho_l\alpha_l\boldsymbol{u}_f$ are the vapor and liquid mass flux, respectively. On the collocated grid, the phase mass flux is computed using a Rhie–Chow interpolation.

More importantly, the ds/dp is the linearized mass transfer term related to the pressure for the pressure correction equation, which can enhance the numerical stability of the cavitation simulation. Inside the "DEFINE_LINEARIZED_MASS_TRANSFER" macro, this term corresponds to the inner variable, SV_MT_DS_DP.

(ii) Second phase fraction equation

In ANSYS Fluent, only the transport equation for the second phase volume fraction is solved using the VOF or mixture model. Normally, the vapor phase is set to be the second phase. Thus, the vapor volume fraction is obtained with the vapor phase continuity equation as presented in equation (4.80). Correspondingly, the discretized form of the equation can be written as follows:

$$\frac{1}{\rho_v}\left(\frac{\rho_v\alpha_v-\rho_v{\alpha_v}^0}{\Delta t}dV+\sum_f \rho_v\alpha_v\boldsymbol{u}_f\boldsymbol{A}_f\right)=\frac{\dot{m}}{\rho_v}dV \quad (4.97)$$

Assume the mass source term $\dot{m}$ can be rewritten as the function of α_v and α_l:

$$\frac{\dot{m}}{\rho_v}=\dot{m}_0+S_l\alpha_l-S_v\alpha_v \quad (4.98)$$

With linearized the mass source term $\dot{m}$, the equation (4.98) can be rewritten as:

$$\frac{1}{\rho_v}\left(\frac{\rho_v\alpha_v-\rho_v{\alpha_v}^0}{\Delta t}dV+\sum_f \rho_v\alpha_v\boldsymbol{u}_f\boldsymbol{A}_f\right)=\left(S_c+S_p\alpha_v\right)dV \quad (4.99)$$

where

$$\begin{cases} S_c=\dot{m}_0+S_l \\ S_p=-(S_v+S_l) \end{cases} \quad (4.100)$$

Here, S_p is the linear part of the source term $\dot{m}$, which is denoted as *lin_to inside the "DEFINE_LINEARIZED_MASS_TRANSFER" macro. S_c is the part of $\dot{m}$ which cannot be linearized.

4.6.2 Compressible mixture/VOF model

In this section, the robust numerical algorithm for the compressible multiphase flows to handle fluid compressibility is introduced (Li & Vasquez, 2013). With the SIMPLE method, velocity and density fields can be decomposed into two parts as follows:

$$\begin{cases} \rho_v = ({\rho_v}^* + \rho_v') = {\rho_v}^* + \left(\frac{\partial {\rho_v}^*}{\partial p}\right) p' \\ \rho_l = ({\rho_l}^* + \rho_l') = {\rho_l}^* + \left(\frac{\partial {\rho_l}^*}{\partial p}\right) p' \\ \boldsymbol{u} = (\boldsymbol{u}^* + \boldsymbol{u}') \end{cases} \quad (4.101)$$

where "$*$" indicates the tentative values and "$'$" indicates the variable correction.

(i) Volume continuity equation

Unlike the incompressible pressure-correction equation, the phase mass, $\rho_v\alpha_v$, $\rho_l\alpha_l$ and the phase flux terms, $\rho_v\alpha_v\boldsymbol{u}$, $\rho_l\alpha_l\boldsymbol{u}$ are computed by:

$$\begin{cases} \rho_v\alpha_v = {\rho_v}^*\alpha_v + \left(\frac{\partial {\rho_v}^*}{\partial p}\right) p'\alpha_v \\ \rho_l\alpha_l = {\rho_l}^*\alpha_l + \left(\frac{\partial {\rho_l}^*}{\partial p}\right) p'\alpha_l \end{cases} \quad (4.102)$$

$$\begin{cases} \rho_v\alpha_v\boldsymbol{u} = ({\rho_v}^* + \rho_v')\alpha_v(\boldsymbol{u}^* + \boldsymbol{u}') = {\rho_v}^*\boldsymbol{u}^*\alpha_v + \left(\frac{\partial {\rho_v}^*}{\partial p}\right) p'\boldsymbol{u}^*\alpha_v + {\rho_v}^*\boldsymbol{u}'\alpha_v + \underbrace{\rho_v'\alpha_v\boldsymbol{u}'}_{\text{high-order}} \\ \rho_l\alpha_l\boldsymbol{u} = ({\rho_l}^* + \rho_l')\alpha_l(\boldsymbol{u}^* + \boldsymbol{u}') = {\rho_l}^*\boldsymbol{u}^*\alpha_l + \left(\frac{\partial {\rho_l}^*}{\partial p}\right) p'\boldsymbol{u}^*\alpha_l + {\rho_l}^*\boldsymbol{u}'\alpha_l + \underbrace{\rho_l'\alpha_l\boldsymbol{u}'}_{\text{high-order}} \end{cases} \quad (4.103)$$

Normally, the high-order correction terms in the equation are omitted due to their small magnitude compared with the other terms and their negligible influence on the resolved field. Then the discretized form of the volume continuity can be written as:

$$\frac{1}{\rho_v}\left(\frac{{\rho_v}^*{\alpha_v}^* + \left(\frac{\partial {\rho_v}^*}{\partial p}\right)p' - {\rho_v}^0{\alpha_v}^0}{\Delta t} dV + \sum_f \left({\rho_{v,f}}^*\boldsymbol{u}^*\alpha_v + \left(\frac{\partial {\rho_v}^*}{\partial p}\right)_f p'\boldsymbol{u}^*\alpha_v + {\rho_{v,f}}^*\boldsymbol{u}'\alpha_v\right)\boldsymbol{A}_f\right) + \frac{1}{\rho_l}\left(\frac{{\rho_l}^*{\alpha_l}^* + \left(\frac{\partial {\rho_l}^*}{\partial p}\right)p' - {\rho_l}^0{\alpha_l}^0}{\Delta t} dV + \sum_f \left({\rho_{l,f}}^*\boldsymbol{u}^*\alpha_l + \left(\frac{\partial {\rho_l}^*}{\partial p}\right)_f p'\boldsymbol{u}^*\alpha_l + \right.\right.$$

$$\rho_{l,f}{}^{*}\boldsymbol{u}'\alpha_l\Big)\boldsymbol{A}_f\Big) = \left(\frac{1}{\rho_v}-\frac{1}{\rho_l}\right)\left[\dot{m}^* - \left(\frac{\partial \dot{m}}{\partial p}\right)^*(p^*-p_v)\right] + \underbrace{\left(\frac{\partial \dot{m}}{\partial p}\right)^*\left(\frac{1}{\rho_v}-\frac{1}{\rho_l}\right)}_{ds/dp}(p-p_v) \tag{4.104}$$

where $\rho_{v,f}{}^{*}\boldsymbol{u}^{*}\alpha_v$ is the phase mass flux at the cell face.

The above equation not only couples the pressure and velocity but also involves the interaction between the flow field and the mass transfer source term. Note that the terms $\frac{\partial \rho_v{}^*}{\partial p}$ and $\frac{\partial \rho_l{}^*}{\partial p}$ are related to the effect of the vapor and liquid compressibility on the pressure correction, respectively. By default, these terms are approximated by the upwind scheme. The compressibility-related term in the transient term and mass transfer source term can be easily linearized, which can significantly enhance the numerical stability without affecting the final solution.

(ii) Second phase fraction equation

With consideration of the compressible effect of the second phase, the discretized form of the volume fraction equation can be written as follows when the second phase is the vapor:

$$\frac{1}{\rho_v}\left(\frac{\rho_v\alpha_v-\rho_v{}^0\alpha_v{}^0}{\Delta t}dV + \sum_f \rho_{v,f}\alpha_v\boldsymbol{u}_f\boldsymbol{A}_f\right) = \left(S_c + S_p\alpha_v\right)dV \tag{4.105}$$

The left-hand side of the equation can be rewritten as:

$$\frac{\alpha_v-\alpha_v{}^0}{\Delta t}dV + \sum_f \alpha_v\boldsymbol{u}_f\boldsymbol{A}_f = \left(S_c + S_p\alpha_v\right)dV + \left\{\underbrace{-\left(\frac{\rho_v-\rho_v{}^0}{\rho_v}\frac{\alpha_v{}^0 dV}{\Delta t}\right) + \left(\sum_f \frac{\rho_v-\rho_{v,f}}{\rho_v}\alpha_v\boldsymbol{u}_f\boldsymbol{A}_f\right)}_{\text{expansion source}}\right\} \tag{4.106}$$

where the last term is the expansion source term accounting for the effect of fluid compressibility on the volume conservation equation. It is composed of two parts: one from the transient term and the other from the advection term.

4.6.3 Pressure limits

As we know, the pressure-based solver can provoke an unbounded pressure field, e.g. negative pressure field. For the compressible flow, it is necessary to limit the pressure since the obtained negative pressure field is out of the predefined range of the fluid material. However, limiting the pressure is a challenging numerical issue, which

will lead to a decrease in the convergence rate and numerical instability. In the case of the multiphase compressible flows, the situation will be more server. As mentioned by Li and Vasquez (2013), it is difficult to directly limit the pressure above zero in the region where only a negligible amount of gas is present. In such a case, the limitation of the pressure must consider the effect of the local flow characteristic. In the sprint of the pressure-limited method proposed by Li and Vasquez (2013), the fluid density is computed using the barotropic law with a pre-described pressure limit when the local pressure turns negative. For instance, the Tait equation for the compressible liquid density with the pressure-limited can be rewritten as:

$$\rho(p)_l = \rho_{l,sat}\left[\frac{max\,(p,p_{lim})+B}{p_v+B}\right]^{1/N} \quad (4.107)$$

and the corresponding sound speed with the pressure-limited is defined as

$$c(p)_l = \sqrt{\frac{\partial p}{\partial \rho}} = \sqrt{\frac{N}{\rho_{l,sat}}(p_v+B)\left[\frac{max\,(p,p_{lim})+B}{p_v+B}\right]^{(N-1)/N}} \quad (4.108)$$

where p_{lim} is the pre-described pressure limit.

Chapter 5: Incompressible cavitation solver

In this chapter, the validation and verification of the incompressible cavitation solver is conducted by using the Rayleigh bubble collapse case. In this case, starting with an initial bubble radius of $R_0 = 4.0$ mm, and a constant pressure of $p_\infty = 1.0$ bar, the bubble collapses under constant pressure, neglecting the effects of viscosity, non-condensable gas, and surface tension. Based on the obtained numerical results, the numerical implementation of the cavitation will be evaluated, and the impact of the condensation coefficient on the modeling of the stationary bubble collapse will be assessed.

5.1 THEORETICAL SOLUTION

The temporal evolution of the bubble radius, R, under a constant ambient pressure p_∞ can be theoretically derived from the Rayleigh-Plesset equation (Brennen, 2014). Neglecting viscosity, non-condensational gas, and surface tension, the Rayleigh-Plesset equation can be simplified to the Rayleigh bubble collapse equation given by:

$$\dot{R}^2 = -[p_\infty - p_v]\left(1 - \frac{R_0^3}{R^3}\right) \qquad (5.1)$$

where p_v is the saturated vapor pressure. The collapse time is defined as $\tau_C = 0.915 R_0 \sqrt{\frac{\rho_l}{p_\infty - p_v}}$ and the radial profile of the pressure $p(r)$ as a function of bubble radius R as:

$$p(r) = \begin{cases} \left[\frac{R}{3r}\left(\frac{R_0^3}{R^3} - 4\right) - \frac{R^4}{3r^4}\left(\frac{R_0^3}{R^3} - 1\right)\right](p_\infty - p_v) + p_\infty & r > R \\ p_v & r < R \end{cases} \qquad (5.2)$$

Combining equation (5.1) and equation (5.2) yields the theoretical temporal evolution of pressure at a fixed observation point during the bubble collapse. Fig. 5.1 shows the time evolution of the pressure at distances of $0.75R_0$, $0.5R_0$, $0.25R_0$, and $0.0R_0$ from the bubble center. Before the interface reaches the observation points, the pressure remains constant. However, once the interface reaches the observation point, the pressure begins to increase monotonically and eventually approaches infinity as the bubble collapses.

The collapse time has traditionally been defined as the time at which the radius of a bubble approaches zero, as stated in Brennen (2014) and Franc and Michel (2006), and denoted as $\tau_{C,R\to 0}$. However, Mihatsch (2017) has proposed an alternative definition for the collapse time, τ_{C,p_max}, which is defined as the time at which the highest pressure is recorded in the field. It is worth noting that, based on the theoretical solution presented in Fig. 5.1(a), there is no difference between these two definitions. Nonetheless, it is not advisable to use $\tau_{C,R\to 0}$ to define the collapse time due to the phenomenon of "dynamic delay," as coined by Bhatt et al. (2015). This refers to the numerical phenomenon where the vapor volume fraction can remain at a high value for a prolonged period after the highest pressure is recorded. As such, it is more appropriate to use τ_{C,p_max} to define the collapse time in this study.

Mass transfer across the interface is considered to be negligible, as suggested by Brennen (2014) and Franc and Michel (2006). Consequently, the flow is governed by inertial forces owing to the constant pressure within the bubble, which does not dampen the motion of the liquid. Specifically, the theoretical pressure field maintains a constant value equal to the saturated vapor pressure inside the bubble, while slightly higher values are observed outside the bubble region, as depicted in Fig. 5.1(a). Moreover, the theoretical density field is completely occupied by vapor inside the bubble and by liquid outside the bubble, as shown in Fig. 5.1(b). Thus, the Rayleigh bubble collapse problem's barotropic model can be simplified as:

$$\rho = \begin{cases} \rho_l & p > p_v \\ \rho_v & p < p_v \end{cases} \qquad (5.3)$$

which is also known as the cut-off model (T. G. Liu et al., 2004). The theoretical $\rho - p$ trajectory at fixed observation points, as depicted in Fig. 5.1(c), demonstrates that the apparent fluid compressibility $\partial\rho \,/\, \partial p$ in the Eulerian framework approaches infinity when the pressure field gets close to the saturated vapor pressure.

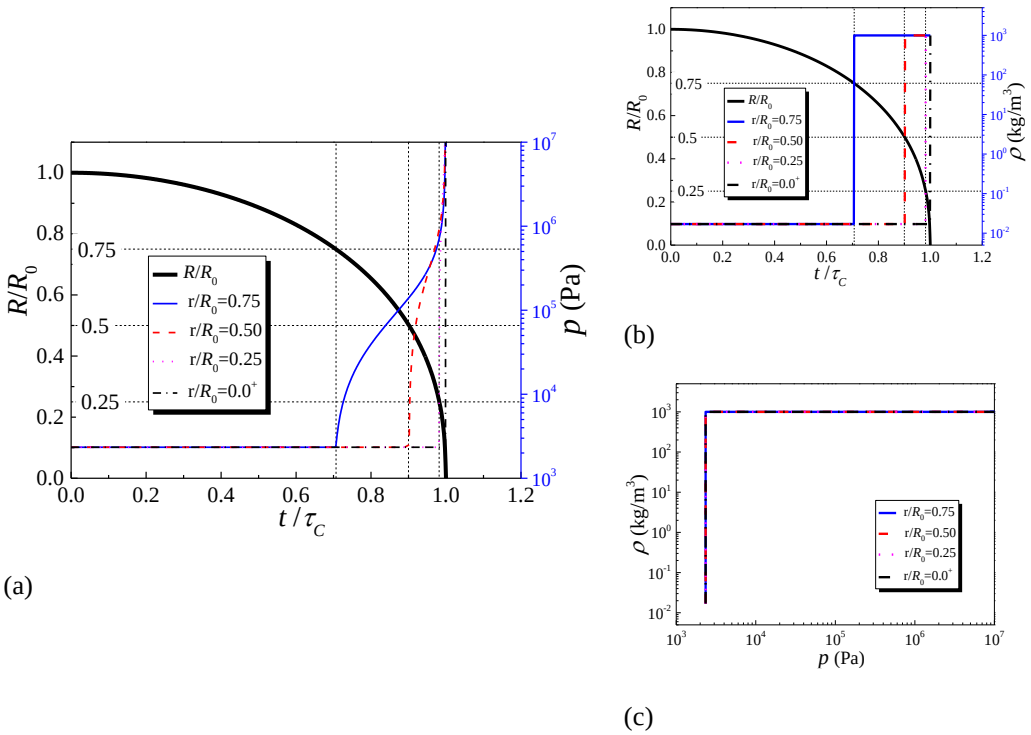

Fig. 5.1 Theoretical time evolution of pressure p, density ρ (b), and ρ-p (c) trajectory at different observation points, in which, the solid black line indicates the time evolution of the bubble interface.

5.2 NUMERICAL SETUP

For the bubble collapse case, the computational domain is shown in Fig. 5.2(a) composed of a quarter sphere with one element layer, and with a domain radius 100 times the initial bubble radius R_0. It is discretized with a structured mesh, illustrated in Fig. 5.2(b). For the boundary, an axis and symmetry boundary conditions are applied to the surface patches shown in Fig. 5.2(a) to obtain the complete spherical bubble. Additionally, a fixed pressure value, $p_{ref} \approx p_\infty = 1\,\text{bar}$, is enforced at the outlet pressure.

The initial state of the simulation entails a stationary bubble with a radius of $R_0 = 0.4\,(\text{mm})$. As displayed in Fig. 5.3(a), the vapor volume fraction within the bubble is initially set to 1.0, and outside the bubble, it is 0.0. Furthermore, Fig. 5.3(b) illustrates that the initial pressure profile within the computational domain's interior should comply with equation (5.2) when $R = R_0$.

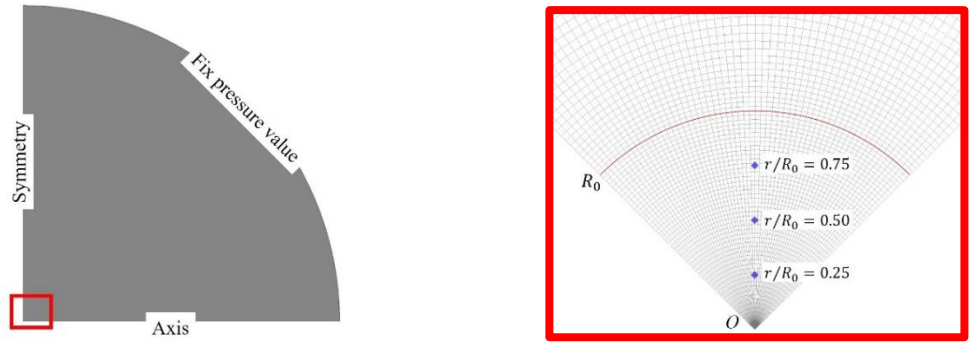

(a) (b)

Fig. 5.2 The boundary types of the individual patches (a) and corresponding block mesh topology (b).

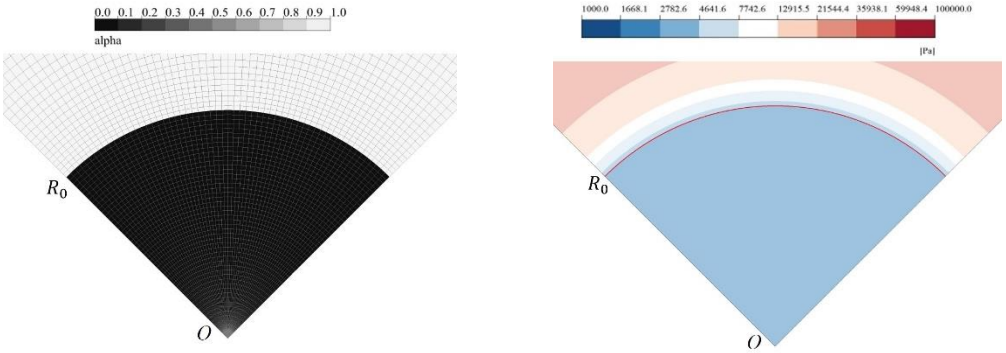

(a) (b)

Fig. 5.3 Initial vapor volume fraction profile with a sharp interface at R_0=0.4 mm (a) and initial pressure distribution (b).

With ANSYS Fluent®, a second-order scheme is used to calculate the spatial field to ensure the accuracy of numerical results. Therefore, the second upwind scheme with the Minmod function is utilized to compute the transport scalar. In addition, the compressive scheme with $\beta = 1.0$ is used for VOF value construction at the face to ensure the boundness of the void volume fraction. To estimate the face pressure, the default PRESTO! scheme has been employed. For transient terms, a first-order implicit time scheme has been utilized. Furthermore, for velocity flux calculations, the momentum-weighted interpolation (MWI) with the Choi correction method has been used. Moreover, the PISO scheme is employed for solving the velocity-pressure coupling. The absolution residual criteria are set to be 10^{-6} for all equations to ensure a balance between computational efficiency and convergence. To ensure that the residual level satisfies the criteria, a maximum of 50 iterations are used for each timestep.

5.3 MESH SENSITIVITY ASSESSMENT

Fig. 5.4 shows how the temporal evolution of bubble radius for different F_c and resolutions converge to a single profile when $R_0/\Delta x$ is equal to or greater than 50. Similarly, Fig. 5.5 illustrates the temporal evolutions of α_v concerning r/R_0 for various F_c and resolutions. The obtained results suggest that outcomes independent of the mesh resolution can be achieved with 5×10^{-7}(s), if $R_0/\Delta x \geq 50$. Consequently, subsequent analyses rely on numerical results that were obtained using $R_0/\Delta x = 100$.

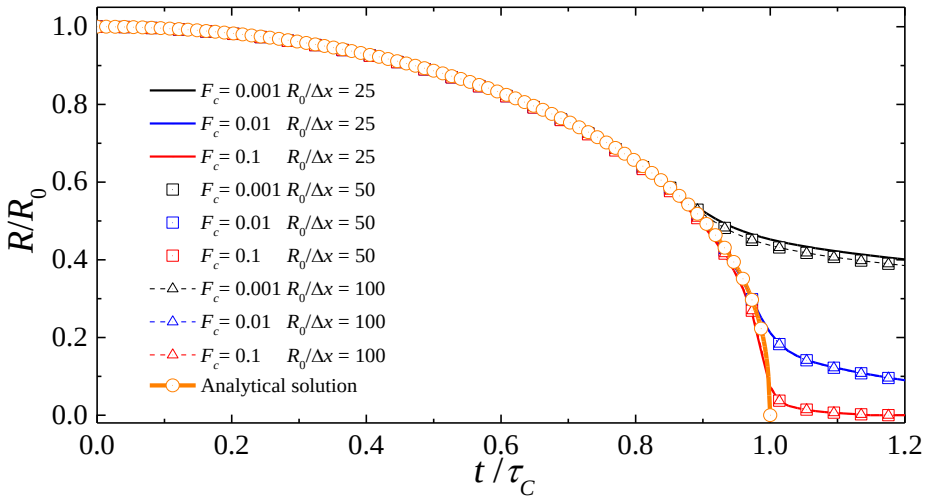

Fig. 5.4 For time step sizes Δt=5×10^{-7} s, the time evolution of the bubble radius $R(t)$ for different mass transfer coefficients F_c and mesh resolutions $R_0/\Delta x$.

$R_0/\Delta x = 25\ F_c = 0.001$ $R_0/\Delta x = 25\ F_c = 0.01$ $R_0/\Delta x = 25\ F_c = 0.1$

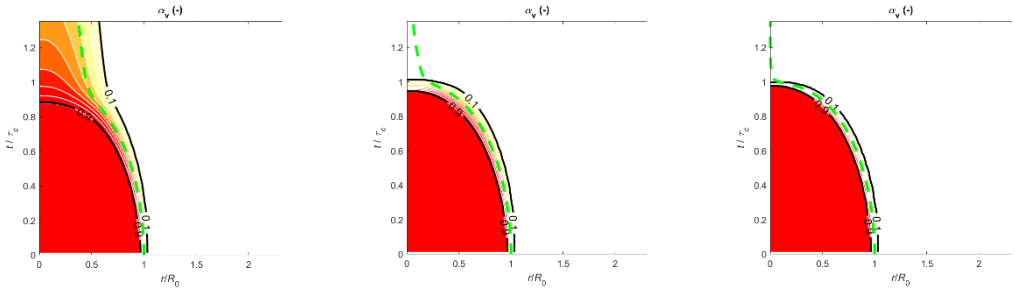

$R_0/\Delta x = 50\ F_c = 0.001$ $R_0/\Delta x = 50\ F_c = 0.01$ $R_0/\Delta x = 50\ F_c = 0.1$

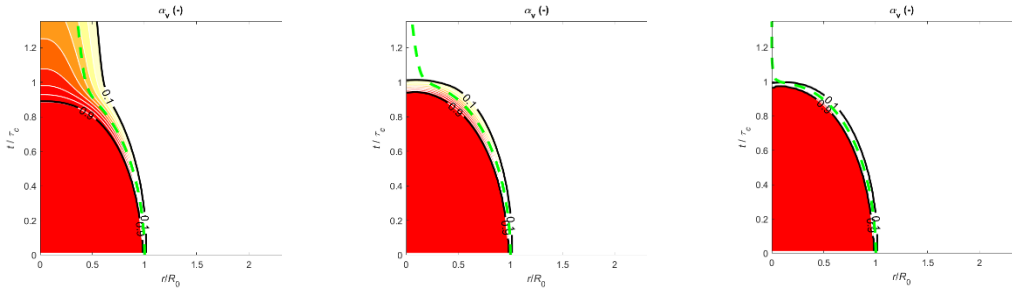

$R_0/\Delta x = 100\ F_c = 0.001$ $R_0/\Delta x = 100\ F_c = 0.01$ $R_0/\Delta x = 100\ F_c = 0.1$

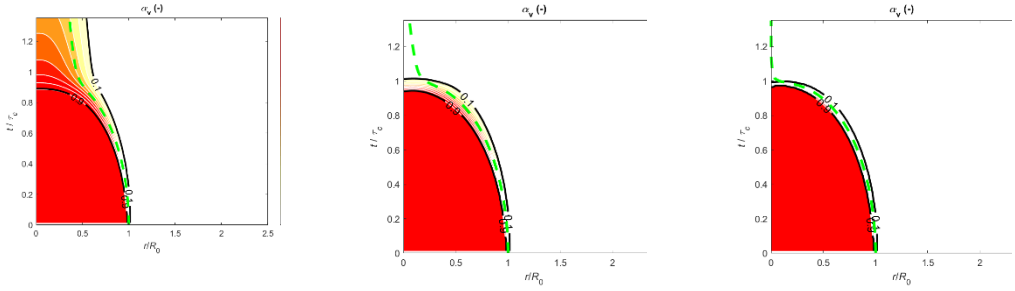

Fig. 5.5 Vapor volume fraction α_v over the non-dimensional radial location r/R_0 and the non-dimensional time t/τ_c for different F_c. The evolution of the reconstructed bubble interface is presented by the green dashed line, where the instantaneous interface is reconstructed from $R=3V_{vap}/(4\pi)^{1/3}$, and V_{vap} is the volume integration of vapor volume fraction over the entire domain.

5.4 EFFECTS OF CONDENSATION COEFFICIENT ON THE COLLAPSE CHARACTERISTICS

To demonstrate the effects of F_c on the collapse characteristics, the evolution of the vapor volume fraction α_v, radial velocity V_r, and the non-dimensional pressure field p/p_∞ are depicted in Fig. 5.6. For the smallest $F_c = 0.001$, a distinct diffusion of the interface is observed to start at $t/\tau_c = 0.8$. This interface diffusion is accompanied by an additional flux inside the bubble, as depicted in Fig. 4.6. Following the bubble collapse at $t/\tau_c > 0.92$, the vapor volume fraction inside the bubble still shows a high value while the mass flux inside the bubble tends to diminish. Conversely, for large values such as $F_c = 0.01$ or $F_c = 0.1$, the interface sharpness is reasonably well-preserved until the final collapse stage. In essence, a higher value of F_c tends to reduce the diffusion of the bubble interface, whereas a lower value of F_c tends to increase the diffusion of the interface, causing a reduction in the bubble collapse time.

Table 5.1 presents the value, time, and location of the maximum pressure identified from the contours of pressure. It must be noted that an increase in F_c results in the convergence of τ_{C,p_max} to τ_C, as previously defined. This finding agrees well with the previous research conducted by Bhatt et al.(2015), Schenke and van Terwisga (2017), and Ghahramani et al. (2019). Additionally, the maximum pressure value generated at the center of the bubble jumps from 1.09×10^6 (Pa) for $F_c = 0.001$, to 9.84×10^6 (Pa) for $F_c = 0.1$, the value of which is proportional to the increases of F_c.

Fig. 5.7(a) illustrates how the $p - \rho$ trajectories are significantly affected by different F_c and observation points. Specifically, at a fixed observation point, the slope

of $p-\rho$ trajectories rises with an increase of F_c. Conversely, at a constant value of F_c, the slope decreases as the bubble approaches.

Table 5.1 Comparison of the collapse time with different F_c.

F_c	p_{max}	$\tau_{C,p\_max}/\tau_c$	r/R_0
0.001	1.09e6	0.92	0.0
0.01	3.54e6	1.00	0.0
0.1	9.84e6	1.00	0.0

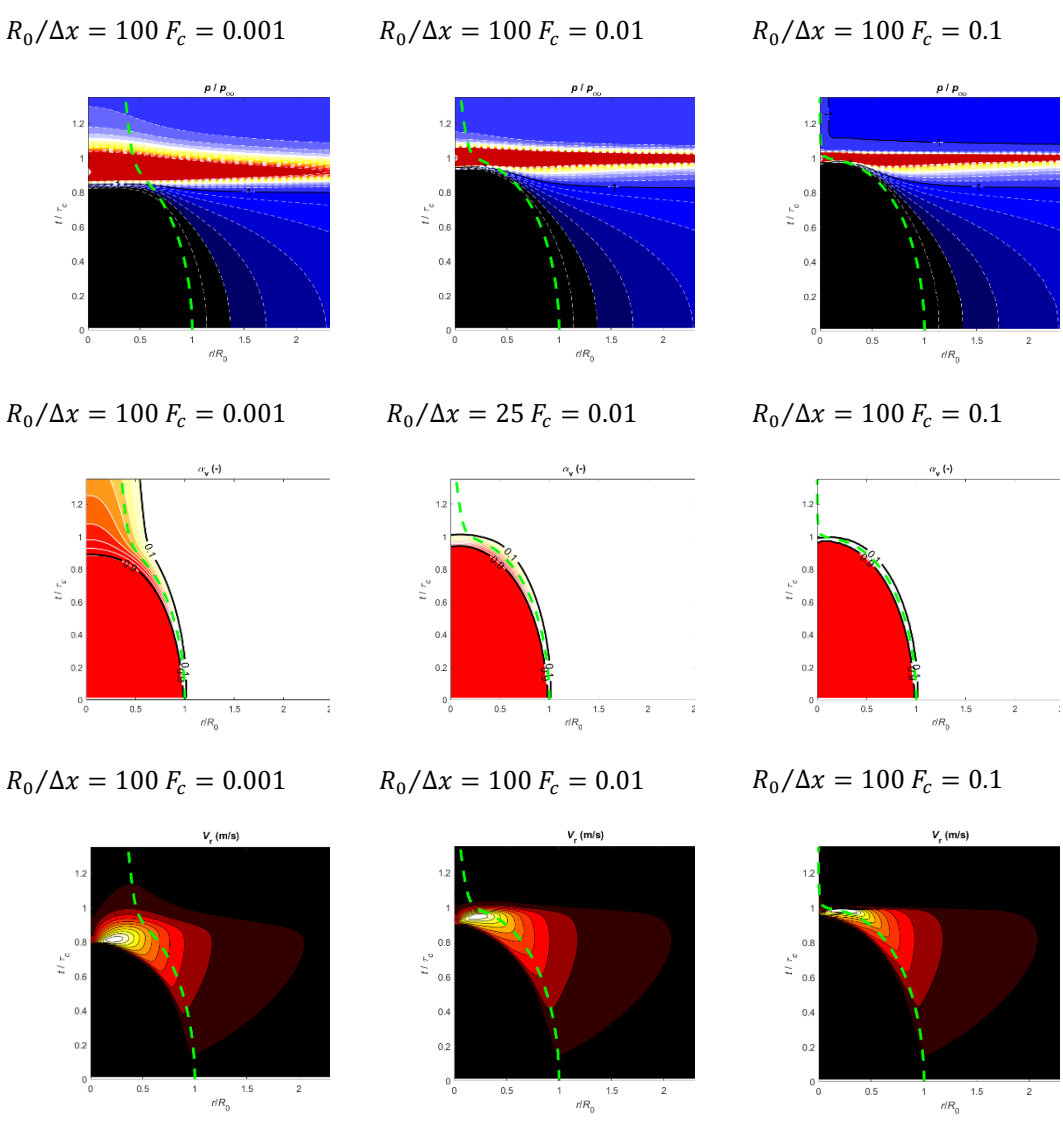

Fig. 5.6 Non-dimensional pressure p/p_∞(top), vapor volume fraction α_v (middle), and radial velocity V_r (bottom) as a function of the non-dimensional radial distance r/R_0 and the non-dimensional time t/τ_c for different F_c. The green dashed line presents the evolution of the reconstructed bubble interface.

Fig. 5.7(b) displays the time evolution of the mixture density for various F_c at three distinct observation points. The results indicate that the local phase transition rate, $\partial\rho/\partial t$, tends to increase with higher values of F_c. Furthermore, Fig. 5.7(c) shows again that the pressure trajectories are significantly influenced by the observation point's location and the condensation mass transfer coefficient. Specifically, at a constant observation point, the slope, $\partial p/\partial t$, rises with increasing F_c. Conversely, at a fixed value of F_c, the slope increases as the bubble center is approached.

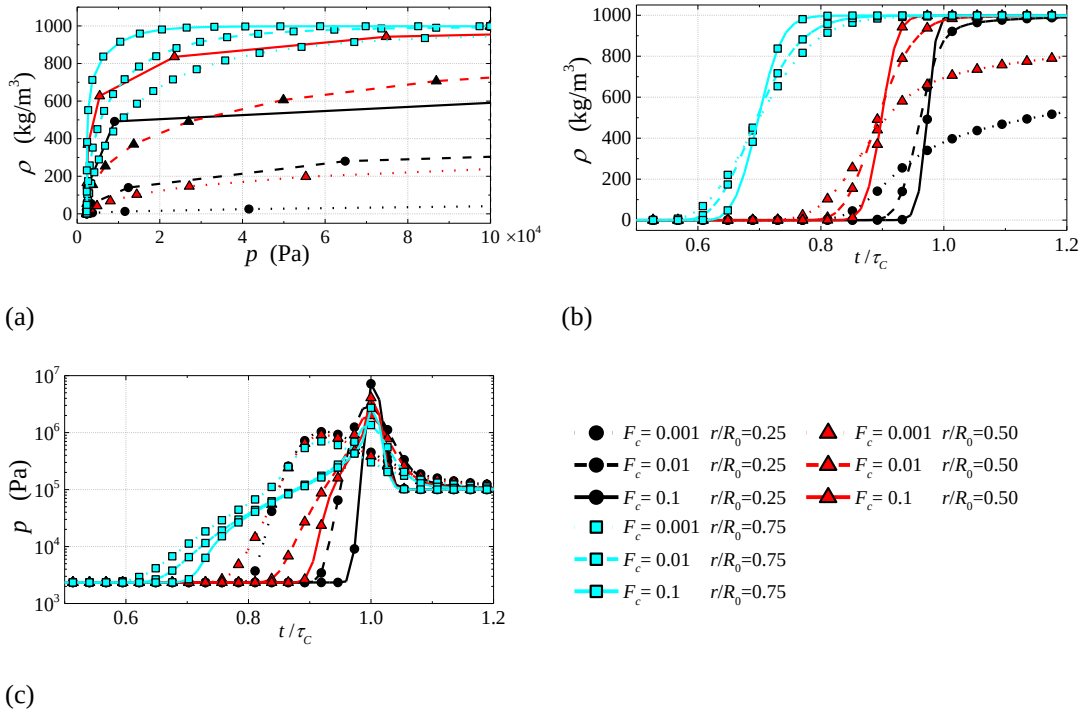

Fig. 5.7 ρ-p trajectories (a), the time evolution of the mixture density ρ (b), and pressure p(c) at the different observation points for the different F_c.

In the spirit of Schenke (2020), it is possible to derive the apparent fluid compressibility for a given finite mass transfer model, which is defined in the Eulerian reference frame as:

$$\frac{\partial\rho}{\partial p}=-\frac{\rho\Gamma+\nabla\rho\cdot\boldsymbol{u}}{\partial p/\partial t}=-\frac{\nabla\rho\cdot\boldsymbol{u}}{\partial p/\partial t}+\frac{(\rho_l-\rho_v)\alpha_v\left(F_c\frac{3}{R_B}\sqrt{\frac{2(p-p_v)}{3\quad\rho_l}}\right)}{\partial p/\partial t} \tag{5.4}$$

And in the Lagrangian reference frame is defined as

$$\frac{D\rho}{Dp}=-\frac{\partial\rho/\partial t+\boldsymbol{u}\cdot\nabla\rho}{\partial p/\partial t+\boldsymbol{u}\cdot\nabla p}=\frac{(\rho_l-\rho_v)\alpha_v\left(F_c\frac{3}{R_B}\sqrt{\frac{2(p-p_v)}{3\quad\rho_l}}\right)}{\partial p/\partial t+\boldsymbol{u}\cdot\nabla p} \tag{5.5}$$

It can be seen as F_c approaches infinity, both Eulerian and Lagrangian fluid compressibility ($\frac{\partial \rho}{\partial p}$ and $\frac{D\rho}{Dp}$) also approach infinity, leading the model to degenerate to the incompressible cutoff model (T. G. Liu et al., 2004). As the mass transfer rate tends towards infinity, the corresponding barotropic model assumes the same form as the one obtained from the Rayleigh bubble collapse equation.

Fig. 5.8 demonstrates numerically that the pressure profile converges to the theoretical solution as F_c increases at various observation points. It confirms that the mass transfer model would theoretically mimic the equilibrium model if the finite transfer rate tended to infinity, and the explicit form of this equilibrium model is the incompressible cut-off model (Schenke, 2020; Schenke & van Terwisga, 2017).

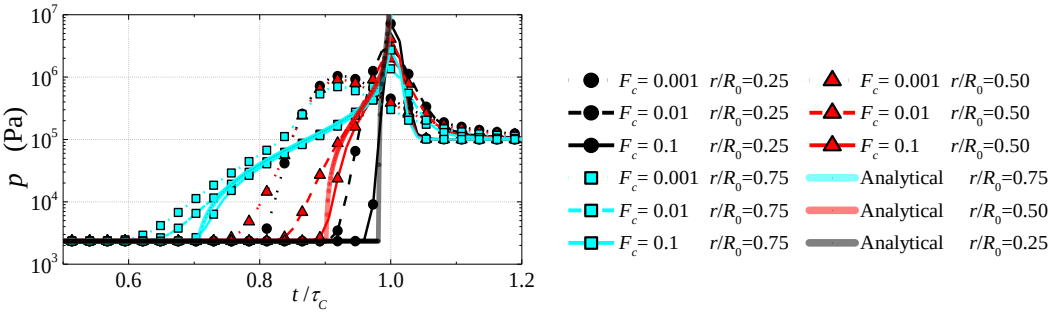

Fig. 5.8 Comparison between the time evolution pressure p at the different observation points and for the different mass transfer coefficients F_c.

5.5 PARTIAL CONCLUSIONS

In this chapter, the homogeneous mixture model coupled with the TEM has been used to investigate the collapse of a single spherical bubble subjected to constant pressure. The good agreement between the numerical results and the theoretical solution validates the implementation of the incompressible cavitation solver. Regarding the cavitation bubble collapse, the results show that the performance of the incompressible cavitation model depends on the selection of the empirical condensation coefficient, F_c. A decrease of F_c tends to increase the diffusion of the interface and to reduce the bubble collapse time. Furthermore, in comparison with the theoretical solution, an increase of F_c tends to generate more precise results. As F_c increases to infinity, the apparent fluid compressibility also tends to approach infinity and the results evolve to the ones predicted by the cut-off model, which is consistent with the barotropic model derived from the Rayleigh bubble collapse.

Chapter 6: Compressible cavitation solver

In Chapter 6, a comprehensive assessment of the sponge layer is conducted using the 1-D test case (Toro, 2009; Schmidt, 2015) and the impacts of several key factors, including tunable parameters, timestep, sponge layer length, and sound speed on the performance of the sponge layer are detailed. Furthermore, the guide for designing the sponge layer is proposed and validated in 2-D test cases. Next, in the following section, we validate the implemented compressible cavitation model using the 1-D and 2-D test cases. When possible, the obtained solution is compared with analytical results to validate the compressible cavitation solver.

6.1 SPONGE LAYER OPTIMIZATION

6.1.1 Compressible liquid Sod shock tube problem

Similar to Schmidt (2015), the case of a compressible liquid Sod shock tube has been used to reproduce the spurious reflections of pressure waves when the normal static pressure boundary conditions are imposed at the edge of the truncated domain. The tube with a length of $L_{tube} = 0.8$ m is considered which is filled with compressible liquid. The tube is initially divided into two regions, each with a length of $L_{tube}/2$, with different pressures. On the left side, the pressure is $p_{Left} = 1.0$ bar while on the right side is $p_{Right} = 0.01$ bar. The flow is initially at rest and the densities on both sides are determined by equation (4.88).

The numerical domain is discretized into 800 uniform cells. Free-slip wall boundary conditions are employed both at the top and bottom faces, while static pressure boundary conditions are applied at both the left and right edges of the tube. Fig. 6.1 illustrates the comparison between the theoretical evolution of the flow field (Toro, 2009) and the results obtained from numerical simulations using static pressure boundary conditions. It can be seen that the flow variables, such as pressure and velocity, fail to leave the domain at the instant $t_4 = 90\,\Delta t$ and lead to an inaccurate distribution of the flow properties.

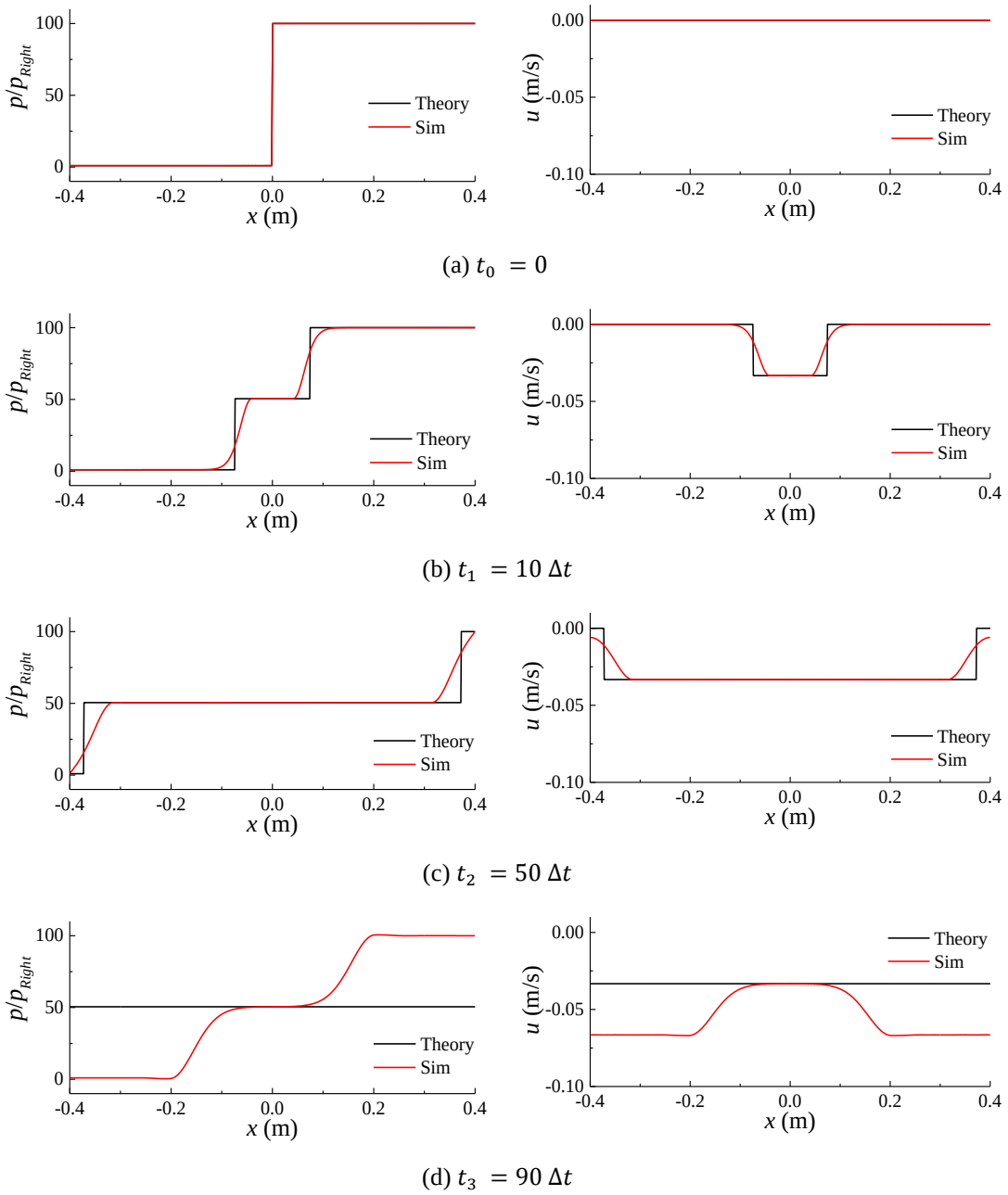

Fig. 6.1 A comparison between theoretical and numerical dimensionless pressures and velocities at four instants, where Δt=5×10^{-6} s.

The reflection coefficient η, defined as the amplitude ratio of the reflected pressure to the incident pressure (Mani, 2012), is used to quantify the reflections as defined by:

$$\eta = \left|\frac{p_{reflected} - p_{incident}}{p_{incident}}\right| \quad (6.1)$$

where $p_{incident}$ is the incident pressure and $p_{reflected}$ is the reflected pressure. In this study, the p_{incident} and $p_{\text{reflected}}$ can be estimated from the pressure profile, as shown in Fig. 6.2. At instant $t = 90\ \Delta t$, the pressure recorded at $x = 0.3$ m (marked

with a circle) can be considered as the reflected pressure. Simultaneously, the pressure recorded at $x = 0$ represents the incident pressure. Based on the pressure profile presented in Fig. 5.1, the reflection coefficient η using the static pressure boundary conditions is determined to be 0.98.

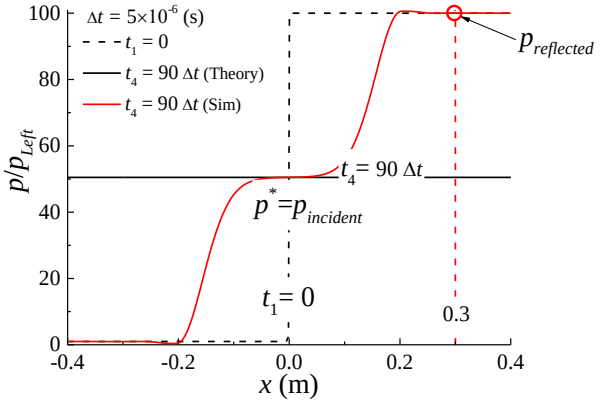

Fig. 6.2 Estimate the reflection coefficient from the result using static pressure boundary condition.

6.1.1 Effects of sponge layer length, time step, and sound speed

Fig. 6.3 displays the schematic of the numerical configuration considering two sponge layers, extended at the end of the computational domain each with a length L = 0.1 m. Furthermore, pressure boundary conditions with specified target values (p_{ref}, u_{ref}) have been applied to both the left and right sides of the computational domain.

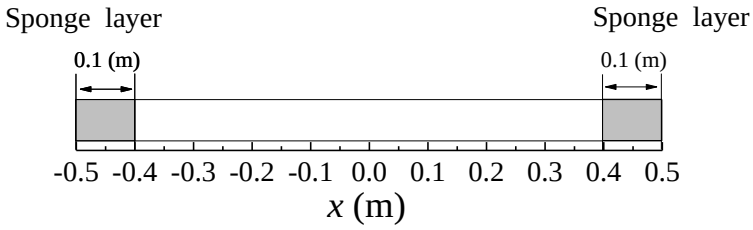

Fig. 6.3 Schematic of the computational domain with two 0.1 m sponge layers.

Until this point, the study has maintained a constant sponge layer length of $L = 0.1$ m and a constant sound speed, as depicted in Fig. 6.3. However, as mentioned in the investigations of several authors (Bodony, 2006; Mani, 2012; Gill et al., 2015), the performance of the sponge layer is proved to be affected by variations in both L and c. In this section, the effects of L, c, and Δt on the performance of the new proposed sponge profile are presented.

Fig. 6.4 presents the dimensionless pressure profile, p/p_{Left}, at a selected instant for different L, and the corresponding reflection coefficients are compared in

Fig. 6.5. It can be seen that the curves of the reflection coefficient obtained from various profiles of the damping coefficient collapse into a single curve as a function of L. An increase in t L leads to a reduction of η in agreement with the design guideline advised by Mani (Mani 2012).

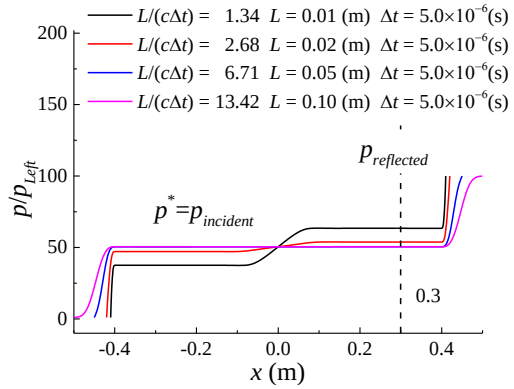

Fig. 6.4 Numerically obtained dimensionless pressure, p/p_{Left}, at instant t=110Δt with different sponge layer lengths L.

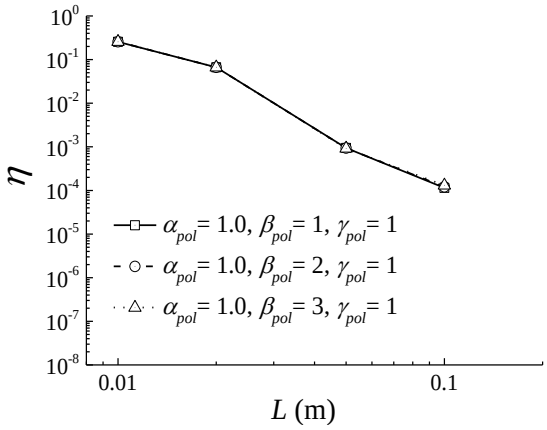

Fig. 6.5 The computed reflection coefficient for various parameter combinations with different sponge layer lengths L.

In the cases of $L = 0.01$ m, Fig. 6.6 presents the p/p_{Left} profile at a selected instant with varying Δt and the corresponding reflection coefficient are compared in Fig. 6.7. It is evident that the reflection coefficient is influenced by Δt. As expected, increasing Δt results in a rise in η which suggests that the reduction in Δt can improve the performance of the sponge layer approach.

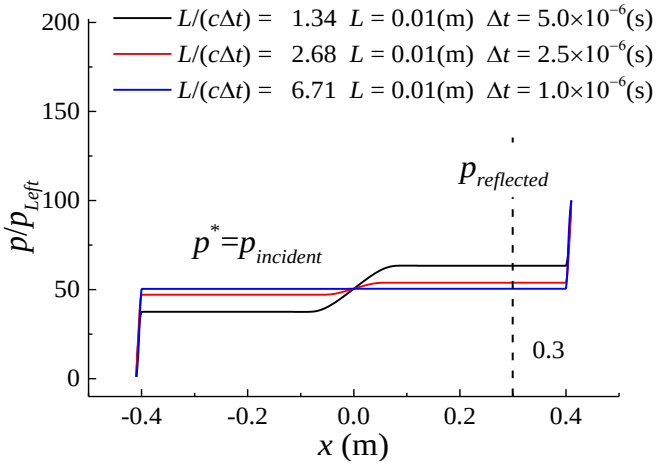

Fig. 6.6 Numerically obtained dimensionless pressure p/p_{Left} at instant t=110Δt with different time step Δt.

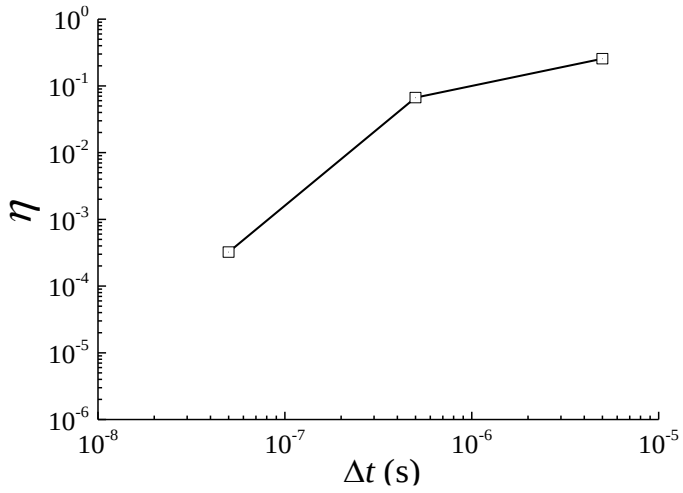

Fig. 6.7 The computed reflection coefficient for different Δt with L=0.01 m.

In the cases of $L = 0.01$ m, Fig. 6.8 illustrates the obtained dimensionless pressure profile p/p_{Left} at a selected instant with different c. Fig. 6.9 presents a comparison of the corresponding reflection coefficients where it can be seen that they are a function of c. Keeping Δt and L constant, an increase of c leads to an increase of η, which suggests that lower values in c could potentially enhance the performance.

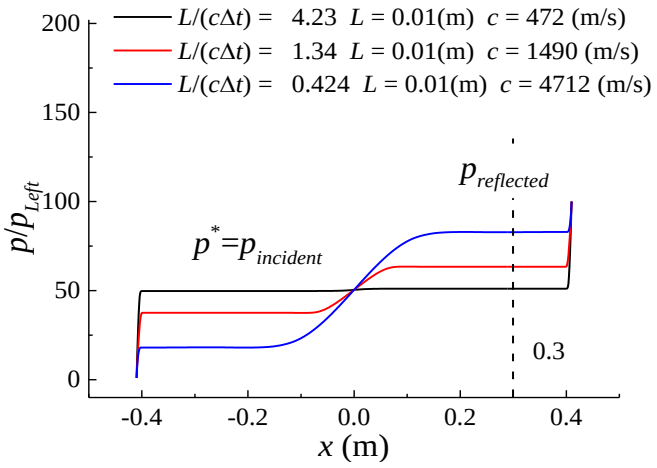

Fig. 6.8 Numerically obtained dimensionless pressure p/p_{Left} at instant t=110Δt with different c.

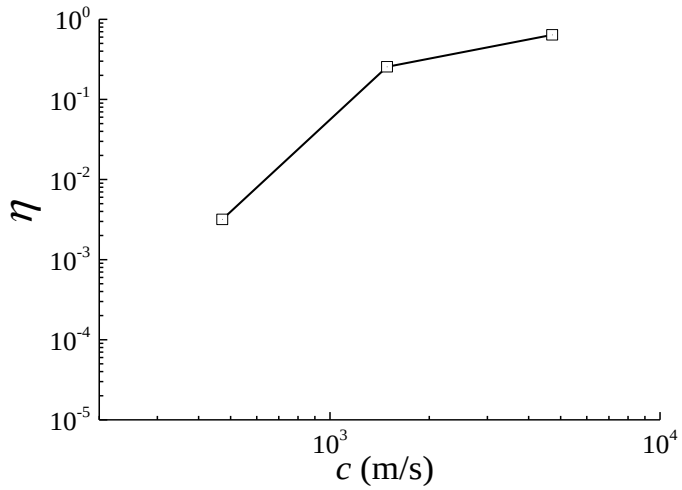

Fig. 6.9 The computed reflection coefficient with different c.

To summarize the effects of L, Δt, and c, a new dimensionless parameter, $L/c\Delta t$ has been introduced. Fig. 6.10 presents the η presented in Fig. 6.6, Fig. 6.8, and Fig. 6.9 as a function of $L/c\Delta t$ where the collapse of the different lines onto the same linear profile indicates that η is an exponential function of $L/c\Delta t$. Moreover, it can be seen that an increase in $L/c\Delta t$ tends to provoke a lower η. Normally, the damping effect on the reflecting pressure is determined by two factors: (i) the overall damping strength within the sponge layer and (ii) the residence time of the reflecting pressure staying inside the sponge layer. As a result, higher values of $L/c\Delta t$ correspond to larger damping strengths or residence times, which can effectively reduce the amplitude of the reflecting pressure. As depicted in Fig. 6.10, the lowest

values of $\eta < 0.1\%$ can be achieved if $L/c\Delta t > 6$. This criterion will be used in the following sections.

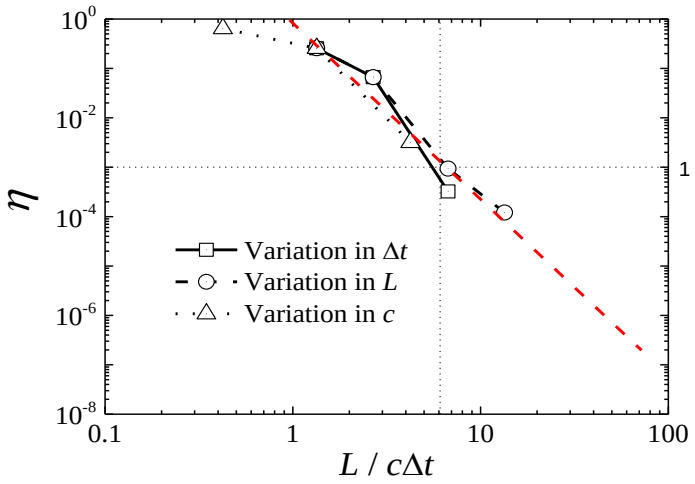

Fig. 6.10 The computed reflection coefficient for different $L/c\Delta t$.

6.2 VALIDATION OF COMPRESSIBLE CAVITATION SOLVER

6.2.1 Case 1: 1-D two-phase time-dependent test case

In this section, the compressible cavitation model is used to describe the fall of the density below the value of the saturated liquid by enforcing two symmetry expansion waves. Similar to the numerical setup given by Schmidt (2015), the domain is given by a 1-D tube with a length of 1 m. At time t=0 s, the tube is full of pure liquid water, and a constant pressure p=0.9 bar. The velocity field is assumed to jump at x=0.5 m from u_L=-10 m/s to u_R=10 m/s. These conditions can force the phase change to occur. Furthermore, the domain was divided into 1000 cells and the time integration was performed with the first-order implicit scheme with Δt=1·10^{-7} s.

To verify the implementation of the compressible cavitation model, the current numerical results are compared with the numerical results obtained by Schmidt (2015). Fig. 6.11 presents the pressure, velocity, vapor volume fraction, and sound speed distribution along the tube at time t =1.5·10^{-4} s in the simulations using the compressible cavitation model and the simulation by Schmidt (2015). No oscillation around the region with a high gradient can be seen. Furthermore, the distribution of the flow fields along the tube is almost identical between the current simulations and the reference simulation. This agreement for the flow field distribution demonstrates the validity of the implemented compressible cavitation model.

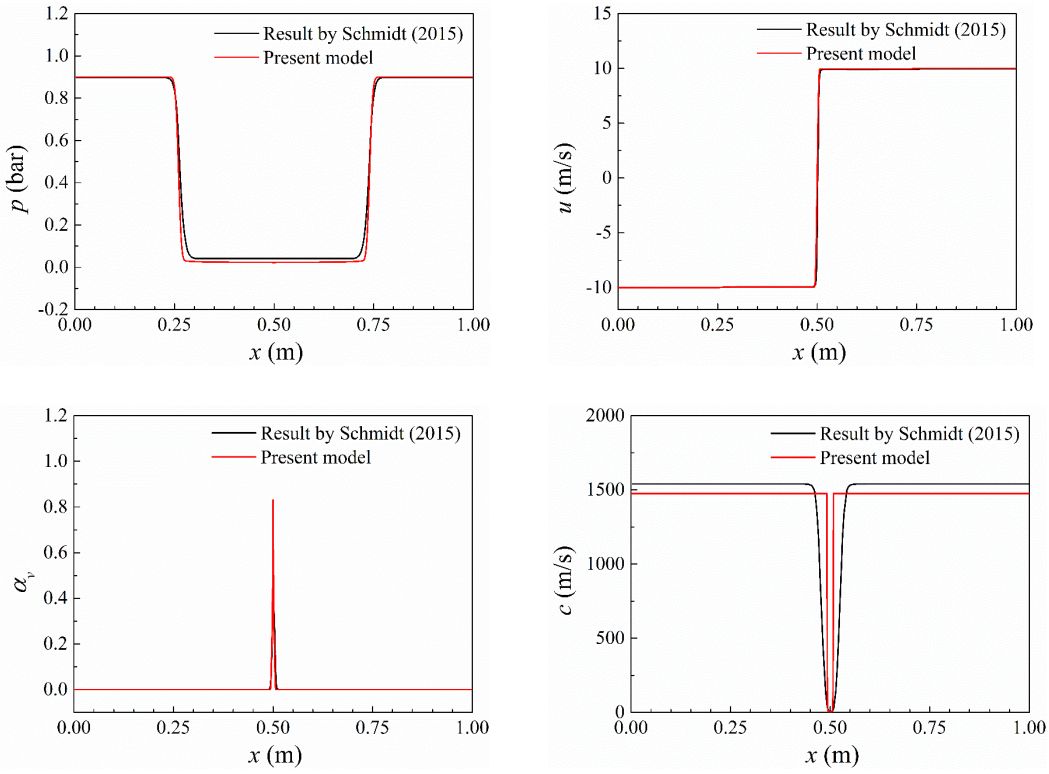

Fig. 6.11 Flow quantities at time t=1.5·10^{-4} s for the 1-D two-phase time-dependent case.

6.2.2 Case 2: 2-D cavitation bubble collapse

The collapse of a spherical bubble in ambient pressure. The computational domain and boundary conditions for the case are shown in Fig. 6.12(a). The computational domain is composed of a quarter sphere with one element layer and a domain radius 50 times the initial bubble radius. To minimize the computational cost, a 2D axisymmetric simulation is conducted. For far-field boundary conditions, all of the variables are set to a fixed value, except for the velocity for which the zero-gradient boundary condition is used. An optimal sponge layer with a length of 0.01 m is imposed at the outlet using a polynomial profile damping function with $\alpha_{pol} = 1.0$, $\beta_{pol} = 3.0$, and $\gamma_{pol} = 1.0$. Note that the value of $L/c\Delta t$ is larger than 6.

The initial radius of the bubble, R_0, is 0.4 mm which was resolved with 50 cells and the time integration was performed with the first-order implicit scheme with Δt =5×10^{-7} s. Furthermore, the initial pressure profile within the interior of the computational domain should comply with the following equation when $R = R_0$:

$$p(r) = \begin{cases} \left[\frac{R}{3r}\left(\frac{R_0^3}{R^3} - 4\right) - \frac{R^4}{3r^4}\left(\frac{R_0^3}{R^3} - 1\right)\right](p_\infty - p_v) + p_\infty & r > R \\ p_V & r < R \end{cases} \quad (6.2)$$

where R is the radius of the bubble, p_∞ is the ambient pressure, p_v is the vapor pressure. Here, according to Franc and Michel (2006), the collapse time is defined as $\tau_c = 0.915 R_0 \sqrt{\frac{\rho_l}{p_\infty - p_v}}$. Fig. 6.12(b) and Fig. 6.12(c) show the initial conditions for vapor volume fraction and pressure, respectively.

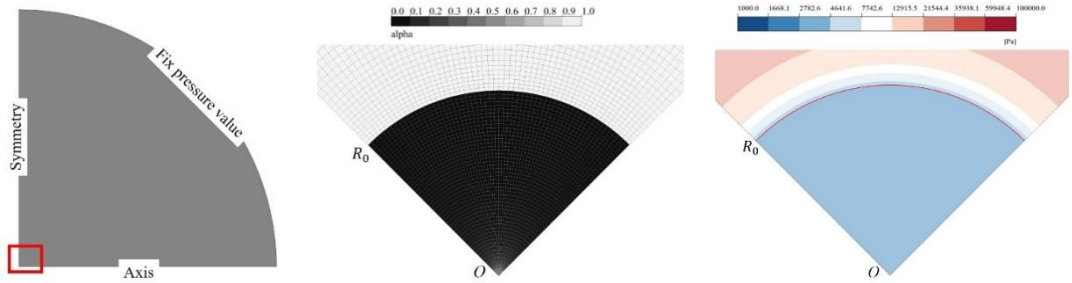

(a) (b) (c)

Fig. 6.12 Bubble collapse simulation, computational domain, boundary conditions (a), initial conditions of vapor volume fraction (b), and pressure (c).

The exact solution of a sphere of vapor subjected to compression due to the surrounding high-pressure liquid has been well established (Brennen, 2014; Koukouvinis et al., 2016; Trummler et al., 2021). In Fig. 6.13, a comparison between the time evolution of the radius of a bubble with and without the sponge layer is presented. It can be seen that without a sponge layer, the unphysical evolution of the bubble radius occurs at $t/\tau_c = 1.8$ after the first rebound of the bubble, as shown in Fig. 6.13. With the sponge layer, the spurious profile in the evolution of the bubble radius is eliminated and the corresponding results are in better agreement with the theoretical prediction (Koukouvinis et al., 2016; Trummler et al., 2021).

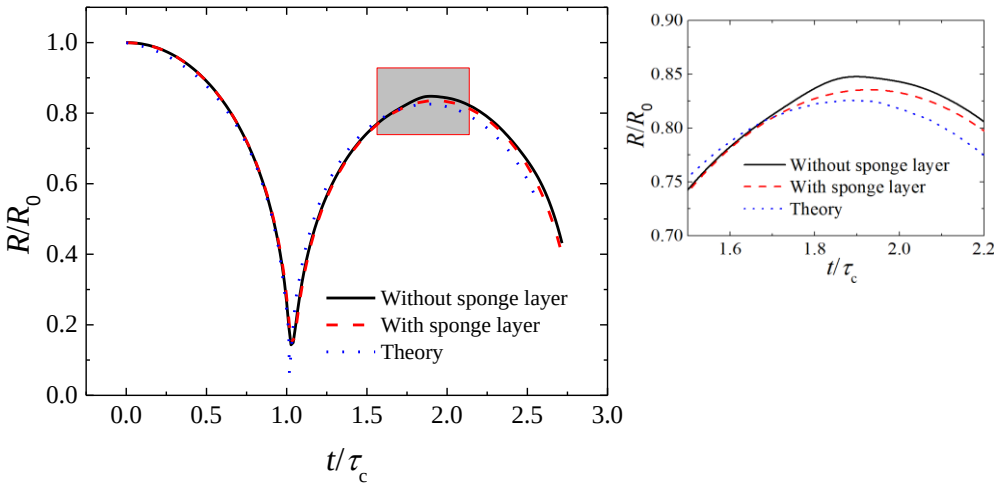

Fig. 6.13 Time evolution of the radius of a bubble.

To assess the performance of the sponge layer, the radial profile of the pressure field with or without the sponge layer has been presented at different times in Fig. 6.14. As shown in Fig. 6.14(a) and Fig. 6.14(b), a pressure wave is formed and propagates outside from the bubble center after the bubble rebound ($t > \tau_c$) and the maximum value of pressure fronts decreases as $1/r$. Without a sponge layer, the pressure wave is reflected when it approaches the fixed pressure boundary condition and causes a spurious profile of the pressure field inside the computational domain, as depicted in Fig. 6.14(c). It is believed that this spurious pressure is the source of the unphysical evolution of the bubble radius as presented in Fig 6.14. In contrast, by using the proposed sponge layer, the reflected pressure wave has been well dampened and the profile of the pressure inside the region of interest is unaffected by the fixed boundary condition. It supports that using the sponge layer with an optimized damping function can significantly suppress the reflection of the pressure and guarantee a reasonable profile of the flow field inside the region of interest.

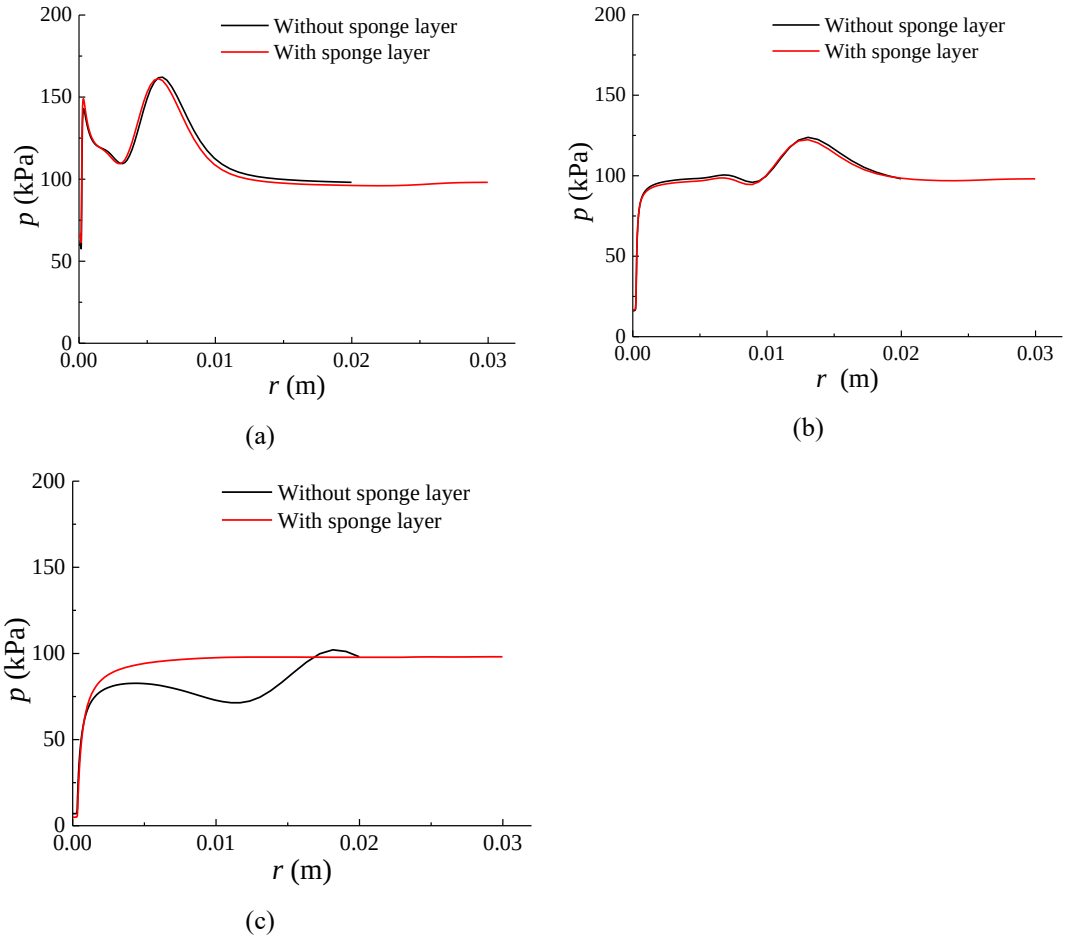

Fig. 6.14 Numerically obtained pressure p at times of (a) t/τ_c=1.22, (b) t/τ_c=1.35 and (c) t/τ_c=1.89 with sponge layer and t/τ_c=1.62 without damping function.

6.2.3 Case 3: Cavitating vortex steet flow over a circular cylinder

The present simulations for non-cavitating or cavitating flow over a stationary cylinder are performed in a large computational domain with -50 ≤ x/D ≤ 50 and -50 ≤ y/D ≤ 50 to avoid the effect of the domain size, as depicted in Fig. 6.15. The cylinder is located at (0, 0) and the number of grid points in the circumferential, radial direction are 480 and 220, respectively. The symbol, θ, represents an angle on the cylinder surface measured from its front stagnation point. We use the inflow condition of $u = u_{ref}$ and the pressure condition of $p = p_{ref}$ on the boundaries of x/D = -50 and x/D = 50, respectively, while using the symmetry condition on the top and bottom boundaries.

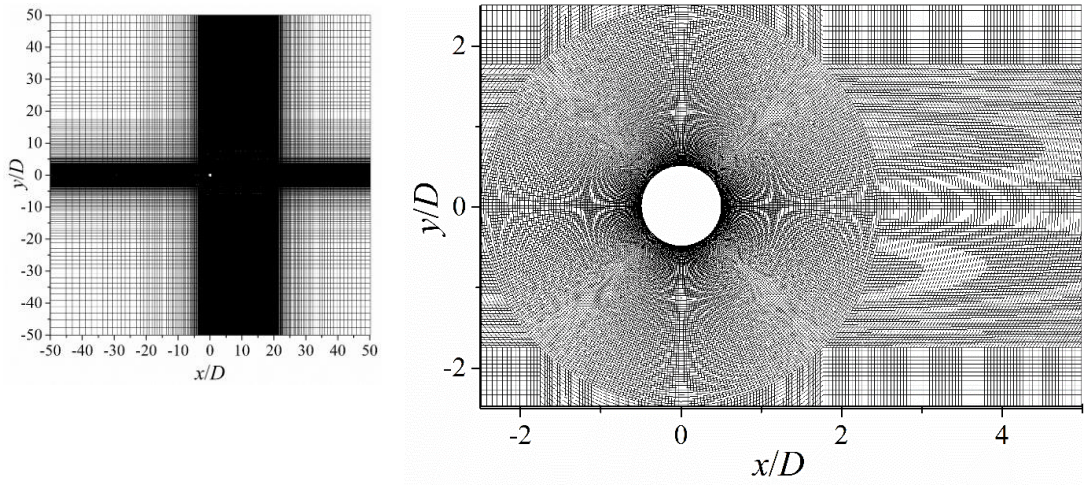

(a) (b)

Fig. 6.15 Computational meshes around a circular cylinder: (a) whole domain and (b) region near the circular cylinder.

The formulas of drag and lift coefficients, denoted as C_D and C_L, can be defined as:

$$C_D = \frac{F_x}{\frac{1}{2}\rho_l {U_{ref}}^2 D} \quad (5.3a)$$

$$C_L = \frac{F_y}{\frac{1}{2}\rho_l {ref}^2 D} \quad (5.3b)$$

where F_x and F_y are the streamwise and transverse components of the force acting on the surface, respectively, U_{ref} is the free-stream velocity, ρ_l is the liquid density, and D is the cylinder diameter.

The present approach is tested for a stationary cylinder immersed in liquid water at Re = 200, referring to the previous studies (Braza et al., 1986; Ding et al., 2007; Seo et al., 2008; Harichandan & Roy, 2012; Qu et al., 2013; Gnanaskandan & Mahesh, 2016b; K. H. Kim & Choi, 2019; Hong & Son, 2021) for unsteady vortex shedding. Vortices are generated on the cylinder surface and detach alternatively from its upper and lower surfaces. As shown in Fig. 6.16, the oscillating flow around the cylinder results in fluctuations in the drag and lift coefficients, C_D, and C_L. The time-averaged of C_D, denoted as $C_{D,av}$, the maximum of C_L, denoted as $C_{L,max}$, and St are listed in Table 6.1. The present results match well with the previously published data using different meshes and methods.

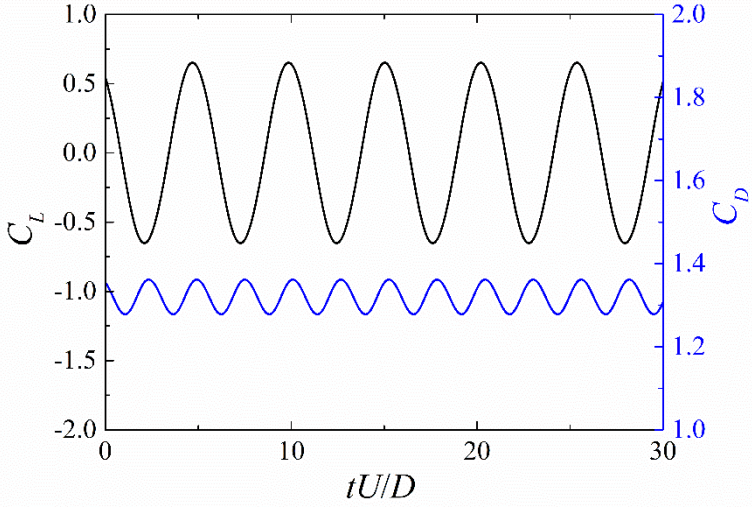

Fig. 6.16 The history of C_D and C_L at the non-cavitation regime.

Table 6.1 Comparison of $C_{D,av}$, $C_{L,max}$, and St for a circular cylinder at Re = 200 without cavitation.

	$C_{D,av}$	$C_{L,max}$	St
Braza et al. (1986)	1.40	0.75	0.20
Ding et al. (2007)	1.35	0.66	0.196
Seo et al. (2008)	1.08	0.60	0.19
Harichandan and Roy (2012)	1.32	0.60	0.194
Qu et al. (2013)	1.32	0.66	0.196
Gnanaskandan et al. (2016b)	-	-	0.198
Kim and Choi (2019)	1.35	0.70	0.197
Hong and Son (2021)	1.32	0.66	0.194

Present	1.32	0.65	0.194

Simulations are extended to cavitating flows at σ = 1.0, As shown in Fig. 6.17, the oscillating flow around the cylinder results in fluctuations in the drag and lift coefficients, C_D, and C_L at σ = 1.0. The corresponding $C_{D,av}$, $C_{L,max}$, and St are listed in Table 6.2. As the liquid pressure decreases to p_v, cavitation occurs around the lateral surface of the cylinder and then the vaporous bubble detaches from the cylinder surface and travels with shedding vortices. As the velocity divergence or dilatation effect due to cavitation elongates and weakens the shedding vortices (Gnanaskandan & Mahesh, 2016b), the computed shedding frequencies are reduced to *St* = 0.17 for σ =1.0, which are comparable to the corresponding predictions of *St* = 0.160 reported by Seo et al. (2008) and Gnanaskandan and Mahesh (2016b), and *St* = 0.177 reported by Hong and Son (2021). Moreover, Fig. 6.18 compares the instantaneous vorticity contour colored with vapor volume fraction at σ=1.0 obtained by Gnanaskandan and Mahesh (2016b) and the present method, showing comparable results.

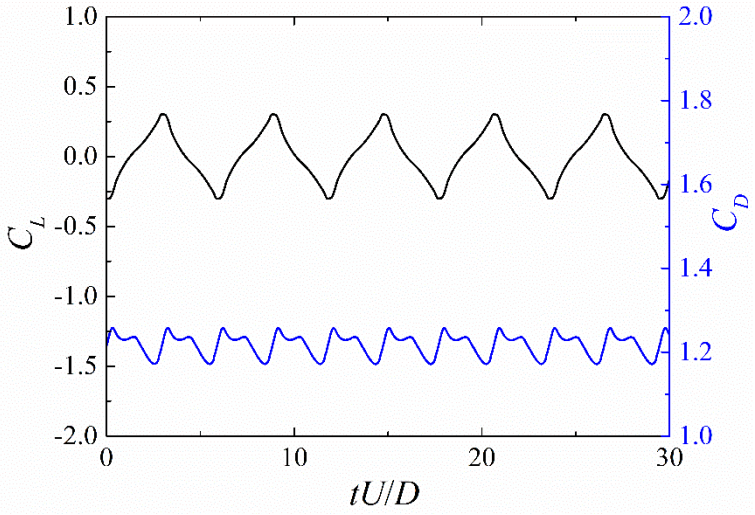

Fig. 6.17 The history of C_D and C_L at σ = 1.0.

Table 6.2 Comparison of $C_{D,av}$, $C_{L,max}$, and *St* for a circular cylinder at *Re* = 200 with σ=1.0.

	$C_{D,av}$	$C_{L,max}$	St
Seo et al. (2008)	1.08	0.42	0.16
Gnanaskandan and Mahesh (2016b)	1.10	0.56	0.16
Hong and Son (2021)	-	-	0.177
Present	1.22	0.30	0.17

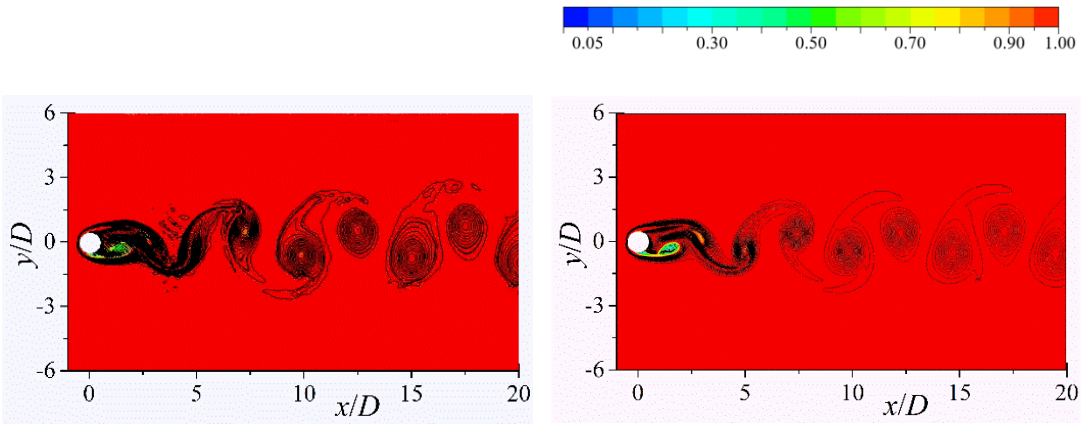

Fig. 6.18 Comparison of the instantaneous vorticity contour colored with vapor volume fraction at σ=1.0: (a) Gnanaskandan and Mahesh (2016b) and (b) the present method.

6.3 PARTIAL CONCLUSIONS

In this chapter, the implemented compressible cavitation solver coupled with the sponge layer boundary conditions has been validated and verified. Concerning the sponge layer boundary condition, it has been found that as long as the dimensionless parameter, $L/(c\Delta t)$, falls below 6, the sponge layer can effectively absorb the pressure reflection at the truncated boundary edge. Furthermore, the compressible cavitation model has been successfully applied to simulate both the cavitation bubble collapse and the vortex shedding behind the circular cylinder. The results obtained from the present compressible cavitation model are generally in line with analytical solutions or previously published data which confirms its capability to simulate the cavitating flow with consideration of the fluid compressibility.

Part III

Chapter 7: Fluid compressibility effects on cavitating vortex street flow

Chapter 7 contains the numerical simulation of the cavitating flow behind the wedge using the incompressible and compressible cavitation solver and demonstrates the influence of fluid compressibility on the dynamics of the cavitating wake. The simulating flow behind the wedge is based on the experiment conducted by Wu et al. (2021), where a wedge with an apex angle of 15º is mounted in a cavitation tunnel. The variation in the profile of the time-resolved void-fraction field and vortex shedding frequency at different cavitation numbers allow for a qualitative comparison against the results obtained by the incompressible and compressible cavitation solvers. The influence of fluid compressibility on the dynamics of the cavitating vortex street flow behind the wedge will be discussed.

7.1 NUMERICAL SETUP

7.1.1 Computational domain and boundary conditions

Fig. 7.1 shows the dimensions of the computational domain. The cross-section, the geometry of the wedge, and its position are in line with the experimental setup from Wu et al. (2021). The cross-section of the tunnel is square and its width is 4*D*, where *D* is the height of the wedge base and is equal to 0.019 m. The span of the wedge is 4*D*. For the incompressible cavitation case, the inlet is located 13.5*D* upstream from the base and the outlet is 19.5*D* downstream from the base. For the compressible cavitating simulation, the inlet is located 25.9 *D* upstream from the base and the outlet is 36.6 *D* downstream from the base.

The flow around the wedge is simulated using the DDES model to capture the globally unstable flow characteristic. Such flow has the feature that the turbulence in the separated zone is independent of the turbulence within the incoming attached boundary layer (Menter, 2015). This flow feature can significantly reduce the mesh resolution. Following the suggestions provided by ANSYS Fluent (Menter, 2015), more than 20 cells per characteristic length, *D*, is sufficient to resolve the main flow instability. Furthermore, the isotropic cell ($\Delta x = \Delta y = \Delta z$) is used in the area near the trailing edge of the wedge to avoid the numerical error resulting from the large aspect

ratio. To assess the effects of mesh refinement on numerical simulations, three meshes with different refinements as listed in Table 7.1 are tested. The topology of mesh M1 around the wedge is depicted in Fig. 7.1(b) and 7.1(c).

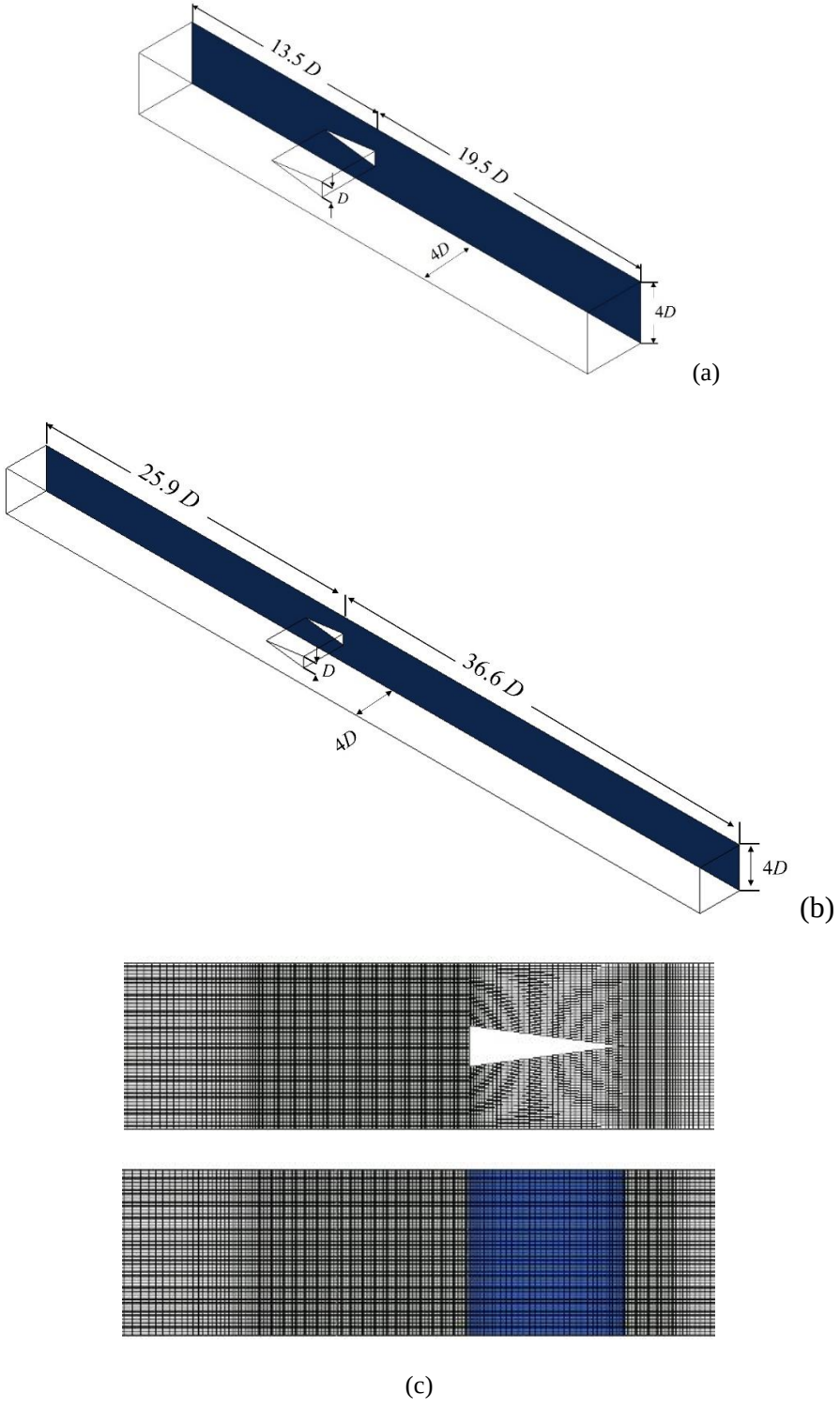

Fig. 7.1 Computational domain for incompressible cavitation model (a) and compressible cavitation model (b) and the mesh topology around the wedge: side view and top view of the mesh around the wedge (c).

Table 7.1 Characteristic of the mesh in the computational domain.

Name	Cells	$D/\Delta x$
M1	1.39×10^6	20
M2	2.75×10^6	26
M3	4.13×10^6	30

For the non-cavitating case, the uniform inflow velocity boundary condition, U_{ref} =6 m/s, is used at the inlet and the outlet boundary condition at the outlet, as shown in Fig. 7.2(a). For σ=1.9, the corresponding total pressure boundary condition is specified at the inlet and the fixed mass flowrate boundary condition at the outlet. To absorb the possible reflected pressure wave generated by the compressible fluid material, the sponge layer (Mani, 2012) is added at the inlet and outlet area, as depicted in Fig. 7.2(b). The boundary conditions for different operating conditions are detailed in Table 7.2.

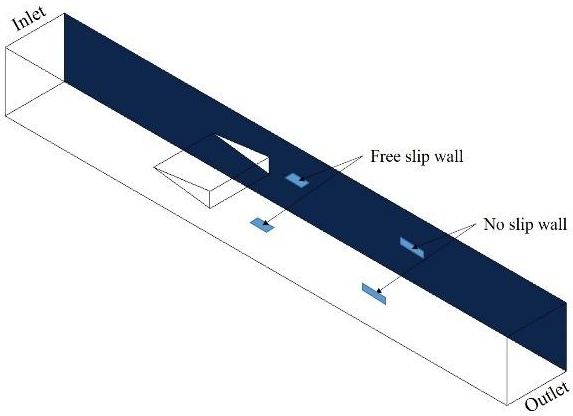

(a)

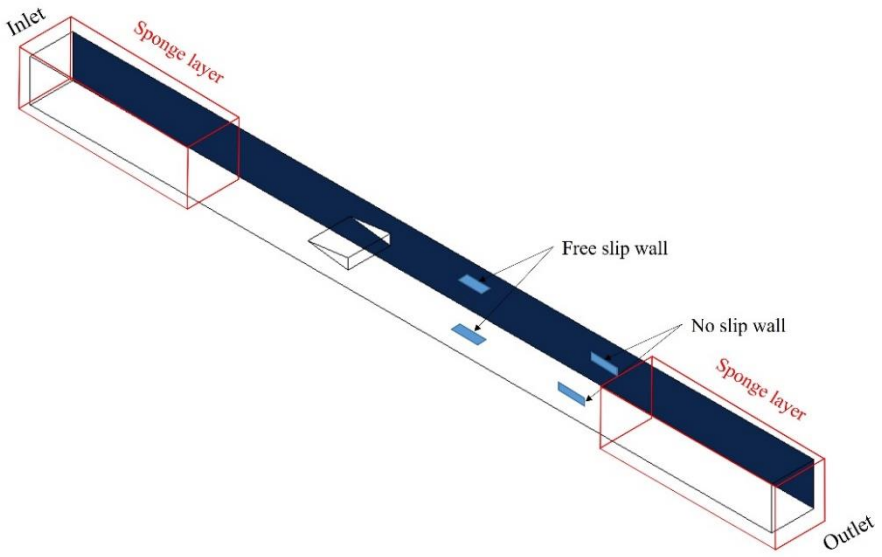

(b)

Fig. 7.2 The boundary condition for the cavitating flow behind the wedge using incompressible (a) and compressible (b) cavitation models.

Table 7.2 The boundary conditions at different operating conditions.

σ	Inlet boundary	Value	Outlet boundary	Value	Top wall	Bottle wall	Other walls
Non-cavitation	Fixed velocity	6 m/s	Outlet	-	FSW	FSW	NSW
1.9	Total pressure	54540 Pa	Mass flowrate	34.656 kg/s	FSW	FSW	NSW

Free slip wall: FSW No slip wall: NSW

All the simulations have been run with ANSYS Fluent using the BCD (bounded Central Difference) advected scheme and a time step of $\Delta t = 5\times10^{-5}$ s where the corresponding advected CFL is below 1 behind the wedge.

7.2 VERIFICATION AND VALIDATION

7.2.1 Verification

Fig. 7.3 shows the lift history in the frequency domain using FFT for different grid refinements at non-cavitation conditions. It can be seen the frequency of the first harmonic converges to the same value which is independent of the mesh number even when the coarse mesh is used. Therefore, to save computational resources, the mesh M1 is used in the following analysis.

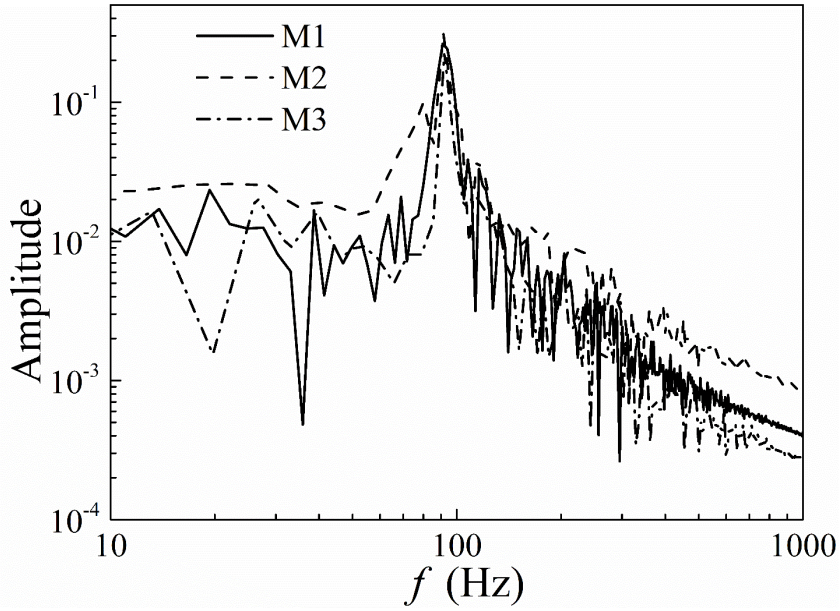

Fig. 7.3 The lift coefficient spectra for three different mesh refinements in the case of the non-cavitating.

7.2.2 Validation: non-cavitating case

As presented in Fig. 7.4, using mesh M1, the first harmonic frequency of 91 Hz corresponding to the vortex shedding frequency is in good agreement with the value of 90 Hz obtained by Wu et al. (2021). Furthermore, the distribution of the numerically obtained C_p on the surface of the wedge is given in Fig. 7.4. Here, the y=±0.5D are the vertices at the trailing edge. It can be seen that, at the centerline of the base of the wedge, the numerical C_p of -1.5 aligns well with the experimental value of -1.5 reported by Wu et al. (2021).

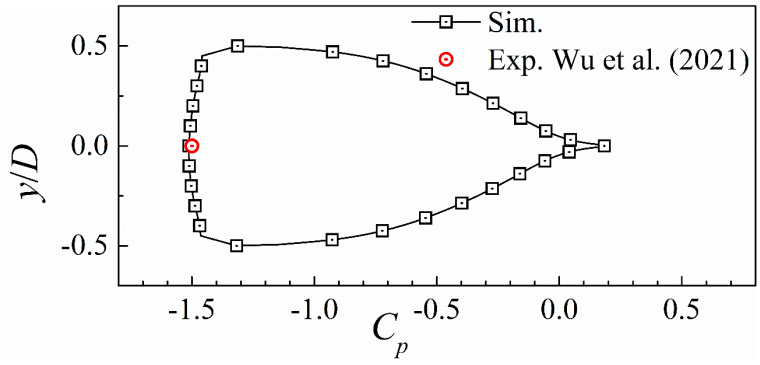

Fig. 7.4 The distribution of the mean pressure coefficient around the surface of the wedge at the non-cavitating condition.

Therefore, it can be concluded that, in the non-cavitating case, the current numerical solution of the unsteady flow field provides a reasonable resemblance to the flow condition in the experiment by Wu et al. (2021).

7.3 FLUID COMPRESSIBILITY EFFECTS

Using the validated incompressible and compressible cavitation modellings presented in Chapter 4, the cavitating wake behind the wedge at U_{ref}=6 m/s and σ=1.9, is investigated numerically to demonstrate the effects of fluid compressibility on the dynamics of the cavitating vortex shedding behind the wedge.

7.3.1 Pressure on the wedge surface

Fig. 7.5 compares the mean pressure coefficient on the wedge surface using incompressible and compressible cavitation solvers. There is an indistinguishable difference in the distributions of C_p obtained by both incompressible and compressible cavitation solvers. As can be seen in Fig. 7.5, the centerline of the base of the wedge, the numerical C_p of -1.4 is in good agreement with the value of -1.45 calculated by Wu et al. (2021).

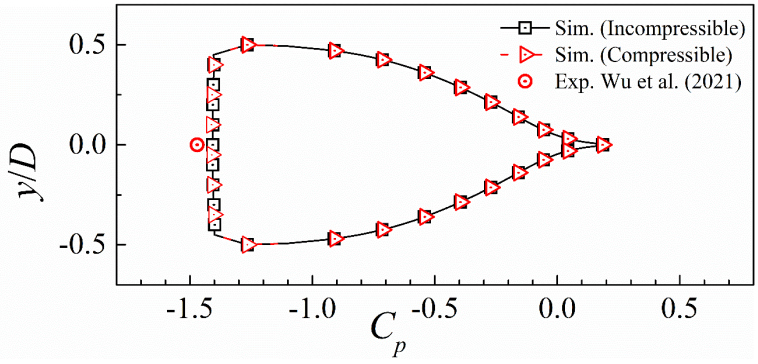

Fig. 7.5 The distribution of the mean pressure coefficient around the surface of the wedge using incompressible and compressible cavitation model at σ = 1.9.

7.3.2 Unsteady loads on the wedge surface

For comparison, Fig. 7.6 shows the C_L history and its spectra for σ=1.9 with different cavitation solvers. It can be seen that both cavitation solvers give the same value of 210 Hz in the first harmonic frequency, which corresponds to the vortex shedding frequency behind the wedge. Such value is in good agreement with the dominant frequency reported by Wu et al. As shown in Fig. 7.6(b), for the lower frequencies (f<800 Hz), the profiles of the spectra obtained with different cavitation

solvers are quite similar. However, at high frequencies (f>1000 Hz), the spectra obtained with the incompressible cavitation solver provoke a lower value in the amplitude against the frequencies. Similar results are also observed in the investigation of cloud cavitation around the hydrofoil conducted by Wang et al. (2020).

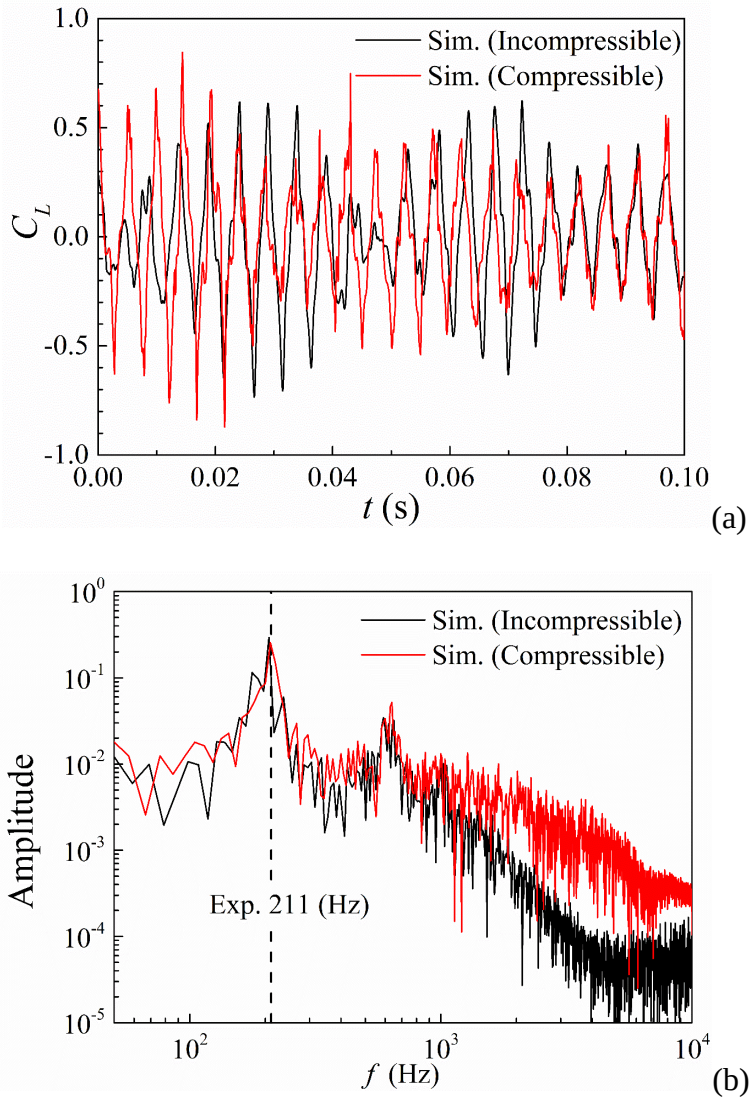

Fig. 7.6 Lift history (a) and its spectra (b) for σ = 1.9 with incompressible (Incomp.) and compressible (Comp.) cavitation models.

7.3.3 Cavity structures

Fig. 7.7 shows the comparison of the numerically obtained cavity structures inside the shed vortices obtained by incompressible and compressible cavitation solvers with the experimental observation by Wu et al. (2021) at σ=1.9. As anticipated, the first few pairs of spanwise vortex cores are filled with vapor, and these cavity structures are advected downstream. Furthermore, the relative positions of the vortex

spacings obtained with the incompressible and compressible cavitation models are quite similar and align with the experimental observation by Wu et al. (2021).

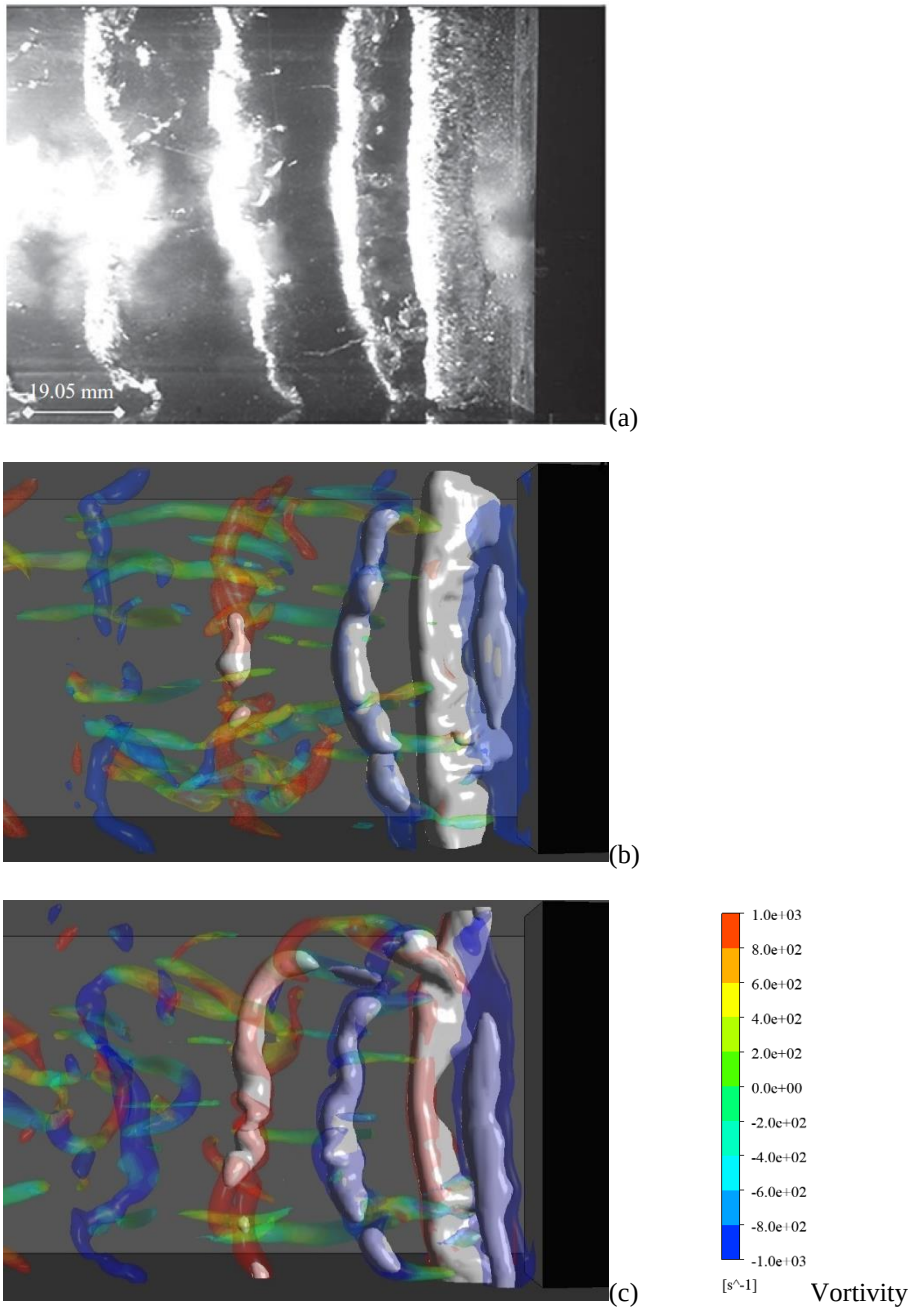

Fig. 7.7 Comparisons of the experimentally (a) and numerically obtained cavity structures (represented with α_v =0.05) inside the vortices (displayed with Q/Q_{max}=0.25) using incompressible (b) and compressible (c) cavitation model at σ = 1.9.

Fig. 7.8 shows periodic shedding of the instantaneous void fraction field corresponding to the first harmonic frequency with incompressible (Incomp.) and compressible (Comp.) cavitation solvers at σ=1.9. For comparison, Fig. 7.8 also

includes the experimental images reported by Wu et al. (2021) using time-resolved X-ray densitometry. The evolution of the cavity structures suggests that the periodic shedding is governed by the alternating shedding vortex street behind the wedge. In each period of shedding, a cavity starts to form and fill the center of the shed vortex. Then, the cavitating vortex is shed from the trailing edge and advected from the attached boundary layer. The alternating cavitating shedding vortices form the vortex street behind the wedge. The comparison between numerical results using incompressible and compressible cavitation solvers and the experiment indicates that both cavitation solvers can capture the main flow characteristic of the cavity structure in the experiment. In the simulation with both cavitation solvers, the cavity structures grow to a size that is comparable to the size of the cavity length in the experimental image (as indicated in Fig. 7.8(a) and Fig. 7.8(c)).

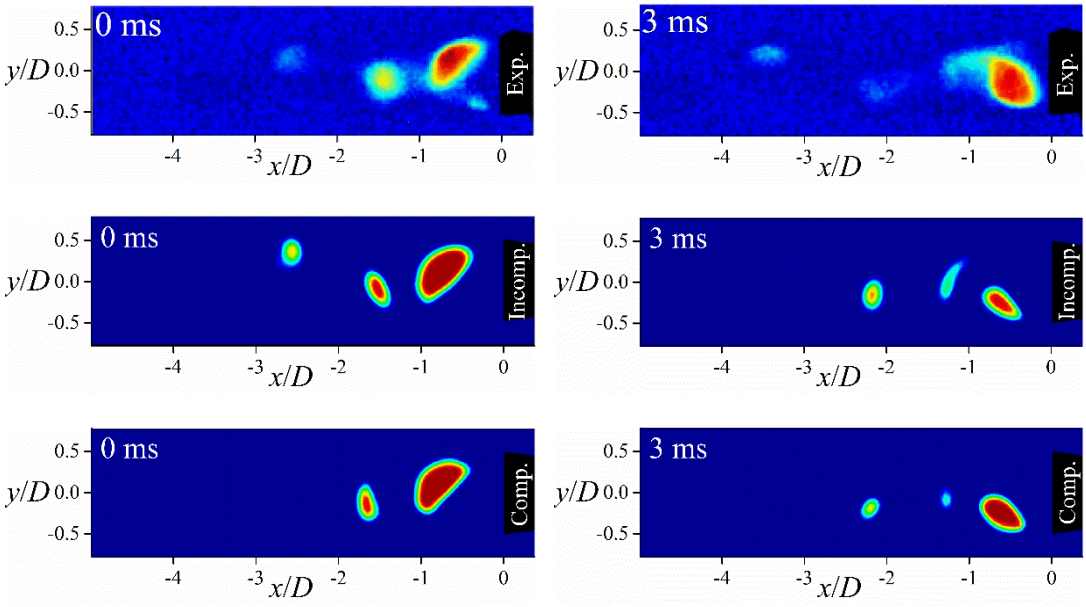

(a)t_0: $t = t_0$ (b)t_1: $t = t_0$+3 ms

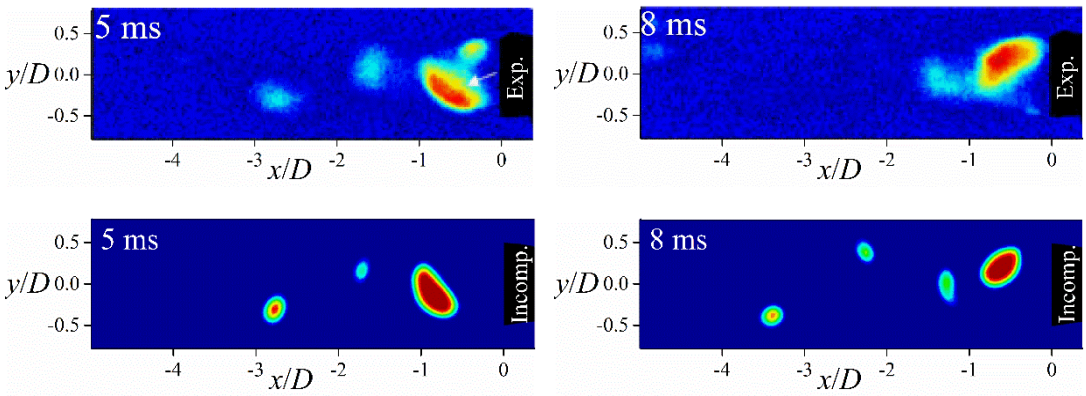

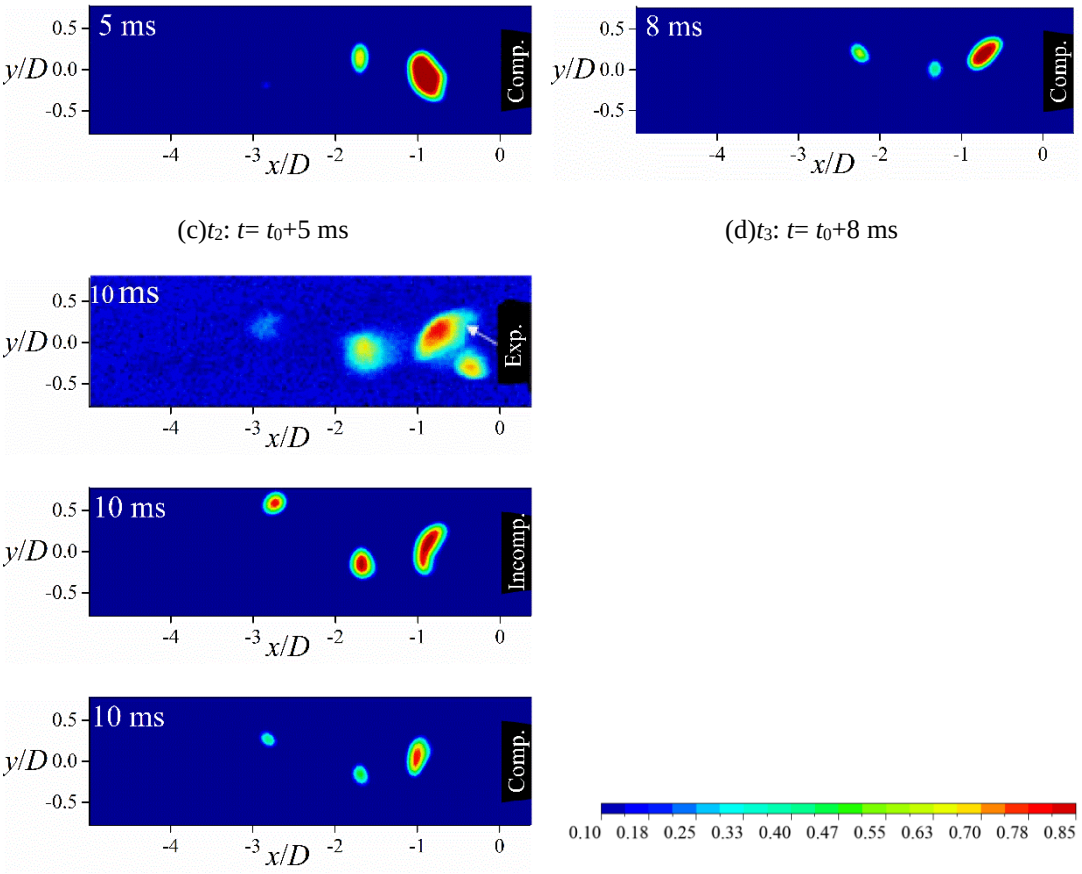

(c)t_2: t= t_0+5 ms

(d)t_3: t= t_0+8 ms

(e)t_4: t= t_0+10 ms

Fig. 7.8 Comparisons of the experimentally (J. Wu et al., 2021) and numerically obtained void-fraction series of cavitating wake using incompressible (Incomp.) and compressible (Comp.) cavitation model at σ = 1.9.

Fig. 7.9 shows the time average void fraction field with incompressible (Incomp.) and compressible (Comp.) cavitation solvers at σ=1.9. For comparison, Fig. 7.9 also includes the experimental results reported by Wu et al. (2021). It can be seen that the simulations with two different cavitation solvers produce almost indistinguishable mean and RMS. void fraction fields behind the wedge at σ = 1.9. The shape of mean cavity structures obtained numerically is comparable to the pattern in the experimental image found by Wu et al. (2021). Note that, there is a downstream offset in the mean and RMS void fraction fields between the numerical and the experimental results. It is believed that this offset may result from the insufficient resolution of the locally unstable flow structures within the detachment area.

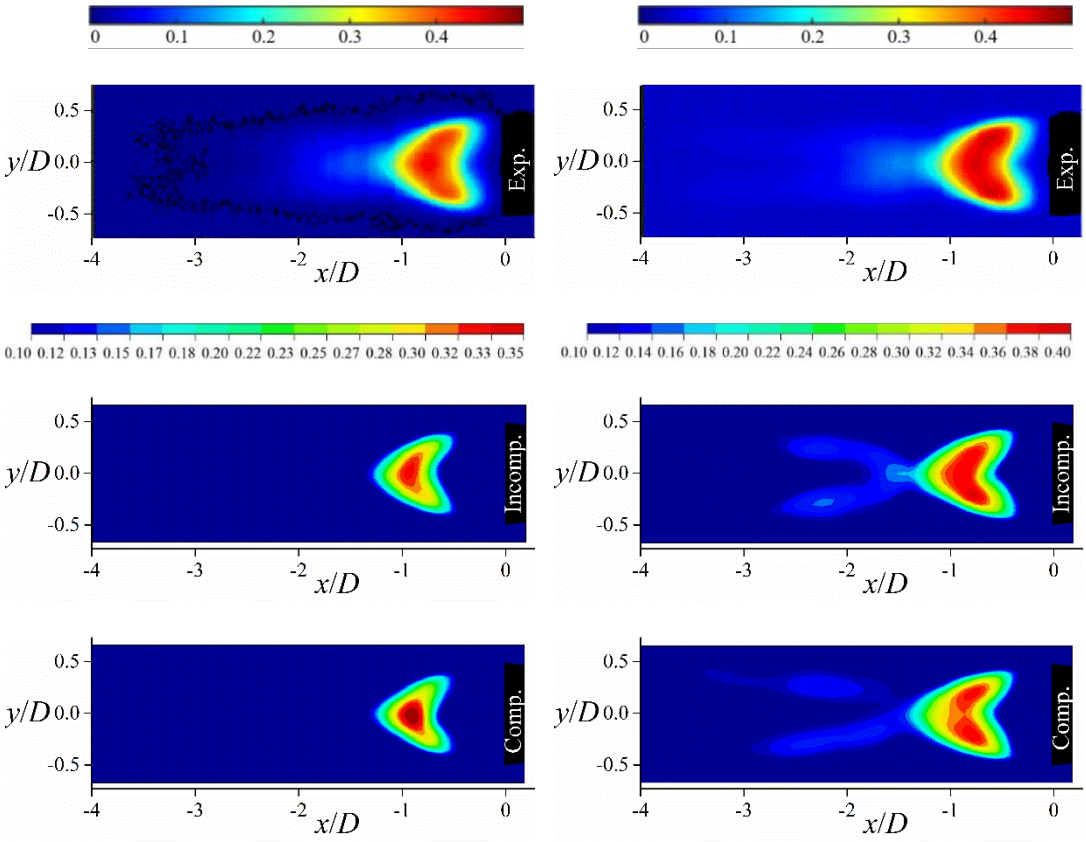

Fig. 7.9 Comparisons of the experimentally (J. Wu et al., 2021) and numerically obtained time average (a) and RMS (b) void-fraction fields using incompressible (Incomp.) and compressible (Comp.) cavitation models at σ = 1.9.

7.4 PARTIAL CONCLUSIONS

In this chapter, the numerical results predicted by the incompressible and compressible cavitation model are compared to assess the effects of the fluid compressibility on the characteristics and dynamics of the cavitating flow behind the wedge. For validation, the experimental results obtained by Wu et al. (2021) have been taken as a reference.

It has been found that the effects of the liquid compressibility on the dynamics of the cavitating wake flow depend on the frequency range:

- For low frequencies, the effects of the liquid compressibility are small and can be negligible.
- For higher frequencies, it amplifies the spectral energy content.

Regarding the prediction of the mean pressure profiles, the dominant vortex shedding frequencies, and the instantaneous and mean void fraction fields, the

simulations performed with incompressible and compressible solvers have provided almost identical results, indicating that compressibility effects on the cavitating vortex shedding behind the wedge are quite small and can be neglected.

Chapter 8: Effects of cavitation on the spatio-temporal distribution of vortex street flow

Chapter 8[1] is devoted to numerically investigating the influence of cavitation on the wake behind a hydrofoil NACA 0009 with a truncated trailing edge using a homogeneous mixture model coupled with a controlled decay SST γ-$Re_{\theta t}$ turbulence model. Using optimal definitions of the inlet turbulent intensity and the empirical condensation and vaporization coefficients of the cavitation model, simulated results have shown a good agreement with experimental data. Based on the numerical results, the influence of cavitation on the trajectories of vortex centers and the morphology of the primary shedding vortices has been revealed using a vortex identification method. The findings highlight that the cavitation development enhances the advected velocity of the shedding vortices while decreasing the streamwise inter-vortex spacing, contributing to the increase of the vortex-shedding frequency.

8.1 NUMERICAL SETUP

8.1.1 Computational domain and boundary conditions

The tests on the hydrofoil NACA 0009 were conducted in the EPFL cavitation tunnel. The test section had a rectangular shape with dimensions of 150×150×750 mm^3. The chord length of the tested hydrofoil NACA 0009 was C=100 mm and its span is 1.5 times C. The geometry of the hydrofoil NACA 0009 is truncated at 90% of the original chord length, where the trailing edge thickness h is specified as 3.22% of C. For more comprehensive information about these experiments and the results, one can refer to the details provided in Ausoni (2009).

Fig. 8.1(a) depicts the rectangular computational domain of the 2D hydrofoil. The inlet is placed at $4C$ upstream of the hydrofoil leading edge and the outlet boundary is set at $6C$ downstream of the trailing edge. The width of the domain is $1.5C$.

This chapter is based on the published paper: Chen, J., & Escaler, X. (2024). Numerical investigation of the cavitation effects on the wake dynamics behind a blunt trailing edge hydrofoil. Ocean Engineering, 302, 117599[1]

This fluid domain and boundary conditions are consistent with the approach used by Chen et al. (2018) and Ye et al. (2020), who employed the same domain with different spanwise lengths for LES simulations. Furthermore, the choice of domain size has been validated by Hu et al. (2020), indicating that numerical differences arising from domain size variations become negligible when the overall streamwise length exceeds 8 C. Hence, the current simulation adopts a rectangular computational domain of $11C \times 1.5C$.

Under cavitation-free conditions, as shown in Fig. 8.1(b), a uniform inflow condition with free stream velocity U_{ref}=20 m/s has been specified at the inlet, resulting in a Reynolds number $Re = U_{ref}H/\nu = 6.4 \cdot 10^4$, where ν is the water kinematic viscosity. The upper and lower walls are considered free slip-walls to remove the effects of blockage on the flow field (J. Kim et al., 2019). Additionally, at the outlet, a pressure of 379 kPa is applied (see Table 1).

Under cavitation conditions, to increase the stability of the numerical simulation, a inlet total pressure coupled with a outlet static pressure has been employed. To determine their exact values, the static pressure difference, Δp, between inlet and outlet has been assumed independent of σ. First, Δp has been estimated based on the non-cavitating results with the following equation:

$$\Delta p = \bar{p}_{total_{inlet}} - 0.5\rho_l {U_\infty}^2 - \bar{p}_{outlet} \quad (8.1)$$

where $\bar{p}_{total_{inlet}}$ is the time average of the inlet total pressure, $\bar{p}_{outlet}$ is the time average of the outlet static pressure. And the inlet static pressure for a given σ, p_{inlet_σ}, has been determined as:

$$p_{inlet_\sigma} = \sigma 0.5\rho_l {U_\infty}^2 + p_v \quad (8.2)$$

Then, the corresponding inlet total pressure, $p_{total_{inlet_\sigma}}$, can be written in terms of inlet static pressure as:

$$p_{total_{inlet_\sigma}} = p_{inlet_\sigma} + 0.5\rho_l {U_\infty}^2 \quad (8.3)$$

With the assumption that Δp is independent of σ, the outlet static pressure, p_{outlet_σ}, can be estimated by the following equation:

$$p_{outlet_\sigma} = p_{inlet_\sigma} - \Delta p \quad (8.4)$$

Note that the numerically obtained incipient cavitation number, σ_i, has been found to differ from the value obtained experimentally. Based on the minimum pressure in the cavitation-free conditions, the numerically obtained σ_i is 1.65, a value

of 65% larger than the one reported by Ausoni et al. (2007). This discrepancy is attributed to the well-organized vortex street predicted by the numerical simulation. This is also consistent with the experimental observation indicating a 50% rise in σ_i when a well-structured vortex street forms behind the hydrofoil at lock-in condition (Ausoni, 2009). The absolute value of the σ_i is not a fundamental factor determining the impact of cavitation on vortex shedding dynamics. Instead, this study has directed its attention towards evaluating the relative differences between values of σ. To match the numerical findings with experimental data, the difference $\Delta\sigma = \sigma - \sigma_i$ has been employed rather than using the ratio σ/σ_i. Consequently, experimental values of σ ranging from 1.3 (non-cavitating) to 0.5 agree with a numerical simulation where σ varies between 1.95 and 1.15. The corresponding boundary conditions applied for the numerical simulation are detailed in Table 8.2. Note that at different $\Delta\sigma$, the numerically obtained time-averaged velocity at the inlet approximates the designated value of 20, exhibiting a relative deviation of less than 0.2%. This observation also confirms the validity of the assumption that Δp remains independent of σ.

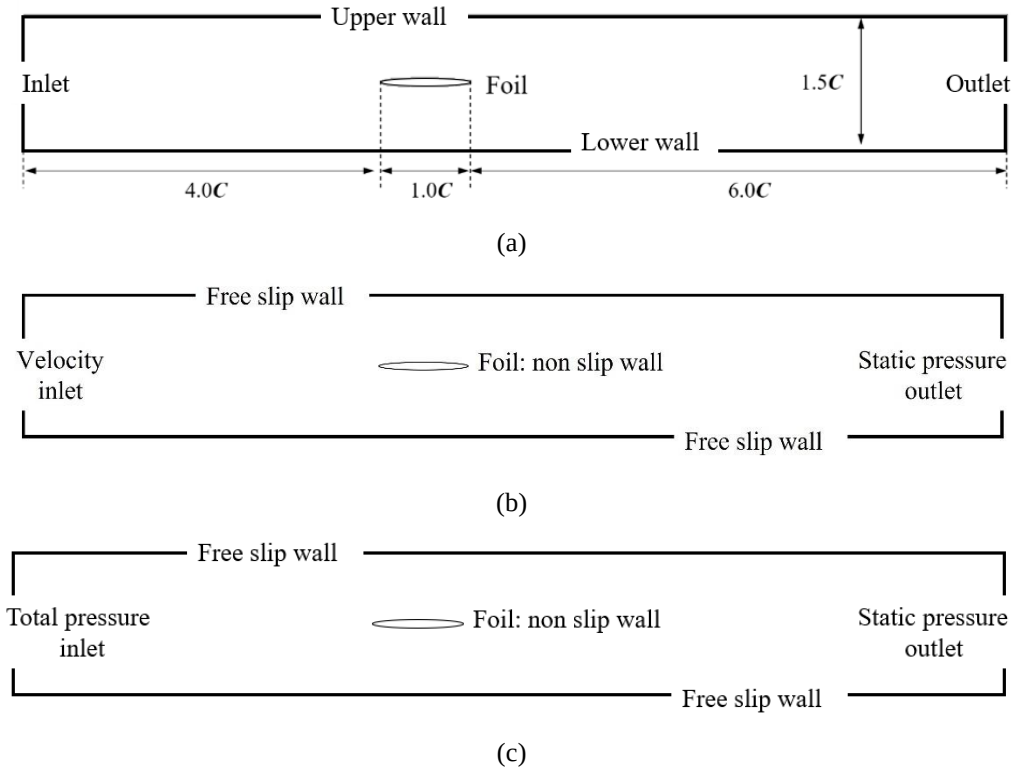

Fig. 8.1 The computational domain (a), and corresponding boundary conditions for the non-cavitating flow simulation (b) and the cavitating flow simulation (c).

Furthermore, the accuracy of numerical predictions regarding the laminar-turbulent transition using SST γ-$Re_{\theta t}$ turbulence model are highly dependent on the

inflow values for the turbulent quantities. Therefore, determining the values of these variables requires further discussion.

Table 8.1 Flow boundary conditions used for the non-cavitating case.

U_{inlet}(m/s)	p_{outlet} (kPa)	$p_{inlet_{total}}$ (kPa)	Δp(kPa)
20 (Exp.)	379	591.6	12.6

Table 8.2 Flow boundary conditions used for the cavitating cases.

$\Delta\sigma$	$p_{inlet_{total}}$ (kPa)	p_{outlet} (kPa)	Δp(kPa)	U_{ref} (m/s)
0.01	542.6	330	12.6	20.03
0.4	466.6	254	12.6	20.02
0.5	447.6	235	12.6	19.98

8.2 VERIFICATION AND VALIDATION

8.2.1 Verification: Grid and timestep sensitivity assessment

To verify the mesh sensitivity, four meshes with different cell elements were tested. As shown in Fig. 8.2, the maximum y^+ for these four meshes are close to 1 and the corresponding spatial resolution near the tailing edge varies from 0.3 to 0.1 mm. More details of the mesh characteristics are summarized in Table 8.3.

Table 8.3 Characteristics of the quad meshes in the computational domain.

Mesh	Hex elements	Total elements	Chordwise element No.	BL element	Max y^+	BL growth factor	Near wake resolution (mm)
M1	39232	109716	100	30	1.2	1.2	0.30
M2	56128	136688	200	36	0.5	1.2	0.20
M3	112832	204824	300	100	0.5	1.1	0.15
M4	135232	239258	400	100	0.5	1.1	0.10

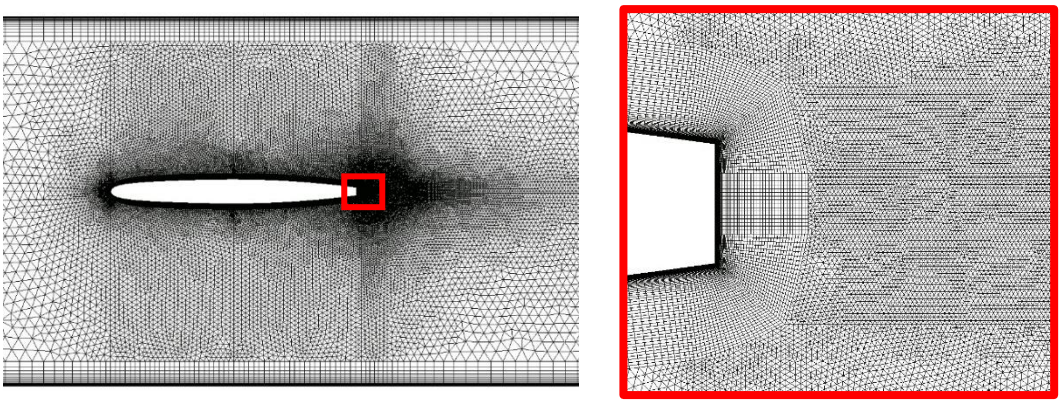

(a) (b)

Fig. 8.2 General overview of the mesh topology (M2) around the hydrofoil (a) and zoomed view at the trailing edge and near wake region (b).

Considering the non-cavitating vortex shedding flow at $Re = 6.64 \times 10^4$ with inlet $TI = 0.6$ and $ERV = 5$, a grid refinement study was conducted by decreasing the resolution both on the hydrofoil surface and in the near wake region. Table 8.4 presents the results with 4 different refinement levels (named M1 to M4), monitoring the maximum lift force coefficients $C_L(\max)$, the maximum moment coefficients $C_M(\max)$, and the time average drag force coefficients $\overline{C_D}$. Here, C_L, C_M, and $\overline{C_D}$ are defined as follows:

$$C_L = \frac{F_y}{0.5\rho_l U_{ref}^2 C} \quad (8.5)$$

$$C_M = \frac{M}{0.5\rho_l U_{ref}^2 C^2} \quad (8.6)$$

$$C_D = \frac{F_x}{0.5\rho_l U_{ref}^2 C} \quad (8.7)$$

where F_y is the total force projected in the transverse direction, M is the moment referring to the center of the hydrofoil, and F_x is the total force projected in the mainstream direction. It can be seen that for the mesh M3 further reduction of the grid size leads to a change of 0.5%, 0.3%, and 0.0% for $C_L(\max)$, $C_M(\max)$, and $\overline{C_D}$, respectively, which indicates that the numerical results are not affected by the grid refinement.

Table 8.4 presents the obtained $C_L(\max)$, $C_M(\max)$, and $\overline{C_D}$ using mesh M3 with different time step sizes Δt, ranging from $1 \cdot 10^{-5}$ to $2 \cdot 10^{-6}$ s. It is observed that for $\Delta t = 5 \cdot 10^{-6}$ s, further decrease in Δt leads to a change of 0.5%, 0.4%, and 0.0% for $C_L(\max)$, $C_M(\max)$, and $\overline{C_D}$, respectively. These small differences in the

monitored parameters imply that the current numerical results are not affected when reducing Δt below $5 \cdot 10^{-6}$ s.

Based on the mesh sensitivity analysis and the effect of Δt, the mesh M3 with $\Delta t = 5 \cdot 10^{-6}$s has been employed in the present numerical study.

Table 8.4 Influence of mesh refinement on several monitored parameters.

Mesh	C_L(max)		C_M(max)		$\overline{C_D}$	
	Results	Relative error (%)	Results	Relative error (%)	Results	Relative error (%)
M1	0.0861	1.8	0.0198	0.5	0.02721	0.1
M2	0.0866	2.4	0.0198	0.7	0.02723	0.0
M3	0.0850	0.5	0.0197	0.3	0.02723	0.0
M4	0.0846	-	0.0197	-	0.02723	-

Table 8.5 Influence of time step sizes on several monitored parameters.

Δt	C_L(max)		C_M(max)		$\overline{C_D}$	
(10^{-6}s)	Results	Relative error (%)	Results	Relative error (%)	Results	Relative error (%)
10	0.0869	2.2	0.0198	1.1	0.0272	0.2
5	0.0850	0.5	0.0197	0.4	0.0272	0.0
2	0.0846	-	0.0196	-	0.0272	-

8.2.2 Validation: boundary layer transition

Boundary layer transition over the circular cylinder

The boundary layer transition over the circular cylinder is considered for validation. Our results obtained with the implemented controlled decay SST γ-$Re_{\theta t}$ model are compared to the experimental results and the published numerical results. The computational domain and mesh are depicted in Fig. 8.3, the diameter of the cylinder is denoted as D. The setup is consistent with the one used by Zheng and Lei (2016) as follows: the distance from the upper, lower, and left boundaries to the cylinder center is 15 D; the distance from the right boundary to the cylinder center is 20 D. Note that, the total grid number used by Zheng and Lei (2016) is 85000, here, more than 110000 grids are used. The Reynolds number based on the cylinder diameter and the inflow velocity is Re=8.5×10^5. Moreover, the inlet turbulence intensity is TI=0.7% with EVR=5.

Fig. 8.4 presents the C_D and C_L as a function of non-dimensional time using the implemented controlled decay SST γ-$Re_{\theta t}$ model. The numerically obtained mean C_D and St are compared to the available experimental and numerical data in Table 8.6. A good agreement is obtained, indicating that the current implementation of the controlled decay SST γ-$Re_{\theta t}$ model is correct and the suitability of this turbulence model in predicting boundary layer transition and the vortex shedding over the cylinder.

Fig. 8.5 shows instantaneous contours of the turbulent intensity using controlled decay SST γ-$Re_{\theta t}$. The local turbulence intensity from the inlet to the leading edge of the circular cylinder remains almost the same as the one at the inlet, suggesting that the controlled decay SST γ-$Re_{\theta t}$ can effectively remove the unrealistic decay of turbulent intensity.

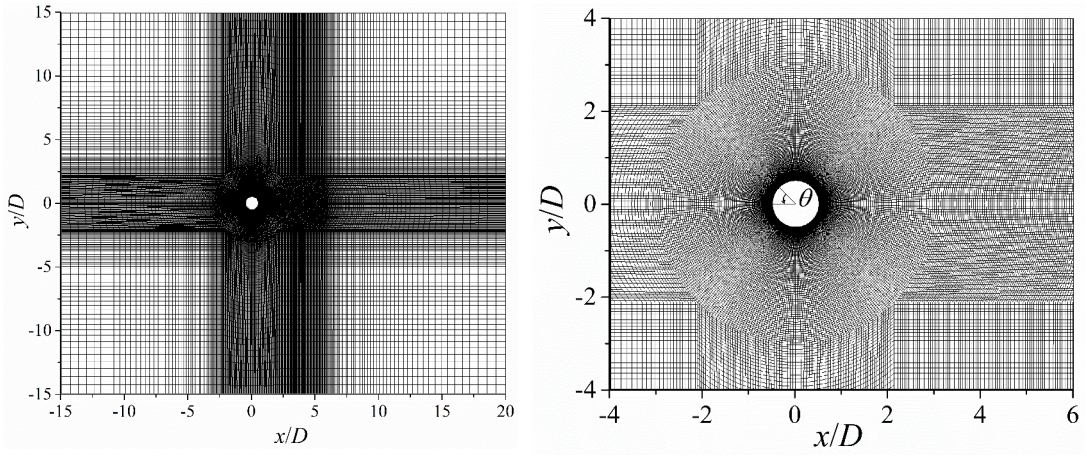

(a) (b)

Fig. 8.3 Computational meshes around a circular cylinder: (a) the whole domain and (b) region near the circular cylinder.

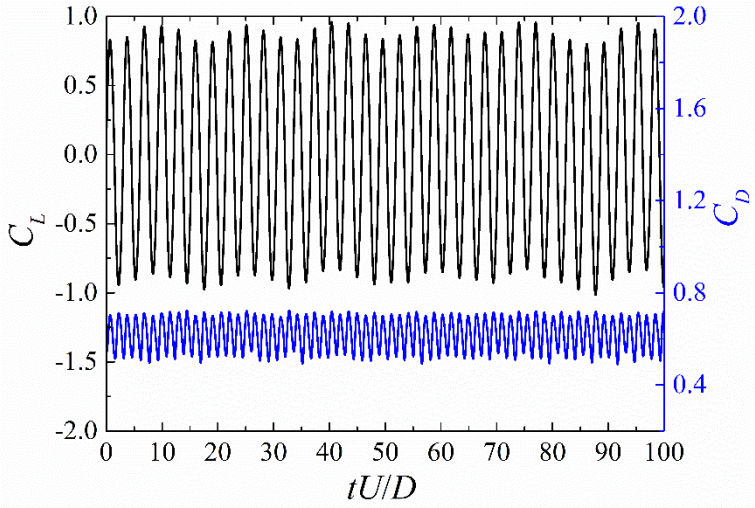

Fig. 8.4 The history of C_D and C_L with TI=0.7% using the controlled decay SST γ-$Re_{\theta t}$ model.

Table 8.6 Comparison of C_D and St for a circular cylinder with the previous investigation.

	Zheng and Lei (2016)	The present	Exp. (Achenbach, 1968)
C_D	0.631	0.621	0.635
St	0.326	0.327	0.33

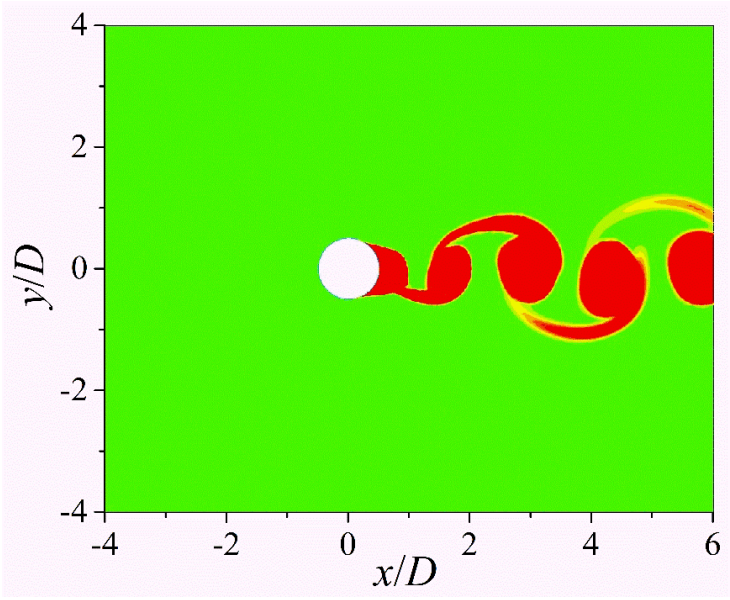

Fig. 8.5 Instantaneous contours of the turbulent intensity using controlled decay SST γ-$Re_{\theta t}$ with inflow TI=0.7%, EVR=5.

Fig. 8.6 compares the numerically obtained time-averaged skin friction coefficient distribution to the experimental data. As shown in Fig. 8.6, using the method by Zheng and Lei (2016), it is found that the laminar separation is located at

point A; transition occurs in the region from point T1 to T2; turbulence reattachment occurs at point B; and turbulence separation happens at point D. Therefore, the information of the boundary layer is listed in Table 8.7 and 8.8 and also compared to the previous numerical and experimental data. In terms of the prediction of the transition onset point and turbulent separation point, the results using the current model are similar to that obtained by Zheng and Lei (2016), suggesting that the correct implementation of the controlled decay SST γ-$Re_{\theta t}$ model.

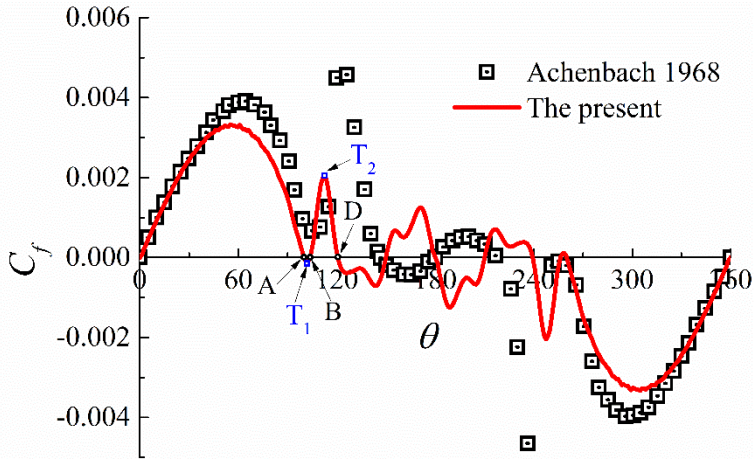

Fig. 8.6 Skin friction coefficient distribution using controlled decay SST γ-$Re_{\theta t}$ with inflow TI=0.7%, EVR=5.

Table 8.7 Comparison of transition onset point with the previous investigation.

	Num. (Zheng and Lei, 2016)	Num.	Exp. (Achenbach, 1968)
Upper surface	103	101	105°
Lower surface	257	259	255°

Table 8.8 Comparison of turbulent separation point with the previous investigation.

	Num. (Zheng and Lei, 2016)	Num.	Exp. (Achenbach, 1968)
Upper surface	123	121	125°
Lower surface	238	239	235°

Boundary layer transition over the blunt trailing edge hydrofoil

To assess the influence of the controlled decay turbulence model on the inflow turbulence variables, a comparative analysis of TI profiles in front of the leading edge was conducted between the SST γ-$Re_{\theta t}$ and the controlled decay SST γ-$Re_{\theta t}$ turbulence models. Fig. 8.7 illustrates TI contours utilizing the SST γ-$Re_{\theta t}$ for $Re = 6.64 \times 10^4$, $TI = 2.0$ % and $EVR = 30$ (case S1, as listed in Table 8.9), and the controlled decay SST γ-$Re_{\theta t}$ for $Re = 6.64 \times 10^4$, $TI = 0.6\%$ and $EVR = 5$ (case CD4, as detailed in Table 8.9).

It can be seen that the local TI obtained using the SST γ-$Re_{\theta t}$ undergoes a significant decay from the inlet to the leading edge of the hydrofoil, showing a decrement of 120%, despite the high EVR. In contrast, using the controlled decay SST γ-$Re_{\theta t}$, the local TI maintains a consistent value at the inlet. These results are aligned with prior numerical investigations suggesting that the controlled decay SST γ-$Re_{\theta t}$ can effectively remove the unrealistic decay of TI inside the computational domain (Spalart & Rumsey, 2007; Zheng & Lei, 2016).

Table 8.9 Ambient turbulence variables in the different simulation conditions.

Case	Turbulence model	TI(%)	EVR	k_{amb}(m^2/s^2)	ω_{amb}(s^{-1})
S1	SST γ-$Re_{\theta t}$	2.0	30	0.24	7961.72
CD1	Controlled decay SST γ-$Re_{\theta t}$	0.1	5	0.0006	119.78
CD2	Controlled decay SST γ-$Re_{\theta t}$	0.2	5	0.0024	479.14
CD3	Controlled decay SST γ-$Re_{\theta t}$	0.5	5	0.015	2994.60
CD4	Controlled decay SST γ-$Re_{\theta t}$	0.6	5	0.0216	4312.22
CD5	Controlled decay SST γ-$Re_{\theta t}$	1.0	5	0.060	11978.40

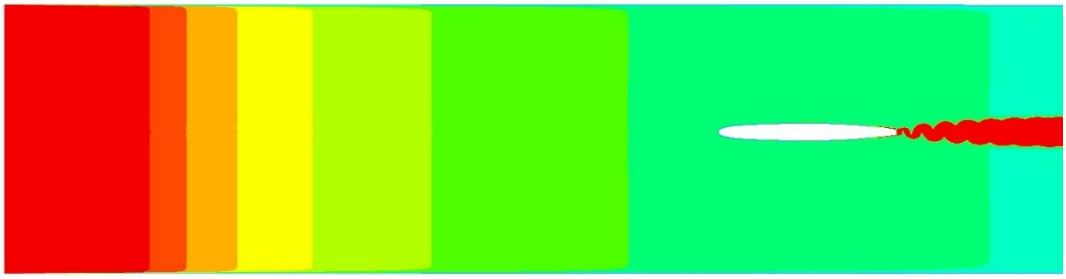

(a)

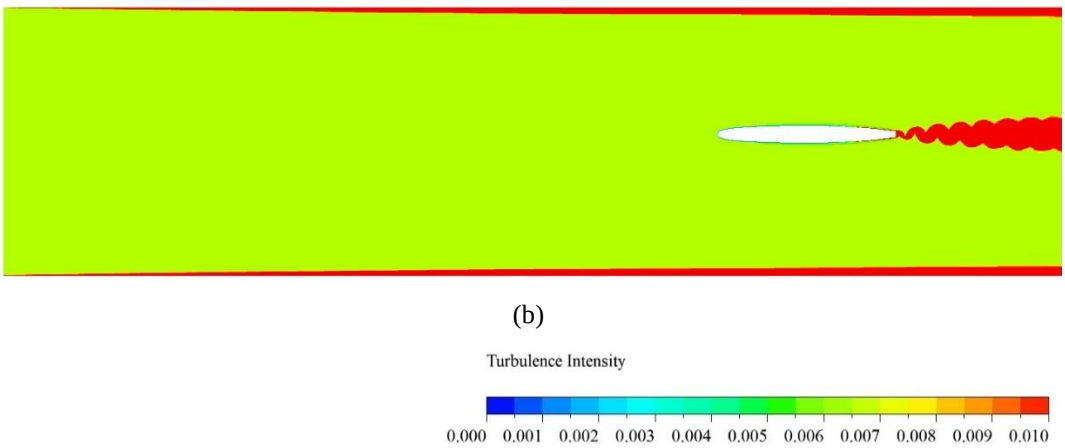

Fig. 8.7 Instantaneous contours of the turbulent intensity using SST γ-$Re_{\theta t}$ with inflow $TI = 2.0\%$, $EVR = 30$ (a) and Controlled decay SST γ-$Re_{\theta t}$ with inflow $TI = 0.6\%$, $EVR = 5$ (b).

Previous numerical results reported that the prediction of the boundary layer transition is sensitive to the inflow ambient flow conditions. As suggested by Menter (2009), the EVR should lie within 1 and 10. Hence, in the current study, EVR has been kept at a constant value of 5. To explore the influence of TI, multiple levels spanning from 0.1% to 1% have been considered. Correspondingly, the inlet boundary conditions specific to each level of TI are detailed in Table 8.9.

Fig. 8.8 provides insight into the impact of TI on the velocity distribution within the boundary layer along the hydrofoil surface and the time-averaged velocity distributions at various locations using the controlled decayed SST γ-$Re_{\theta t}$ turbulence model. The results have been compared with experimental data from Ausoni (2009).

In the context of Fig. 8.8, y denotes the normal distance from the wall and U_{mean} is the velocity component parallel to the surface, normalized by the external velocity U_e. The figure illustrates time-averaged velocity distributions within the boundary layer at relative chord lengths x/C of 0.1, 0.3, 0.4, 0.6, 0.7, 0.8, 0.85, 0.9, and 0.95. This depiction enables an examination of how varying TI levels affect the velocity distribution within the boundary layer. For $x/C \leq 0.3$, the time-averaged velocity distribution along the hydrofoil surface exhibits a limited sensitivity to varying levels of TI. However, when considering $x/C \geq 0.4$, the overall profile of the time-averaged velocity, predicted specifically with $TI = 0.6$ %, demonstrates a better agreement with the experiments.

Furthermore, the time-average wall friction coefficients, $\tau_w/0.5\rho_l U_{ref}^2$, with different levels of TI are compared in Fig. 8.9(a). A distinctive jump is observed in the

wall friction coefficient distribution which marks the end of the boundary layer transition. The predicted positions for the transition end, using $TI = 0.1\%$, 0.2%, 0.5%, 0.6%, and 1.0%, are located at $0.95C$, $0.92C$, $0.89C$, $0.84C$, and $0.30C$, respectively. Notably, the numerically obtained transition of $0.84C$ with $TI = 0.6\%$ resembles more accurately the experimental values of $0.85 \pm 0.05C$ reported by Ausoni (2009). Fig. 8.9(b) compares the evolutions of the time-averaged pressure coefficients, C_p, for different levels of *TI*. It can be seen that all curves fall on the same one, indicating the lack of sensitivity of the minimum C_p to the level of *TI* which is located at a distance of $0.03C$ from the leading edge with a value of -0.45.

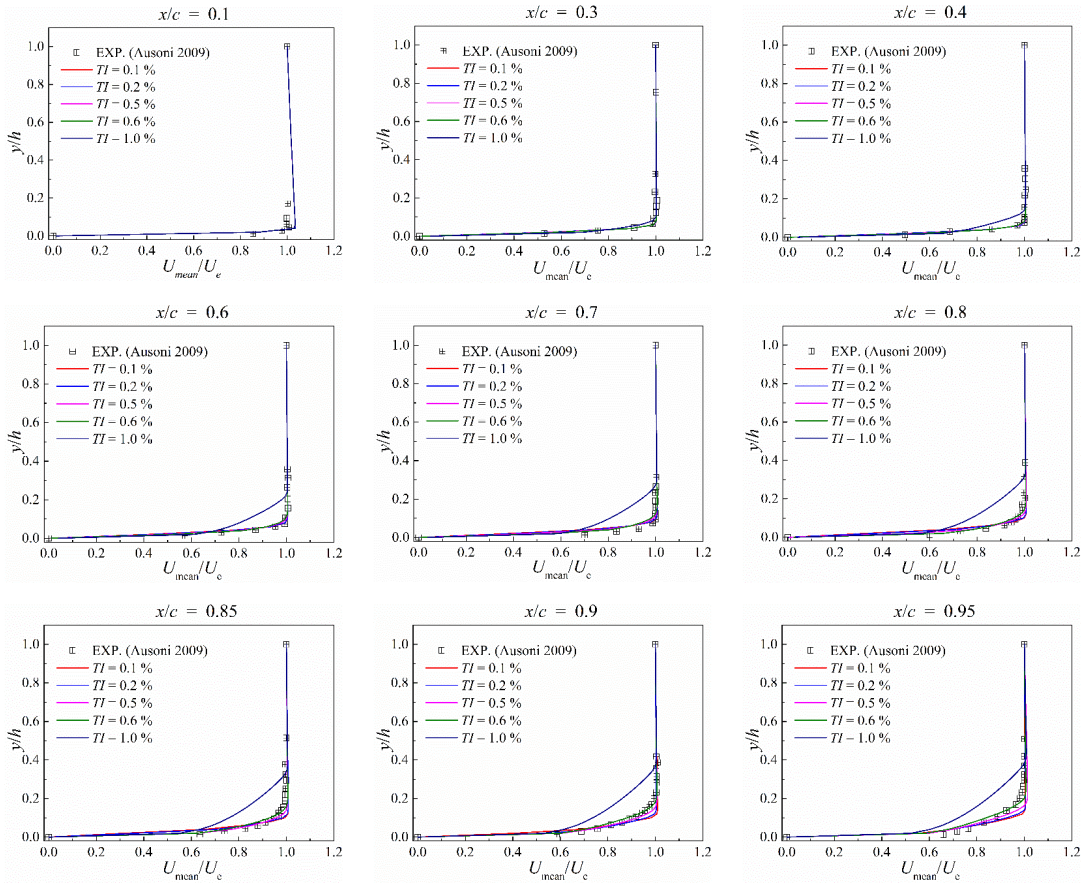

Fig. 8.8 Time-averaged velocity distribution near the surface of the hydrofoil.

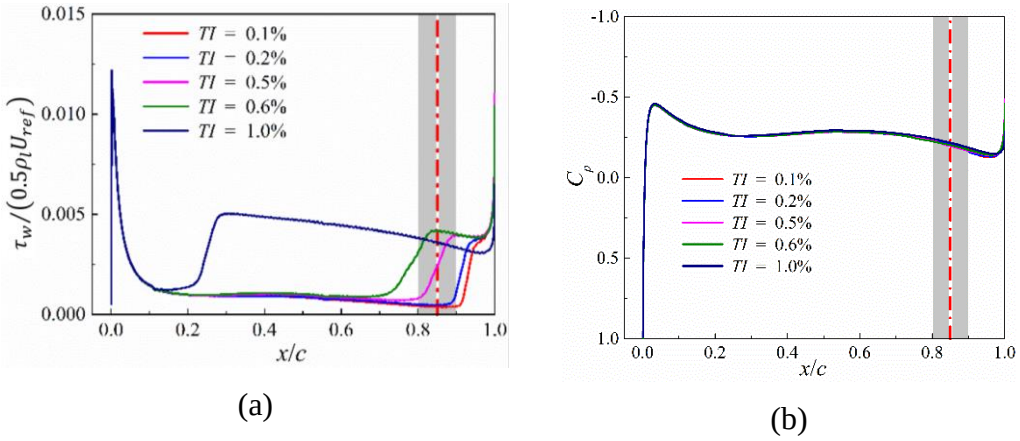

(a) (b)

Fig. 8.9 Time-averaged wall friction coefficients (a) and pressure coefficients (b) on the hydrofoil surface along the chord.

The Fast Fourier Transform (FFT) has been employed to identify the dominant vortex shedding frequency for the time history of C_L, as depicted in Fig. 8.10. However, a higher resolution in the frequency domain via FFT needs a longer time signal. In the case of periodic signals, such as the ones shown in Fig. 8.10(a), increasing the time duration with a small timestep, e.g. $\Delta t = 5 \cdot 10^{-6}$s, substantially increases computational costs and makes FFT less efficient. To overcome this drawback, the "curve fitter" tool provided by Matlab has been applied to extract the vortex shedding frequency based on the C_L history.

In Fig. 8.10(b), with σ = 1.95 (non-cavitating case), the value of the f_{vs} derived from FFT is 1440 (Hz), while Fig. 8.10(c) shows that using the curve fitter tool it is 1437.2 (Hz). To further validate the "curve fitter" method, the f_{vs} values obtained from the C_L history at $\Delta\sigma = 0.01$ are compared in Fig. 8.11 which shows a deviation of less than 0.22%, suggesting a negligible difference between both methods.

Under the non-cavitating case (σ = 1.95), the curve-fitter method determines f_{vs} to be 1437.2 Hz which exhibits a good agreement with the experimental measurement of 1425 Hz reported by Ausoni et al. (2007), presenting a relative error of less than 0.9%.

In summary, the simulation conducted with $TI = 0.6\%$ and $EVR = 5$ agrees well with the experimental measurements in terms of the velocity distribution, the boundary layer transition position, and the primary vortex shedding frequency. As a result, this particular set of inlet boundary conditions, in conjunction with the

controlled decay SST $\gamma - Re_{\theta t}$ turbulence model, have been chosen for further numerical investigations.

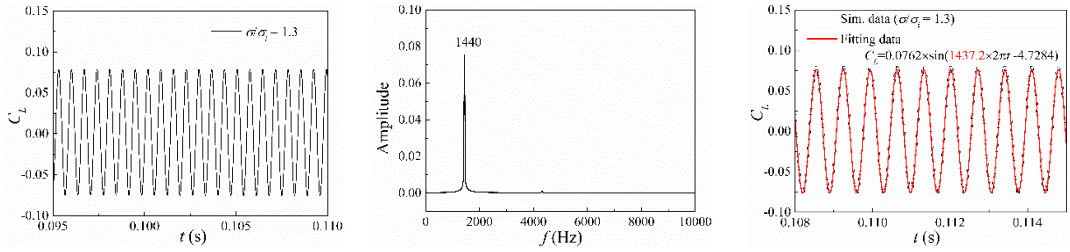

(a) (b) (c)

Fig. 8.10 The history of C_L (a) and the corresponding primary frequency obtained by FFT (b) and Matlab curve fitter (c) at σ = 1.95.

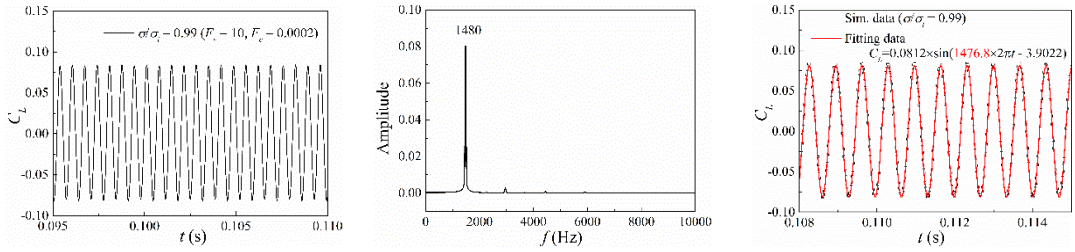

(a) (b) (c)

Fig. 8.11 The history of C_L (a) and the corresponding primary frequency obtained by FFT (b) and Matlab curve fitter (c) at $\Delta\sigma = 0.01$.

8.2.3 Validation: the cavitation model empirical coefficients

Previous numerical studies highlighted the sensitivity of unsteady cavitating flow simulations to cavitation model empirical coefficients F_v and F_c (Morgut et al., 2011; Yakubov et al., 2015; Geng & Escaler, 2020). Consequently, tuning them has been necessary to improve the agreement between simulations and experimental observations. For that, three simulations were conducted with different coefficient sets (F_v, F_c): (10,0.01), (50,0.0002) and (50,0.01).

Fig. 8.12 presents a comparative analysis of C_L under cavitating conditions as well as the corresponding vorticity field. Results obtained with empirical coefficients of (50, 0.0002) and (10, 0.0002) exhibit indistinguishable trends in both the $C_L$and the vorticity field. However, the comparison between results obtained with values of (50, 0.0002) and (50, 0.01) reveals a notable impact of F_c on the C_L and the vorticity field. In Fig. 8.12, the increase in F_c from 0.0002 to 0.01 distinctly induces a sharp pulse in the C_L. Meanwhile, as F_c increases from 0.0002 to 0.01, there is a significant reduction

in vorticity magnitude within the vortical core. These observations suggest a high dependence of the cavitating wake dynamics behind the hydrofoil NACA 0009 on the model empirical coefficients.

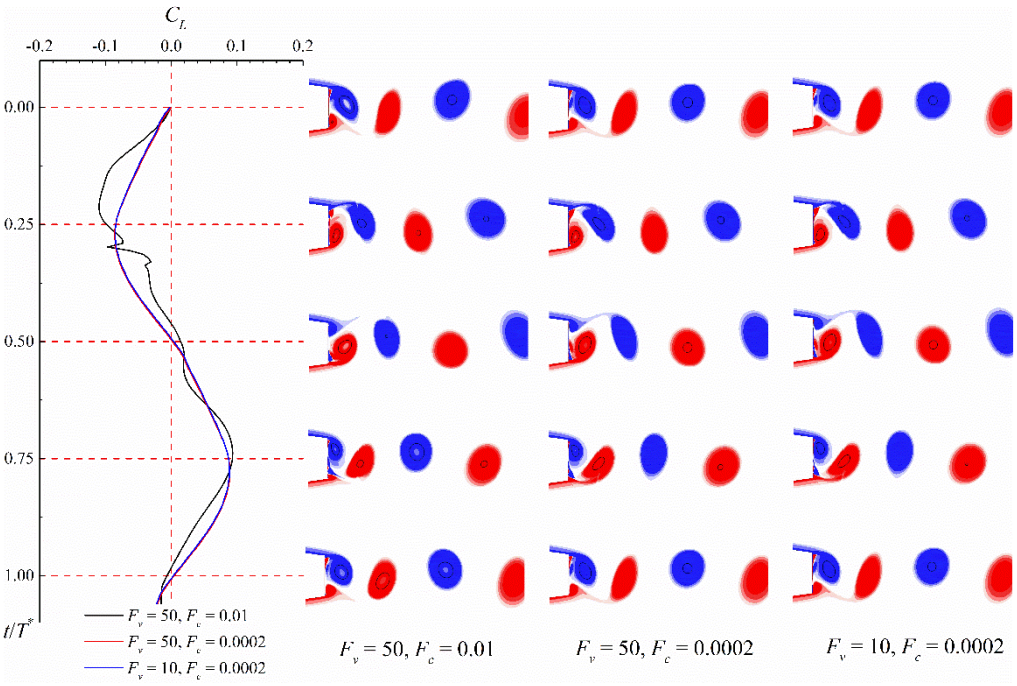

Fig. 8.12 The numerical history of the lift coefficient and vorticity field with different coefficient sets at $\Delta\sigma$=0.4.

To calibrate the cavitation model coefficients, a range of values was explored: F_v from 1 to 50 and F_c from 0.0002 to 0.02. As the experimental data (Ausoni, 2009) displayed in Fig. 8.13, a distinct linear relationship between the vortex-shedding frequency f_{vs}/f_n can be established, where f_n = 890 Hz is the natural frequency of the first torsion mode. A linear regression analysis on this dataset produced a fitted slope of -0.246, as depicted in Fig. 8.13. This slope value serves as an objective function to assess the numerical results obtained using different empirical coefficients.

The vortex shedding frequencies at $\Delta\sigma = 0.01$ and $\Delta\sigma = 0.4$ were used to calculate the simulated fitted slope. Fig. 8.14 illustrates the error contour plot between the simulated fitted slopes and the measured value from the experiments. It can be seen that the maximum error in the fitted slope exceeds 50% for the simulation using values of (50, 0.02). Conversely, the local minimum error in the fitted slope is less than 3% for cases using values of (10, 0.0002) or (1, 0.01).

To confirm the optimal coefficients, simulations at $\Delta\sigma = 0.5$ were also carried out. Table 8.10 presents both the measured and predicted f_{vs} using (10, 0.0002) or (1, 0.01). The simulation with coefficients (1, 0.01) overestimates f_{vs} by approximately 2.32%. while the one using coefficients (10, 0.0002) yields a better prediction, reducing the error to approximately 0.3%.

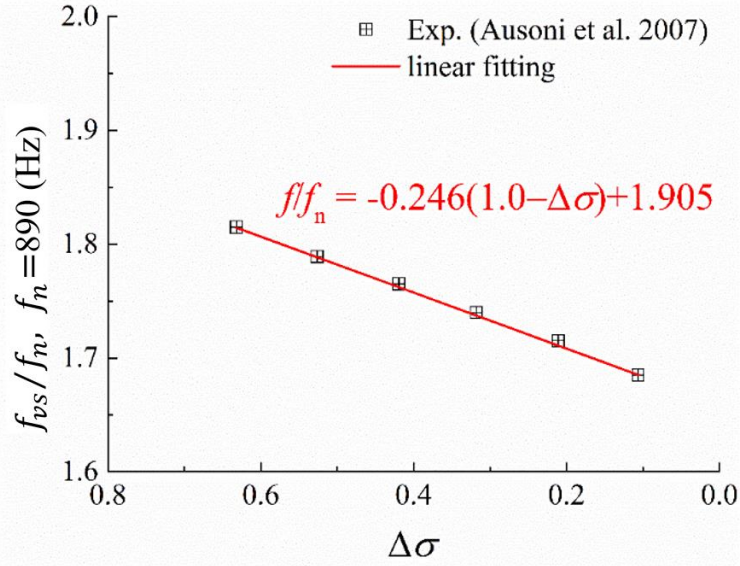

Fig. 8.13 Linear regression analysis of f_{vs}/f_n and $\Delta\sigma$.

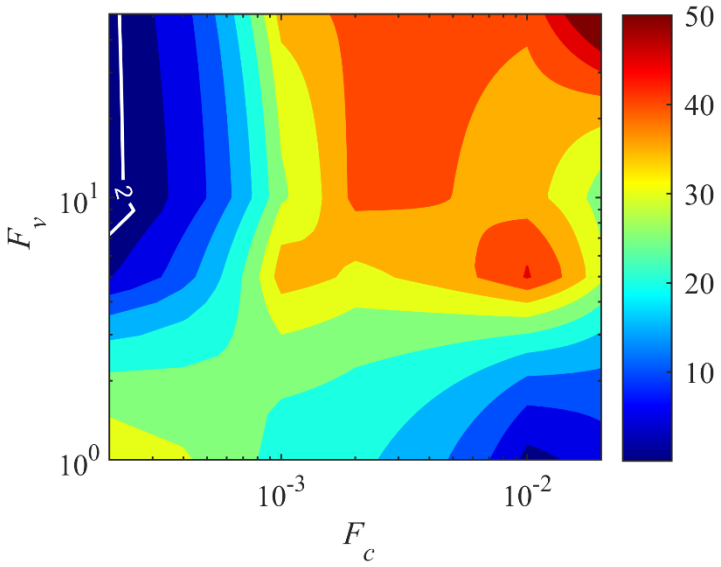

Fig. 8.14 The contour of the relative error to the fitted slope with different (F_c, F_v).

Table 8.10 Comparison between the measured and the predicted vortex shedding frequency with empirical vaporization and condensation coefficients (1, 0.01) and (10, 0.0002) for $\Delta\sigma$=0.5.

	Exp. $\Delta\sigma = 0.5$ (Ausoni, 2009)	(1, 0.01)	(10, 0.0002)
f_{vs} (Hz)	1590	1555	1595
Error (%)	-	2.20	0.3

Fig. 8.15 shows the comparison between the measured and the f at different σ. It can be seen that the prediction using $F_v = 10$ and $F_c = 0.0002$ is improved, resulting in an overall error of less than 0.7%. Hence, the following studies have been based on a cavitation model using $F_v = 10$ and $F_c = 0.0002$.

As follows, the simulated cavitating flows for three distinct cavitation numbers will be compared with the non-cavitating case.

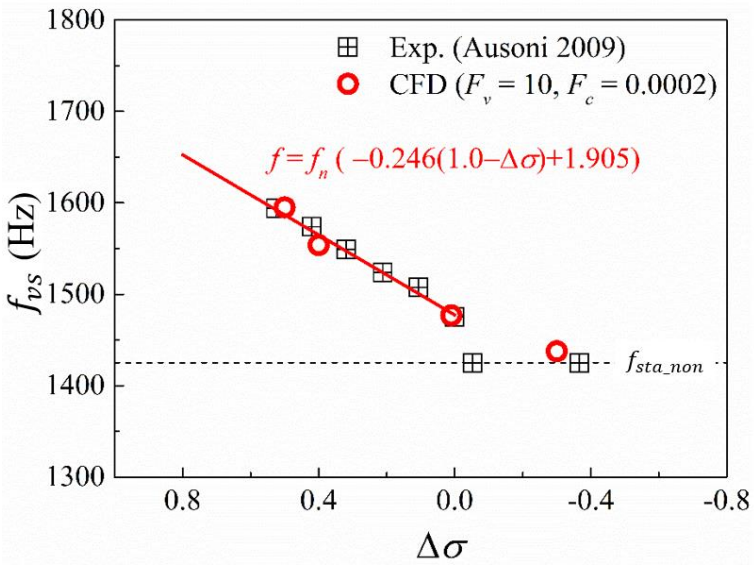

Fig. 8.15 Comparison of the vortex shedding frequency between simulation and experiment using the empirical coefficients F_v = 10 and F_c = 0.0002.

8.3 EFFECTS OF CAVITATION ON UNSTEADY LOADS

Fig. 8.16 displays the C_L and C_D time evolutions for non-cavitating and cavitating conditions. Table 8.11 presents the average $C_{L,max}$ and C_D calculated from the instantaneous values. With the development of the cavitation from $\Delta\sigma = 0.01$ to $\Delta\sigma = 0.5$, a noticeable increase in the magnitude of the load on the hydrofoil is

observed. Specifically, there is a 19.8% increase in $\overline{C_{L,max}}$ and a 23.9% increase in $\overline{C_D}$. This finding correlates with the experimental measurements conducted by Ramamurthy and Bhaskaran (1977), indicating that a reduction in the cavitation number leads to a rise in C_D.

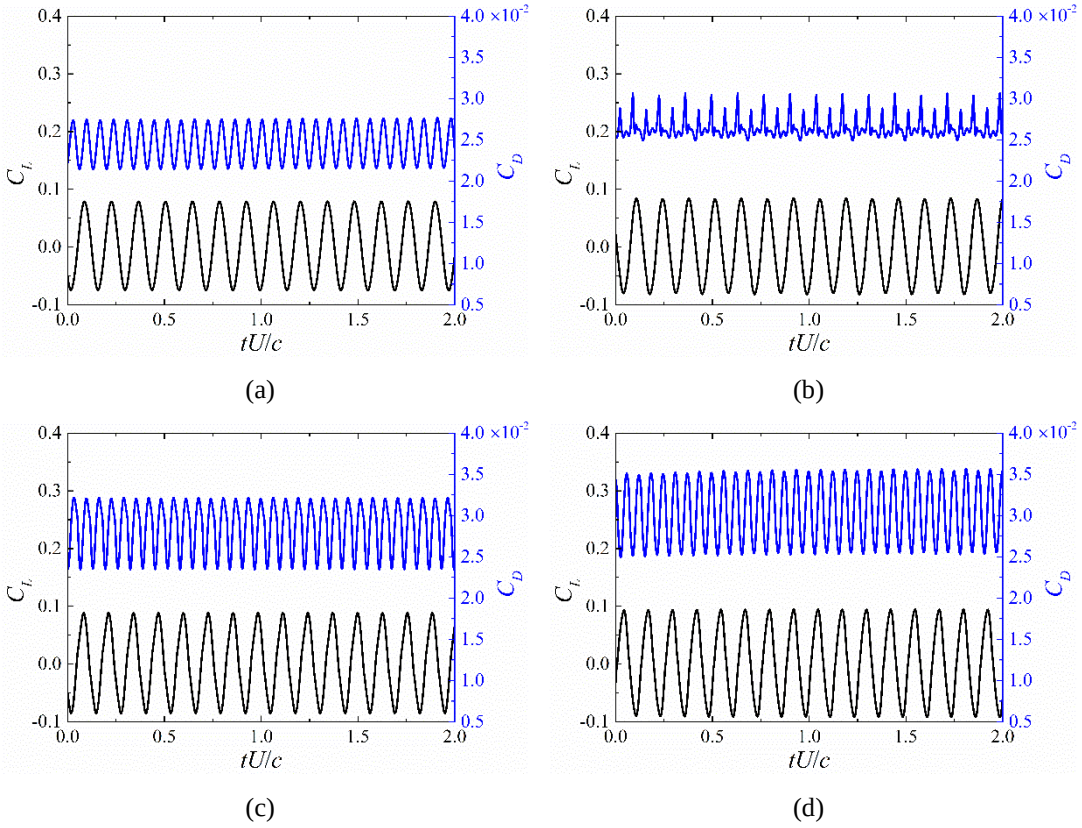

Fig. 8.16 Lift and drag coefficient history for σ=1.95 (a), $\Delta\sigma$=0.01 (b), $\Delta\sigma$=0.4 (c), and $\Delta\sigma$=0.5 (d).

Table 8.11 $\overline{C_{L,max}}$ and $\overline{C_D}$ obtained at different $\Delta\sigma$.

$\Delta\sigma$	$\overline{C_{L,max}}$	$\overline{C_D}$
σ = 1.95 (Non cavitating)	0.0788	0.0246
0.99	0.0843	0.0264
0.4	0.0884	0.0284
0.5	0.0944	0.0305

8.4 EFFECTS OF CAVITATION ON VORTEX STREET DYNAMICS

8.4.1 Vortex boundary and center identification methods

Traditionally, the vortex center can be determined using simple field criteria (Decaix et al., 2018), for example, minimum of pressure, maximum of axial vorticity, maximum of the Q criterion (Hunt, 1987), and maximum of λ_2 (Jeong & Hussain,

1995). However, these criteria may fail in the cavitating flow with high advection effects. To solve it, Huang and Green (2015) have proposed two new non-local vortex center identification method within the Lagrangian coherent structures. The first one involves the following steps:

1) identifying the vortex boundary using the negative finite-time Lyapunov exponent (nFTLE) criterion (Haller & Yuan, 2000; Haller, 2015; C. Huang et al., 2022) obtained from the velocity field data over the domain of interest, as shown in Fig. 8.17(a),

2) enclosing the boundary of the nFTLE with a specific rectangle plane, as shown in Fig. 8.17(b),

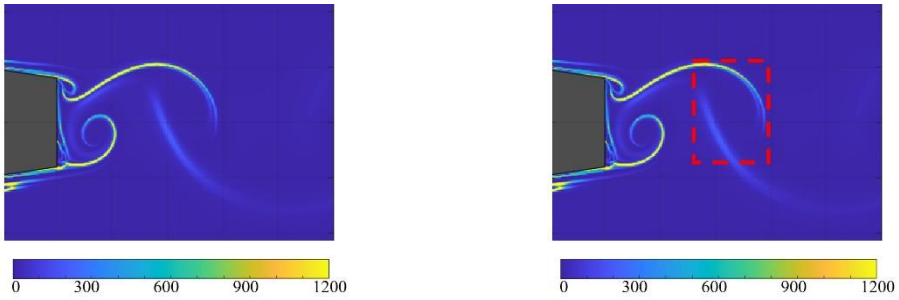

(a) (b)

Fig. 8.17 Contour of nFTLE (a) and the rectangle enclosing the ridges of the nFTLE field (b).

3) exporting the flow field within the rectangle for further analysis, and

4) determining the vortical centers on the rectangle plane using the minimum of Γ_1 criteria (Graftieaux et al., 2001) defined as:

$$\Gamma_1(P) = \frac{1}{N}\sum_{i=1}^{N}\frac{(\boldsymbol{PM}\times(\boldsymbol{U_M})\cdot\boldsymbol{n_z})}{\|\boldsymbol{PM}\|\cdot\|\boldsymbol{U_M}\|}dS \quad (8.8)$$

where S is a rectangular domain of fixed size and geometry, centered on P as shown in Fig. 8.18(a) and M lies in S. Here, N are the number of points M inside S, and $\boldsymbol{n_z}$ is the unit vector normal to the detection plane. $\|\cdot\|$ represents the Euclidean norm of the vector. To simplify, the vortex center determined using the Γ_1 function will be referred to as Γ_1 center.

The second method consists in determining the vortical centers on the rectangle plane using the "center of mass" of Q, as sketched in Fig. 8.18(b). For simplicity, the vortex center determined using the "center of mass" of Q will be termed as Q center.

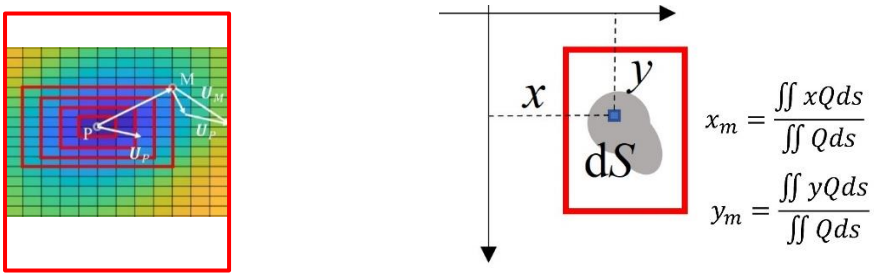

(a) (b)

Fig. 8.18 Demonstration of the calculation of Γ_1 criteria (a) and the "center of mass" of Q on the selected plane.

8.4.2 Tracking of the vortex center

The ridges of the nFTLE field have been employed to outline the boundaries of the shed vortices at $\Delta\sigma = 0.5$, as depicted in Fig. 8.19(a). Note that, the integration time for the calculation of nFTLE is $60\Delta t$ and a further increase in the integration time only changes the absolute value of nFTLE but not the location of the ridges (Green et al., 2007). Following the vortex boundary identification methods presented in previous sections, rectangular planes were utilized to enclose these boundaries. In Fig. 8.19(a) and 8.19(b), three distinct rectangular planes are applied to encompass vortices A, B, and C. Subsequently, the vortex center has been determined using either Γ_1 function (Graftieaux et al., 2001) or the "center of mass" of Q criterion (Y. Huang & Green, 2015) within this designated plane, as demonstrated in Fig. 8.19(c). Upon the comparison, a notable discrepancy in the position of the vortex center has been observed between the Γ_1 function and the Q criterion. More specifically, the position of the Γ_1 center has been found to lie outside the vapor cavity (marked with a solid line), as illustrated in Fig. 8.19(c). Conversely, the Q center approximately resides at the midpoint of the cavity, which appears to be closer to the expected physical reality. Therefore, the Q center has been selected to calculate the vortex centers in the subsequent sections.

The location of the vortex shedding occurrence holds significant importance due to its direct correlation with the history of unsteady forces acting on solid bodies (Sarpkaya, 1976). To synchronize the initiation of vortex shedding for different σ, the instant that the lower vortex A (as indicated in Fig. 8.20(a)) begins to form has been defined as the point when C_L approaches its minimum value (Z. Wang et al., 2018). Fig. 8.20 illustrates the temporal evolution of nFTLE, Q center and C_L at selected instants with different cavitation levels. As anticipated, the increase of cavitation leads

to a reduction in the periodic time, T, of the lift fluctuation. Moreover, the presence of cavitation ($\Delta\sigma = 0.5$, $\Delta\sigma = 0.4$) does not initiate the formation of any new vortices during the shedding process. Therefore, the influence of cavitation seems to primarily affect the primary shedding vortices rather than inducing the formation of additional vortices.

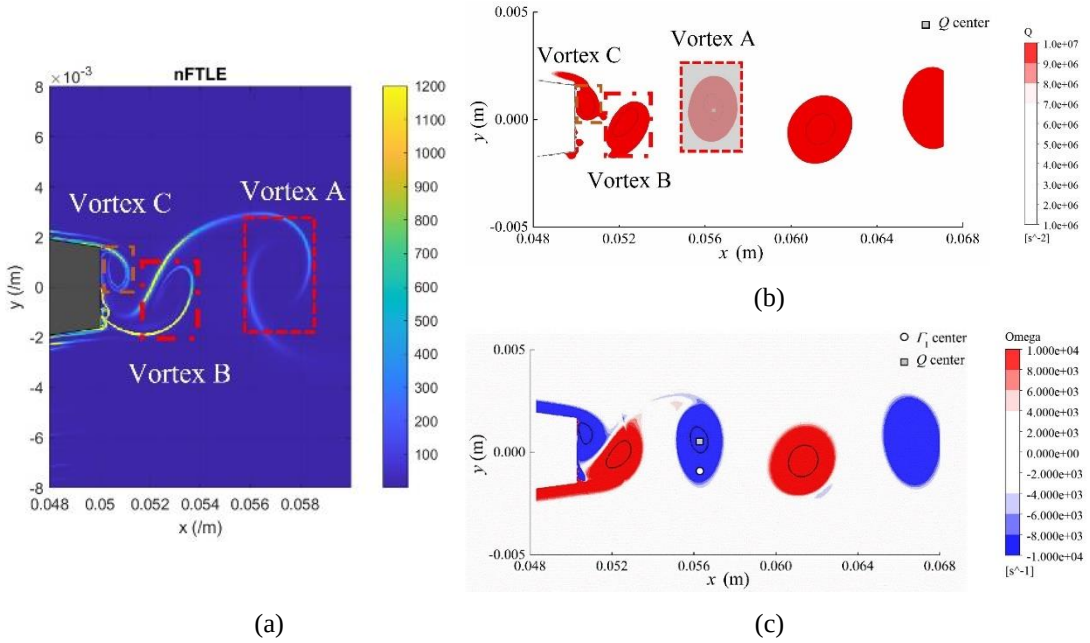

Fig. 8.19 Example of vortex center identification: identification of vortex boundary using ridges of nFTLE and enclosed rectangle(a); the contour of Q and Q center (b); the relative position of Γ_1 center and Q center to the cavity (c).

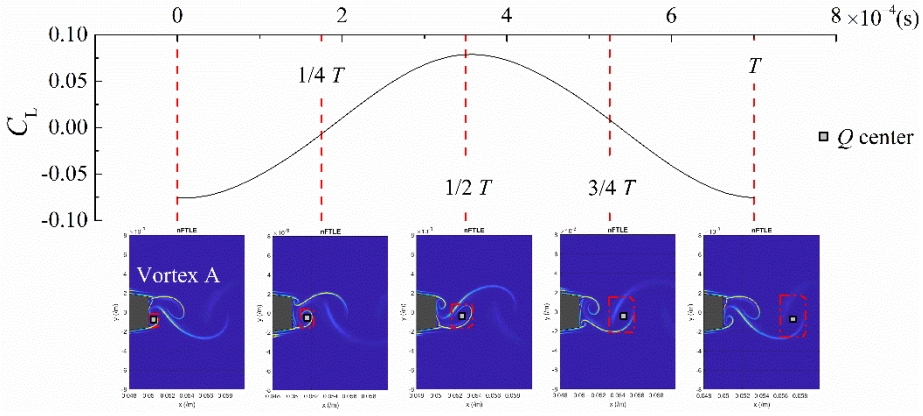

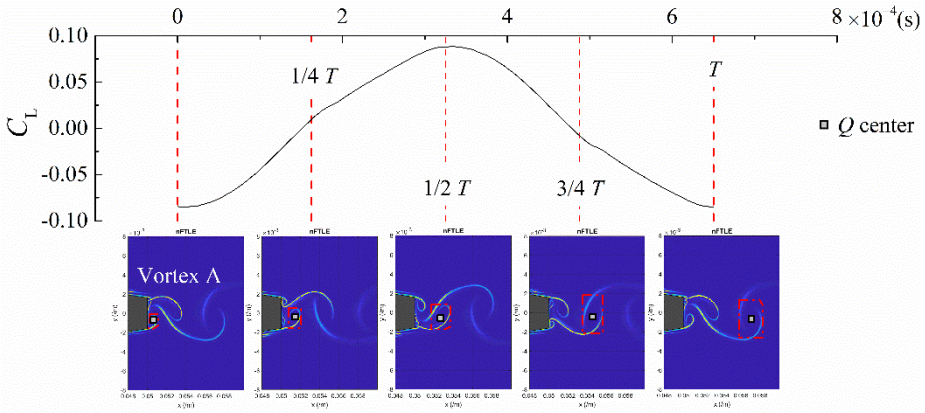

(b)

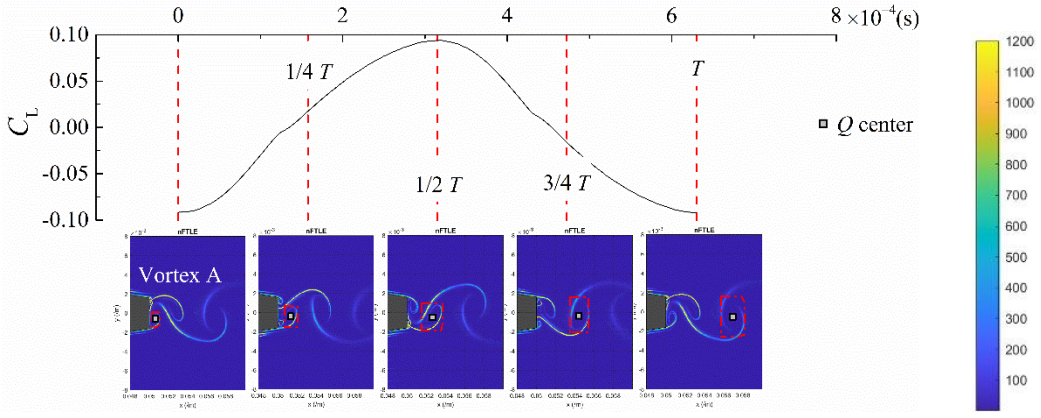

(c)

Fig. 8.20 Instantaneous snapshots of the shedding vortices and the trajectories of Q center at (a) $\sigma = 1.95$ (Non-cavitating), (b) $\Delta\sigma = 0.4$, and (c) $\Delta\sigma = 0.5$.

8.4.3 Vortex shedding frequency and morphology

To assess the impact of cavitation on the primary vortices, the trajectories of the Q center were traced at different σ, as depicted in Fig. 8.21. The time interval between neighbouring points was $10\Delta t$, and the total time for tracing the trajectories of the Q center was $140\Delta t$, approximating the periodic time of C_L in non-cavitating conditions. It can be seen that C_L approaches its minimum value, and the initial point of the vortex center trajectory gradually shifts further downstream with increased cavitation development. Simultaneously, this position of the initial point converges closer to the wake center.

To assess the influence of the cavitation on the vortex advection velocity in the horizontal direction, the time evolution of the vortex center trajectory in the horizontal axis has been plotted in Fig. 8.22 at different σ. Here, the y axis denotes the displacement of the vortex center at time t to the initial point. The results show that

the vortex center horizontal distance increases with the development of cavitation. Using a linear regression, the U_{adv} can be determined as depicted in Fig. 8.22. For $\sigma = 1.95$ (non-cavitating), it is 15.22 m/s, and at $\Delta\sigma = 0.4$, it rises to 15.44 m/s. Furthermore, at $\Delta\sigma = 0.5$, it reaches 15.82 m/s. These results reveal that the presence and development of cavitation can increase the advected velocity of the vortices, showing a 3.9% increase in advected velocity at $\Delta\sigma = 0.5$. This value is in good agreement with the one reported in the experiments carried out by Ausoni et al. (2007), where they noted a similar 4% increase in advected velocity at $\Delta\sigma = 0.4$.

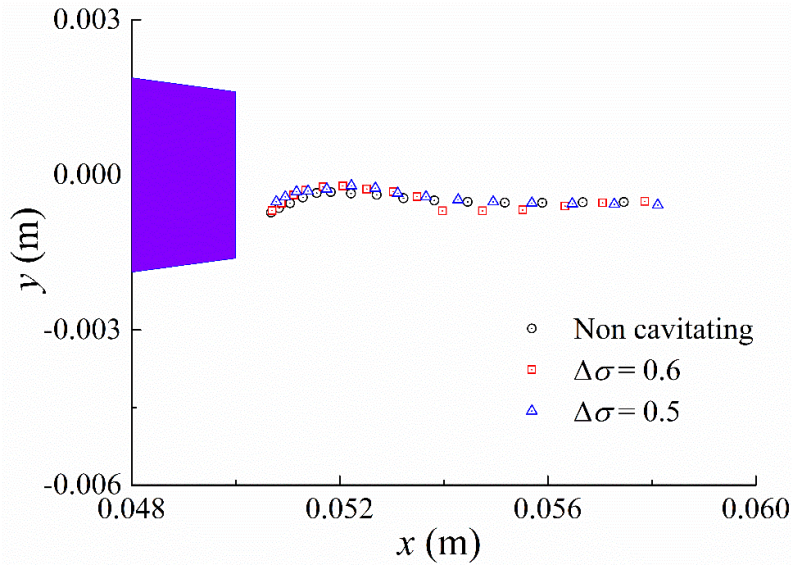

Fig. 8.21 The successive position of the vortex center at different cavitation numbers.

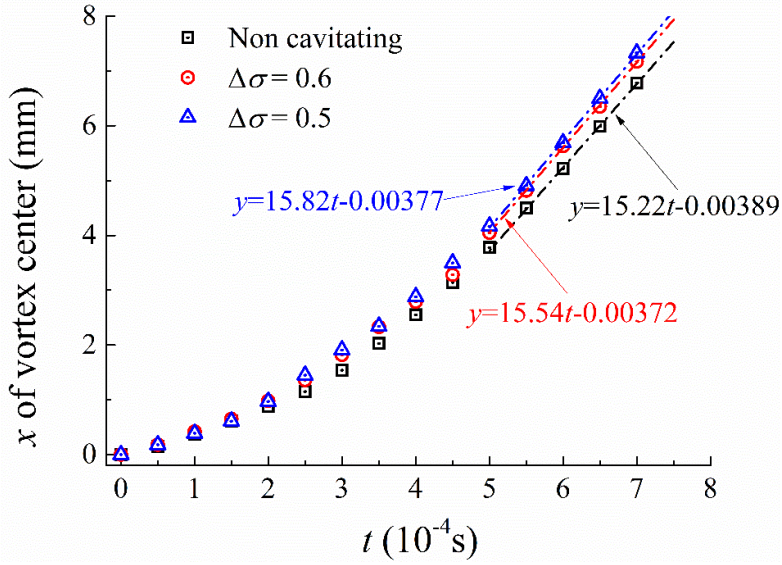

Fig. 8.22 The relative displacement of the vortex center trajectory in the horizontal direction.

Fig. 8.23 displays the contours of vorticity and the positions of the vortex centers at different σ. Calculated from the centers positions, a_v has been tabulated in Table 8.12. For $\sigma = 1.95$ (non-cavitating), a_v is 5.819 mm. With the decrease of cavitation number to $\Delta\sigma = 0.4$, a_v is reduced to 5.454 mm. Furthermore, at $\Delta\sigma = 0.5$, it is further decreased to 5.323 mm. These results demonstrate that the presence and development of cavitation leads to a reduction in a_v. As σ decreases, the rise in St is associated with an increase of U_{adv} and a reduction of a_v.

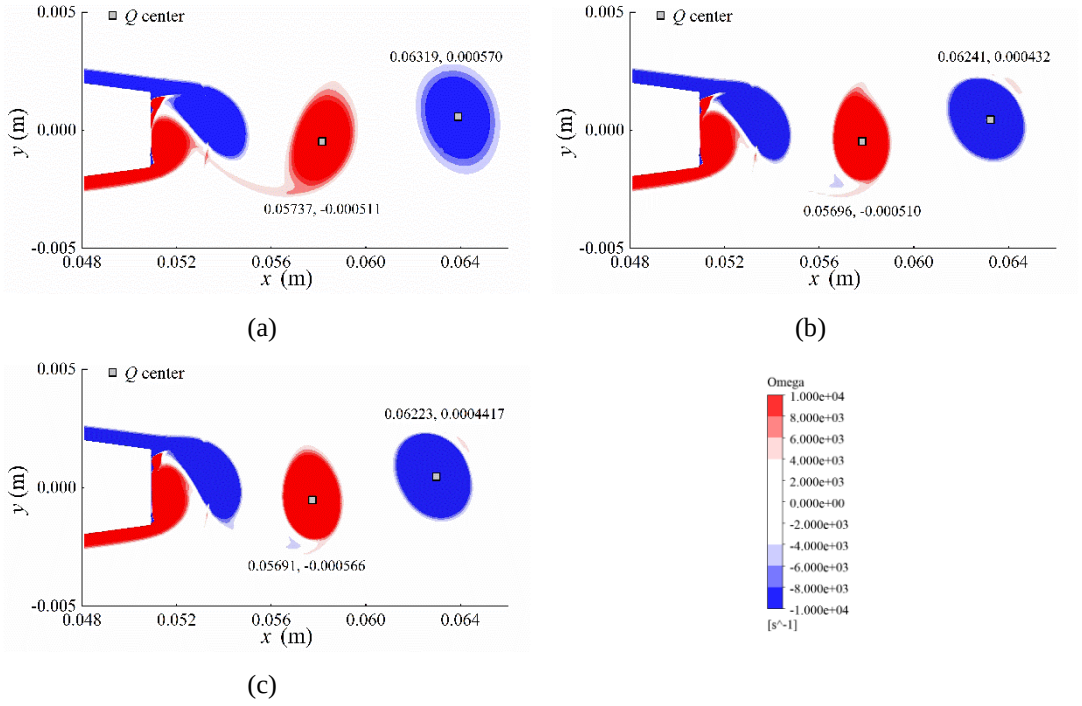

(a) (b) (c)

Fig. 8.23 The contour of the vorticity and the position of the vortex center at (a) $\sigma = 1.95$ (Non-cavitating), (b) $\Delta\sigma = 0.4$, and (c) $\Delta\sigma = 0.5$.

Table 8.12 Summary of the influence of cavitation on the primary shedding vortices

$\Delta\sigma$ or σ	St	U_{adv}(m/s)	a_v (mm)
$\sigma = 1.95$	0.2315	15.22	5.819
$\Delta\sigma = 0.4$	0.2503	15.54	5.454
$\Delta\sigma = 0.5$	0.2568	15.82	5.323

In Fig.8.24, the changes in St, U_{adv}, and a_v relative to the non-cavitating cases are plotted. At $\Delta\sigma = 0.4$, it can be seen that an 8.1% increase in St corresponds to a 2.1% increase of U_{adv} and to a 6.6% reduction of a_v. Then at $\Delta\sigma = 0.5$, a 10.9%

increase in St is associated with a 3.9% increase of U_{adv} and an 9.3% reduction of a_v. Therefore, it can be concluded that both factors contribute to the increase of the vortex shedding frequency. Nevertheless, it becomes evident that the reduction of a_v tends to dominate the vortex shedding frequency change in front of the increase of St.

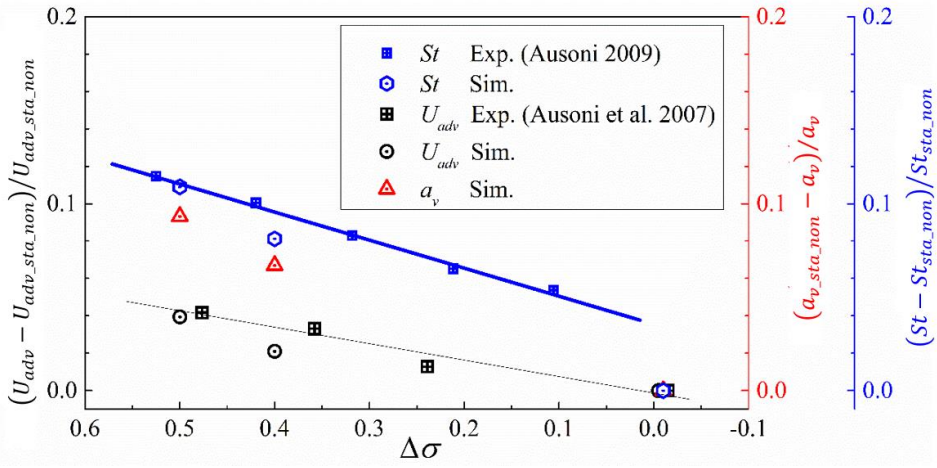

Fig. 8.24 Evolution of *St*, U_{adv}, and α_v relative to the non-cavitating case.

8.5 DISCUSSION

The fact that the development of cavitation provokes an increase of U_{adv} requires further explanations, despite the variety of results present in different studies. For example, Ausoni et al. (2007) proposed the vorticity levels within the vortex core increase due to the occurrence and development of cavitation and they attributed it to a higher U_{adv}. They referred to the findings of Sridhar and Katz (1999), suggesting that microscopic bubbles within the vortex core can amplify the peak vorticity. Furthermore, according to the theoretical analysis by Arndt and Keller (Arndt & Keller, 1992), cavitation within the core seems to increase both peak vorticity inside the cores and tangential velocity outside the core. These studies imply that vapor formation enhances the vorticity levels, particularly through the evaporation of water. However, Gnanaskandan and Mahesh (2016b) presented opposite results, highlighting that vapor condensation notably amplifies vorticity within the cavity. Their numerical results showed that water evaporation induces volume expansion, resulting in positive velocity divergence, while vapor condensation causes volume reduction and negative velocity divergence. According to the vorticity transport equation (Foeth et al., 2008), the negative velocity divergence is the source for generating the vorticity inside the vortical flow structures. An alternative explanation for the rise of $U_{adv}$was proposed

by Belahadji et al. (1995), suggesting that the development of cavitation reduces the virtual mass of the vortex, consequently increasing U_{adv}. As noted by the same authors, examining such a claim is quite difficult. On the other hand, the mechanism accounting for the reduction in a_v was given by Young and Holl (1966). Using the inviscid vortex street model coupled with the sink term, they deduced that the condensation of vapor or the reduction of the vaporous radius inside the vortices could align the vortices themselves closer.

As we can see, the arguments of Gnanaskandan and Mahesh (2016b) and Young and Holl (1966) have emphasized the importance of the effect of condensation on the dynamics of the vortex shedding. This is also supported by two observations on the hydrofoil NACA 0009 that f is more sensitive to F_c rather than to F_v. First, as presented in Fig. 8.12, it can be observed that the variation in C_L in presence of cavitation results from F_c increasing from 0.0002 to 0.01. Second, as illustrated in Fig. 8.14, at the optimal region (upper-left area) of the contour, the obtained linear regression slope of St remains relatively consistent as F_v varies between 5 and 50. Notably, this slop exclusively correlates with F_c and exhibits no dependency on F_v.

Moreover, the present results have confirmed the influence of cavitation on the reduction in a_v, which can partially explain the increase of f_{vs}. Previous observations reported by Young and Holl (1966) have found a 21.2% increase of f_{vs} corresponding to an 18.3% reduction of a_v for the cavitating wake behind a wedge with apex angle of 30º at $\sigma/\sigma_i = 0.3$ as well as a 10.9% increase of f_{vs} with a 9.3% reduction of a_v at $\Delta\sigma = 0.5$ for the cavitation behind a blunt hydrofoil. These results present a ratio between the reduction rate of a_v and the increase rate of f_{vs} of about 0.863, which align well with the value of 0.853 obtained in the present work.

8.6 PARTIAL CONCLUSIONS

In this chapter, a homogeneous mixture model coupled with a controlled decay SST γ-$Re_{\theta t}$ turbulence model has been used to investigate the influence of cavitation on the wake behind a truncated hydrofoil NACA 0009 for different levels of cavitation. Based on the numerical results, it has been concluded that:

- Using optimized values of the inlet turbulence intensity (TI =0.6%) and of the cavitation model empirical coefficients ($F_v = 10$, $F_c = 0.0002$), the predicted

vortex shedding frequencies at different cavitation levels are in good agreement with the experimental results.

- Cavitation significantly impacts the wake flow dynamics, notably increasing the shedding frequency of the primary vortices. For instance, with a 50% reduction of σ in relation to non-cavitating conditions, a 10.8% increase in shedding frequency has been predicted. Moreover, the cavitation growth also increases the hydrodynamic loads acting on the hydrofoil surface.
- Using a vortex identification method, the influence of cavitation on the trajectories of the centers and the morphology of the primary shedding vortices has been identified. It has been found that cavitation development enhances the advected velocity of the vortices while decreasing the streamwise inter-vortex spacing. Both factors are believed to contribute to the increase of the vortex shedding frequency and the reduction of the advected velocity tends to dominate this increase.

Chapter 9: Characteristics of the cavitating vortex street flow behind the oscillating hydrofoil

Chapter 9 contains the numerical investigation of the cavitating flow behind the blunt trailing edge hydrofoil NACA 0009 that is subjected to forced oscillation. The objective is to examine the combined effects of hydrofoil oscillation and cavitation on the flows and the resulting dynamic response.

9.1 MATHEMATICAL FORMULATION

In the following, the single degree of freedom (SDOF) equation of motion is used to describe the oscillation of the blunt trailing edge hydrofoil NACA 0009 in vacuum:

$$J_s\ddot{\alpha} + \zeta_s\dot{\alpha} + K_s\alpha = M_{ex}(t) \quad (9.1)$$

where α, $\dot{\alpha}$, and $\ddot{\alpha}$ are the angular displacement, velocity, and acceleration of the hydrofoil, respectively. J_s, ζ_s, and K_s are the moment of inertia, damping, and stiffness of the body, respectively. Moreover, $M_{ex}(t)$ represents the external excitation moment acting on the hydrofoil surface. In VIV, the vortex-induced moment $M_{vs}(t)$ can be regarded as the primary source of the external excitation moment.

When the solid body vibrates in a surrounding viscous fluid, its dynamic response is influenced by the additional unsteady fluid moment $M_f(t)$ and the external excitation $M_{vs}(t)$, as illustrated in Fig. 9.1. The former moment is induced by the body's acceleration, velocity, and displacement. Assuming that the flow response to the body motion is a linear function of the body's displacement and its first and second derivatives, the unsteady fluid moment $M_f(t)$ can be modeled using the concept of the added properties and expressed as follows:

$$-\left(J_f\ddot{\alpha} + \zeta_f\dot{\alpha} + K_f\alpha\right) = M_f(t) \quad (9.2)$$

where J_f is the added moment of inertia, ζ_f is the added damping, K_f is the added stiffness. Submit equation (9.2) into equation (9.1) and then:

$$\left(J_s + J_f\right)\ddot{\alpha} + \left(\zeta_s + \zeta_f\right)\dot{\alpha} + \left(K_s + K_f\right)\alpha = M_{vs}(t) \quad (9.3)$$

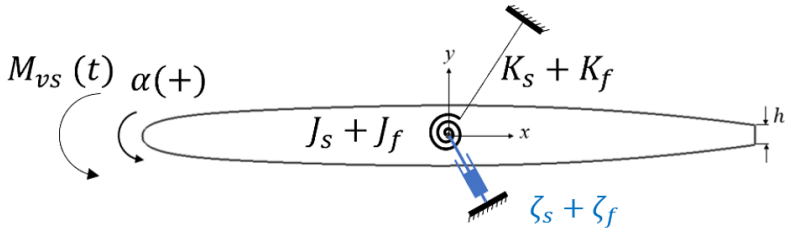

Fig. 9.1 Sketch of the SDOF motion of the hydrofoil submerged in a viscous fluid.

9.2 METHODS TO IDENTIFY THE ADDED PROPERTIES

The added moment of inertia can be defined as the in-phase component of the fluid moment related to the body acceleration and the added damping (fluid damping) can be defined as an in-phase component of the fluid moment related to the body velocity. Here, added stiffness is small and can be neglected (Dehkharqani et al., 2019) thus $K_f = 0$ is adopted in the following analysis.

Two methods are available for the identification of hydraulic added properties: (i) the projection method (Gauthier et al., 2017) and (ii) the "curve fitter" method (Roig et al., 2021). Each of them will be detailed as follows:

9.2.1 Projection method

Given that the body's displacement has been prescribed in the form of harmonic motion, the averaged J_f and ζ_f can be obtained by projecting the resulting fluid moment signal, $M_f(t)$, on the prescribed body acceleration and velocity, respectively.

Multiplying equation (9.2) with $\ddot{\alpha}$ or $\dot{\alpha}$ and integrating the obtained equation over the cycles of the forced oscillation, it can be expressed as:

$$\left(-J_f \int_{t_0}^{t_0+2\pi/\omega_{ex}} (\ddot{\alpha} \cdot \ddot{\alpha})\, dt\right) + \left(-\zeta_f \int_{t_0}^{t_0+2\pi n/\omega_{ex}} (\dot{\alpha} \cdot \ddot{\alpha})\right) = \int_{t_0}^{t_0+2\pi n/\omega_{ex}} \{[M(t) - M_{vs}(t)] \cdot \ddot{\alpha}\} dt \quad (9.4a)$$

$$\left(-J_f \int_{t_0}^{t_0+2\pi n/\omega_{ex}} (\ddot{\alpha} \cdot \dot{\alpha})\, dt\right) + \left(-\zeta_f \int_{t_0}^{t_0+2\pi n/\omega_{ex}} (\dot{\alpha} \cdot \dot{\alpha}) dt\right) = \int_{t_0}^{t_0+2\pi n/\omega_{ex}} \{[M(t) - M_{vs}(t)] \cdot \dot{\alpha}\} dt \quad (9.4b)$$

Where, ω_{ex} is the forced angular velocity and is equal to $2\pi f_{ex}$. Here, the term $\int_{t_0}^{t_0+2\pi n/\omega_{ex}} \ddot{\alpha} \cdot \dot{\alpha}\, dt$ is 0 since the acceleration, $\ddot{\alpha}$, is out phase of the velocity, $\dot{\alpha}$. Then, J_f and ζ_f can be estimated by:

$$J_f = \frac{\int_{t_0}^{t_0+2\pi n/\omega_{ex}} \{[M(t)-M_{vs}(t)]\cdot\ddot{\alpha}\}dt}{\int_{t_0}^{t_0+2\pi n/\omega_{ex}} (\ddot{\alpha}\cdot\ddot{\alpha})dt} \quad (9.5)$$

$$\zeta_f = \frac{\int_{t_0}^{t_0+2\pi n/\omega_{ex}} \{[M(t)-M_{vs}(t)]\cdot\dot{\alpha}\}dt}{\int_{t_0}^{t_0+2\pi n/\omega_{ex}} (\dot{\alpha}\cdot\dot{\alpha})dt} \quad (9.6)$$

where n is the number of the forced oscillation cycles and T_{ex} is the period of the forced oscillation cycles and is equal to $1/f_{ex}$.

In the lock-off conditions, the dominant frequency of $M_f(t)$ is due to the prescribed $\ddot{\alpha}$ and $\dot{\alpha}$ and differs from the dominant frequency of $M_{vs}(t)$. Consequently, as n increases, $\int_{t_0}^{t_0+2\pi n/\omega_{ex}} [M_{vs}(t)\cdot\ddot{\alpha}]\,dt$ can decrease to 0. Then, the equations (9.5) and (9.6) can be simplified to:

$$J_f = \lim_{n\to\infty} \frac{\int_{t_0}^{t_0+2\pi n/\omega_{ex}} (M(t)\cdot\ddot{\alpha})dt}{\int_{t_0}^{t_0+2\pi n/\omega_{ex}} (\ddot{\alpha}\cdot\ddot{\alpha})dt} \quad (9.7)$$

$$\zeta_f = \lim_{n\to\infty} \frac{\int_{t_0}^{t_0+2\pi n/\omega_{ex}} (M(t)\cdot\dot{\alpha})dt}{\int_{t_0}^{t_0+2\pi n/\omega_{ex}} (\dot{\alpha}\cdot\dot{\alpha})dt} \quad (9.8)$$

In the lock-in regimes, it is difficult to split the moment $M(t)$ into the fluid moment and the moment induced by the vortex shedding $M_{vs}(t)$. As a result, equations (9.7) and (9.8) can be used to estimate the J_f and ζ_f as well.

9.2.2 "Curve fitter" method

Considering that the flow field is influenced by both the vortex shedding and the prescribed oscillation, the moment acting on the hydrofoil can be decomposed into the two harmonic signals as follows:

$$M(t) = M_{vs}(t) + M_f(t) \quad (9.9)$$

$$M_{vs}(t) = A_{vs}\sin(2\pi f_{vs}t + \varphi_{vs}) \quad (9.10)$$

$$M_f(t) = A_f\sin(2\pi f_{ex}t + \varphi_f) \quad (9.11)$$

where A_{vs} is the amplitude of the moment induced by the vortex shedding and A_f is the amplitude of the fluid moment. The φ_{vs} and φ_f represents the phase angle of the moment induced by the vortex shedding and the fluid moment, respectively.

Using MATLAB®'s "curve fitter" tool, two harmonic signals can be extracted from the discrete-time history of the moment. Subsequently, based on the definition of

J_f and ζ_f, these two coefficients can be calculated from the parameters of the decomposed two harmonic signals as follows:

$$J_f = \frac{-A_f \sin(\varphi_f)}{\alpha_0 (2\pi f_{ex})^2} \quad (9.12)$$

$$\zeta_f = \frac{A_f \cos(\varphi_f)}{\alpha_0 2\pi f_{ex}} \quad (9.13)$$

where α_0 is the amplitude of the oscillation of the hydrofoil.

9.2.3 Validation of two methods

As detailed in section 9.2.1, the estimation of J_f and ζ_f depends on n. To assess the sensitivity of J_f and ζ_f to n, an analysis was conducted. In Fig. 9.2, at f_{ex}/f_{sta_non}=0.4, values of J_f and ζ_f obtained using the projection method and the "curve fitter" method are plotted against different values of n. It can be seen that when $n > 30$, the variations in J_f and ζ_f resulting from the further increase in n are negligible. Moreover, the projection method exhibits a better convergence compared to the curve fitter method, even with a lower value of n. Therefore, for the subsequent sections, the projection method is used to estimate J_f and ζ_f with $n = 30$. Note that, the "curve fitter" method is employed to extract information regarding the amplitude of the decomposed harmonic signal, such as A_{vs}, A_f, f_{vs}, and f_{ex}.

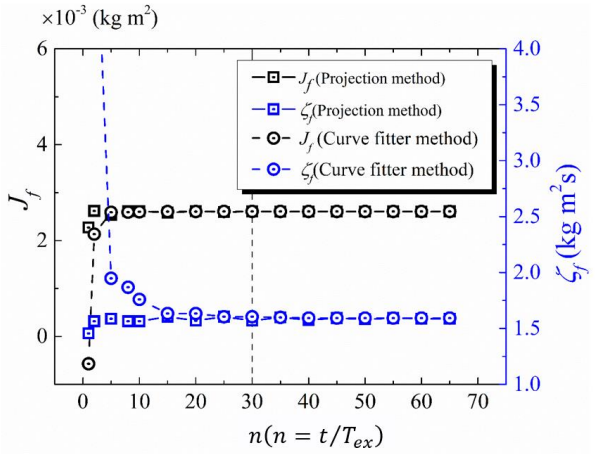

Fig. 9.2 The sensitivity of J_f and ζ_f to n using the projection method and curve fitter method.

9.3 NUMERICAL SETUP

The computational domain and boundary conditions have been detailed in section 8.1.1. The computational domain is discretized with a hybrid mesh to enable a dynamic mesh, as shown in Fig. 9.3. The whole computational domain can be divided into three sub-regions, two of which have been discretized with a structured mesh, while the interior sub-region 2 connecting these two sub-regions has been discretized with an unstructured mesh. When the dynamic mesh is activated, the sub-region 1 moves together with the hydrofoil, which is set to be a rigid body, while the sub-region 3, which is adjacent to the upper and bottom walls, remains fixed. The unstructured mesh inside the connecting sub-region 2 will deform to adapt to the motion of the hydrofoil.

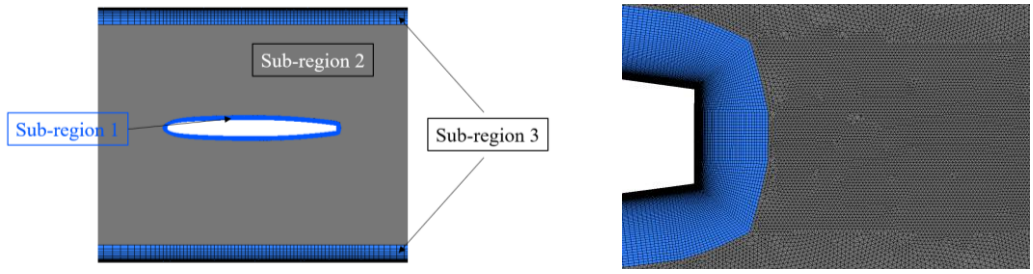

(a) (b)

Fig. 9.3 Division of the computational domain of the hydrofoil NACA0009 with a truncated trailing edge (a) and mesh topology around the trailing edge (b).

As sketched in Fig. 9.4, the motion of the hydrofoil is subject to various excitation frequencies, f_{ex}, ranging from 0.4 f_{sta_non} to 1.6 f_{sta_non}, where f_{sta_non} represents the frequency of the vortex shedding behind the stationary hydrofoil at the cavitation-free region. The mean angle of attack is kept constant at 0° while the oscillation amplitude, α_0, is set to 0.1°. Thus, the instantaneous incidence angle of hydrofoil varies between $-\alpha_0$ and $+\alpha_0$ according to the following harmonic law:

$$\alpha = \alpha_0 \sin(\omega_{ex} t + \pi/2) \quad (9.14)$$

where $\omega_{ex} = 2\pi f_{ex}$ is the oscillating angular velocity.

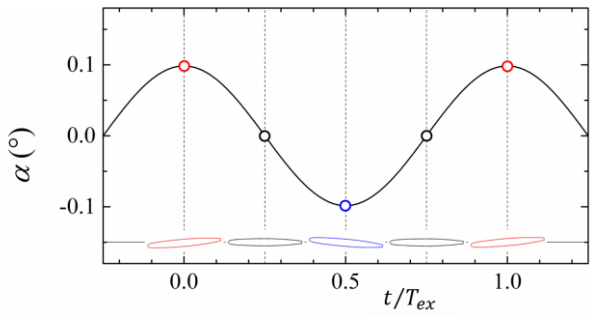

Fig. 9.4 Sketch of the motion of hydrofoil.

9.4 NON-CAVITATING FLOW

The oscillating hydrofoil at f_{ex}/f_{sta_non}=1.0 is considered. This condition is known as the lock-in condition, where the forced oscillation frequency is equal to the vortex shedding frequency, as shown in Fig. 9.12. In the non-cavitating regime, the ambient pressure is chosen as p_{ref} = 4.2 bar, which corresponds to σ=2.1. Fig. 9.5 plots the evolution of the instantaneous C_M and $C_{p\,min}$ at the stationary condition and f_{ex}/f_{sta_non} =1.0 during the whole vortex-shedding cycle. It can be seen that, compared to the stationary condition, the maximum of C_M acting on the oscillating hydrofoil surface increases from 0.022 to 0.17 with a maximum of $C_{p\,min}$ decreasing from -1.65 to -2.8.

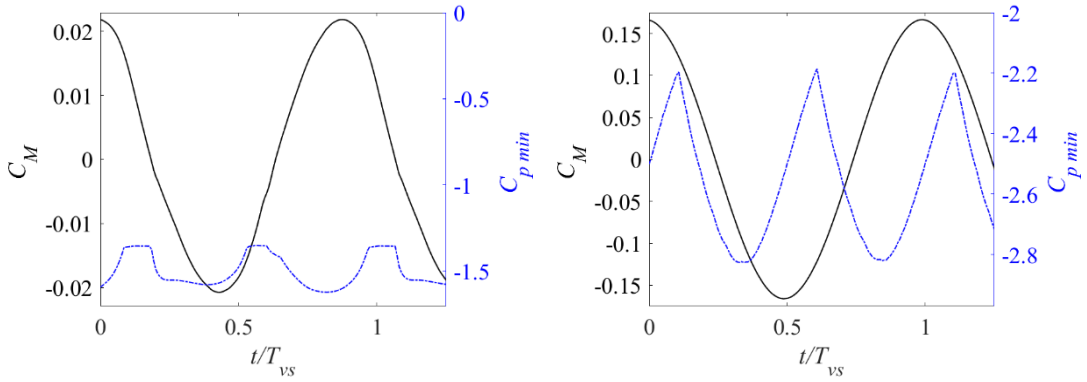

(a) (b)

Fig. 9.5 Instantaneous C_M and $C_{p\,min}$ at the stationary condition (a) and f_{ex}/f_{sta_non}=1.0 (b).

Fig. 9.6 illustrates the C_p field and the vorticity contours near the trailing edge of the hydrofoil throughout one cycle of hydrofoil movement. Alternating shedding of vortices from the upper and lower parts of the trailing edge is observed. The vortex-shedding behavior for the oscillating hydrofoil mirrors that of the stationary case. At *t*

= 0, when the hydrofoil ascends from α = 0.1 º with a minimum acceleration of -$\alpha_0\omega_{ex}{}^2$, the local C_p behind the trailing edge reaches a minimum value of C_p = -2.54 within the vortex shed from the upper surface (Fig. 9.6(a)), corresponding to the maximum value of the moment (Fig. 9.7). At t = 0.25 T_{ex}, when the cylinder moves from α = 0.1 º to α = 0.0 º with the maximum angular velocity of $\alpha_0\omega_{ex}$ during the oscillation period, the local C_p behind the trailing edge hits a minimum value of C_p = - 2.70 within the vortex shed from the lower surface (Fig. 9.6(b)). When the hydrofoil descends to α = -0.1 º with a maximum acceleration of $\alpha_0\omega_{ex}{}^2$ at t = 0.5 T_{ex}, the local C_p behind the trailing edge reaches a minimum value of C_p = -2.54 within the vortex shed from the lower surface (Fig. 9.6(c)). When the hydrofoil returns to α = 0.0 º with the minimum angular velocity of $-\alpha_0\omega_{ex}$ at t = 0.75 T_{ex}, the local C_p behind the trailing edge has a minimum value of C_p = -2.68 within the vortex shed from the upper surface (Fig. 8.6(d)).

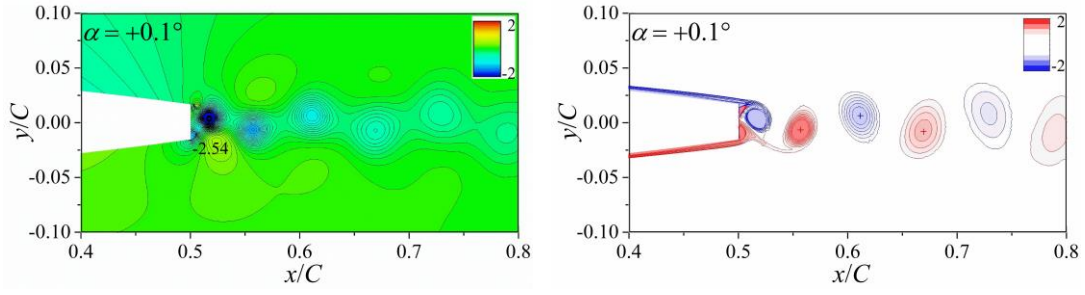

(a)

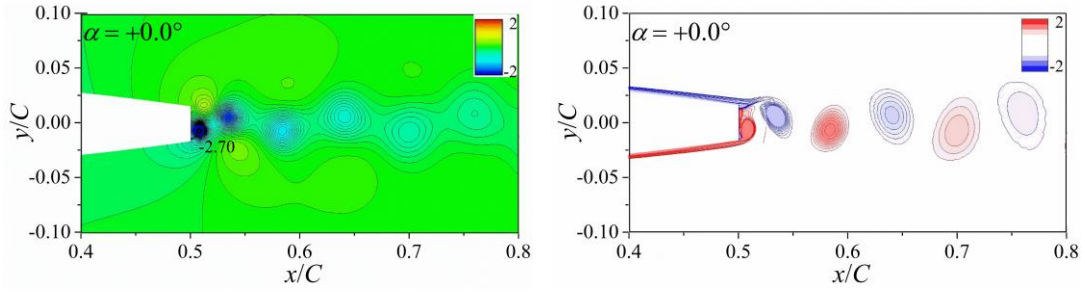

(b)

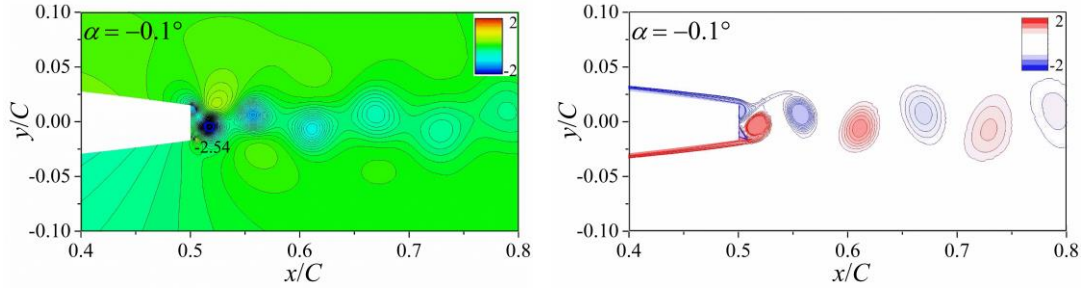

(c)

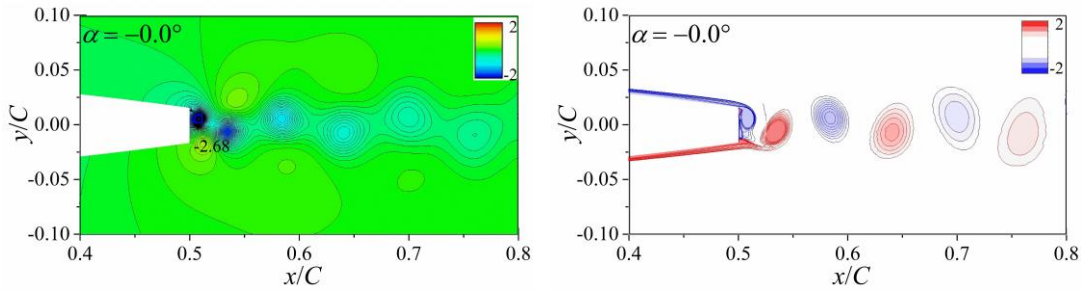

(d)

Fig. 9.6 Instantaneous C_p field (left) and vorticity contours (right) for an oscillating hydrofoil at f_{ex}/f_{sta_non}=1.0 and σ = 2.1: (a) t = 0, (b) t = 0.25 T_{ex}, (c) t = 0.5 T_{ex} and (d) t = 0.75 T_{ex}.

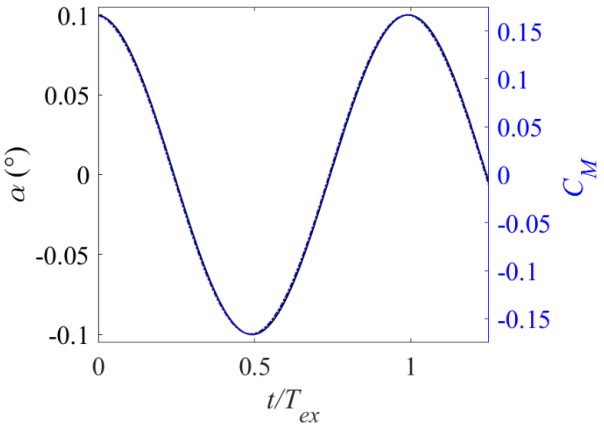

Fig. 9.7 Time evolution of the hydrofoil angle displacement, α, and C_M.

9.5 EFFECTS OF CAVITATION

Simulations are conducted with different values of $\Delta\sigma$ to investigate the influence of cavitation on the flow dynamics around the oscillating hydrofoil. $\Delta\sigma$ is varied while keeping f_{ex}/f_{sta_non}=1.0 and the other parameters same as in the case of the stationary hydrofoil.

Figs. 9.8–9.10 present the vorticity contours, C_p fields, and the vapor volume fraction contours at three different cavitation numbers ($\Delta\sigma$ = 0.2, 0.4, 0.5), respectively. Cavitation primarily occurs within the vortical center shed from the trailing edge, with no cavities observed on the hydrofoil surface, even as the cavitation number decreases to a low value of $\Delta\sigma$ = 0.5. It can be seen that, regarding the profiles of vorticity and pressure field, the effects resulting from the decrease in cavitation

number are negligible. However, as anticipated, the lower cavitation number leads to the generation of more cavity structures within the shedding vortices, as evident in the vapor volume fraction contours.

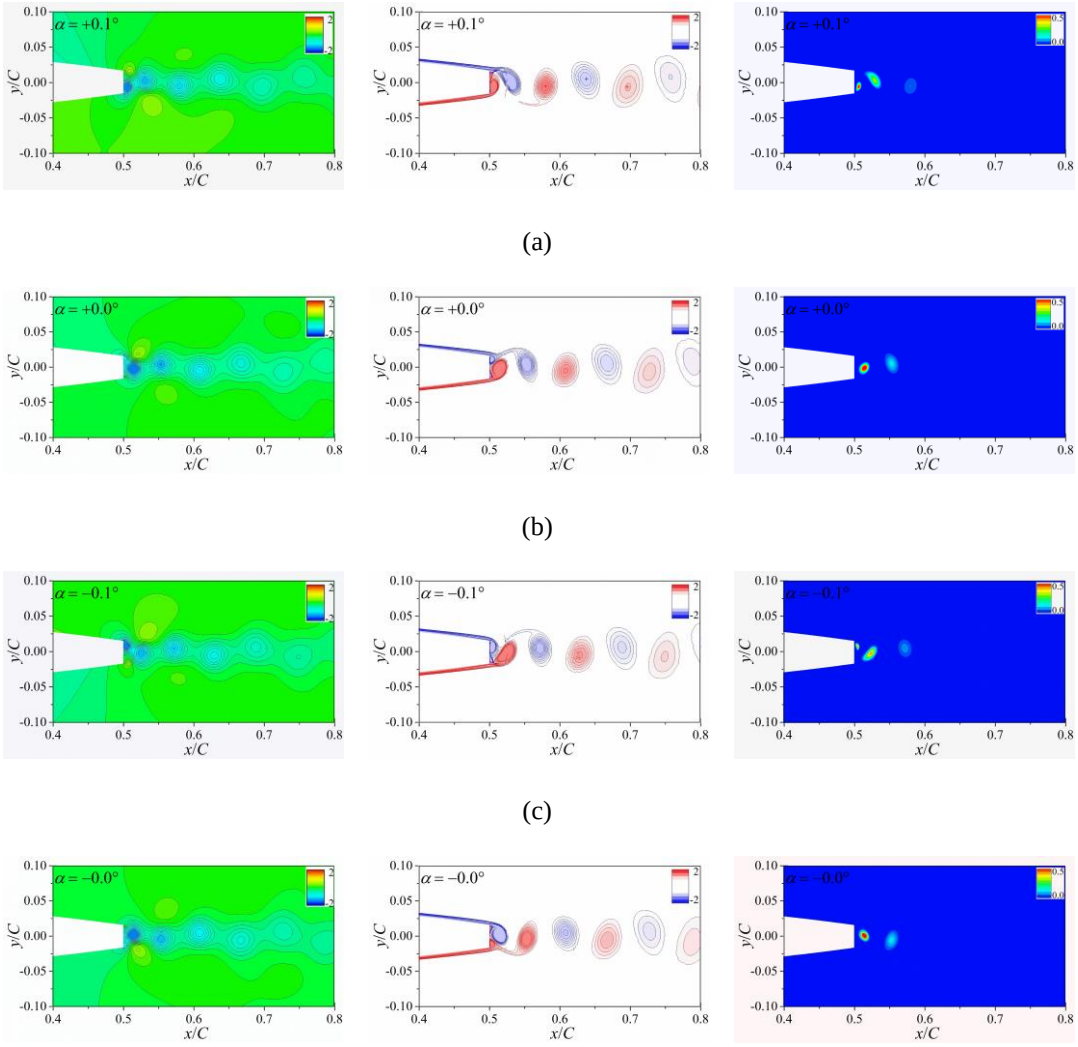

(a)

(b)

(c)

(d)

Fig. 9.8 Instantaneous C_p field (left), vorticity contours (middle), and vapor volume fraction contours (right) for an oscillating hydrofoil at f_{ex}/f_{sta_non}=1.0 and $\Delta\sigma$= 0.2: (a) t = 0, (b) t = 0.25 T_{ex}, (c) t = 0.5 T_{ex} and (d) t = 0.75 T_{ex}.

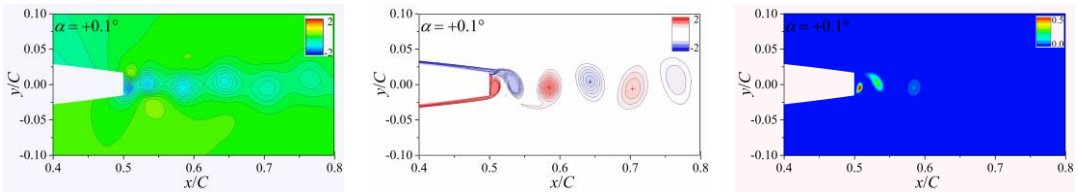

(a)

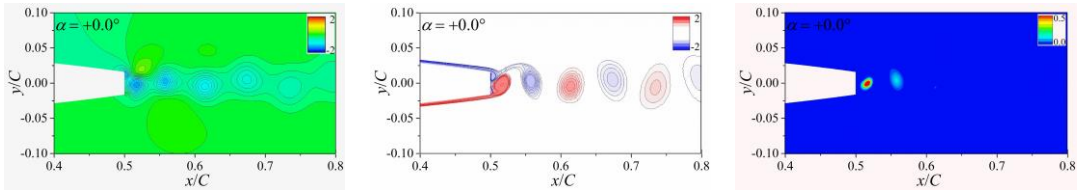

(b)

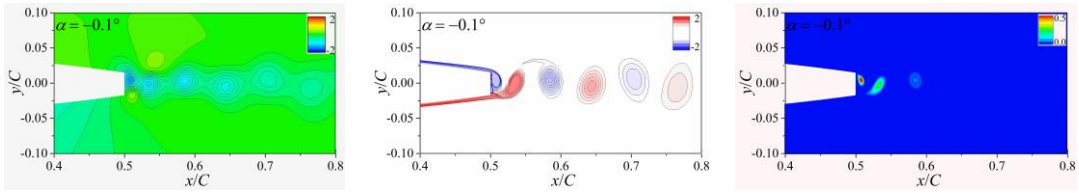

(c)

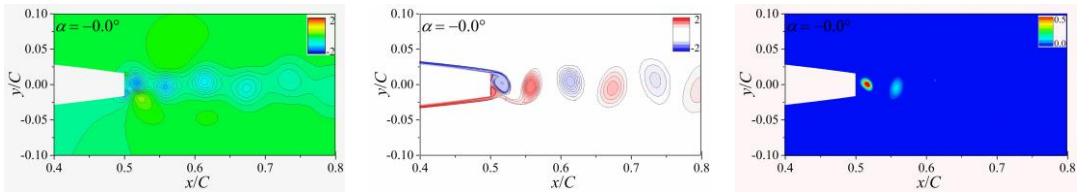

(d)

Fig. 9.9 Instantaneous C_p field (left), vorticity contours (middle), and vapor volume fraction contours (right) for an oscillating hydrofoil at f_{ex}/f_{sta_non}=1.0 and $\Delta\sigma$= 0.4: (a) t = 0, (b) t = 0.25 T_{ex}, (c) t = 0.5 T_{ex} and (d) t = 0.75 T_{ex}.

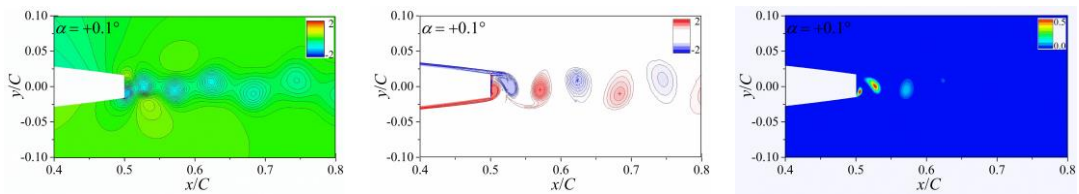

(a)

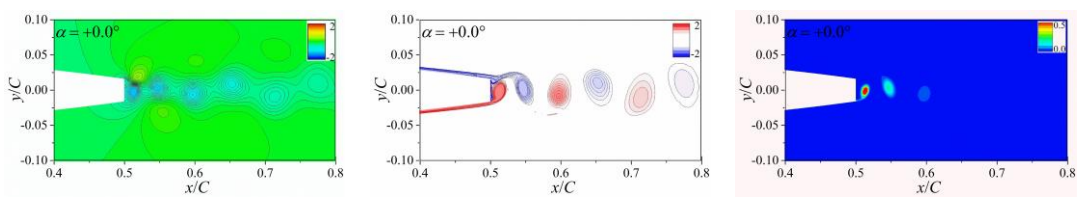

(b)

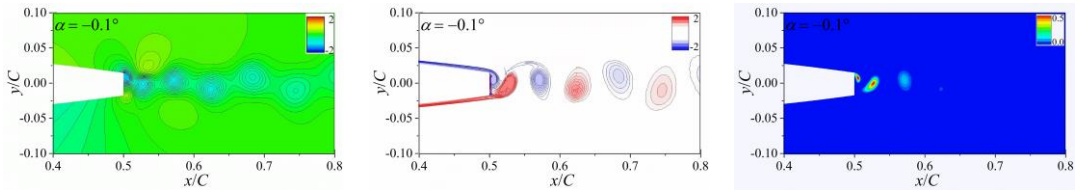

(c)

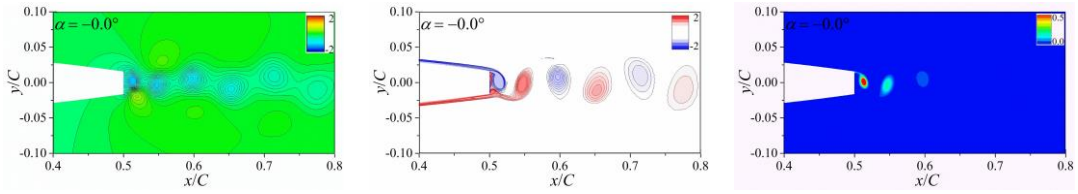

(d)

Fig. 9.10 Instantaneous C_p field (left), vorticity contours (middle), and vapor volume fraction contours (right) for an oscillating hydrofoil at f_{ex}/f_{sta_non}=1.0 and $\Delta\sigma$= 0.5: (a) t = 0, (b) t = 0.25 T_{ex}, (c) t = 0.5 T_{ex} and (d) t = 0.75 T_{ex}.

The associated C_M on the hydrofoil alongside the angle displacement, α, are plotted in Fig. 9.11. It can be seen that the time evolution of α does not align precisely with C_M, indicating a phase angle, φ, between them. Moreover, φ is observed to vary with changes in the cavitation number. In the non-cavitating regime, illustrated in Fig. 9.11(a), φ exhibits a positive value, indicating that C_M lags behind α. Conversely, in the cavitating regime, φ exhibits a negative value, suggesting that C_M moves ahead of α.

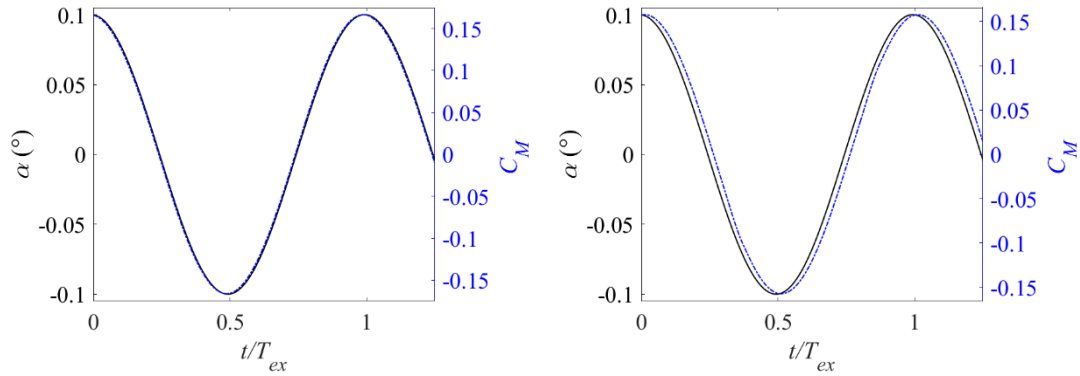

(a) (b)

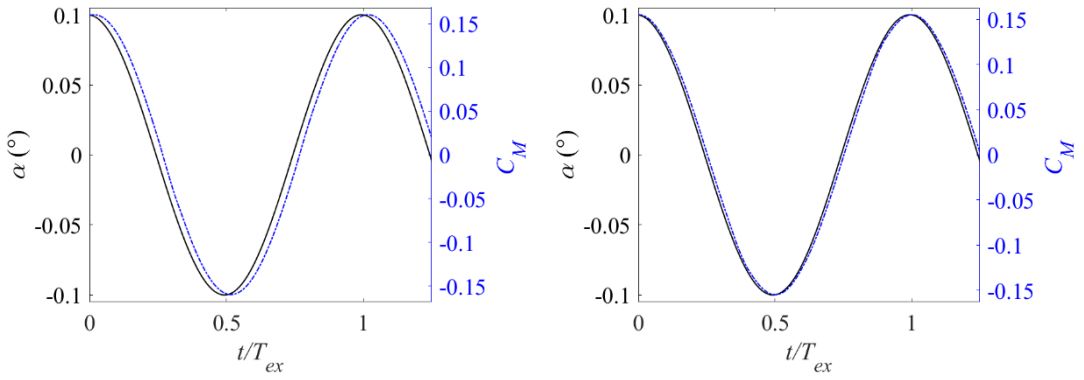

(c) (d)

Fig. 9.11 Time evolution of the hydrofoil angle displacement, α, and C_M at σ= 2.1 (a), $\Delta\sigma$= 0.2 (b), $\Delta\sigma$= 0.4 (c), and $\Delta\sigma$= 0.5 (d) with f_{ex}/f_{sta_non}=1.0.

To investigate the impacts of cavitation on the dynamic response of a blunt trailing edge hydrofoil undergoing forced oscillation, J_f, ζ_f, and φ were estimated for varying levels of cavitation development utilizing the projection method, and the results are summarized in Table 9.1. It is observed that in the presence of cavitation, J_f exhibits a decrease from 0.0024 to approximately 0.0022. However, the influence of decreasing σ on ζ_f and φ does not follow a monotonous trend. Specifically, as σ decreases from 2.1 to $\Delta\sigma$ =0.5, ζ_f increases from -0.50 to 3.11 (at $\Delta\sigma$ =0.4), subsequently it decreases to 1.19 ($\Delta\sigma$=0.5). Meanwhile, in terms of φ, it increases from 1.35 to 356.55, albeit with a minor decrease at $\Delta\sigma$= 0.4. In terms of C_M, the cavitating case exhibits a significant decrease compared to the non-cavitating regime. When $\Delta\sigma \leq 0.4$, the amplitudes of C_M tends to increase as cavitation number decreases. However, a further decrease in the cavitation number results in a decrease in the amplitudes of C_M.

Table 9.1 Comparison of J_f, ζ_f, φ, and C_M at f_{ex}/f_{sta_non}=1.0 with different cavitation development levels.

	J_f	ζ_f	φ(°)	C_M
σ= 2.1	0.0024	-0.50	1.35	0.1660
$\Delta\sigma$= 0.2	0.0022	2.48	352.91	0.1578
$\Delta\sigma$= 0.4	0.0022	3.11	351.26	0.1604
$\Delta\sigma$= 0.5	0.0022	1.19	356.55	0.1552

9.6 EFFECTS OF FORCED OSCILLATION FREQUENCY ON DYNAMIC RESPONSES

9.6.1 On response characteristics

Considering that the system is exposed to both the vortex shedding and the forced oscillation, the moment acting on the hydrofoil can be decomposed into these two frequencies. MATLAB®'s "curve fitter" tool was employed to extract these frequencies from the discrete-time moment history, and the outcomes have been visualized in Fig. 9.12 for both non-cavitating (σ= 2.1) and cavitating ($\Delta\sigma$= 0.5) regimes.

For the non-cavitating regime, as shown in Fig. 9.12(a), it can be seen that the system exhibits different response characteristics depending on the range of forced oscillation. The vortex shedding frequency, f_{vs}, is different than the forced oscillation frequency, f_{ex}, when $f_{ex}/f_{sta\_non} < 0.89$, which indicates the system is governed by two distinct excitation frequencies in the so-called lock-off condition. In addition, it is observed that with the increase of the forced oscillation frequency, there is a significant reduction in the vortex shedding frequency. For instance, the vortex shedding falls around 3.8% at f_{ex}/f_{sta_non} =0.8, compared to the vortex shedding frequency without forced oscillation. In the range where 0.89< f_{ex}/f_{sta_non} <1.07, f_{vs} is equal to f_{ex} and the lock-in condition occurs. After this point and for f_{ex}/f_{sta_non} >1.07, f_{vs} is no longer equal to f_{ex}, and the system returns to the lock-off condition again.

For the cavitating regime, shown in Fig. 9.12(b), f_{vs} is different than f_{ex} when f_{ex}/f_{sta_non} <0.89 in the lock-off condition. The increase of f_{ex}, the reduction of f_{vs} at the cavitating regime is more significant than the one at the non-cavitation regime. More specifically, the vortex shedding falls 11.1% at f_{ex}/f_{sta_non} =0.8, compared to f_{vs} without forced oscillation. Regarding the lock-in regime, it is observed that it is further extended in the range from 0.89 to 1.15, which means a 7.5% increase towards the upper bound of the lock-in regime in comparison without cavitation. With further increases of f_{ex} above f_{ex}/f_{sta_non} >1.15, the lock-off condition is again achieved.

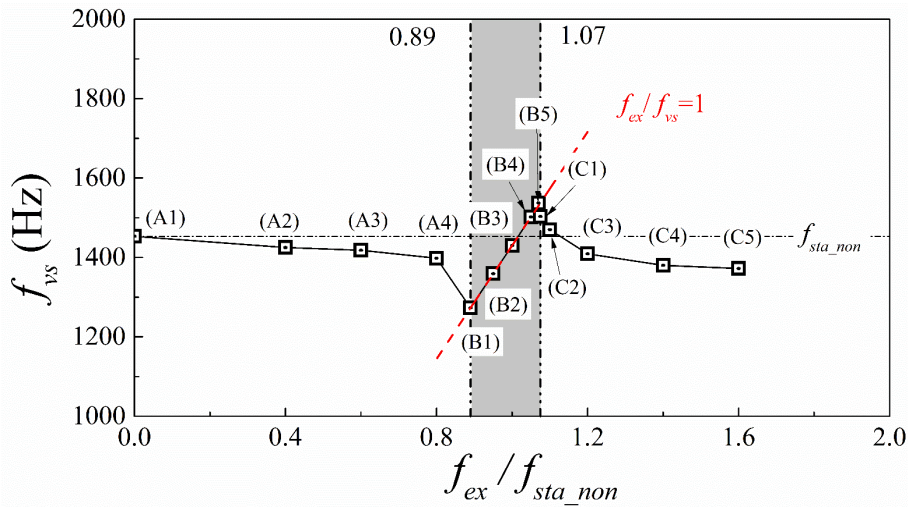

(a)

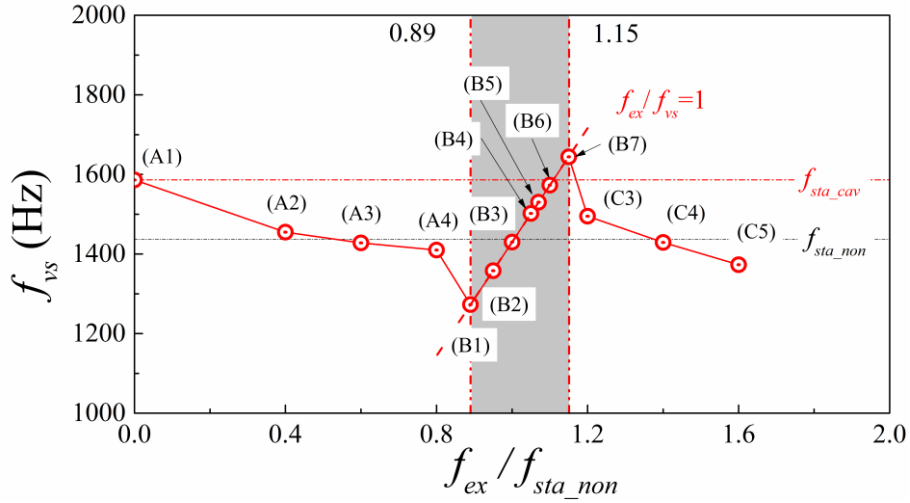

(b)

Fig. 9.12 Evolution of the vortex shedding frequency as a function of the forced oscillation frequency under the non-cavitating (a) and cavitating regimes (b).

9.6.2 On unsteady moment

Lock-off condition

Fig. 9.13 represents the dimensionless decomposed amplitudes of the fluid moment coefficient C_{M_f} and vortex-induced moment coefficient C_{M_vs} using MATLAB®'s "curve fitter" tool. For the non-cavitating regime, it can be seen that the behaviours of the amplitudes of C_{M_f} and C_{M_vs} depends on the range of forced oscillation. Furthermore, over the entire region of f_{ex}, the amplitude of C_{M_f} demonstrates a continuously increasing trend with the rise of f_{ex}/f_{sta_non}. In regions where the ratio f_{ex}/f_{sta_non} is less than 0.89, the amplitude of C_{M_vs} demonstrates a

decreasing trend with the rise of the ratio. Conversely, the amplitude of C_{M_vs} tends to decrease in regions where the ratio f_{ex}/f_{sta_non} is higher than 1.07.

For the cavitating regime, it is obvious that the behaviours of the amplitudes of the fluid moment C_{M_f} and vortex-induced moment C_{M_vs} depends on the variation of forced oscillation frequencies. Similar to the non-cavitating regime, the amplitude of the fluid moment C_{M_f} demonstrates a continuously increasing trend with the rise of f_{ex}/f_{sta_non}. Furthermore, in regions where the ratio is less than 0.89, the amplitude of the fluid moment C_{M_vs} demonstrates a decreasing trend with the rise of f_{ex}/f_{sta_non}, except at the point A(2) as present in Fig. 9.13(b). At that point, the amplitude of the fluid moment C_{M_vs} is notably lower compared to other points. Conversely, the amplitude of the fluid moment C_{M_vs} tends to decrease in regions where the ratio is higher than 1.15.

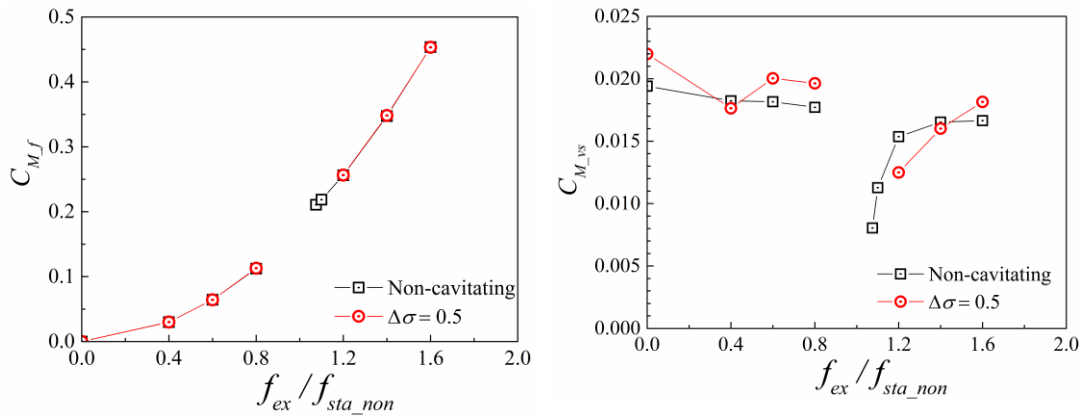

(a) (b)

Fig. 9.13 The amplitudes of the fluid moment C_{M_f} (a) and vortex-induced moment C_{M_vs} (b) at non-cavitating (σ= 2.1) and $\Delta\sigma$= 0.5 using the fitting tool of MATLAB®.

Lock-in condition

Under lock-in conditions, the time histories of C_M and α over one cycle of forced oscillation at non-cavitating and cavitating regimes are plotted in Fig. 9.14 and 9.15, respectively. Additionally, the associated amplitudes of C_M and phase angle φ are plotted against the forced oscillation frequencies in Fig. 9.16 and Fig. 9.17, respectively.

It can be seen that, in both regimes, the amplitude of C_M exhibits a continuously increasing trend with the increase of f_{ex}. Specifically, for the non-cavitating regime,

C_M increases from 0.13 at f_{ex}/f_{sta_non}=0.89 to 0.21 at f_{ex}/f_{sta_non}=1.07. For the cavitating regime, C_M increases from 0.13 at f_{ex}/f_{sta_non} =0.89 to 0.18 at f_{ex}/f_{sta_non}=1.07 and further approximates 0.23 at f_{ex}/f_{sta_non}=1.15. It is indicated that the presence of cavitation induces a reduction in the amplitude of C_M within the lock-in regime, except at the point f_{ex}/f_{sta_non}=0.95. Furthermore, the jump of φ has shifted from f_{ex}/f_{sta_non}=0.95 to 1.1 due to the cavitation. Thus, cavitation serves as a factor that leads to a decrease in the amplitude of C_M and an increase in φ within the lock-in regime.

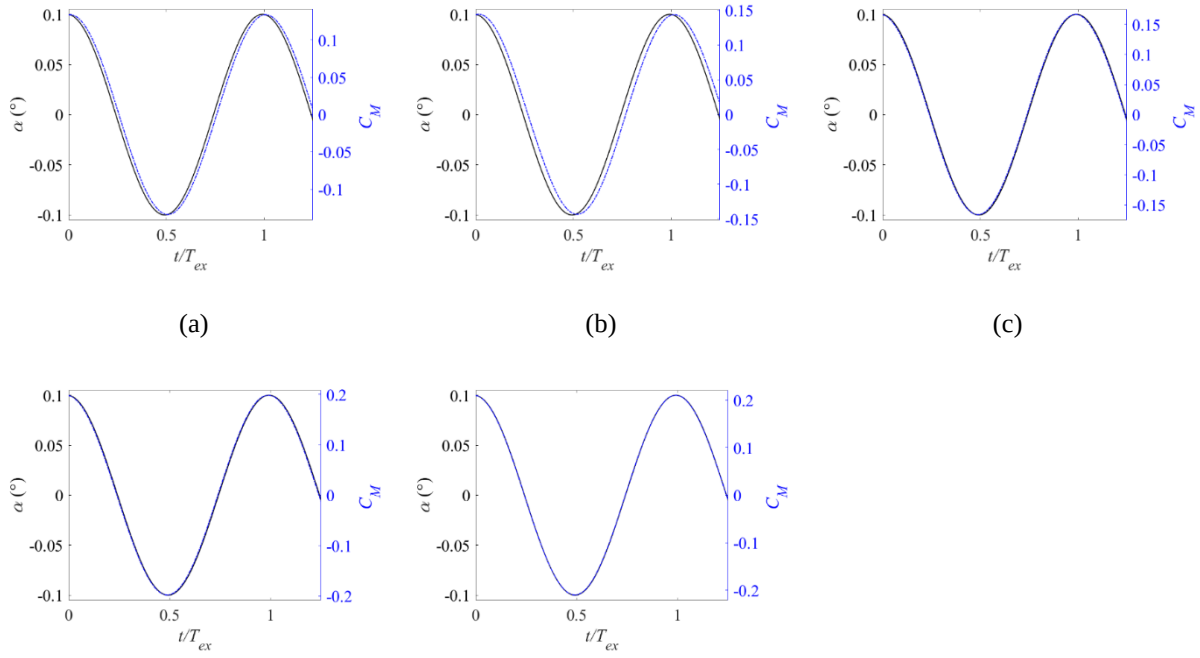

(a) (b) (c)

(d) (e)

Fig. 9.14 The time histories of the incidence and the numerical obtained hydrodynamic torque at non-cavitating regime (σ= 2.1) and different f_{ex}/f_{sta_non}: (a) B1 0.89; (b) B2 0.95; (c) B3 1.0; (d) B4 1.05; (e) B5 1.07.

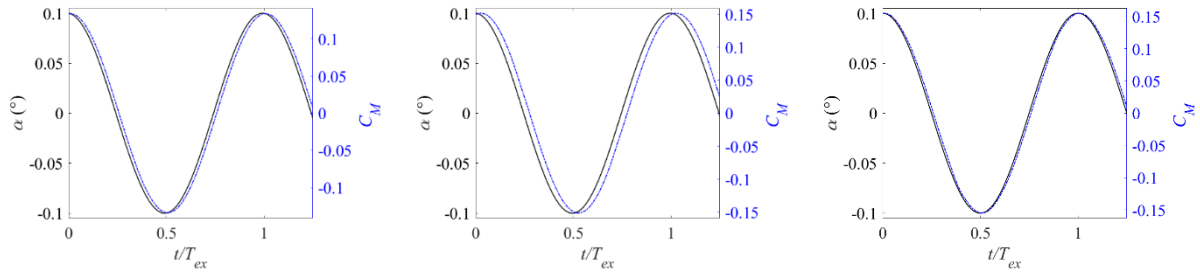

(a) (b) (c)

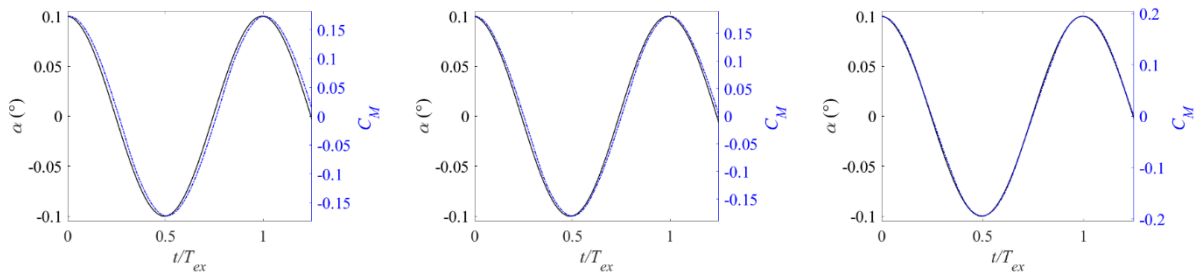

(d) (e) (f)

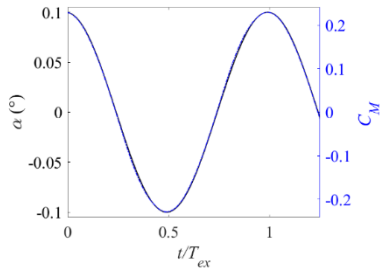

(g)

Fig. 9.15 The time histories of the incidence and the numerical obtained hydrodynamic torque at cavitating regime ($\Delta\sigma$=0.5) and different f_{ex}/f_{sta_non} : (a) B1 0.89; (b) B2 0.95; (c) B3 1.0; (d) B4 1.05; (e) B5 1.07; (f) B6 1.10; (g) B6 1.15.

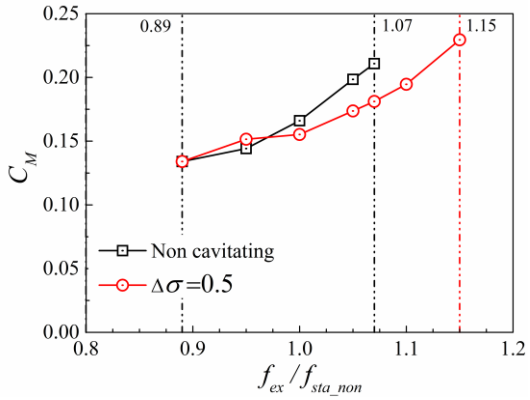

Fig. 9.16 The amplitudes of C_M at the non-cavitating and cavitating regimes.

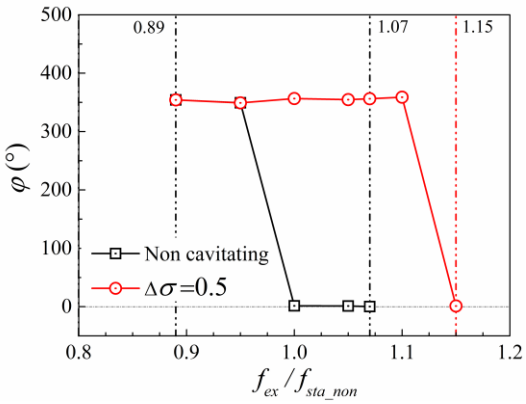

Fig. 9.17 The relationship between the phase angle φ and the forced oscillation frequency f_{ex}/f_{sta_non} at the non-cavitating and cavitating regimes.

9.6.3 On added properties

Fig. 9.18 shows the response characteristics corresponding to J_f, ζ_f, and φ as a function of the oscillating frequency for both the non-cavitating and the cavitating regimes, respectively.

In the non-cavitating regimes (Fig. 9.18(a)), as f_{ex}/f_{sta_non} increases to 0.95, J_f gradually decreases to the minimum value of 0.0022. Conversely, as f_{ex}/f_{sta_non} increases to 1.07, J_f progressively increases to the maximum value of 0.0026. Moreover, a slight decay in J_f is observed as f_{ex}/f_{sta_non} further increases. On the other hand, in the cavitating regimes (Fig. 8.18(a)), as f_{ex}/f_{sta_non} increases to 1.0, J_f continuously decreases to the minimum value of 0.0022. Then, as f_{ex}/f_{sta_non} increases to 1.07, J_f maintains the same value and further increases in f_{ex}/f_{sta_non} provokes an increase in J_f. Comparing the curves of J_f in non-cavitating and cavitation regimes, it can be seen that these two curves fall on the same one, indicating the insensitivity of J_f to the presence of the cavitation for the lock-off condition (f_{ex}/f_{sta_non}<0.89 and f_{ex}/f_{sta_non}>1.15). Within the cavitating lock-in condition (0.89<f_{ex}/f_{sta_non}<1.15), the obtained J_f in the non-cavitating regime is higher than the one in the cavitating regime except at f_{ex}/f_{sta_non}= 0.95, suggesting the reduction in J_f due to the presence of cavitation. It is believed that the increase of J_f at f_{ex}/f_{sta_non}= 0.95 may result from the increase of C_M, as shown in Fig. 9.16.

In the non-cavitating regimes (Fig. 9.18(b)), as f_{ex}/f_{sta_non} increases to 0.95, ζ_f gradually increase to the maximum value of 3.6. Within this range, a slight decrease

in ζ_f is observed at the lower limit of the lock-in regime at f_{ex}/f_{sta_non} =0.89. Subsequently, a transition in ζ_f from the positive to the negative is observed during the range 0.95< f_{ex}/f_{sta_non} <1.0. Moreover, ζ_f increases as f_{ex}/f_{sta_non} further increases. In the cavitating regimes (Fig. 9.18(b)), as f_{ex}/f_{sta_non} increases to 0.95, ζ_f gradually increase to the maximum value of 3.9. Then, as f_{ex}/f_{sta_non} increases to 1.15, a general decreasing trend in ζ_f is observed with a slight increase in μ_f is observed near f_{ex}/f_{sta_non}=1.05. Correspondingly, a transition in ζ_f from the positive to the negative is observed during the range 1.10<f_{ex}/f_{sta_non}<1.15. Moreover, ζ_f increases as f_{ex}/f_{sta_non} further increases. Comparing the curves of ζ_f in non-cavitating and cavitation regimes, it can be seen that the cavitation effects on the ζ_f is complex and varies across different frequency ranges. At the lock-off condition, specifically at f_{ex}/f_{sta_non}=0.4, 1.4, and 1.6, cavitation results in a reduction in ζ_f. However, in the range from 0.8 to 1.2, a general increasing trend in ζ_f is observed in the presence of cavitation. Furthermore, the presence of cavitation leads to an increase in f_{ex}/f_{sta_non} where the transition of ζ_f from the positive to the negative sign occurs, shifting from 0.95 to 1.1.

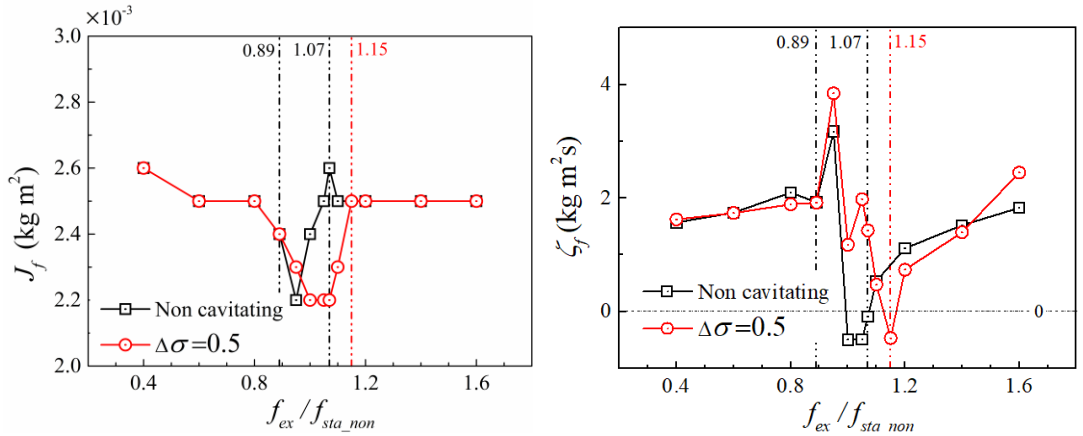

(a) (b)

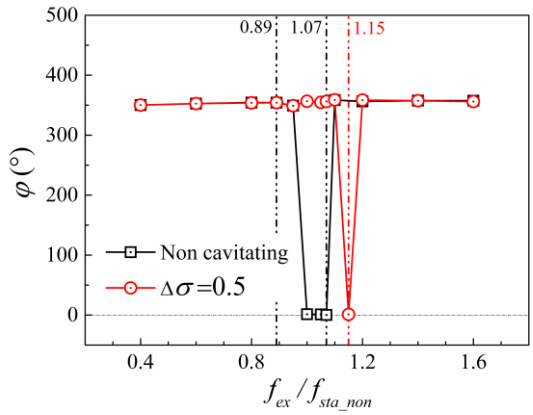

(c)

Fig. 9.18 The comparison of J_f (a), ζ_f(b), and φ(c) as a function of f_{ex}/f_{sta_non} at the non-cavitating regime and $\Delta\sigma$= 0.5.

In the non-cavitating regimes (Fig. 9.18(c)), φ maintains a negative value within $1.0 < f_{ex}/f_{sta\_non} < 1.07$ and the transition of φ from positive to negative sign occurs between $0.95 < f_{ex}/f_{sta\_non} < 1.00$. In the cavitating regimes (Fig. 9.18(c)), a negative value of φ is observed at f_{ex}/f_{sta_non}=1.15, and the transition of φ from the positive to the negative sign occurs between $1.10 < f_{ex}/f_{sta\_non} < 1.15$. Hence, the increase in f_{ex}/f_{sta_non} where the transition of φ from positive to negative sign occurs aligns with the findings for ζ_f in the presence of cavitation.

9.6.4 On the pressure and vorticity fields

In terms of vortical structures, it can be seen that two different modes of vortex shedding occur in the non-cavitation lock-in regime. To demonstrate these two modes, the pressure field and vorticity fields are plotted in Fig. 9.19 when it moves to the maximum displacement angle. At the beginning of the lock-in range, e.g., f_{ex}/f_{sta_non} =0.89 and 0.95, the vortex formed on the lower side of the hydrofoil starts to shed and the associated minimum pressure is located at the shedding vortex as well. However, as f_{ex}/f_{sta_non} further increases, e.g., f_{ex}/f_{sta_non}=1.0 and 1.07, the vortex formed on the upper side of the hydrofoil is shed. Such change in the timing of shed vortical structures has also been observed in the wakes of circular cylinders subjected to forced oscillations (Hassanpour et al., 2023) or inlet velocity perturbations (Gauthier et al., 2017).

In cavitating lock-in, a similar behavior also occurs: as shown in Fig. 9.20, from $f_{ex}/f_{sta\_non} = 0.89$ to 1.1, the vortex formed on the upper side of the hydrofoil is

shed. Meanwhile, at $f_{ex}/f_{sta\_non} = 1.15$, the vortex formed on the lower side of the hydrofoil is shed when the hydrofoil is near its minimum pitching angle.

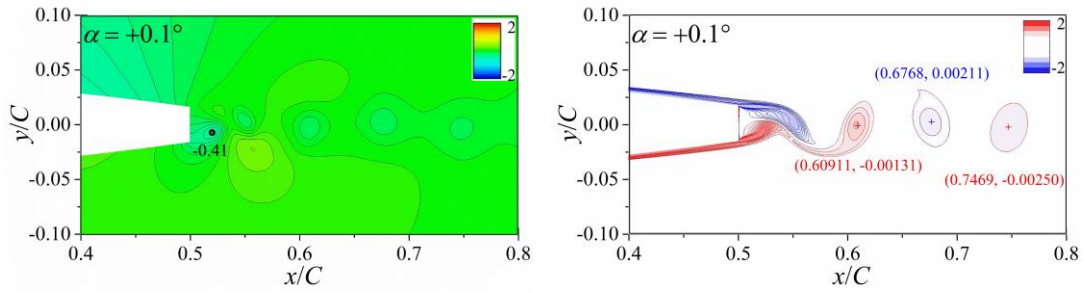

(a)

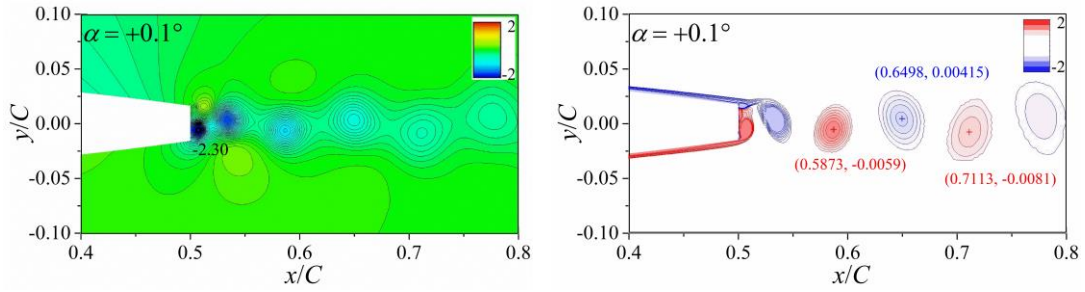

(b)

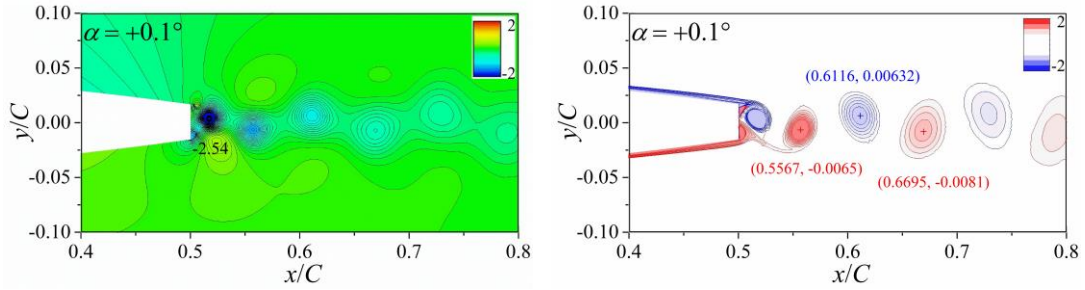

(c)

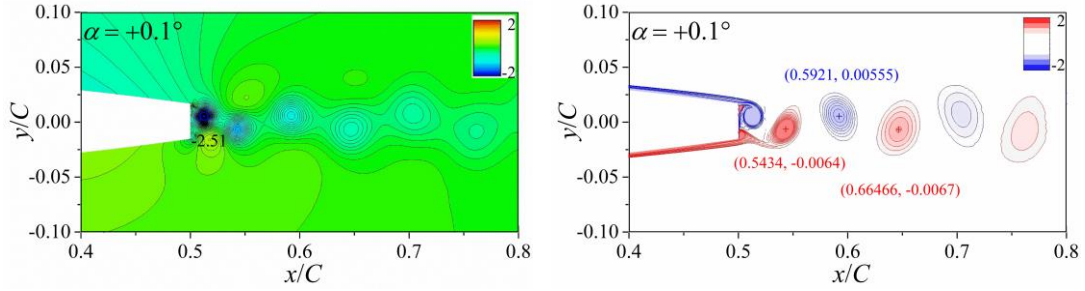

(d)

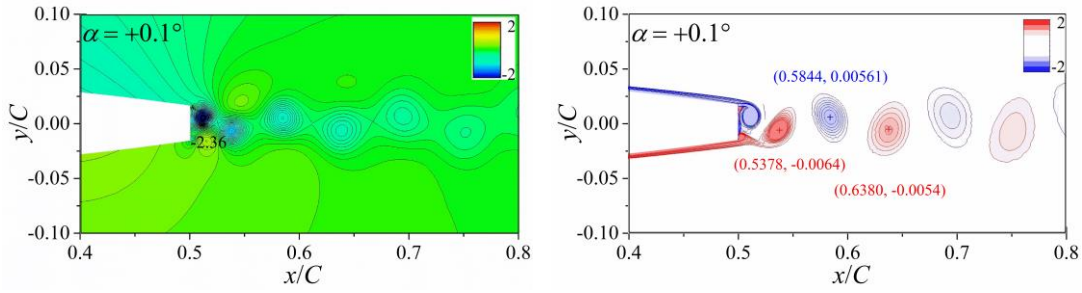

(e)

Fig. 9.19 Instantaneous C_p field (left), vorticity contours (right) for an oscillating hydrofoil at non-cavitating regime with different f_{ex}/f_{sta_non}: (a)0.89; (b)0.95; (c)1.00; (d)1.05; (e)1.07.

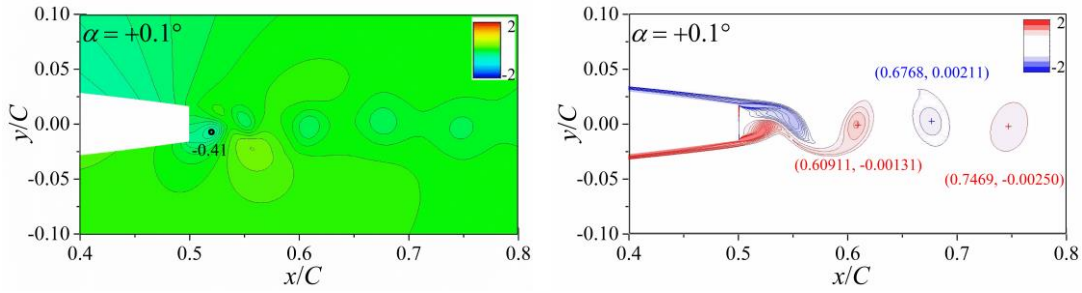

(a)

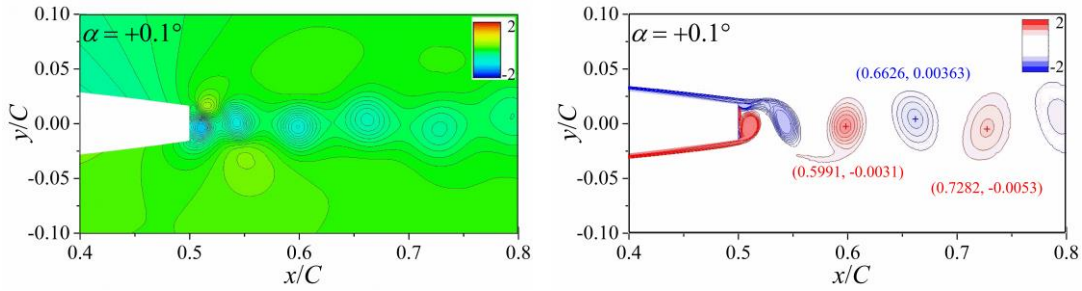

(b)

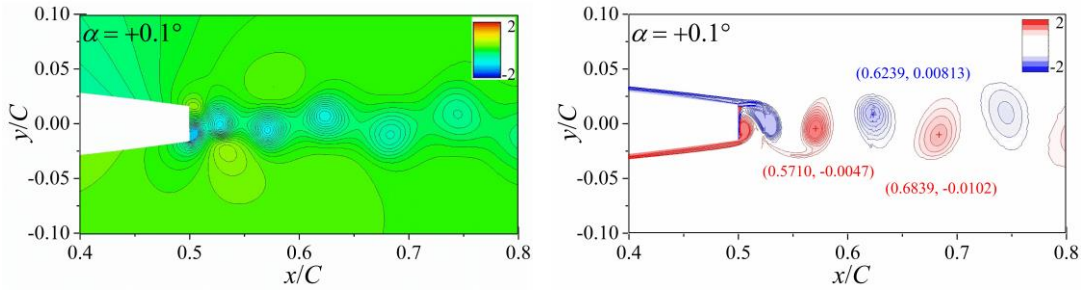

(c)

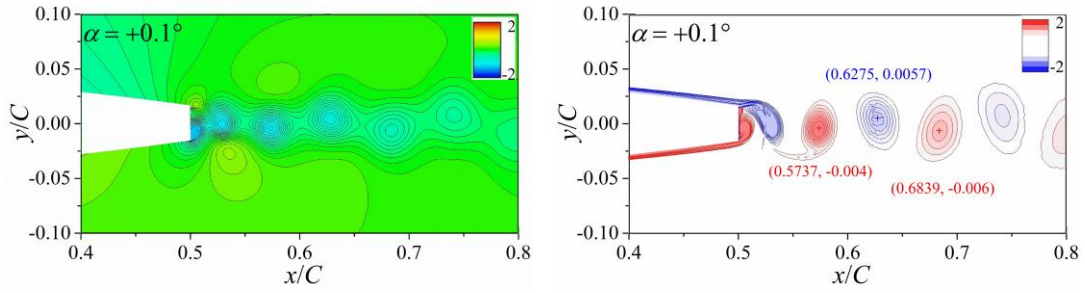

(d)

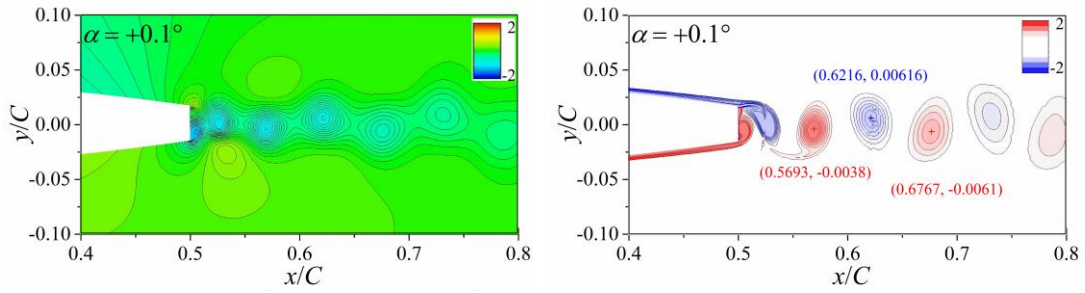

(e)

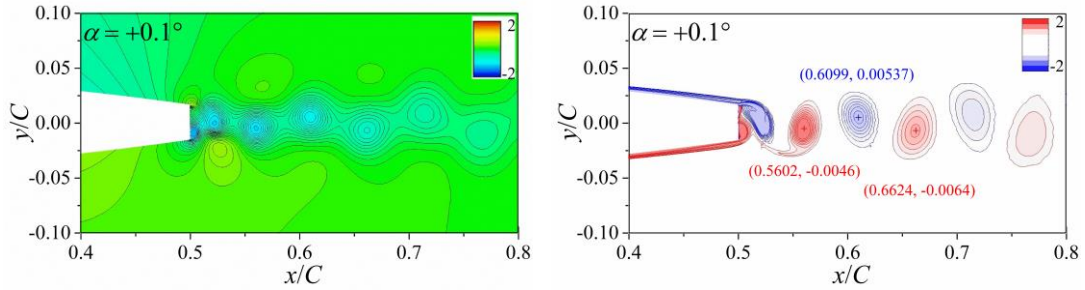

(f)

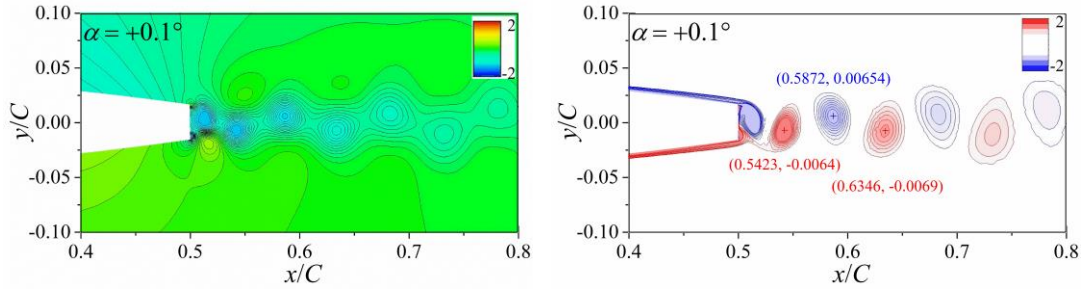

(g)

Fig. 9.20 Instantaneous C_p field (left), vorticity contours (right) for an oscillating hydrofoil at non-cavitating regime with different f_{ex}/f_{sta_non}: (a)0.89; (b)0.95; (c)1.00; (d)1.05; (e)1.07; (f)1.10; (g)1.15;

9.7 EFFECTS OF FORCED OSCILLATION ON CAVITATION

9.7.1 On cavitation inception

Assuming that the liquid water cannot withstand any tension and vapor appears instantaneously when the local pressure drops below the saturated pressure p_v, then the relationship between the minimum pressure coefficient, $C_{p\,min}$, and cavitation inception number, σ_i, is established as follows:

$$\sigma_i = C_{p\,min} \tag{9.15}$$

In Fig. 9.21, the obtained $C_{p\,min}$ are plotted against f_{ex}/f_{sta_non} under the non-cavitating regime. It reveals a non-monotonic relationship as the $C_{p\,min}$ does not consistently decrease with the increase of f_{ex}/f_{sta_non}. Specifically, $C_{p\,min}$ decrease from -1.65 at f_{ex}/f_{sta_non}=0.0 to -3.60 at f_{ex}/f_{sta_non}=1.4 and then follows a slight increase at f_{ex}/f_{sta_non}=1.6, meanwhile, as f_{ex}/f_{sta_non} approaches the boundaries of the lock-in regime, it causes a decrease in $C_{p\,min}$ and the local maxima of $C_{p\,min}$ are found at f_{ex}/f_{sta_non}=0.89 and f_{ex}/f_{sta_non}=1.07, corresponding to the boundaries of the lock-in regime.

Interestingly, at the lower boundary of the lock-in regime (f_{ex}/f_{sta_non}=0.89), $C_{p\,min}$ approaches the maxima of -0.67, significantly higher the value of $C_{p\,min}$ at the stationary condition. Consequently, the oscillation frequency of f_{ex}/f_{sta_non}=0.89 tends to decrease σ_i.

Conversely, at the upper bound of the lock-in regime (f_{ex}/f_{sta_non}=1.07), $C_{p\,min}$ approaches the maxima of -2.36, lower than the value of $C_{p\,min}$ at the stationary condition. Thus, compared to the stationary condition, the oscillation frequency of f_{ex}/f_{sta_non}=1.07 tends to increase σ_i.

Therefore, it can be concluded that the oscillation frequency of the hydrofoil can affect the cavitation inception. While the general trend is for σ_i to gradually increase with the increase of f_{ex}/f_{sta_non}, as the forced oscillation frequency approaches the boundary of the lock-in regime, it causes a local decrease in σ_i. Particularly, at the lower boundary of the lock-in regime, a significant decrease in σ_i is observed compared to the stationary hydrofoil.

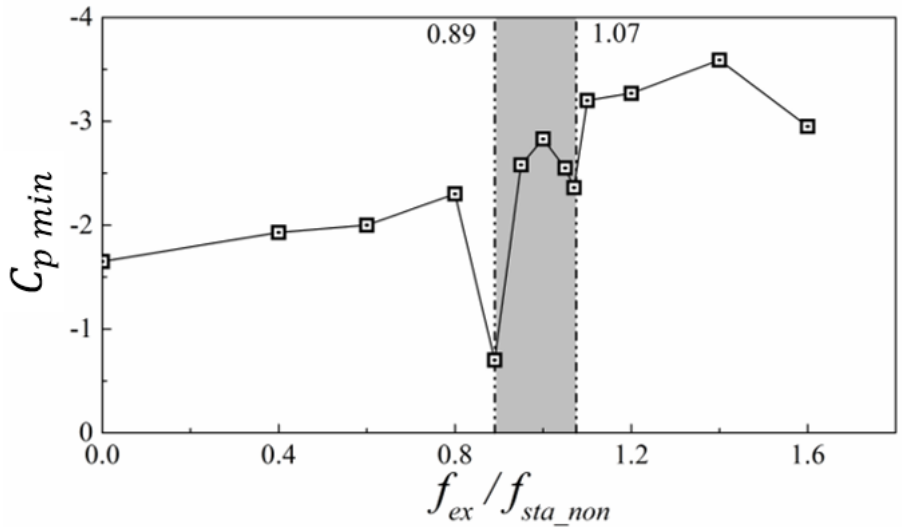

Fig. 9.21 The $C_{p\ min}$ in the computational domain as a function of f_{ex}/f_{sta_non}.

9.7.2 On developed cavitation

Fig. 9.22 presents the contours of vapor volume fraction behind the trailing edge at different f_{ex}/f_{sta_non}. When f_{ex}/f_{sta_non}<0.89, the corresponding contours are displayed ranging from point (A1) to (A4). It can be seen that the length of the cavitating wake monotonically decreases with the increase of f_{ex}/f_{sta_non}.

When 0.89< f_{ex}/f_{sta_non} <1.15, the corresponding contours are displayed ranging from point (B1) to (B7). It is observed that, at the beginning of the lock-in regime, e.g., f_{ex}/f_{sta_non}=0.89, the vapor cavity does not appear inside the wake which explains why the lower bound of the lock-in regime does not change when cavitation occurs. At f_{ex}/f_{sta_non}=0.95, the presence of cavitation inside the vortical structures within the wake is again observed. For further increase of f_{ex}/f_{sta_non}, the length of cavitating wakes monotonically increases as shown in points (B3)~(B7). Furthermore, when f_{ex}/f_{sta_non} >1.15, a shrink of the cavitating wake length is observed as shown in points (C3)~ (C5).

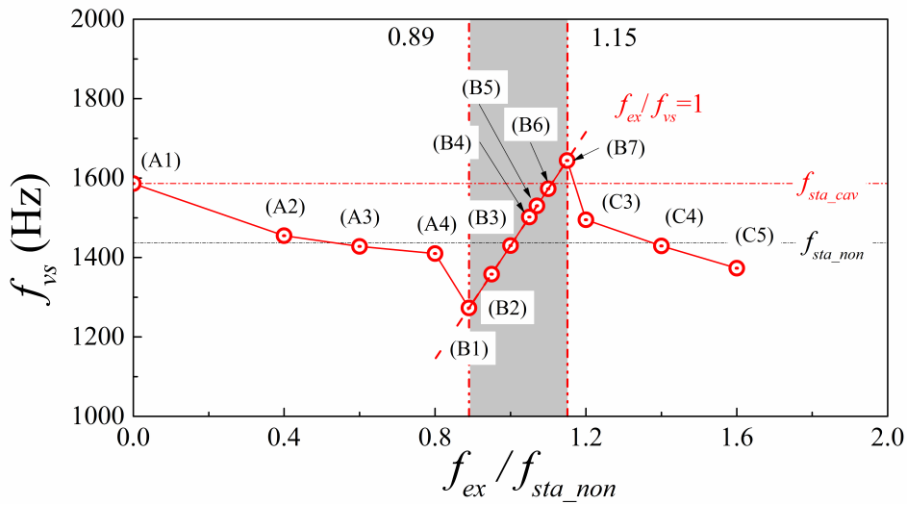

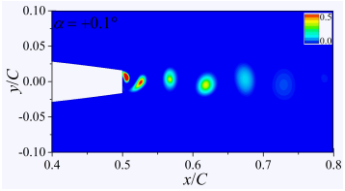

(A1)

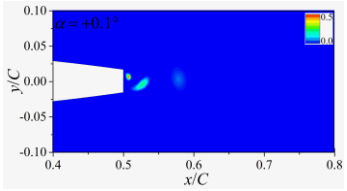

(A2)

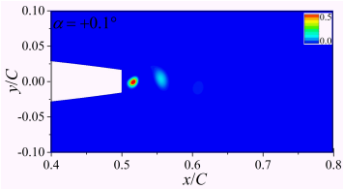

(A3)

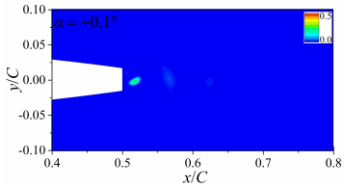

(A4)

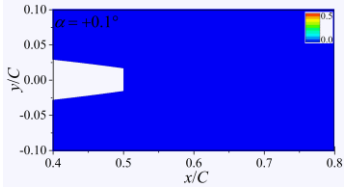

(B1)

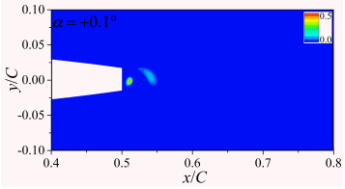

(B2)

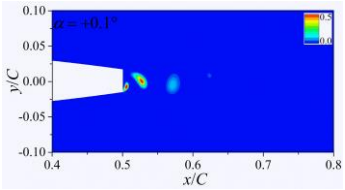

(B3)

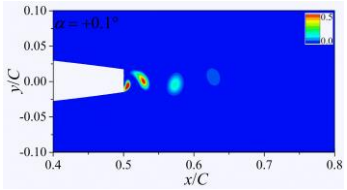

(B4)

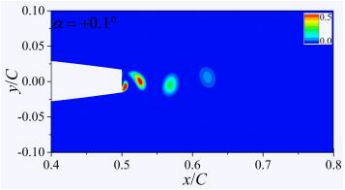

(B5)

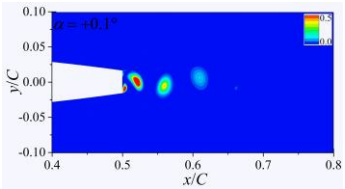

(B6)

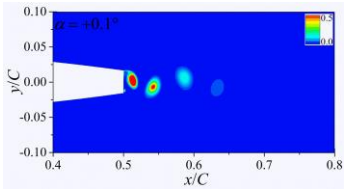

(B7)

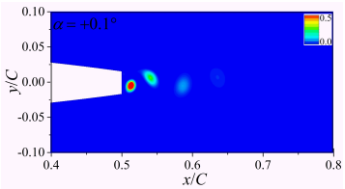

(C3)

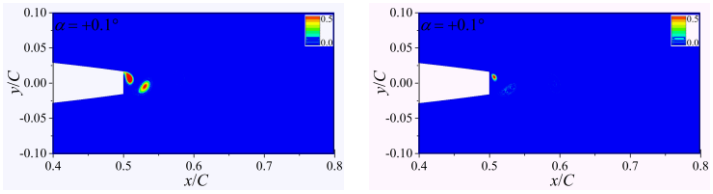

(C4) (C5)

Fig. 9.22 Vapor volume fraction contours in the near wake at different values of f_{ex}/f_{sta_non}.

9.8 PARTIAL CONCLUSIONS

In this chapter, a numerical study on the interactions between the vortex shedding behind a blunt trailing edge hydrofoil NACA 0009, the cavitation development, and the oscillation frequency of the hydrofoil has been conducted. The observations and results can be summarized as follows:

Regarding the effects of cavitation when the excitation frequency, f_{ex}, is equal to the vortex shedding frequency behind the hydrofoil under non-cavitating and stationary conditions, f_{sta_non}, in the lock-in regime:

- In comparison to the non-cavitating regime, cavitation generally decreases the moment coefficient, C_M. As cavitation occurs, the increase or decrease of C_M depends on the cavitation development. Specifically, before the cavitation number exceeds a certain threshold, the development of cavitation leads to C_M decreases. Conversely, as the cavitation number decreases further, C_M decreases. Similarly, relative to the non-cavitating regime, cavitation provokes an increase in the phase angle between the momentum and the force oscillation, φ. As cavitation occurs, the increase or decrease in φ depends on the cavitation development. When the cavitation number is above a certain value, φ experiences a reduction as the cavitation number decreases. However, as the cavitation number decreases further, it causes an increase in φ.
- For the added properties, the obtained added moment of inertia, J_f, is independent of the cavitation number. Compared to the non-cavitating regime, cavitation generally increases the added damping, ζ_f. However, as cavitation occurs, the increase or decrease of ζ_f depends on the cavitation development. When the cavitation number is above a certain value, the development of cavitation results

in a significant increase of ζ_f. As the cavitation number further decreases, it leads to a drop of ζ_f.

Regarding the effects of f_{ex} on dynamic response:

- The overall dynamic response of the system, e.g. during the lock-in and lock-off regimes, is primarily determined by the variation of f_{ex}/f_{sta_non} while also being influenced by the presence of cavitation. Specifically, concerning the bounds of the lock-in regime, the upper bound tends to increase with the presence of cavitation compared to the non-cavitating condition.
- At the lock-off regime, the fluid moment coefficient, C_{M_f}, is insensitive to the development of cavitation. However, the components of the vortex-induced moment coefficient, C_{M_vs}, general decreases as f_{ex}/f_{sta_non} gets closer to the bounds of the lock-in regime. At the lock-in regime, cavitation can lead to a decrease in C_M and an increase in φ.
- In the lock-off regime, the cavitation effect on J_f is small and it can be neglected. However, the cavitation on ζ_f depends on both f_{ex}/f_{sta_non} and the presence of cavitation. At the lock-in regime, cavitation can provoke a decrease of J_f and an increase of ζ_f.
- The change in the timing of shed vortices has been observed in both non-cavitating and cavitating wakes. However, the presence of cavitation tends to increase the value of f_{ex}/f_{sta_non} at which the change occurs. Under the non-cavitating regime, the change in the timing of shed vortices occurs at f_{ex}/f_{sta_non}=1.0. Conversely, it increases to f_{ex}/f_{sta_non}=1.15 under cavitating conditions.

Regarding the effects of f_{ex} on vortex street cavitation:

- f_{ex} can indeed influence the cavitation inception level, σ_i, which in general exhibits a gradual increase as f_{ex}/f_{sta_non} increases. Moreover, as f_{ex} approaches the bounds of the lock-in regime, it causes a local decrease in σ_i. In particular, at its lower bound, σ_i decreases to a level that prevents the occurrence of cavitation.
- The length of the cavitating wake is affected by the variation of f_{ex}. Specifically, the maximum cavitating wake length appears at the stationary condition. Then, it gradually decreases as f_{ex}/f_{sta_non} increases and vanishes at the lower bound of

the lock-in regime when f_{ex}/f_{sta_non} =0.89. From this oscillating frequency onwards throughout the lock-in regime, the length of the cavitating wake monotonically increases as f_{ex}/f_{sta_non} increases. After that, it experiences a slight decrease with further increases in f_{ex}/f_{sta_non}.

Part IV

Chapter 10: Conclusions

In the present thesis, a numerical solver has been developed that is capable of accounting for the cavitating vortex street flow behind bluff bodies. Using this solver, a series of numerical studies on cavitating vortex street flow behind a blunt trailing edge hydrofoil NACA 0009 have been conducted by predicting the boundary layer transition. As a result, the effects of cavitation on flow dynamics and its interaction with vortex-induced vibration have been examined.

The implementation of the incompressible cavitation solver has been validated and verified using a 2D bubble collapse case. The solver has successfully captured the evolution of the bubble collapse and it has shown the dependency of the predictions on the empirical condensation coefficient. Additionally, a compressible cavitation solver with suitable boundary conditions has been developed and validated using two benchmark test cases: a 1D shock tube and a 2D bubble collapse. Furthermore, the results obtained with the compressible cavitation model have been compared with previously published data of the cavitating vortex shedding flow behind a circular cylinder. In summary, all the results have confirmed the capability of the proposed compressible cavitation solver to simulate cavitating flows with consideration of fluid compressibility.

Using the validated incompressible and compressible cavitation solvers, the influence of fluid compressibility on the cavitating vortex street flow has been examined numerically. A comparison has been made between simulations obtained using the incompressible and the compressible cavitation solvers for cavitating vortex street flow over a wedge. The results have shown that the impact of fluid compressibility on the dynamics of the cavitating wake flow depends on the frequency range: at lower frequencies, the effects of fluid compressibility are minimal and can be disregarded. However, fluid compressibility has been observed to amplify spectral energy at higher frequencies. Furthermore, almost identical numerical results with and without consideration of liquid compressibility have been obtained in terms of predicted mean pressure profiles, dominant vortex shedding frequencies, and instantaneous and mean void fraction fields. Consequently, these results suggest that

compressibility effects on cavitating vortex shedding behind a wedge are relatively small and can be neglected.

More specifically, a comprehensive and detailed numerical study of the cavitating vortex street flow over a truncated hydrofoil NACA 0009 has been conducted focusing on boundary layer transition, vortex street dynamics, and cavitation effects. High-fidelity numerical simulations have been performed using a controlled decay SST γ-$Re_{\theta t}$ turbulence model with optimized inlet turbulence intensity and empirical coefficients for the cavitation model. It has been observed that cavitation has a significant impact on the wake flow dynamics, notably increasing the shedding frequency of the primary vortices. Additionally, cavitation growth leads to increased hydrodynamic loads on the hydrofoil surface. Furthermore, cavitation development enhances the advected velocity of the vortices while decreasing the streamwise inter-vortex spacing. Both factors are believed to contribute to the increase of the vortex shedding frequency while the reduction of streamwise inter-vortex spacing tends to dominate this increase.

Additionally, a series of numerical simulations have been conducted to analyze the cavitating vortex street flow over a blunt trailing edge hydrofoil NACA 0009 under forced oscillation at different frequencies. It has been observed that the dynamic response to the oscillating frequency is influenced by the presence of cavitation. In the lock-in regime, cavitation appears to widen the upper bound of this regime. When compared to non-cavitating conditions, the dynamic response of the blunt trailing edge hydrofoil shows a decrease in the added moment of inertia and an increase in the added damping with the presence of cavitation. Moreover, the timing of the vortex shedding will change with the presence of cavitation.

Lastly, it has been observed that the oscillation of the hydrofoil affects the dynamics of cavitation within the shed vortices. Specifically, the oscillation frequency of the hydrofoil influences cavitation inception. Generally, the cavitation inception number gradually increases with the forced oscillation frequency. It is noted that as the oscillating frequency approaches the bounds of the lock-in regime, there are local decreases in cavitation inception number. In particular, the maximum decrease in cavitation inception number is observed at the lower bound of the lock-in regime where it prevents the cavitation occurrence. Besides, the length of the cavitating wake

is influenced by the variation of the oscillation frequency, and the maximum cavitating wake length occurs under stationary conditions.

Chapter 11: Perspectives

In the present work, the significant effects of wake cavitation on the characteristics of the vortex street in terms of shedding frequency, unsteady loads, and morphology have been numerically identified and investigated in blunt trailing edge hydrofoils. Moreover, the study has numerically explored the interactions between cavitation and VIVs. However, due to the complexity of this problem, there are some issues which should be more deeply investigated in the near future:

(i) Regarding the numerical modelling:

Indeed, the capability of the numerical model to capture how vortex shedding frequency depends on cavitation and boundary layer transition is crucial for accurately predicting such flow. Therefore, the accuracy of the simulations relies heavily on the performance of both the cavitation model for predicting the advected cavitating flow and the turbulence model for predicting the boundary layer transition. Due to the limited computational resources, the controlled decay SST γ-$Re_{\theta t}$ model has been used in the current study. However, owing to the inherent disadvantages of RANS models, very limited information about the wake has been obtained. Moreover, reproducing the vortex span-wise organization and dislocation is another important issue for predicting the unsteady loads acting on the hydrofoil which requires more advanced 3D turbulence models. Therefore, the understanding of this problem could be improved by employing scale-resolved models, e.g. DES γ-$Re_{\theta t}$ or wall-resolved LES. Concerning the modeling of cavitation, the interaction between the cavitation and the advected vortices needs to be considered. Until now, the accuracy of the cavitating wake flow prediction depends heavily on user experiences, such as the selection of the cavitation models and the empirical factors inside the source term accounting for the mass transition. Future investigations should focus on developing a free-parameter cavitation model that could reduce or remove the dependence on empirical factors selected by user experience.

(ii) Regarding the interaction between cavitation and VIVs:

The interaction between cavitation and VIVs is very complex. Specifically, the presence of cavitation is found to modify the added properties, e.g. added moment of

inertia and fluid damping, and the loads acting on the solid body. Moreover, the presence of cavitation can also affect the state of the VIVs and may widen the lock-in regime. On the other hand, the oscillation of the body can alter the occurrence and development of cavitation in terms of cavitation inception and morphology. Note that, the current study is based on two-dimensional simulations neglecting the the vortex span-wise organization and dislocation. Therefore, to further assess the interaction between cavitation and VIVs, a 3D simulation with more advanced turbulence and cavitation models needs to be conducted.

(iii) Regarding the assessment of the control method:

In practical applications, either VIVs or cavitation can cause tremendous damage to engineering structures and the interaction between them can alter the characteristics of the fluid-structure system. Both passive and active control methods have been undertaken to mitigate wake flow and reduce load fluctuations. Optimizing trailing edge geometry constitutes a passive control method, whereas flow blowing, suction, and ventilation fall under the active control category. However, a predominant focus of these control methods has been centered on minimizing drag penalties, with comparatively less attention being paid to assessing their impact on the occurrence and development of cavitation. Thanks to the good performance of the numerical model used in this study in simulating the cavitating vortex street flow, this high-fidelity numerical approach could be very useful to comprehensively evaluate the performance of wake control methods with consideration of cavitation.

References

Achenbach, E. (1968). Distribution of local pressure and skin friction around a circular cylinder in cross-flow up to Re = 5 × 106. *Journal of Fluid Mechanics*, *34*(4), 625–639. https://doi.org/10.1017/S0022112068002120

Agarwal, K., Ram, O., Lu, Y., & Katz, J. (2023). On the pressure field, nuclei dynamics and their relation to cavitation inception in a turbulent shear layer. *Journal of Fluid Mechanics*, *966*, A31. https://doi.org/10.1017/jfm.2023.368

Akcabay, D. T., Chae, E. J., Young, Y. L., Ducoin, A., & Astolfi, J. A. (2014). Cavity induced vibration of flexible hydrofoils. *Journal of Fluids and Structures*, *49*, 463–484. https://doi.org/10.1016/j.jfluidstructs.2014.05.007

Arndt, R. E. A. (1976). Semiempirical analysis of cavitation in the wake of a sharp-edged disk. *Journal of Fluids Engineering*, *98*(3), 560–562. https://doi.org/10.1115/1.3448395

Arndt, R. E. A. (1981). Cavitation in fluid machinery and hydraulic structures. *Annual Review of Fluid Mechanics*, *13*(1), 273–326.

Arndt, R. E. A., & Keller, A. P. (1992). Water quality effects on cavitation inception in a trailing vortex. *Journal of Fluids Engineering*, *114*(3), 430–438. https://doi.org/10.1115/1.2910049

Ausoni, P. (2009). *Turbulent vortex shedding from a blunt trailing edge hydrofoil*. École Polytechnique Fédérale de Lausanne.

Ausoni, P., Farhat, M., Escaler, X., Egusquiza, E., & Avellan, F. (2007). Cavitation influence on von Kármán vortex shedding and induced hydrofoil vibrations. *Journal of Fluids Engineering*, *129*, 966–973.

Babajee, J., & Arts, T. (2012). Investigation of the laminar separation-Induced transition with the γ-Reθt transition model on low-pressure turbine rotor blades at steady conditions. *ASME Turbo Expo 2012: Turbine Technical Conference and Exposition*, 1167–1178. https://doi.org/10.1115/GT2012-68687

Belahadji, B., Franc, J. P., & Michel, J. M. (1995). Cavitation in the rotational structures of a turbulent wake. *Journal of Fluid Mechanics*, *287*, 383–403.

Benaouicha, M., & Astolfi, J.-A. (2012). Analysis of added mass in cavitating flow. *Journal of Fluids and Structures*, *31*, 30–48. https://doi.org/10.1016/j.jfluidstructs.2012.03.003

Bhatt, A., Ganesh, H., & Ceccio, S. L. (2023). Partial cavity shedding on a hydrofoil resulting from re-entrant flow and bubbly shock waves. *Journal of Fluid Mechanics*, *957*, A28.

Bhatt, M., Gnanaskandan, A., & Mahesh, K. (2015). Evaluation of finite rate homogenous mixture model in cavitation bubble collapse. *Journal of Physics: Conference Series*, *656*, 012136. https://doi.org/10.1088/1742-6596/656/1/012136

Blevins, R. D., & Scanlan, R. H. (1977). Flow-induced vibration. *Journal of Applied Mechanics*, *44*(4), 802. https://doi.org/10.1115/1.3424205

Bodony, D. J. (2006). Analysis of sponge zones for computational fluid mechanics. *Journal of Computational Physics*, *212*(2), 681–702. https://doi.org/10.1016/j.jcp.2005.07.014

Brandao, F. L., Bhatt, M., & Mahesh, K. (2020). Numerical study of cavitation regimes in flow over a circular cylinder. *Journal of Fluid Mechanics*, *885*, A19. https://doi.org/10.1017/jfm.2019.971

Brandao, F. L., & Mahesh, K. (2022). Large-eddy simulation of cavitation inception in a shear flow. *International Journal of Multiphase Flow*, *146*, 103865. https://doi.org/10.1016/j.ijmultiphaseflow.2021.103865

Braza, M., Chassaing, P., & Minh, H. H. (1986). Numerical study and physical analysis of the pressure and velocity fields in the near wake of a circular cylinder. *Journal of Fluid Mechanics*, *165*, 79–130. https://doi.org/10.1017/S0022112086003014

Brennen, C. E. (2014). *Cavitation and bubble dynamics*. Cambridge university press.

Brunhart, M., Soteriou, C., Gavaises, M., Karathanassis, I., Koukouvinis, P., Jahangir, S., & Poelma, C. (2020). Investigation of cavitation and vapor shedding mechanisms in a Venturi nozzle. *Physics of Fluids*, *32*(8), 083306. https://doi.org/10.1063/5.0015487

Budich, B., Schmidt, S. J., & Adams, N. A. (2018). Numerical simulation and analysis of condensation shocks in cavitating flow. *Journal of Fluid Mechanics*, *838*, 759–813. https://doi.org/10.1017/jfm.2017.882

Cakmakcioglu, S. C., Bas, O., Mura, R., & Kaynak, U. (2020). A revised one-equation transitional model for external aerodynamics. *AIAA*, *7*. https://doi.org/10.2514/6.2020-2706

Callenaere, M., Franc, J. P., Michel, J. M., & Riondet, M. (2001). The cavitation instability induced by the development of a re-entrant jet. *Journal of Fluid Mechanics*, *444*, 223–256.

Chen, J., Li, Y. J., & Liu, Z. Q. (2018). Large eddy simulation of boundary layer transition flow around NACA0009 blunt trailing edge hydrofoil at high Reynolds number. *IOP Conference Series: Earth and Environmental Science*, *163*(1), 012044. https://doi.org/10.1088/1755-1315/163/1/012044

Cheng, H., Long, X., Ji, B., Peng, X., & Farhat, M. (2021). A new Euler-Lagrangian cavitation model for tip-vortex cavitation with the effect of non-condensable gas. *International Journal of Multiphase Flow*, *134*, 103441. https://doi.org/10.1016/j.ijmultiphaseflow.2020.103441

Choi, H., Jeon, W.-P., & Kim, J. (2008). Control of flow over a bluff body. *Annual Review of Fluid Mechanics*, *40*(2008), 113–139. https://doi.org/10.1146/annurev.fluid.39.050905.110149

Choi, H., & Moin, P. (2012). Grid-point requirements for large eddy simulation: Chapman's estimates revisited. *Physics of Fluids*, *24*(1), 011702. https://doi.org/10.1063/1.3676783

Choi, J., & Ceccio, S. L. (2007). Dynamics and noise emission of vortex cavitation bubbles. *Journal of Fluid Mechanics*, *575*, 1–26. https://doi.org/10.1017/S0022112006003776

Choi, J., Hsiao, C.-T., Chahine, G., & Ceccio, S. (2009). Growth, oscillation and collapse of vortex cavitation bubbles. *Journal of Fluid Mechanics*, *624*, 255–279. https://doi.org/10.1017/S0022112008005430

Coutier-Delgosha, O., Reboud, J. L., & Delannoy, Y. (2003). Numerical simulation of the unsteady behaviour of cavitating flows. *International Journal for Numerical Methods in Fluids*, *42*(5), 527–548. https://doi.org/10.1002/fld.530

Coutu, A., Proulx, D., & Coulson, S. (2003). Dynamic assessment of hydraulic turbines. *Water Power XIII*, 1–10.

De La Torre, O., Escaler, X., Egusquiza, E., & Farhat, M. (2013). Experimental investigation of added mass effects on a hydrofoil under cavitation conditions. *Journal of Fluids and Structures*, *39*, 173–187. https://doi.org/10.1016/j.jfluidstructs.2013.01.008

De La Torre, O., Escaler, X., Egusquiza, E., & Farhat, M. (2014). Numerical and experimental study of a nearby solid boundary and partial submergence effects on hydrofoil added mass. *Computers & Fluids*, *91*, 1–9. https://doi.org/10.1016/j.compfluid.2013.12.003

Decaix, J., Dreyer, M., Balarac, G., Farhat, M., & Münch, C. (2018). RANS computations of a confined cavitating tip-leakage vortex. *European Journal of Mechanics - B/Fluids*, *67*, 198–210. https://doi.org/10.1016/j.euromechflu.2017.09.004

Dehkharqani, A. S., Aidanpää, J.-O., Engström, F., & Cervantes, M. J. (2019). A review of available methods for the assessment of fluid added mass, damping, and stiffness with an emphasis on hydraulic turbines. *Applied Mechanics Reviews*, *70*(050801). https://doi.org/10.1115/1.4042279

Deshpande, M., Feng, J., & Merkle, C. L. (1997). Numerical modeling of the thermodynamic effects of cavitation. *Journal of Fluids Engineering*, *119*(2), 420–427. https://doi.org/10.1115/1.2819150

Ding, H., Shu, C., Yeo, K. S., & Xu, D. (2007). Numerical simulation of flows around two circular cylinders by mesh-free least square-based finite difference methods. *International Journal for Numerical Methods in Fluids*, *53*(2), 305–332. https://doi.org/10.1002/fld.1281

Donaldson, R. M. (1956). Hydraulic-turbine runner vibration. *Transactions of the American Society of Mechanical Engineers*, *78*(5), 1141–1144. https://doi.org/10.1115/1.4013957

Ducoin, A., Young, Y. L., & Sigrist, J. F. (2011). Hydroelastic responses of a flexible hydrofoil in turbulent, cavitating flow. *ASME 2010 3rd Joint US-European Fluids Engineering Summer Meeting Collocated with 8th International Conference on Nanochannels, Microchannels, and Minichannels*, 493–502. https://doi.org/10.1115/FEDSM-ICNMM2010-30310

Egerer, C. P., Hickel, S., Schmidt, S. J., & Adams, N. A. (2014). Large-eddy simulation of turbulent cavitating flow in a micro channel. *Physics of Fluids*, *26*(8), 085102. https://doi.org/10.1063/1.4891325

Egerer, C. P., Schmidt, S. J., Hickel, S., & Adams, N. A. (2016). Efficient implicit LES method for the simulation of turbulent cavitating flows. *Journal of Computational Physics*, *316*, 453–469. https://doi.org/10.1016/j.jcp.2016.04.021

Foeth, E. J., van Terwisga, T., & van Doorne, C. (2008). On the collapse structure of an attached cavity on a three-dimensional hydrofoil. *Journal of Fluids Engineering*, *130*(071303). https://doi.org/10.1115/1.2928345

Folden, T. S., & Aschmoneit, F. J. (2023). A classification and review of cavitation models with an emphasis on physical aspects of cavitation. *Physics of Fluids*, *35*(8), 081301. https://doi.org/10.1063/5.0157926

Franc, J. P., & Michel, J. M. (2006). *Fundamentals of cavitation*. Springer science & Business media.

Ganesh, H., Mäkiharju, S. A., & Ceccio, S. L. (2016). Bubbly shock propagation as a mechanism for sheet-to-cloud transition of partial cavities. *Journal of Fluid Mechanics*, *802*, 37–78.

Gauthier, J. P., Giroux, A. M., Etienne, S., & Gosselin, F. P. (2017). A numerical method for the determination of flow-induced damping in hydroelectric turbines. *Journal of Fluids and Structures*, *69*, 341–354. https://doi.org/10.1016/j.jfluidstructs.2017.01.004

Geng, L., & Escaler, X. (2020). Assessment of RANS turbulence models and Zwart cavitation model empirical coefficients for the simulation of unsteady cloud cavitation. *Engineering Applications of Computational Fluid Mechanics*, *14*(1), 151–167. https://doi.org/10.1080/19942060.2019.1694996

Georgiadis, N. J., Rizzetta, D. P., & Fureby, C. (2010). Large-eddy simulation: Current capabilities, recommended practices, and future research. *AIAA Journal*, *48*(8), 1772–1784. https://doi.org/10.2514/1.J050232

Germano, M., Piomelli, U., Moin, P., & Cabot, W. H. (1991). A dynamic subgrid-scale eddy viscosity model. *Physics of Fluids A: Fluid Dynamics*, *3*(7), 1760–1765. https://doi.org/10.1063/1.857955

Gerrard, J. H. (1961). An experimental investigation of the oscillating lift and drag of a circular cylinder shedding turbulent vortices. *Journal of Fluid Mechanics*, *11*(2), 244–256. https://doi.org/10.1017/S0022112061000494

Ghahramani, E. (2018). *A Realizable Hybrid Mixture-Bubble Model for Cavitating Flows*. Chalmers University of Technology.

Ghahramani, E., Arabnejad, M. H., & Bensow, R. E. (2018). Realizability improvements to a hybrid mixture-bubble model for simulation of cavitating flows. *Computers & Fluids*, *174*, 135–143. https://doi.org/10.1016/j.compfluid.2018.06.025

Ghahramani, E., Arabnejad, M. H., & Bensow, R. E. (2019). A comparative study between numerical methods in simulation of cavitating bubbles. *International Journal of Multiphase Flow*, *111*, 339–359. https://doi.org/10.1016/j.ijmultiphaseflow.2018.10.010

Ghahramani, E., Ström, H., & Bensow, R. E. (2021). Numerical simulation and analysis of multi-scale cavitating flows. *Journal of Fluid Mechanics*, *922*, A22. https://doi.org/10.1017/jfm.2021.424

Gill, J. R., Fattah, R. J., & Zhang, X. (2015). *Evaluation and Development of Non-Reflective Boundary Conditions for Aeroacoustic Simulations*. 2677. https://doi.org/10.2514/6.2015-2677

Gnanaskandan, A., & Mahesh, K. (2016a). Large Eddy Simulation of the transition from sheet to cloud cavitation over a wedge. *International Journal of Multiphase Flow*, *83*, 86–102. https://doi.org/10.1016/j.ijmultiphaseflow.2016.03.015

Gnanaskandan, A., & Mahesh, K. (2016b). Numerical investigation of near-wake characteristics of cavitating flow over a circular cylinder. *Journal of Fluid Mechanics*, *790*, 453–491. https://doi.org/10.1017/jfm.2016.19

Graftieaux, L., Michard, M., & Grosjean, N. (2001). Combining PIV, POD and vortex identification algorithms for the study of unsteady turbulent swirling flows. *Measurement Science and Technology*, *12*, 1422. https://doi.org/10.1088/0957-0233/12/9/307

Gummer, J. H., & Hensman, P. C. (1992). A review of stay vane cracking in hydraulic turbines. *International Water Power & Dam Construction*, *44*(1), 32–42.

Haller, G. (2015). Lagrangian coherent structures. *Annual Review of Fluid Mechanics*, *47*(2015), 137–162. https://doi.org/10.1146/annurev-fluid-010313-141322

Haller, G., & Yuan, G. (2000). Lagrangian coherent structures and mixing in two-dimensional turbulence. *Physica D: Nonlinear Phenomena*, *147*(3), 352–370. https://doi.org/10.1016/S0167-2789(00)00142-1

Harichandan, A. B., & Roy, A. (2012). Numerical investigation of flow past single and tandem cylindrical bodies in the vicinity of a plane wall. *Journal of Fluids and Structures*, *33*, 19–43. https://doi.org/10.1016/j.jfluidstructs.2012.04.006

Hassanpour, M., Morton, C., & Martinuzzi, R. J. (2023). Relationship between wake and cylinder dynamics for a cylinder undergoing modulated vortex-induced vibrations. *Physics of Fluids*, *35*(12), 123602. https://doi.org/10.1063/5.0174172

Hong, S., & Son, G. (2021). Numerical simulation of cavitating flows around an oscillating circular cylinder. *Ocean Engineering*, *226*, 108739. https://doi.org/10.1016/j.oceaneng.2021.108739

Hsiao, C.-T., Ma, J., & Chahine, G. L. (2017). Multiscale tow-phase flow modeling of sheet and cloud cavitation. *International Journal of Multiphase Flow*, *90*, 102–117. https://doi.org/10.1016/j.ijmultiphaseflow.2016.12.007

Hu, J., Li, X., Zhu, J., Ning, X., Wan, Q., & Lin, C. (2023). Effect of cavitation on fluid-structure interaction of a cantilever hydrofoil. *Ocean Engineering*, *288*, 116025. https://doi.org/10.1016/j.oceaneng.2023.116025

Hu, J., Wang, Z., Chen, C., & Guo, C. (2020). Vortex shedding simulation of hydrofoils with trailing-edge truncation. *Ocean Engineering*, *214*, 107529. https://doi.org/10.1016/j.oceaneng.2020.107529

Huang, B., Ducoin, A., & Young, Y. L. (2013). Physical and numerical investigation of cavitating flows around a pitching hydrofoil. *Physics of Fluids*, *25*(10), 102109. https://doi.org/10.1063/1.4825156

Huang, C., Borthwick, A. G. L., & Lin, Z. (2022). Lagrangian coherent structures in flow past a backward-facing step. *Journal of Fluid Mechanics*, *947*, A4. https://doi.org/10.1017/jfm.2022.631

Huang, Y., & Green, M. A. (2015). Detection and tracking of vortex phenomena using Lagrangian coherent structures. *Experiments in Fluids*, *56*(7), 147. https://doi.org/10.1007/s00348-015-2001-z

Hunt, J. C. R. (1987). *Vorticity and vortex dynamics in complex turbulent flows*. *11*, 21–35. https://doi.org/10.1139/tcsme-1987-0004

Iyer, C. O., & Ceccio, S. L. (2002). The influence of developed cavitation on the flow of a turbulent shear layer. *Physics of Fluids*, *14*(10), 3414–3431. https://doi.org/10.1063/1.1501541

Jeong, J., & Hussain, F. (1995). On the identification of a vortex. *Journal of Fluid Mechanics*, *285*, 69–94. https://doi.org/10.1017/S0022112095000462

Ji, B., Luo, X., Arndt, R. E. A., & Wu, Y. (2014). Numerical simulation of three dimensional cavitation shedding dynamics with special emphasis on cavitation–vortex interaction. *Ocean Engineering*, *87*, 64–77. https://doi.org/10.1016/j.oceaneng.2014.05.005

Jones, L. E., Sandberg, R. D., & Sandham, N. D. (2008). Direct numerical simulations of forced and unforced separation bubbles on an airfoil at incidence. *Journal of Fluid Mechanics*, *602*, 175–207. https://doi.org/10.1017/S0022112008000864

Kashyap, S. R., & Jaiman, R. K. (2023). Unsteady cavitation dynamics and frequency lock-in of a freely vibrating hydrofoil at high Reynolds number. *International Journal of Multiphase Flow*, *158*, 104276. https://doi.org/10.1016/j.ijmultiphaseflow.2022.104276

Katz, J. (1984). Cavitation phenomena within regions of flow separation. *Journal of Fluid Mechanics*, *140*, 397–436. https://doi.org/10.1017/S0022112084000665

Kawanami, Y., Kato, H., Yamaguchi, H., Tanimura, M., & Tagaya, Y. (1997). Mechanism and control of cloud cavitation. *Journal of Fluids Engineering*, *119*(4), 778–794. https://doi.org/10.1115/1.2819499

Kim, I. (2019). Separated rows structure of vortex streets behind triangular objects. *Journal of Fluid Mechanics*, *862*, 216–226. https://doi.org/10.1017/jfm.2018.993

Kim, J., Jeong, S., & Ahn, B. (2019). Numerical and experimental study on unsteady behavior of cavitating flow around a two-dimensional wedge-shaped body. *Journal of Marine Science and Technology*, *24*(4), 1256–1264. https://doi.org/10.1007/s00773-019-00623-6

Kim, K. H., & Choi, J. I. (2019). Lock-in regions of laminar flows over a streamwise oscillating circular cylinder. *Journal of Fluid Mechanics*, *858*, 315–351. https://doi.org/10.1017/jfm.2018.787

Knapp, R. T. (1955). Recent investigations of the mechanics of cavitation and cavitation damage. *Transactions of the American Society of Mechanical Engineers*, *77*(7), 1045–1054. https://doi.org/10.1115/1.4014586

Koukouvinis, P., Gavaises, M., Supponen, O., & Farhat, M. (2016). Simulation of bubble expansion and collapse in the vicinity of a free surface. *Physics of Fluids*, *28*(5), 052103. https://doi.org/10.1063/1.4949354

Kubota, A., Kato, H., & Yamaguchi, H. (1992). A new modelling of cavitating flows: A numerical study of unsteady cavitation on a hydrofoil section. *Journal of Fluid Mechanics*, *240*, 59–96. https://doi.org/10.1017/S002211209200003X

Laberteaux, K. R., & Ceccio, S. L. (2001). Partial cavity flows. Part 1. Cavities forming on models without spanwise variation. *Journal of Fluid Mechanics*, *431*, 1–41.

Langtry, R. B., & Menter, F. R. (2009). Correlation-based transition modeling for unstructured parallelized computational fluid dynamics codes. *AIAA Journal*, *47*(12), 2894–2906. https://doi.org/10.2514/1.42362

Lee, S.-J., Lee, J.-H., & Suh, J.-C. (2015). Further validation of the hybrid particle-mesh method for vortex shedding flow simulations. *International Journal of Naval Architecture and Ocean Engineering*, *7*(6), 1034–1043. https://doi.org/10.1515/ijnaoe-2015-0072

Leroux, J.-B., Astolfi, J. A., & Billard, J. Y. (2004). An experimental study of unsteady partial cavitation. *J. Fluids Eng.*, *126*(1), 94–101.

Li, H., & Vasquez, S. A. (2013). Numerical simulation of steady and unsteady compressible multiphase flows. *ASME 2012 International Mechanical Engineering Congress and Exposition*, 2239–2251. https://doi.org/10.1115/IMECE2012-87928

Liu, T. G., Khoo, B. C., & Xie, W. F. (2004). Isentropic one-fluid modelling of unsteady cavitating flow. *Journal of Computational Physics*, *201*(1), 80–108. https://doi.org/10.1016/j.jcp.2004.05.010

Liu, X., Zhou, L., Escaler, X., Wang, Z., Luo, Y., & De La Torre, O. (2017). Numerical simulation of added mass effects on a hydrofoil in cavitating flow using acoustic fluid–structure interaction. *Journal of Fluids Engineering*, *139*(041301). https://doi.org/10.1115/1.4035113

Lockey, K. J., Keller, K., Sick, M., Staehle, M. H., & Gehrer, A. (2006). Flow-induced vibrations at stay vanes: Experience on site and CFD simulations. *International Water Power & Dam Construction*, *5*, 102–106.

Lopes, R., Eça, L., Vaz, G., & Kerkvliet, M. (2021). Assessing numerical aspects of transitional flow simulations using the RANS equations. *International Journal of Computational Fluid Dynamics*, *35*(3), 157–178. https://doi.org/10.1080/10618562.2020.1870962

Madabhushi, A., & Mahesh, K. (2023). A compressible multi-scale model to simulate cavitating flows. *Journal of Fluid Mechanics*, *961*, A6.

Mani, A. (2012). Analysis and optimization of numerical sponge layers as a nonreflective boundary treatment. *Journal of Computational Physics*, *231*(2), 704–716. https://doi.org/10.1016/j.jcp.2011.10.017

Menter, F. R. (2009). Review of the shear-stress transport turbulence model experience from an industrial perspective. *International Journal of Computational Fluid Dynamics*, *23*(4), 305–316. https://doi.org/10.1080/10618560902773387

Menter, F. R. (2015). *Best practice: Scale-resolving simulations in ANSYS CFD*. ANSYS Germany GmbH.

Michelassi, V., Wissink, J., & Rodi, W. (2002). Analysis of DNS and LES of flow in a low pressure turbine cascade with incoming wakes and comparison with experiments. *Flow, Turbulence and Combustion*, *69*(3), 295–329. https://doi.org/10.1023/A:1027334303200

Mihatsch, M. S. (2017). *Numerical prediction of erosion and degassing effects in cavitating flows* [Technische Universität München]. https://mediatum.ub.tum.de/1306652

Morgut, M., Nobile, E., & Biluš, I. (2011). Comparison of mass transfer models for the numerical prediction of sheet cavitation around a hydrofoil. *International Journal of Multiphase Flow*, *37*(6), 620–626. https://doi.org/10.1016/j.ijmultiphaseflow.2011.03.005

Naudascher, E., & Rockwell, D. (1980). Oscillator-model approach to theidentification and assessment offlow-induced vibrations in a system. *Journal of Hydraulic Research*. https://doi.org/10.1080/00221688009499568

Niedźwiedzka, A., Schnerr, G. H., & Sobieski, W. (2016). Review of numerical models of cavitating flows with the use of the homogeneous approach. *Archives of Thermodynamics*, *37*(2).

O'Hern, T. J. (1990). An experimental investigation of turbulent shear flow cavitation. *Journal of Fluid Mechanics*, *215*, 365–391. https://doi.org/10.1017/S0022112090002683

Papillon, B., Brooks, J., Deniau, J., & Sabourin, M. (2006). Solving the guide vanes vibration problem at Shasta. *HydroVision 2006*, 121–126.

Prandtl, L. (1904). Über Flüssigkeitsbewegung bei sehr kleiner Reibung. *Mathematiker-Kongresses in Heidelberg*, *8*.

Qu, L., Norberg, C., Davidson, L., Peng, S.-H., & Wang, F. (2013). Quantitative numerical analysis of flow past a circular cylinder at Reynolds number between 50 and 200. *Journal of Fluids and Structures*, *39*, 347–370. https://doi.org/10.1016/j.jfluidstructs.2013.02.007

Ram, O., Agarwal, K., & Katz, J. (2020). On the mechanisms that sustain the inception of attached cavitation. *Journal of Fluid Mechanics*, *901*, R4. https://doi.org/10.1017/jfm.2020.646

Ramamurthy, A. S., & Balachandar, R. (1990). The near wake characteristics of cavitating bluff sources. *Journal of Fluids Engineering*, *112*(4), 492–495. https://doi.org/10.1115/1.2909433

Ramamurthy, A. S., & Bhaskaran, P. (1977). *Constrained flow past cavitating bluff bodies*.

Roig, R., Chen, J., de la Torre, O., & Escaler, X. (2021). Understanding the influence of wake cavitation on the dynamic response of hydraulic profiles under lock-in conditions. *Energies*, *14*(19), Article 19. https://doi.org/10.3390/en14196033

Sandberg, R. D., Michelassi, V., Pichler, R., Chen, L., & Johnstone, R. (2015). Compressible direct numerical simulation of low-pressure turbines—Part I: Methodology. *Journal of Turbomachinery*, *137*(051011). https://doi.org/10.1115/1.4028731

Sandhu, J. P. S., & Ghosh, S. (2021). A local correlation-based zero-equation transition model. *Computers & Fluids*, *214*, 104758. https://doi.org/10.1016/j.compfluid.2020.104758

Sarpkaya, T. (1976). Forces on cylinders near a plane boundary in a sinusoidally oscillating fluid. *Journal of Fluids Engineering*, *98*(3), 499–503. https://doi.org/10.1115/1.3448383

Sarpkaya, T. (2004). A critical review of the intrinsic nature of vortex-induced vibrations. *Journal of Fluids and Structures*, *19*(4), 389–447. https://doi.org/10.1016/j.jfluidstructs.2004.02.005

Sauer, J., & Schnerr, G. H. (2001). Development of a new cavitation model based on bubble dynamics. *ZAMM - Journal of Applied Mathematics and Mechanics / Zeitschrift Für Angewandte Mathematik Und Mechanik*, *81*(S3), 561–562. https://doi.org/10.1002/zamm.20010811559

Sayadi, T., Hamman, C. W., & Moin, P. (2013). Direct numerical simulation of complete H-type and K-type transitions with implications for the dynamics of turbulent boundary layers. *Journal of Fluid Mechanics*, *724*, 480–509. https://doi.org/10.1017/jfm.2013.142

Schaefer, J. W., & Eskinazi, S. (1959). An analysis of the vortex street generated in a viscous fluid. *Journal of Fluid Mechanics*, *6*(2), 241–260. https://doi.org/10.1017/S0022112059000593

Schenke, S. (2020). *Cavitation implosion loads from energy balance considerations in numerical flow simulations* [Delft University of Technology]. https://repository.tudelft.nl/islandora/object/uuid%3A9b8243b3-cc41-4c70-a95d-158c7ad96bb8

Schenke, S., & van Terwisga, T. (2017). Simulating compressibility in cavitating flows with an incompressible mass transfer flow solver. *Proceedings of the 5th International Symposiumon Marine Propulsion*.

Schmidt, S. J. (2015). *A low Mach number consistent compressible approach for simulation of cavitating flows*. Technical University of Munich.

Seo, J. H., Moon, Y. J., & Shin, B. R. (2008). Prediction of cavitating flow noise by direct numerical simulation. *Journal of Computational Physics*, *227*(13), 6511–6531. https://doi.org/10.1016/j.jcp.2008.03.016

Spalart, P. R., & Rumsey, C. L. (2007). Effective inflow conditions for turbulence models in aerodynamic calculations. *AIAA Journal*, *45*(10), 2544–2553. https://doi.org/10.2514/1.29373

Sridhar, G., & Katz, J. (1999). Effect of entrained bubbles on the structure of vortex rings. *Journal of Fluid Mechanics*, *397*, 171–202. https://doi.org/10.1017/S0022112099006187

Sumer, B. M. (2006). *Hydrodynamics around cylindrical strucures*. World Scientific.

Tiwari, A., Pantano, C., & Freund, J. B. (2015). Growth-and-collapse dynamics of small bubble clusters near a wall. *Journal of Fluid Mechanics*, *775*, 1–23. https://doi.org/10.1017/jfm.2015.287

Tong, S.-Y., Zhang, S., Wang, S.-P., & Li, S. (2022). Characteristics of the bubble-induced pressure, force, and impulse on a rigid wall. *Ocean Engineering*, *255*, 111484. https://doi.org/10.1016/j.oceaneng.2022.111484

Toro, E. F. (2009). *Riemann solvers and numerical methods for fluid dynamics: A practical introduction*. Springer. https://doi.org/10.1007/b79761

Trummler, T., Schmidt, S. J., & Adams, N. A. (2021). Effect of stand-off distance and spatial resolution on the pressure impact of near-wall vapor bubble collapses. *International Journal of Multiphase Flow*, *141*, 103618. https://doi.org/10.1016/j.ijmultiphaseflow.2021.103618

Vaca-Revelo, D., & Gnanaskandan, A. (2023). Numerical assessment of the condensation shock mechanism in sheet to cloud cavitation transition. *International Journal of Multiphase Flow*, *169*, 104616. https://doi.org/10.1016/j.ijmultiphaseflow.2023.104616

Von Kármán, T. (1912). GöttingenÜber den Mechanismus des Widerstandes, den ein bewegter Körper in einer Flüssigkeit erfährt. *Göttingen Math. Phys. Klasse*, *1912*(40), 547–556.

Wang, C., Wang, G., & Huang, B. (2020). Characteristics and dynamics of compressible cavitating flows with special emphasis on compressibility effects. *International Journal of Multiphase Flow*, *130*, 103357. https://doi.org/10.1016/j.ijmultiphaseflow.2020.103357

Wang, L., & Tian, F.-B. (2020). Numerical study of sound generation by three-dimensional flexible flapping wings during hovering flight. *Journal of Fluids and Structures*, *99*, 103165. https://doi.org/10.1016/j.jfluidstructs.2020.103165

Wang, R., & Xiao, Z. (2020). Transition effects on flow characteristics around a static two-dimensional airfoil. *Physics of Fluids*, *32*(3), 035113. https://doi.org/10.1063/1.5144860

Wang, W., Zhou, L., Tao, R., Song, X., & Wang, Z. (2023). Numerical simulation of dynamic characteristics of hydrofoil structure under cavitation conditions. *Ocean Engineering*, *280*, 114937. https://doi.org/10.1016/j.oceaneng.2023.114937

Wang, Z., Huang, B., Zhang, M., Wang, G., & Zhao, X. (2018). Experimental and numerical investigation of ventilated cavitating flow structures with special emphasis on vortex shedding dynamics. *International Journal of Multiphase Flow*, *98*, 79–95. https://doi.org/10.1016/j.ijmultiphaseflow.2017.08.014

Williamson, C. H. (1996). Vortex dynamics in the cylinder wake. *Annual Review of Fluid Mechanics*, *28*(1), 477–539.

Williamson, C. H. K., & Govardhan, R. (2004). Vortex-induced vibrations. *Annual Review of Fluid Mechanics*, *36*(Volume 36, 2004), 413–455. https://doi.org/10.1146/annurev.fluid.36.050802.122128

Wu, J., Deijlen, L., Bhatt, A., Ganesh, H., & Ceccio, S. L. (2021). Cavitation dynamics and vortex shedding in the wake of a bluff body. *Journal of Fluid Mechanics*, *917*, A26.

Wu, J., Ganesh, H., & Ceccio, S. (2019). Multimodal partial cavity shedding on a two-dimensional hydrofoil and its relation to the presence of bubbly shocks. *Experiments in Fluids*, *60*, 1–17.

Wu, W., & Piomelli, U. (2018). Effects of surface roughness on a separating turbulent boundary layer. *Journal of Fluid Mechanics*, *841*, 552–580. https://doi.org/10.1017/jfm.2018.101

Xing, T., & Frankel, S. H. (2002). Effect of cavitation on vortex dynamics in a submerged laminar jet. *AIAA Journal*, *40*(11), 2266–2276. https://doi.org/10.2514/2.1563

Yakubov, S., Maquil, T., & Rung, T. (2015). Experience using pressure-based CFD methods for Euler–Euler simulations of cavitating flows. *Computers & Fluids*, *111*, 91–104. https://doi.org/10.1016/j.compfluid.2015.01.008

Yan, Y., Chen, C., Fu, H., & Liu, C. (2014). DNS study on Λ-vortex and vortex ring formation in flow transition at Mach number 0.5. *Journal of Turbulence*, *15*(1), 1–21. https://doi.org/10.1080/14685248.2013.871023

Ye, C., Wang, F., Wang, C., & van Esch, B. P. M. (2020). Assessment of turbulence models for the boundary layer transition flow simulation around a hydrofoil. *Ocean Engineering*, *217*, 108124. https://doi.org/10.1016/j.oceaneng.2020.108124

Young, J. O., & Holl, J. W. (1966). *Effects of cavitation on periodic wakes behind symmetric wedges*.

Young, Y. L., Chang, J. C., Smith, S. M., Venning, J. A., Pearce, B. W., & Brandner, P. A. (2022). The influence of fluid–structure interaction on cloud cavitation about a rigid and a flexible

hydrofoil. Part 3. *Journal of Fluid Mechanics*, *934*, A2. https://doi.org/10.1017/jfm.2021.1017

Zeng, Y., Yao, Z., Huang, B., Wu, Q., & Wang, F. (2022). Experimental investigation of the hydrodynamic damping of a vibrating hydrofoil in cavitating flow. *Ocean Engineering*, *266*, 112734. https://doi.org/10.1016/j.oceaneng.2022.112734

Zheng, Z., & Lei, J. (2016). Application of the γ-Reθ transition model to simulations of the flow past a circular cylinder. *Flow, Turbulence and Combustion*, *97*(2), 401–426. https://doi.org/10.1007/s10494-016-9706-9

Zhou, H., Li, X., Qi, H., & Yu, C. (2019). Subgrid-scale model for large-eddy simulation of transition and turbulence in compressible flows. *Physics of Fluids*, *31*(12), 125118. https://doi.org/10.1063/1.5128061

Zwart, P., Gerber, A. G., & Belamri, T. (2004, January 1). A two-phase flow model for predicting cavitation dynamics. *Fifth International Conference on Multiphase Flow*.

Appendix

The example of the ZGB cavitation model using ANSYS Fluent macro "DEFINE_LINEARIZED_MASS_TRANSFER".

```
#include "udf.h"
DEFINE_LINEARIZED_MASS_TRANSFER(cav_source,cell,thread,from_index,from_species_index,
to_index, to_species_index, {
real vof_nuc = RP_Get_Real("mp/cvt/cfx/vof-nuc");
real r_b = RP_Get_Real("mp/cvt/cfx/r-bubbles");
real F_evap = RP_Get_Real("mp/cvt/cfx/f-evap");
real F_cond = RP_Get_Real("mp/cvt/cfx/f-cond");
real c_evap = 3.0*F_evap*vof_nuc/r_b;
real c_cond = 3.0*F_cond/r_b;
real P_SAT = RP_Get_Real("mp/cvt/vapor-p");
Thread *liq = THREAD_SUB_THREAD(thread, from_index);
Thread *vap = THREAD_SUB_THREAD(thread, to_index);
real m_dot, dp, m_source;
real p_op = RP_Get_Real ("operating-pressure");
real press = C_P(cell, thread) + p_op;
real rho_l = C_R(cell,liq);
real rho_v = C_R(cell,vap);
real vof_l = C_VOF(cell,liq);
real vof_v = C_VOF(cell,vap);
real r_rho_lv = 1./rho_v - 1./rho_l;
m_dot = 0.;
m_source = 0.0;
if (press <= P_SAT)
{
dp = P_SAT - press;
dp = MAX(dp, 1e-4);
m_dot = c_evap*rho_v*sqrt(2/3.0*dp/rho_l);
m_source = m_dot*vof_l;
*d_mdot_d_vof_from = m_dot;
*d_mdot_d_vof_to = -m_dot;
}
else
{
dp = press - P_SAT;
dp = MAX(dp, 1e-4);
m_dot = -c_cond*rho_v*sqrt(2/3.0*dp/rho_l);
m_source = m_dot*vof_v;
*d_mdot_d_vof_from = m_dot;
*d_mdot_d_vof_to = -m_dot;
}
/* ++++++++++ ds/dp term +++++++++++++++ */
if(NNULLP(THREAD_STORAGE(thread, SV_MT_DS_DP)))
C_STORAGE_R(cell,thread,SV_MT_DS_DP) = ABS(r_rho_lv*m_source/(2*dp));
return m_source;
}
```

List of publications

Journal articles

Chen, J., & Escaler, X. (2024). Numerical investigation of the cavitation effects on the wake dynamics behind a blunt trailing edge hydrofoil. *Ocean Engineering*, 302, 117599

Chen, J., Geng, L., & Escaler, X. (2020). Numerical investigation of the cavitation effects on the vortex shedding from a Hydrofoil with blunt trailing edge. *Fluids*, 5(4), 218.

Chen, J., & Escaler, X. Improving the simulation of compressible cavitation flows using sponge boundary layers. Submitted to *Ocean Engineering*.

Chen, J., Geng, L., & Escaler, X. A novel barotropic model for simulating compressible cavitating flows. Submitted to *Flow, Turbulence and Combustion*.

Geng, L., Chen, J., & Escaler, X. (2020). Improvement of cavitation mass transfer modeling by including Rayleigh–Plesset equation second order term. *European Journal of Mechanics-B/Fluids*, 84, 313-324.

Roig, R., Chen, J., de la Torre, O., & Escaler, X. (2021). Understanding the influence of wake cavitation on the dynamic response of hydraulic profiles under lock-in conditions. *Energies*, 14(19), 6033.

Conference papers

Chen, J., & Escaler, X. (2023). Effects of cavitation on the vortex shedding behind a truncated hydrofoil subjected to forced oscillation. *In 4th IAHR Asian Working Group Symposium on Hydraulic Machinery and Systems*, August 12-16, 2023, Kashgar, China.

Chen, J., & Escaler, X. (2022). Mass transfer rate effects on the cavitating vortex shedding flow around a circular cylinder at a low Reynolds number. *In IOP Conference Series: Earth and Environmental Science*.

Chen, J., Geng, L., De La Torre, O., & Escaler, X. (2021, June). Assessment of turbulence models for the prediction of Bénard-Von Kármán vortex shedding behind

a truncated hydrofoil in cavitation conditions. In *IOP Conference Series: Earth and Environmental Science*.

Chen, J., Geng, L., & Escaler, X. (2021). Large Eddy Simulation of the transient cavitating vortical flow in the wake of a hydrofoil. *In CAV2021: The International Symposium on Cavitation*, May 10-13, 2021, Daejon, Korea (pp. 1-6).